Interpretation of Seafloor Magnetotelluric Data using Thin-Sheet Modelling

by

Graham Stewart Heinson

A thesis submitted for the degree of Doctor of Philosophy of
the Australian National University

March 1991

Statement

Except as noted throughout the text and in the acknowledgements, the research described in this thesis is solely that of the author.

Graham Heinson

....

G. S. Heinson

Acknowledgements

During the three years of my Ph.D. study at the Research School of Earth Sciences, ANU, I have been very fortunate to interact with many people in Canberra, amongst the wider Australian Earth sciences community, and internationally. Many have contributed considerably to my research interests and general scientific training. However, my principal thanks goes to my supervisor, Dr Ted Lilley, who has provided generous scientific help, advice and a plethora of ideas throughout. I wish to thank Ted for his time and interest invested in all aspects of my scientific activity, and look forward to maintaining academic and social contact long into the future.

Participation in the EMRIDGE deployment cruise on the R. V. Hakhuomaru, and retrieval cruise on the R. V. Parizeau, were made possible by invitations from the chief scientists, Professor Segawa and Dr Lawrie Law. On both cruises I joined an Australian group led by Dr Antony White, from the Flinders University of South Australia. I would like to thank the other EMRIDGE collaborators, Profs Yukutake and Segawa and Drs Hamano and Utada from the University of Tokyo, Japan, and Dr Lawrie Law, from the Pacific Geoscience Centre, Canada, for their hospitality on both cruises, and encouragement and help in processing the seafloor data. I also participated in a subsequent instrument retrieval cruise from South Australia on the R. V. Franklin, by invitation of the chief scientist Professor Chris von der Borch, again joining Dr White's group. I wish to particularly thank Dr White and his family for their hospitality in Canada and Adelaide.

Some thoughts and analysis contained in this thesis were spawned from hours of discussions with Dr Antony White, and Dr Steven Constable from the Scripps Institution of Oceanography. I would particularly like to thank Dr Constable for patiently explaining a range of subtle ideas pertaining to the research topic in this thesis, both at the ANU and at the Scripps Institution of Oceanography, and for generous hospitality in both locations. Many ideas in this thesis stem directly from Dr Constable's research, and I have tried to acknowledge these in the text.

Mrs Merren Sloane spent hours processing the EMRIDGE data and assisted with many other aspects of my Ph.D. research at the ANU. I wish to thank Merren for her time and enthusiasm, and apologise for the untidyness of my part of the office. Analysis of Tasman Project data was greatly aided by the previous work by Drs Ian Ferguson, Nathan Bindoff and Richard Kellett, and many fruitful discussions with them were important factors in developing research ideas contained in this thesis.

Computer codes used in this thesis were kindly supplied by J. T. Weaver (University of Victoria, B.C., Canada), G. D. Egbert (Oregon State University, Oregon, U.S.A.), J. R. Booker (University of Washington, Washington, U.S.A.), R. L. Parker, S. C. Constable and C deGroot-Hedlin (Scripps Institution of Oceanography, California, U.S.A), G. Fischer and B. V. Le Quang (Neuchatel Observatory, Switzerland) and I. J. Feguson (University of Manitoba, Winnipeg, Canada). Most of the diagrams in this thesis were generated by PLOTXY, CONTOUR and COLOR supplied by R. L. Parker and S. C. Constable. I would like to acknowledge additional drafting of figures by Ted Lilley, Merren Sloane, Clementine Krayshek and Bronwyn Dunshea. The Computer Services Centre at the ANU have kindly assisted with many computation problems over three years and have complied with numerous unreasonable requests for disk storage space.

My advisers at ANU, Drs Brian Kennett and Geoff Davies, were always helpful and available, and have contributed greatly to my understanding of Earth. At the Research School of Earth Sciences many conversations considerably widened my appreciation of the research project. I wish to express my thanks to Profs Anton Hales, Kurt Lambeck, Ted Ringwood and Drs Ian Jackson, Jean Braun and Bill McDonough in particular for their help and time donated to explaining many basic questions about the nature of Earth. Discussions with other fellow students from the Research School of Earth Sciences on scientific and not so scientific issues, have always been welcome.

My time as a research student at the ANU was made possible by the award to me in Britain of a Commonwealth Scholarship and Fellowship Plan Award from the Association of Commonwealth Universities, and I am most grateful for the opportunities their scholarship created. I also wish to acknowledge the financial assistance for participation at various conferences by the Geological Society of Australia, the Australian Society of Exploration Geophysicists and IAGA.

Socially, my three years in Canberra have been extremely busy and very enjoyable. In particular my warmest thanks go to Bronwyn Dunshea for her love and support throughout my project, especially during the writing period. I wish to also express my sincere thanks to Ted and Penny Lilley for their generous hospitality and many wonderful meals over the years.

Abstract

Observations of the fluctuations of Earth's electric and magnetic fields can be used to generate magnetotelluric (MT) and geomagnetic depth sounding (GDS) response functions, which provide a measure of Earth's electrical conductivity structure. Electrical conduction is primarily determined by the temperature of sub-solidus minerals, the porosity, the fluid saturation, and the melt fraction; thus seafloor MT and GDS methods may be used to probe the structure of active tectonic regions, and to map the thermal evolution of 'dry' lithosphere with age.

Seafloor topography and the continental margins have a profound influence on the electric currents induced in the highly-conducting salt-water of the oceans. Three-dimensional (3D) modelling, using the thin-sheet approximation, shows that electric current channelling around coastlines and towards deep ocean may distort observed MT and GDS estimates in such a manner that a simple one-dimensional (1D) interpretation of them is not valid.

Analysis of new electric and magnetic field measurements, from instruments deployed across the Juan de Fuca Ridge in the northeast Pacific Ocean, show that observed electromagnetic (EM) induction effects are dominated by the elevation of the ridge axis and the proximity of deeper ocean, south of the Blanco Fracture Zone. Thin-sheet modelling demonstrates that observed GDS response functions are consistent with just the changes in bathymetry, implying there is no linear magma chamber at the ridge, despite recent evidence of intense ridge-axis hydrothermal activity. Beneath the Juan de Fuca Ridge, a 'dry' upper lithosphere at temperatures less than 1000 °C is a required feature of the modelling to reproduce observations. Below this layer, 1D inversions suggest a large fraction of decompressional melt, as the conductance over depths 70 to 200 km is higher than interpreted for older oceanic lithosphere.

Anisotropy in Tasman Project seafloor MT soundings is diagnostic of an electrically resistive upper lithosphere: although Tasman Sea lithosphere of age 55 to 90 Ma is probably cooler than that beneath the Juan de Fuca Ridge, changes in the electrical conductance with age are not resolved. Thin-sheet modelling suggests that differences in the conductivity profile for 65 Ma lithosphere below 80 km, and the laboratory measured conductivity of olivine at temperatures of 800 to 1350 °C, are not the result of 3D induction effects in the Tasman Sea alone. If observed high conductivities are the result of sub-solidus olivine conduction, unrealistic upper mantle temperatures of ~1500 °C are implied. Partial melting is unlikely as the sole mechanism for the high conductivities, as improbably large melt fractions (> 5%) are required: other explanations advanced instead include enhanced conductivity of grain boundaries and the presence of volatiles or hydrogen ions in sub-solidus olivine. There is little evidence for major changes in structure with age across the Tasman Sea.

Table of Contents

page

Chapter 1 : Introduction

Chapter 2 : Seafloor Electromagnetic Experiments

Chapter 3 : The Thin-Sheet Electromagnetic Approximation

Chapter 4 : The Conductivity of the Oceanic Upper Mantle: Forward-Calculations From Laboratory Data

Chapter 5 : Thin-Sheet Modelling of Coastlines, Ocean Basins and Seafloor Topography

Chapter 6 : EMRIDGE : Electromagnetic Exploration of the Juan de Fuca Ridge

Chapter 7 : A Tasman Project Thin-Sheet Model and the Conductivity Structure Beneath the Tasman Sea

Chapter 8 : Conclusions

Note Added 10th July, 1991

It has been pointed out by Professor J. T. Weaver that a number of thin-sheet models included in this thesis do not adequately meet condition (d) on page 85 below, especially those which include a resistive layer (of conductivity much less than 10^{-3} $S.m^{-1}$) directly beneath the thin-sheet. While condition (c) on page 84 requires grid-node spacing to be less than a certain fraction of the skin depth in the underlying layer (suggested by Weaver in his 1982 paper to be about one-third), condition (d) means that grid-node spacing should also be greater than another smaller fraction (approximately one-tenth) of the same skin depth. Then, with a thin-sheet of 15 x 15 grid-nodes, the total area covered will be not less than one or two skin depths in horizontal extent (by condition (d)), and also not more than approximately five skin depths in horizontal extent (by condition (c)).

Thus, in chapter 5 below and elsewhere, the "correction factors" (defined on page 119, eq. 5.3) arise in the first instance quite simply from departures of the models tested from these conditions. Re-computing Fig. 5.2 (page 117) but expanding the grid-node spacing to comply with conditions (c) and (d) as the lithospheric conductivity is decreased produces the values in Fig. A below.

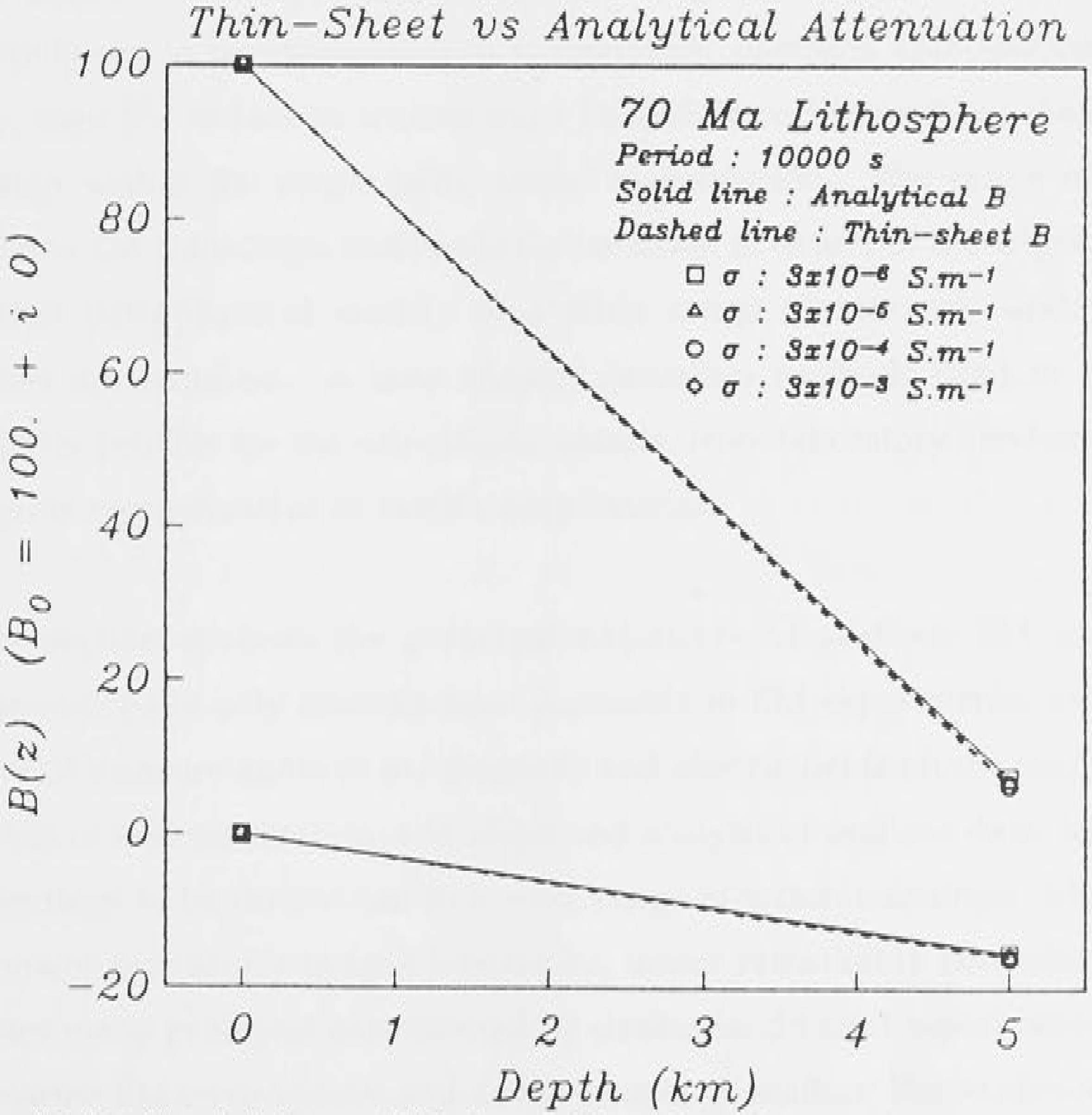

Figure A As for Fig. 5.2 (page 117), but with a thin-sheet of horizontal extent two skin-depths across.

Similarly, the electric field values within the sheet (Table 5.4, page 118) are re-computed in Table A. From inspection of Fig. A and Table A, it be seen there is agreement between model computation and analytical response (see Fig. 5.1, page 117). This point is the one discussed on page 179 of Weaver (1982) and page 186 of McKirdy *et al.* (1985).

Table A As for Table 5.4 (page 118), but with a thin-sheet of horizontal extent two skin-depths across. The amplitude is in units of mV.m^{-1}, and the phase is in degrees.

Upper Lithosphere Conductivity (S.m^{-1})	Analytical Sea-Surface Electric Field		Thin-Sheet Ocean Electric Field		Analytical Seafloor Electric Field	
	Amplitude	Phase	Amplitude	Phase	Amplitude	Phase
3x10^{-6}	4.5916	10.87	4.5736	9.55	4.5377	8.85
3x10^{-5}	4.5912	10.87	4.5624	9.61	4.5373	8.85
3x10^{-4}	4.5877	10.86	4.5552	9.63	4.5339	8.84
3x10^{-3}	4.5527	10.83	4.5158	9.41	4.4992	8.78

Chapter 1 : Introduction

1.1 Introduction

In this chapter, an outline of the basic physical and mathematical theory of electromagnetic (EM) soundings is provided with emphasis on the application of EM techniques used for seafloor experiments. The objectives of this chapter are to provide the background theory required for the analysis of data from the Tasman Sea, and the Juan de Fuca Ridge in the northeast Pacific Ocean, and for the processing of synthetic data from forward and inverse model studies. Much of this material is reproduced from published literature and reference is made to the principal sources wherever possible. The material is included here as it provides the raison d'etre for EM studies, and shows how information on Earth's structure is derived from surface or seafloor measurements. In addition, some of this background theory is expanded in later chapters, to take account of the particular unique aspects of seafloor EM observations, and to analyse the output of modelling algorithms.

The second section of this chapter examines the sensitivity of EM methods to the physical state of Earth. If interpretations in terms of physical parameters other than electrical conductivity are to be made, such as temperature, chemical composition, melt fraction and porosity, then EM induction studies must be understood in terms of the physics of electrical conduction within the target body under investigation. The range of depths which are accessible to EM soundings, and hence the variation in nature of the targets of such soundings, imply that petrophysical studies of a wide range of minerals under varying physical conditions are required. A later chapter describes methods used to determine electrical conductivity profiles for the sub-oceanic mantle, from laboratory conductivity measurements on minerals representative of Earth's deep interior.

The last section reviews the principal objectives of seafloor EM soundings. Seafloor environments have only recently been accessible to EM experiments, owing to the technical difficulty of measurements of the magnetic and electric fields on the seafloor. However, new techniques of instrumentation, and improved analysis of seafloor data, have allowed seafloor EM soundings to be carried out in a wide range of tectonic settings. Moreover, the seafloor environment provides a unique laboratory, under remarkably controlled conditions, which eliminates many problems encountered by similar land-based experiments. Brief descriptions of the marine EM environment and developments in seafloor EM studies are given, to indicate the importance of such measurements to understanding of Earth's oceans and tectonic structure.

1.2 The Physics of Electromagnetic Induction

1.2.1 Basic Equations of Electromagnetic Induction

The whole of classical EM theory can be based on four differential equations, first enunciated by Maxwell, and Ohm's Law. Here, the following definitions are made, with the appropriate SI units, shown in Table 1.1.

Table 1.1 Electric and Magnetic Quantities and SI units.

Electric and Magnetic Quantities	SI Units
Magnetic induction : **B**	tesla or T
Magnetic field intensity : **H**	amp.m^{-1} or A.m^{-1}
Electric field : **E**	volt.m^{-1} or V·m^{-1}
Current-density : J	amp.m^{-2} or A.m^{-2}
Resistance : R	ohm or Ω
Conductance : G	siemens or S
Resistivity : ρ	ohm.m or Ω.m
Conductivity : σ	mho.m^{-1} or siemens.m^{-1} or S.m^{-1}
Electric permittivity : ε	farads.m^{-1} or F.m^{-1}
Absolute permittivity : ε_o	8.845 x 10^{-12} F.m^{-1}
Magnetic permeability : μ	henry.m^{-1} or H.m^{-1}
Absolute permeability : μ_o	1.246 x 10^{-6} H.m^{-1}
Electric charge density : q	coulomb.m^{-3} or C.m^{-3}

Conductivity is the reciprocal of resistivity: there is little agreement in the EM scientific community as to which term is more appropriate to describe the electrical properties of Earth. In this thesis, both terms will be used quite freely, as both are required to emphasise the processes of EM induction in the Earth. For example, the high resistivity (low conductivity) of the lithosphere is almost invisible to one-dimensional (1D) magnetotelluric (MT) techniques, which have greatest sensitivity to high conductivity (low resistivity) regions; however, the high resistivity (low conductivity) of the lithosphere has a profound effect on two-dimensional (2D) and three-dimensional (3D) interpretations of MT data. Figures showing Earth's electrical structure will be in terms of conductivity: there is general agreement that conductivity increases with depth in the mantle, and the rise in conductivity is analogous to increases in other properties of Earth with depth, such as density, temperature and seismic wave velocity. Reference will also be made to the conductance of a body. For a body of uniform conductivity, the conductance is defined here as the product of conductivity with the thickness, which is generally measured vertically.

Maxwell's equations use the vectors which describe the magnetic field **H** and **B**, and two analogous electric vectors **E** and **D**. A fifth vector used is **J**, the current-density, and finally the scalar electric charge density q. Maxwell's equations (1.1 - 1.4), the constitutive equations (1.5 - 1.7) for a stationary conductor, and the EM boundary conditions (1.8 - 1.10) across an interface between two media can be expressed as

$$\nabla \times \mathbf{H} = \mathbf{J} + \frac{\partial \mathbf{D}}{\partial t} \tag{1.1}$$

$$\nabla \times \mathbf{E} = -\frac{\partial \mathbf{B}}{\partial t} \tag{1.2}$$

$$\nabla . \mathbf{B} = 0 \tag{1.3}$$

$$\nabla . \mathbf{D} = q \tag{1.4}$$

$$\mathbf{J} = \sigma \mathbf{E} \tag{1.5}$$

$$\mathbf{D} = \varepsilon \mathbf{E} \tag{1.6}$$

$$\mathbf{B} = \mu \mathbf{H} \tag{1.7}$$

Tangential **E** is continuous across the interface of two media (1.8)

The discontinuity in tangential **H** across the interface of two media is equal to the surface current-density in the perpendicular direction (1.9)

Normal **B** is continuous across the interface of two media (1.10)

The fundamental equation of EM induction in a stationary conductor is the diffusion equation. By eliminating **E** from eqs 1.1 and 1.2, and assuming **D** can be ignored, the diffusion equation can be formulated as

$$\nabla^2 \mathbf{B} = \sigma\mu \frac{\partial \mathbf{B}}{\partial t} \tag{1.11}$$

Alternatively, **B** can be eliminated from eqs 1.1 to 1.4 to give

$$\nabla^2 \mathbf{E} = \sigma\mu \frac{\partial \mathbf{E}}{\partial t} + \nabla \frac{q}{\varepsilon} \tag{1.12}$$

Here, the magnetic permeability μ and the electrical permittivity ε in the half-space and in the insulator are assumed to be isotropic, uniform, period-independent and equal to their absolute values μ_0 and ε_0, shown in Table 1.1. Equation 1.11 is valid if the small contribution to the current-density made by displacement currents is ignored, which is equivalent to the condition that

$$\frac{\partial D}{\partial t} \ll J \qquad (1.13)$$

Using scale arguments, if T is the period of inducing EM field, then

$$\frac{\partial D}{\partial t} = o(\frac{D}{T}) = o(\frac{\varepsilon J}{\sigma T}) \qquad (1.14)$$

so that eq. 1.13 is satisfied if $T \gg \varepsilon/\sigma$. For Earth, the maximum electrical permittivity and minimum conductivity are approximately 100 ε_0 and 10^{-7} $S.m^{-1}$ respectively: when these values are substituted into eq. 1.13, it implies that $T \gg 0.001$ s. The minimum period used for seafloor EM observations of natural fluctuations of Earth's magnetic and electric fields is of the order of one minute, so that it is legitimate to ignore the displacement currents in eq. 1.11. However, it is not legitimate to ignore the effect of electrostatic charges on **E** in eq. 1.12. Electrostatic charges occur when the current has a component parallel to the gradient of conductivity, or flows across a conductivity discontinuity (Parkinson, 1983).

The magnetic field **B** may be expressed by the Fourier transform as an infinite sum of superimposed sine waves. Equation 1.11 is linear in **B**, so it may be solved in terms of an infinite sum of equations, each involving **B** at a single frequency. Considering a sine wave of angular frequency ω, the magnetic field can be expressed as

$$B(t) = B_o e^{+i\omega t} \qquad (1.15)$$

where B_o is a complex number, t is the time and $i = \sqrt{-1}$. The spatial variation of **B** is also expressed this way, if B_o is written as

$$Bo = B' e^{iky} \qquad (1.16)$$

When the diffusion equation is applied to a single sine wave, eq. 1.11 can be written

$$\nabla^2 \mathbf{B} = i\omega\mu\sigma \mathbf{B} = k^2 \mathbf{B} \qquad (1.17)$$

so that $k^2 = i\omega\mu\sigma$.

1.2.2 Analytical Solutions for Induction in a Half-Space

Analytical solutions exist for 1D conductivity structures generally. In this section the case of an uniform horizontal oscillatory magnetic field and a semi-infinite conductor with a horizontal boundary is considered, shown in Figure 1.1.

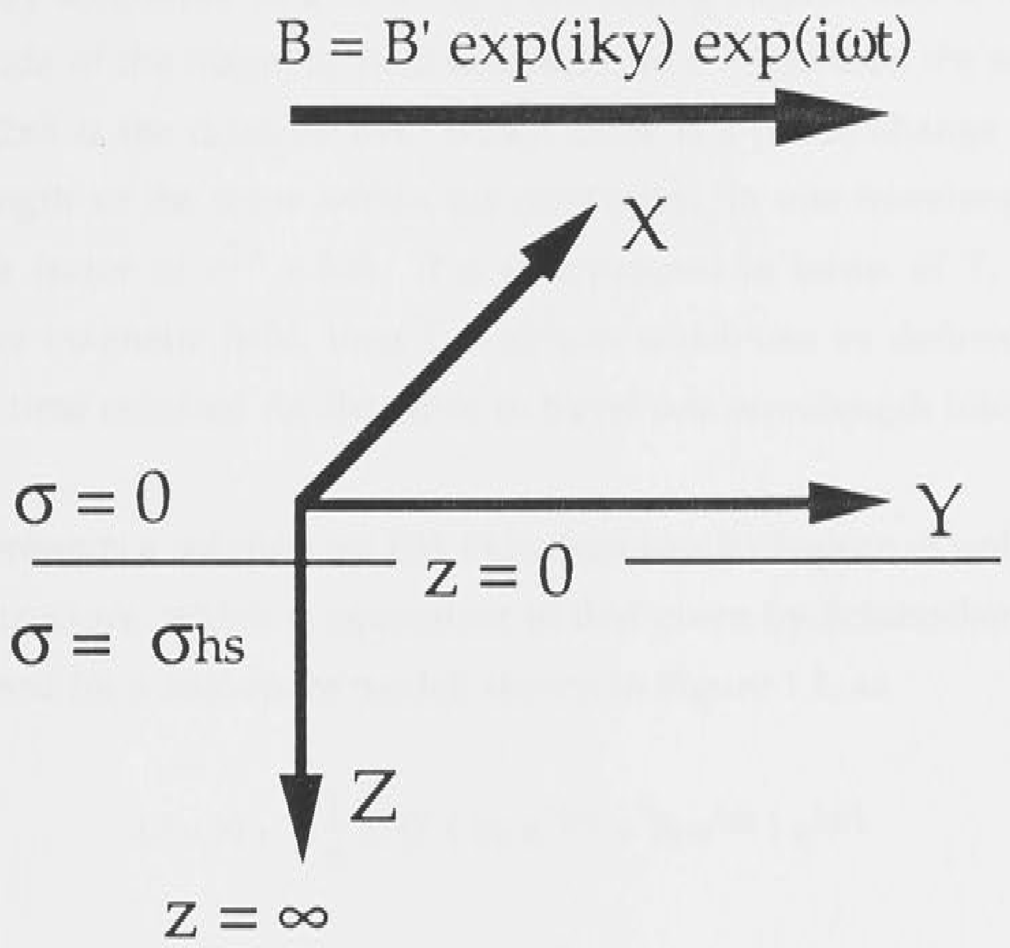

Figure 1.1 Schematic illustration of half-space conductivity model, with the coordinate systems used in this thesis. The X and Y axes are in arbitrary orientation, but in practice are often aligned with the geomagnetic north (H) and geomagnetic east (D) directions. An external sinusoidal source-field of angular frequency ω, amplitude B' and wavenumber k is also shown.

If the oscillating field is regarded as a wave, then such conditions imply that the wavelength is infinite, outside the conductor. The magnetic field within the conductor can be expressed as a damped wave with magnitude

$$B = B_o \, e^{\alpha z} \, e^{i\omega t} \tag{1.18}$$

where B_o is real, the boundary of the interface between insulator and half-space is at $z = 0$, and z increases positively into the conductor. Substituting eq. 1.18 into eq. 1.17 gives

$$\alpha = \pm(1+i)\sqrt{\frac{\omega\sigma\mu}{2}} \tag{1.19}$$

The skin depth δ can be defined such that $\delta = \sqrt{\frac{2}{\omega\sigma\mu}}$: eq. 1.18 can be expressed as

$$B = B_o \, e^{-z/\delta} \, e^{i(\omega t - z/\delta)} \tag{1.20}$$

Only the negative sign solution for α from eq. 1.19 is taken, as the solution with positive sign would correspond to a field increasing exponentially into the conductor, which does not satisfy the boundary conditions as $z \to \infty$. It can clearly be seen that at the skin depth δ in Earth, the magnitude of the magnetic field is a factor of e^{-1} less than the surface value. The vertical distance $2\pi\delta$ is the distance over which there is a phase change of 2π; this can be called the 'wavelength' of the wave within the conductor. In one wavelength, the amplitude will decrease by a factor of $e^{2\pi} = 535$. If ω is expressed in terms of T, the period of the inducing sine wave magnetic field, then $T = \pi\delta^2\mu\sigma$, which can be defined as the 'diffusion time', which is the time required for the wave to travel one wavelength into the conductor.

Parkinson (1983) presents a solution for EM induction in a half-space of uniform conductivity and in a layered structure, which is equivalent to that given by Schmucker (1970). A scalar potential U is defined for a half-space model, shown in Figure 1.1, as

$$U(y,z) = -\frac{1}{\upsilon} e^{i\upsilon y} \left(B_e e^{-\upsilon z} + B_i e^{\upsilon z} \right) e^{i\omega t} \tag{1.21}$$

which represents an elliptically polarised wave travelling in the -Y-direction with a velocity of ω/υ. This is the velocity of the source of the field, rather than being the velocity of propagation of the EM wave. The subscripts $_i$ and $_e$ refer to the internal and external parts of the magnetic field respectively. Neglecting the displacement currents in eq. 1.11 is equivalent to assuming that the propagation velocity is negligible. More complicated fields can be considered as the summation of waves of this type, so it sufficient to solve only this for this case. Thus, eq. 1.21 represents the field above the conductive half-space.

The field within the half-space can be expressed by a vector potential in the X direction, with magnitude

$$A_x = F(y) \left(C e^{-\alpha z} + D e^{\alpha z} \right) e^{i\omega t} \tag{1.22}$$

where A satisfies the vector equation

$$\nabla^2 \mathbf{A} = \sigma\mu \frac{\partial \mathbf{A}}{\partial t} \tag{1.23}$$

It is straightforward to show that $F(y) = \exp [\, i \sqrt{\alpha^2 - k^2}\, y \,]$. At the surface $z = 0$, the boundary conditions for the horizontal component (eqs 1.9) gives

$$i e^{i\upsilon y} \left(B_e + B_i \right) = F(y) \left(-\alpha C + \alpha D \right) \tag{1.24}$$

Substituting the expression for F(y) in this equation implies that $\alpha^2 = \upsilon^2 + k^2$, and so $F(y) = e^{i\upsilon y}$. The vertical component boundary condition leads to

$$e^{i\upsilon y}\ (B_e - B_i) = i\upsilon\ e^{i\upsilon y}\ (C + D) \qquad (1.25)$$

Within the conductive half-space, A_x cannot increase without limits as $z \to \infty$, so that $D = 0$. Eliminating C from eqs 1.24 and 1.25 leads to

$$\frac{B_i}{B_e} = \frac{(\alpha - \upsilon)}{(\alpha + \upsilon)} \qquad (1.26)$$

From eqs 1.22 and 1.26, the ratio of the vertical to horizontal components of the magnetic field is

$$\frac{B_z}{B_y} = i\upsilon \frac{1}{\alpha} = i\upsilon \frac{1}{\upsilon^2 + k^2} \qquad (1.27)$$

As the electric current flows horizontally, i.e. parallel to the discontinuity in conductivity, there is no electrostatic charge across the interface, so that eq. 1.12 may be expressed as

$$\mathbf{E} = - \frac{\partial \mathbf{A}}{\partial t} \qquad (1.28)$$

The resulting magnitude of electric field in the X-direction, omitting the time factor, is

$$E_x = - \frac{\omega}{\alpha} e^{i\upsilon y}\ e^{-\alpha z}\ (B_e + B_i) \qquad (1.29)$$

so that at the surface

$$\frac{E_x}{B_y} = \frac{i\omega}{\alpha} = \frac{i\omega}{\sqrt{\upsilon^2 + k^2}} \qquad (1.30)$$

Similarly, it can be shown that

$$\frac{E_y}{B_x} = - \frac{i\omega}{\alpha} = - \frac{i\omega}{\sqrt{\upsilon^2 + k^2}} \qquad (1.31)$$

1.2.3 Analytical Solutions for Induction in a Layered Half-Space

The method described for induction in a half-space can be generalised to any number of horizontal uniform strata. Figure 1.2 shows the notation used for a flat earth model with a layered conductivity structure.

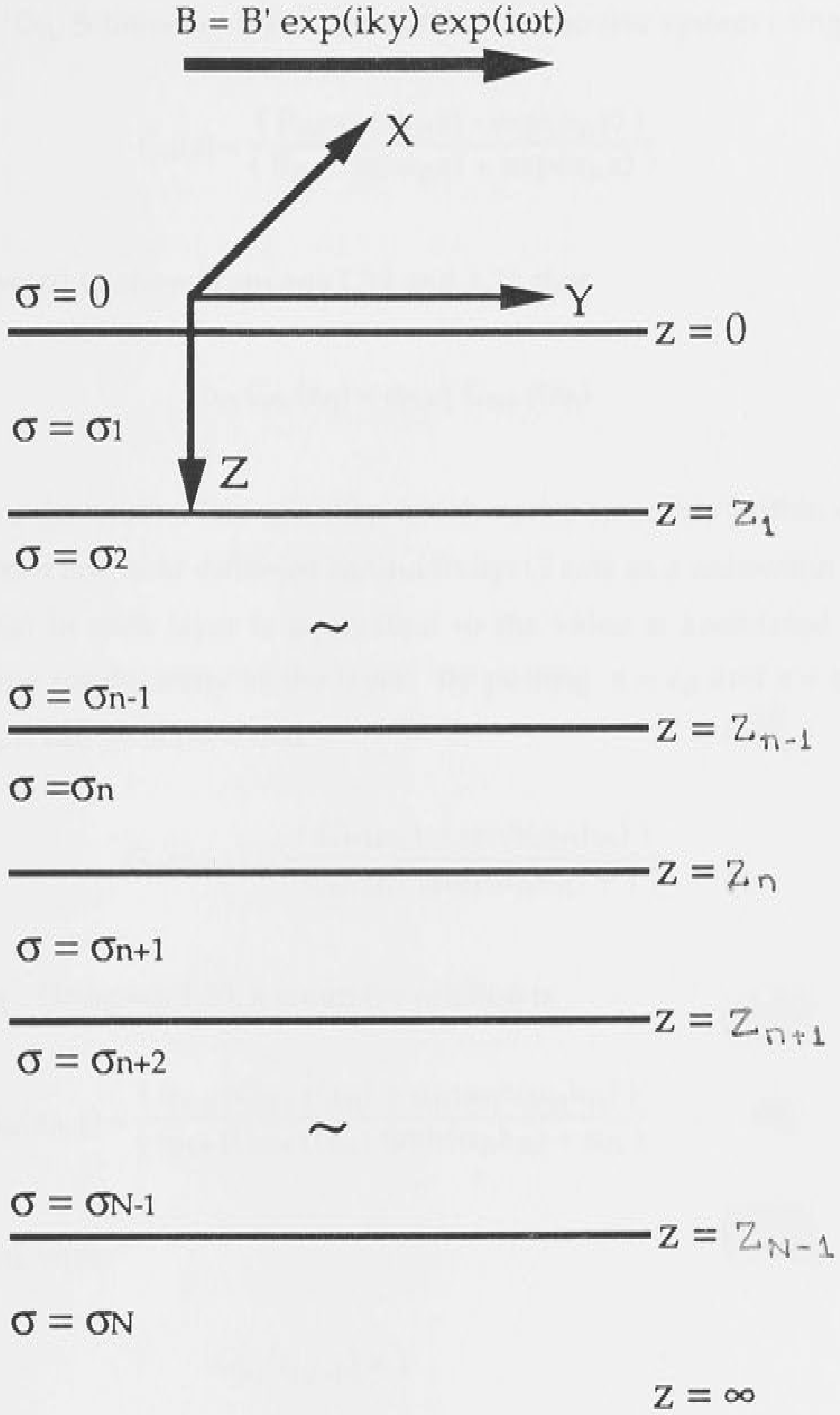

Figure 1.2 Schematic illustration of a layered half-space conductivity model, with conductivity varying with depth only.

In the n^{th} slab, the vector potential can be defined as in eq. 1.22. At the boundary of the n^{th} and $n+1^{th}$ slab,

$$\begin{aligned}&-\alpha_n C_n \exp(-\alpha_n z_n) + \alpha_n D_n \exp(\alpha_n z_n)\\ &= -\alpha_{n+1} C_{n+1} \exp(-\alpha_{n+1} z_n) + \alpha_{n+1} D_{n+1} \exp(\alpha_{n+1} z_n)\end{aligned} \tag{1.32}$$

$$\begin{aligned}&C_n \exp(-\alpha_n z_n) + D_n \exp(\alpha_n z_n)\\ &= C_{n+1} \exp(-\alpha_{n+1} z_n) + D_{n+1} \exp(\alpha_{n+1} z_n)\end{aligned} \tag{1.33}$$

By writing $R_n = C_n/D_n$, Schmucker (1970) has defined a recursive system using the function

$$G_n(z) = \frac{(R_n \exp(-\alpha_n z) - \exp(\alpha_n z))}{(R_n \exp(-\alpha_n z) + \exp(\alpha_n z))} \tag{1.34}$$

and it is straightforward to show from eqs 1.32 and 1.33 that

$$\alpha_n G_n (z_n) = \alpha_{n+1} G_{n+1}(z_n) \tag{1.35}$$

The parameter G is a dimension-less quantity which varies smoothly within each layer but is discontinuous between layers of different conductivity: G acts as a correction factor, such that the product $G(z)\alpha(z)$ in each layer is equivalent to the value α associated with a uniform half-space of the same conductivity as the layer. By putting $z = z_n$ and $z = z_{n-1}$ into eq. 1.34 and eliminating R_n, it can be shown that

$$G_n(z_{n-1}) = \frac{(G_n(z_n) + \tanh(\alpha_n h_n))}{(G_n(z_n) \tanh(\alpha_n h_n) + 1)} \tag{1.36}$$

where $h_n = z_n - z_{n-1}$. Using eq. 1.35, a recursive relation is

$$G_n(z_{n-1}) = \frac{(\alpha_{n+1} G_{n+1}(z_n) + \alpha_n \tanh(\alpha_n h_n))}{(\alpha_{n+1} G_{n+1}(z_n) \tanh(\alpha_n h_n) + \alpha_n)} \tag{1.37}$$

which can be started with

$$G_N(z_{N-1}) = 1 \tag{1.38}$$

It can then be shown that the ratio of vertical to horizontal components of the magnetic field, and the ratio of the horizontal electric to the horizontal magnetic field are given by

$$\frac{B_z}{B_y} = \frac{\upsilon}{\alpha_1 G_1(0)} \tag{1.39}$$

$$\frac{E_x}{B_y} = -\frac{i\omega}{\alpha_1 G_1(0)} \tag{1.40}$$

Finally, the horizontal components of the electric field **E** and the magnetic field **B** can be calculated at any depth in one layer of a layered half-space, from Schmucker's (1970) recursive relationship, eq. 1.36. It can be shown that the ratio of the electric field **E**(z) at depth z within any layer is related to the value of **E** at the surface of that layer, defined to be $\mathbf{E}_o$, by the expression

$$E(z) = E_0 \{ \cosh(\alpha z) - G \sinh(\alpha z) \} \quad (1.41)$$

where α and G are the appropriate parameters, defined in eqs 1.19 and 1.34, for the top of the layer in question. The horizontal magnetic field **B**(z) can similarly be related to the magnetic field at the surface of the layer $\mathbf{B}_0$, by

$$B(z) = B_0 \frac{\alpha G}{\alpha(z)\, G(z)} E_0 \{ \cosh(\alpha z) - G \sinh(\alpha z) \} \quad (1.42)$$

In eq. 1.42, α and G are the parameters at the top of the layer, whilst $\alpha(z)$ and $G(z)$ are the parameters at a depth z within the layer. The expression $\{ \cosh(\alpha z) - G \sinh(\alpha z) \}$ is continuous across a horizontal boundary, so if z is made equal to the thickness of the layer in the layered half-space, **E** and **B** at the top of the layer may be related to **E** and **B** at the lower interface. Hence, a recursive relationship can be established in which the electric and magnetic fields at any depth in a layered half-space can be expressed in terms of the field components at the interface with the insulator.

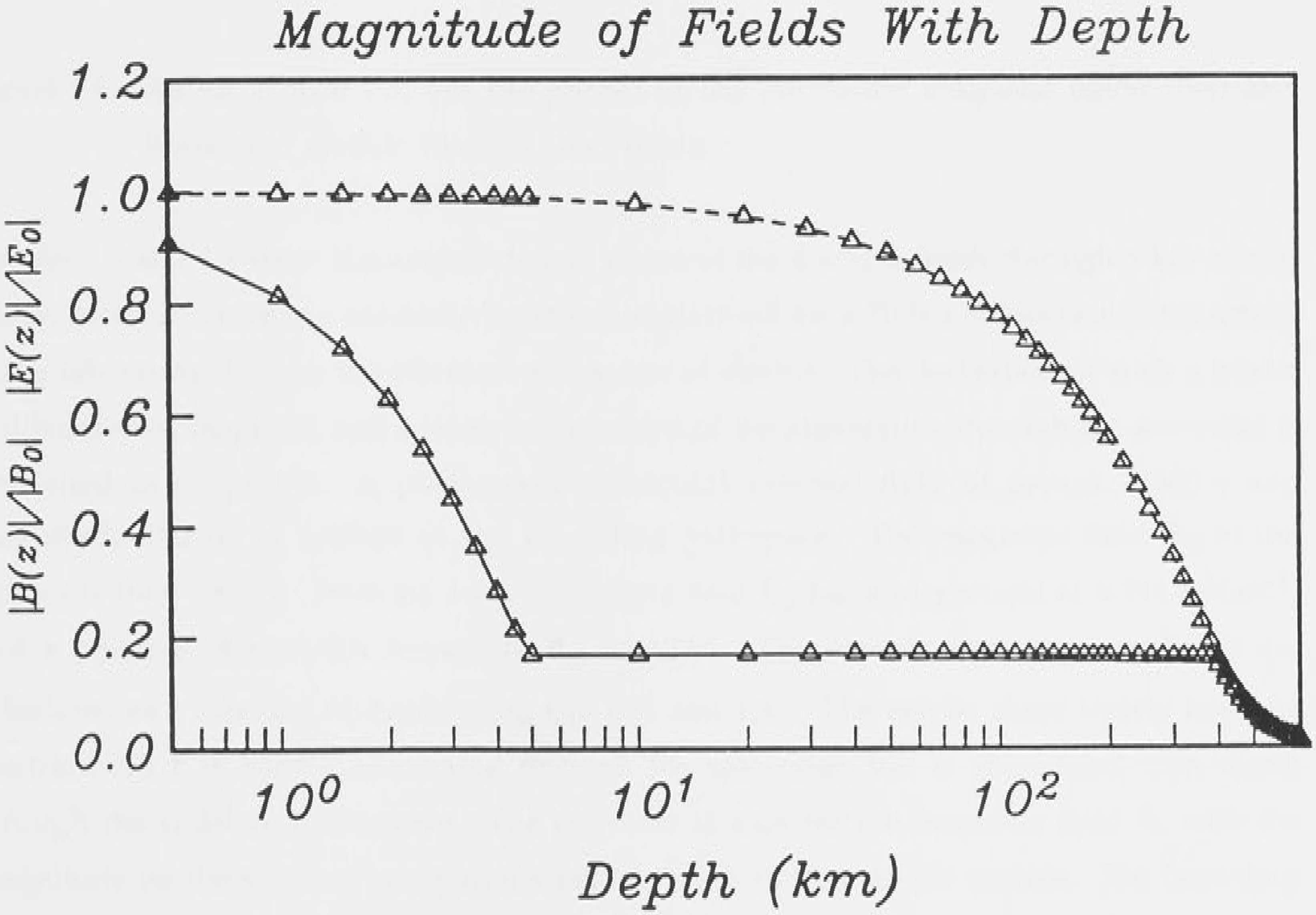

Figure 1.3 The amplitudes of the horizontal magnetic (solid line) and horizontal electric (dashed line) fields, through 5 km of sea-water and a layered conductivity structure representative of the sub-oceanic upper mantle. The amplitudes of the fields are normalised with respect to the surface fields.

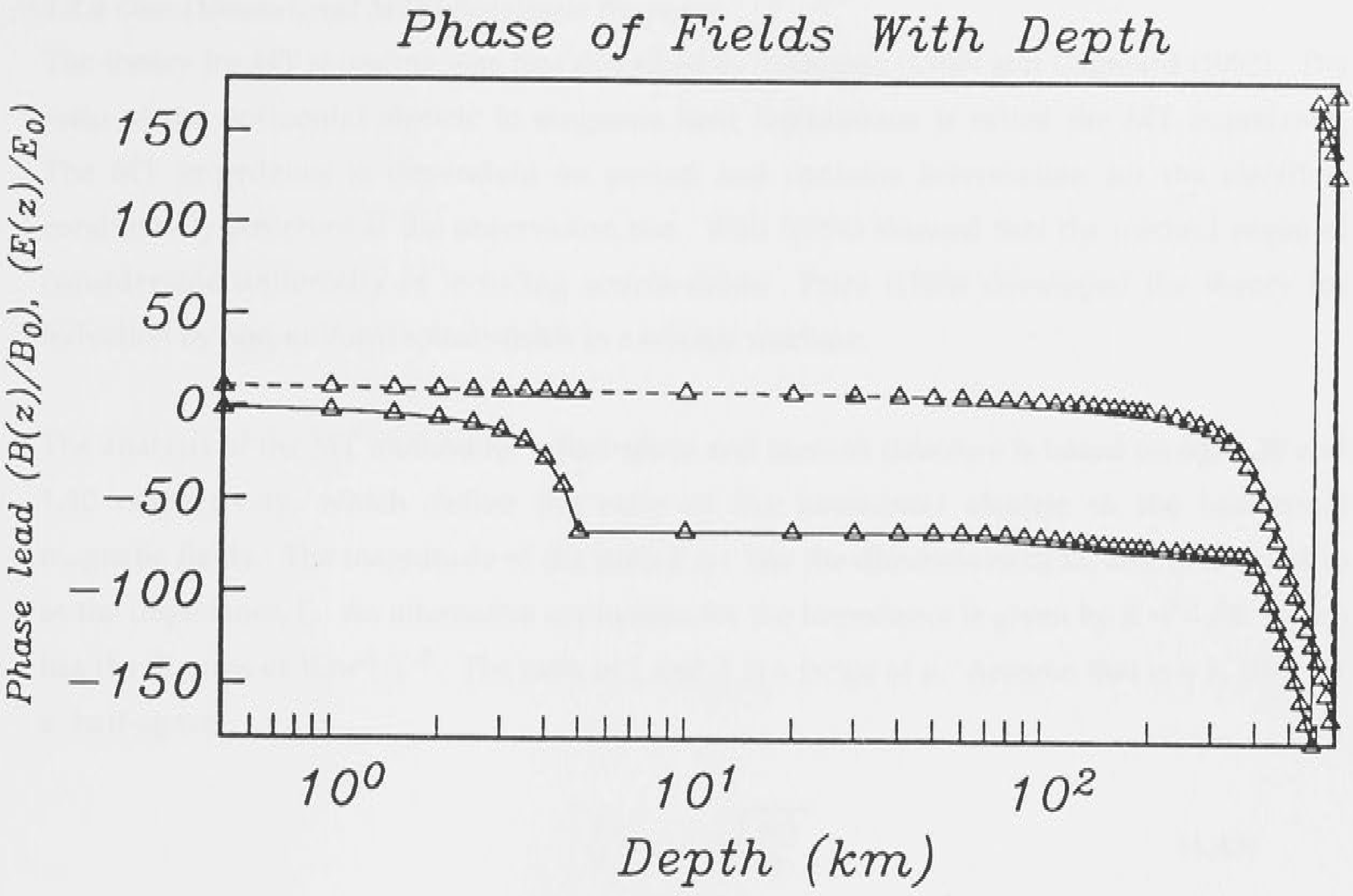

Figure 1.4 As for Figure 1.3, but the phases of the horizontal magnetic (solid line) and horizontal electric (dashed line) fields.

Figures 1.3 and 1.4 show the amplitude and phase of the **E** and **B** fields through 5 km of sea-water, beneath which is a conductivity structure derived for a 70 Ma sub-oceanic lithosphere using laboratory data on the electrical properties of olivine. The derivation of such a model is discussed in chapter 4, and a closer examination of the attenuation through the sea-water is presented in chapter 5. A plane-wave sinusoidal external field of period 10000 s and magnitude 100 nT is applied in the insulating half-space. The magnetic field $\mathbf{B}_0$ at the surface is thus 100 nT. From eq. 1.40, the electric field E_0 has a magnitude of 4.591 $\mathrm{mV.m^{-1}}$, and a positive phase with respect to $\mathbf{B}_0$ of 10.9°. The electric and magnetic fields are calculated as a function of depth using eqs 1.41 and 1.42. The results show clearly how the electric field **E** is hardly attenuated through the sea-water, but is attenuated with depth through the resistive lithosphere. The converse is true for the magnetic field **B**, with the magnitude on the seafloor being approximately 15 % of that on the surface. The boundary conditions, stated in eqs 1.8 and 1.9, are evident, as **B** is discontinuous across an interface, whilst E varies smoothly across the discontinuities in the conductivity structure. Finally, the graphs show that **E** always has a positive phase lead over **B**, increasing in conductive layers (such as the salt-water of the ocean), but remaining almost constant in resistive layers.

1.2.4 One-Dimensional Magnetotelluric Response

The theory for MT sounding was first described by Tikhonov (1950) and Cagniard (1953). The ratio of the horizontal electric to magnetic field fluctuations is called the MT impedance. The MT impedance is dependent on period and contains information for the electrical conductivity structure at the observation site. Wait (1954) showed that the method required considerable uniformity of inducing source-fields. Price (1962) developed the theory for induction by non-uniform source-fields in a layered medium.

The analysis of the MT method for a half-space and layered structure is based on eqs 1.30 and 1.40 respectively, which define the ratio of the horizontal electric to the horizontal magnetic fields. The magnitude of the ratio E/H has the dimensions of Ω, and is referred to as the impedance, ζ. An alternative expression for the impedance is given by $Z = E/B$ which has the SI units of $V.m^{-1}.T^{-1}$. The ratio of ζ and Z is a factor of μ. Assume that $\alpha = k$, then for a half-space

$$\frac{E_x}{B_y} = \sqrt{i}\sqrt{\frac{\omega\mu}{\sigma}} \qquad (1.43)$$

$$\frac{E_y}{B_x} = -\sqrt{i}\sqrt{\frac{\omega\mu}{\sigma}} \qquad (1.44)$$

These expressions are related by an equation involving the impedance ζ_{ij},

$$E_i = \zeta_{ij} H_j \qquad (1.45)$$

where ζ_{ij} are the elements of a 2 x 2 complex tensor. For a 1D layered half-space, it is easy to show that ζ_{xy} is equal to $-\zeta_{yx}$ and $\zeta_{xx} = \zeta_{yy} = 0$. Eliminating **E**, **H** and **B** from eqs 1.43 and 1.44 gives

$$\rho = \frac{1}{\sigma} = \frac{|\zeta|^2}{\omega\mu} \qquad (1.46)$$

where ρ is equal to the reciprocal of the conductivity σ, and is the resistivity of the half-space. For a layered half-space, the impedance at the top of any layer n can be written

$$\zeta_n = \frac{i\omega\mu}{\alpha_n G_n} \qquad (1.47)$$

and so at the interface of the layered half-space with the insulator, which is layer 1 in Figure 1.2,

$$\rho_a = \frac{1}{\sigma_a} = \frac{|\zeta|^2}{\omega\mu} = \frac{\omega\mu}{|\alpha_1 G_1|^2} \qquad (1.48)$$

where ρ_a is now defined as the apparent resistivity, and σ_a is the apparent conductivity. The apparent resistivity is the resistivity of that uniform half-space which possesses the same response as the layered half-space. A measure of the depth of penetration of induction into a layered half-space may be obtained by substituting the apparent conductivity into the skin depth equation 1.19, so that

$$\delta_a = \frac{\sqrt{2}}{|\alpha_1 G_1|} \qquad (1.49)$$

Another common representation of the MT impedance response function ζ is defined by the parameter c, called the inductive scale length, with units of m (Schmucker, 1970; Weidelt, 1972),

$$c = \frac{\zeta}{i\omega\mu} \qquad (1.50)$$

and hence a measure of the depth of penetration of geomagnetic induction is given by

$$\delta_a = |c| = \frac{1}{|\alpha_1 G_1|} \qquad (1.51)$$

It has been suggested that the real part of c be used as the scale length (Larsen, 1975). Schmucker & Jankowsky (1972) show that the real part of c gives a weighted mean depth of the current distribution.

The phase ϕ of the apparent resistivity ρ_a is related to its magnitude through a dispersion relationship (Bailey, 1970; Fischer & Schnegg, 1980; Parker 1983). In this thesis, the phase of the apparent resistivity is defined as being equal to the phase of the impedance. For a half-space, eq.1.43 can be formulated to show that

$$E_x = \pm(1+i)\sqrt{\frac{\omega\mu}{2\sigma}}\, B_y, \qquad (1.52)$$

and so the phase is given by the following expression

$$\phi = \arctan\left(\frac{\text{Imag}(\zeta)}{\text{Real}(\zeta)}\right) = \arctan\left(\frac{\pm 1}{\pm 1}\right) \qquad (1.53)$$

which shows that ϕ is either 45° or 225°. If the definition of phase lag or lead is for the range -180° to 180°, the phase for a half-space is 45°, which corresponds to a phase lead of **E** relative to **B**. It is pertinent to note that this phase definition corresponds to a time dependence of $e^{+i\omega t}$. If a time dependence of $e^{-i\omega t}$ is specified, then the phase of the half-space is -45°, and is equivalent to a lag of **E** relative to **B**.

For a layered half-space, a similar relationship between **E** and **B** gives

$$E_x = i\omega \frac{B_y}{\alpha_1 G_1(0)} \tag{1.54}$$

It can be shown that for a 1D electrical conductivity structure, assuming a time dependence of $e^{+i\omega t}$, the phase is always between 0 and 90°. The MT response of a layered structure is sensitive to the conductance of the layers, rather than the independent parameters of conductivity and depth. Greatest sensitivity is present for highly conducting layers; a resistive layer placed in the layered structure will have little effect on the MT response at the surface. This is a consequence of the physics of induction in a layered Earth. Electromagnetic coupling between layers is by mutual induction: EM energy is propagated through a resistive layer with relatively little attenuation, so has little influence on the MT response at the surface.

1.2.5 Vertical Gradient Sounding Method

In the vertical gradient sounding (VGS) method, horizontal magnetic fields are measured at points separated vertically. The attenuation of the horizontal components between the two sounding sites is directly related to orthogonal, horizontal electric current flow between the two sites, and hence can be related to the MT impedance. From equations 1.37 and 1.47 one may obtain

$$\zeta_1 = \frac{\{ \zeta_2 + i\omega\mu \tanh(\alpha_1 h_1) / \alpha_1 \}}{\{ 1 + \alpha_1 \zeta_2 \tanh(\alpha_1 h_1) / i\omega\mu \}} \tag{1.55}$$

where ζ_1 and ζ_2 are the impedances at the top of the surface layer and the top of the underlying layer. A similar expression may easily be defined for the relationship between ζ_2 and ζ_1

$$\zeta_2 = \frac{\{ \zeta_1 - i\omega\mu \tanh(\alpha_1 h_1) / \alpha_1 \}}{\{ 1 - \alpha_1 \zeta_1 \tanh(\alpha_1 h_1) / i\omega\mu \}} \tag{1.56}$$

A complex transfer function R may be defined as the ratio of the horizontal magnetic field at the top of the surface layer to the horizontal magnetic field at the surface of the underlying layer, so that $R = H_1 / H_2$. It can be shown from eq. 1.37 that the impedance ζ_2 at the surface of the underlying layer is given by

$$\zeta_2 = \frac{\{ i\omega\mu - R\, i\omega\mu \cosh(\alpha_1 h_1) \}}{\{ R\, \alpha_1 \sinh(\alpha_1 h_1) \}} \tag{1.57}$$

An expression for ζ_1 can be derived from eqs 1.55 and 1.57.

1.2.6 Departures from One-Dimensionality

Only a very brief outline will be given of the extension of geomagnetic induction theory to 2D and 3D electrical conductivity structures. Analytical solutions of 2D and 3D EM induction problems exist only for a few special cases, which are generally unlike Earth's conductivity structure. Thus, solutions of 2D problems are usually forward-modelled by numerical methods (e.g. Brewitt-Taylor & Weaver, 1976; Wannamaker *et al.*, 1986) and recently, methods have been developed to invert data for the optimum 2D structure (Smith & Booker, 1991; deGroot-Hedlin & Constable, 1990). However, it is worth reviewing the 2D induction theory, as many EM induction problems can be simplified to a 2D geometry.

The theory for 2D induction is based on Maxwell's equations, the constitutive equations and EM boundary conditions, given in eqs 1.1 - 1.10. Figure 1.5 shows a 2D model, where there is variation in conductivity structure in the y- and z-directions, so that $\sigma = \sigma(y,z)$. The 2D induction problem can be decomposed into a solution for a magnetic plane-wave source-field polarised parallel to the strike of the conductivity structure, called the transverse magnetic (TM) mode, and for the electric field parallel to the strike of the structure, called the transverse electric (TE) mode (Berdichevsky & Zhdanov, 1984). These two modes are also known as B- (or H-) polarisation and E-polarisation respectively. In this thesis, the former is preferred, as the terms E- and B-polarisation are used in later 3D modelling to describe the polarisations of the inducing magnetic field, which for 3D structures, by definition, will not be aligned with strike.

Patra & Mallick (1980) show that the diffusion equation applies to 2D conductivity structures

$$\frac{\partial^2 K}{\partial y^2} + \frac{\partial^2 K}{\partial z^2} = \lambda^2 K \tag{1.58}$$

where $\lambda^2 = i\omega\mu\sigma(y,z)$. For the TM mode, K is replaced by B_x, and the EM field components are now given by $B = (B_x, 0, 0)$, $E = (0, E_y, E_z)$.

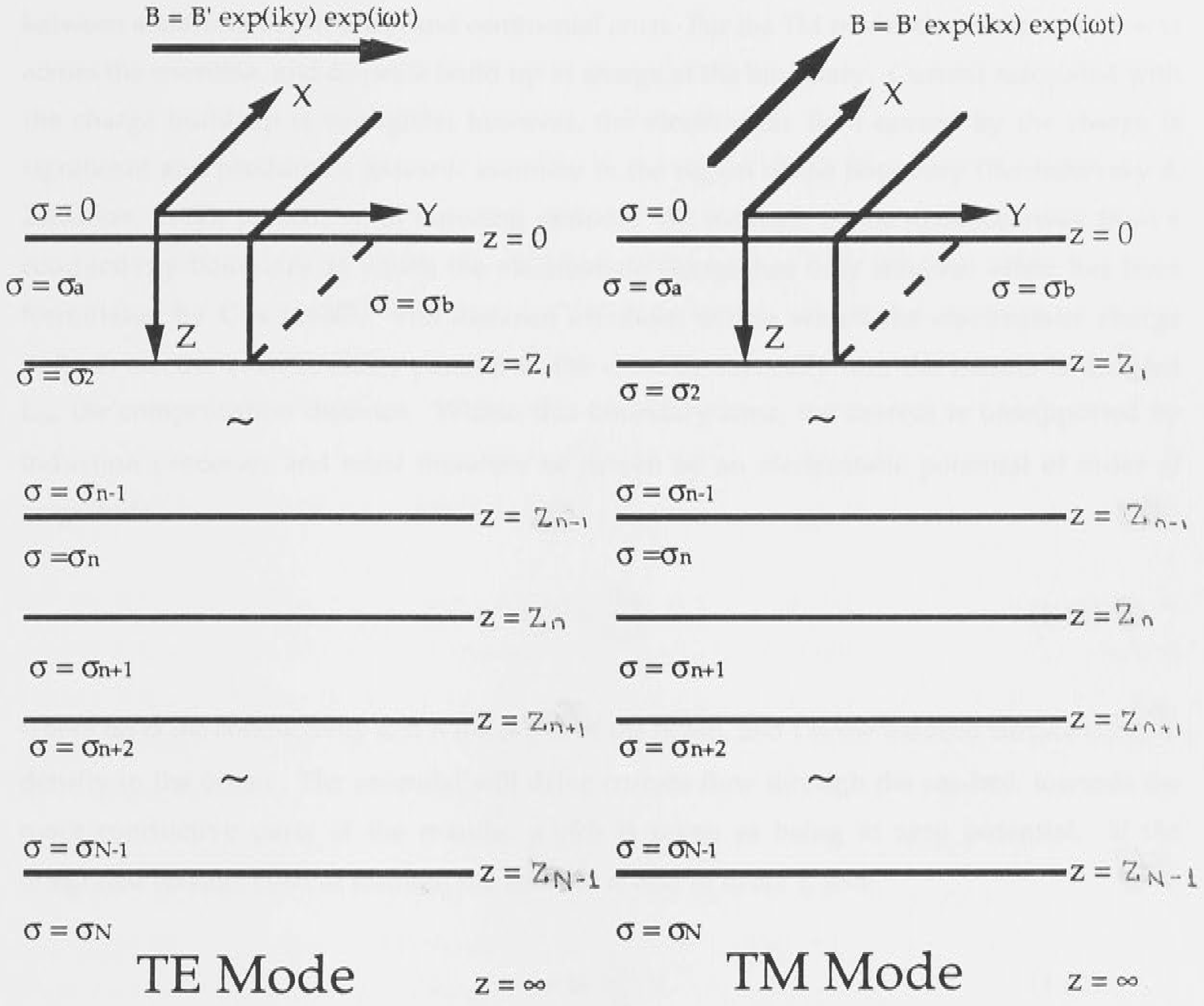

Figure 1.5 Schematic illustration of a 2D model, with a conductivity boundary in the top layer, underlain by a layered half-space conductivity model, with conductivity varying with depth only. The two polarisations of the external magnetic field correspond to the TE and TM modes.

The electric field components are related to B_x by

$$\frac{\partial B_x}{\partial y} = -\mu\sigma(y,z)\, E_z \quad \text{and} \quad \frac{\partial B_x}{\partial z} = \mu\sigma(y,z)\, E_y \tag{1.59}$$

K is replaced by Ex in the TE mode, and the EM field components are now given by B = (0, B_y, B_z), E = (E_x, 0, 0), so that the magnetic field components are related to E_x by

$$\frac{\partial E_x}{\partial y} = i\omega\, B_z \quad \text{and} \quad \frac{\partial E_x}{\partial z} = -i\omega\, B_y \tag{1.60}$$

It is instructive to examine the physical basis of 2D EM induction, in terms of the contact between a uniform depth ocean and continental crust. For the TM mode, electric current flow is across the coastline, and causes a build up of charge at the boundary. Current associated with the charge build up is negligible; however, the electrostatic field caused by the charge is significant and produces a galvanic anomaly in the region of the boundary (Berdichevsky & Zhdanov, 1984), present at all inducing periods. An estimate of the distance away from a conductivity boundary at which the electrostatic charge has only minimal effect has been formulated by Cox (1980). The distance off-shore within which the electrostatic charge deflects electric current either parallel to the coast or vertically into the mantle is denoted L_o, the compensation distance. Within this boundary zone, the current is unsupported by induction processes and must therefore be driven by an electrostatic potential of order of magnitude

$$V = \frac{JL_o}{\sigma_o h} \tag{1.61}$$

where σ_o is the conductivity and h the depth of the ocean, and J is the induced surface current-density in the ocean. The potential will drive current flow through the sea-bed, towards the more conductive parts of the mantle, which is taken as being at zero potential. If the integrated leakage current through the sea-bed is also of order J, then

$$J = \sigma_r \left(\frac{L_o}{H}\right) V \tag{1.62}$$

where σ_r and H are the conductivity and thickness of the resistive upper lithosphere. Eliminating J/V from eqs 1.61 and 1.62 shows that

$$L_o = \sqrt{\frac{\sigma_o}{\sigma_r} h\ H} \tag{1.63}$$

An analogous compensation distance on the land side of the coastline can also be written, by replacing the σ_o, the conductivity of sea-water by σ_c, the conductivity of continental crust. A 2D coastline model, of resistive continental crust and conductive sea-water, overlying a resistive lithosphere was used by Ranganayaki & Madden (1980) to show that the magnitude of E, denoted here by the scalar value E, perpendicular to the coastline could be expressed as

$$E = E_o \left(1 - \exp\left(- \frac{y}{L_o} \right) \right) \quad y > 0 \tag{1.64}$$

$$E = E_c (1 + \sqrt{\frac{L_o}{L_c}} \exp (- \frac{y}{L_c})) \quad y < 0 \qquad (1.65)$$

where the origin of the y coordinate was centred on the coastline, with y positive on the ocean side, L_o and L_c are the compensation distances in the ocean and in the continental crust, and E_o and E_c are the magnitudes of E in the ocean and on land respectively at distances far from the coastline. Thus, the magnitude of E in the ocean drops to very low values at the coastline, and recovers exponentially with the adjustment distance L_o. Lilley *et al.* (1989) show that the observed TM impedance values across the Tasman Sea are well modelled by eq. 1.64, and indicate a compensation distance of 400 km. On the land side, the electric field will be a maximum close to the coastline, and decreases inland to the 1D value. As L_c is much less than L_o by a factor of of ten, or greater, the electric field will approach the 1D value over much shorter distances than on the ocean side.

For the TE case, electric charge does not build up at the coastline. However, an anomaly is created by an excess of electric current flowing through the ocean. There is an anomalous electric field parallel to the coastline, an anomalous horizontal magnetic field perpendicular to the boundary, and an anomalous vertical magnetic field induced by the excess current. Such an anomaly is termed an inductive galvanic type (Berdichevsky & Zhdanov, 1984). The magnitude of the anomaly will decrease as the period of induction increases. The anomalous vertical magnetic field associated with a TE anomaly at the coastline constitutes the geomagnetic coast effect. Berdichevsky & Zdhanov (1984) show that the TM anomaly depends upon local conductivity structure, while the TE anomaly depends on the mean value of the integrated conductivity of the upper layer over a large vicinity of the observation site.

For 3D conductivity structures, the EM fields cannot be resolved into distinct polarisations. The diffusion equation, given in eqs 1.11 and 1.12, cannot be solved analytically, except in special cases where the 3D structure has symmetrical properties. Few numerical algorithms exist to forward-model 3D EM problems, although in principal, a finite element, or finite difference solution can be formulated relatively simply. However, solving 3D EM problems by numerical methods requires considerable computer resources. Thus, many strictly 3D problems, such as EM induction in the oceans and lithosphere, are treated as 2D coastline models, to simplify numerical computation.

1.2.7 Current Channelling and Leakage

There are conflicting published definitions of channelling effects, which have been variously termed 'current deviation', 'current deflection', 'current gathering', 'current leakage', 'current concentration' and 'current channelling'. In this thesis, the definition of Jones (1983) is used of a perturbation of current flow, which is not supported by EM induction, and which has a DClike expression. Electric currents, induced outside the study area, are deflected into the area of interest by charge accumulations at conductance boundaries; these charge accumulations have an appreciable electrostatic potential. Current channelling is reserved for 3D structures only; charge accumulation at 2D boundaries cannot deflect electric current parallel to the boundary. In this thesis, two forms of channelling will be defined. The term 'current channelling' is reserved for electric field distributions in a horizontal plane. For example, current channelling at 3D coastlines will deflect electric current within the ocean itself. The other definition is that of 'leakage', to describe the deflection of horizontal electric currents in a vertical direction, which for oceanic induction, is manifest as current flow into the lithosphere from the sea-water.

A measure of the leakage of induced electric current into the resistive mantle is given by the 2D divergence of the surface current-density **J** in the ocean (McKirdy & Weaver, 1983). The depth of the ocean is small in comparison to the skin depth in the underlying mantle. As the volume current-density j is solenoidal in quasi-static theory,

$$\frac{\partial j_x}{\partial x} + \frac{\partial j_y}{\partial y} = -\frac{\partial j_z}{\partial z} \qquad (1.66)$$

within the ocean, where the z-axis points downwards into the mantle. The surface current-density **J** in the ocean is defined

$$\mathbf{J} = \lim_{\delta \to +0} \int_{-0}^{\delta} (j_x \mathbf{x} + j_y \mathbf{y})\, dz \qquad (1.67)$$

where **x** and **y** are unit vectors, and δ is the depth of the ocean normalised to the skin depth in the mantle. In the limit

$$\frac{\partial J_x}{\partial x} + \frac{\partial J_y}{\partial y} = \lim_{\delta \to +0} [- j_z]_0^{\delta} \qquad (1.68)$$

The volume current-density is zero at the interface with the insulating half-space. At the sea-bed, j_z is continuous across the interface, so that

$$\nabla . \mathbf{J} = \frac{\partial J_x}{\partial x} + \frac{\partial J_y}{\partial y} = - j_{seafloor} \qquad (1.69)$$

Here, $j_{seafloor}$ is the vertical current at the sea-bed leaking into the lithosphere: if there is no leakage, $j_{seafloor} = 0$. For the TE polarisation, with an electric current flowing perpendicular to the coast in the y-direction, McKirdy & Weaver (1983) summarised the following possibilities that can arise

(i) $\frac{\partial J_x}{\partial x}+\frac{\partial J_y}{\partial y}\neq 0;\ \frac{\partial J_y}{\partial y}\neq 0$ Channelling and leakage.

(ii) $\frac{\partial J_x}{\partial x}\neq 0;\ \frac{\partial J_y}{\partial y}=0$ Leakage, but no channelling.

(iii) $\frac{\partial J_x}{\partial x}=-\frac{\partial J_y}{\partial y}\neq 0$ Channelling, but no leakage.

(iv) $\frac{\partial J_x}{\partial x}=\frac{\partial J_y}{\partial y}=0$ No channelling or leakage.

1.2.8 Two- and Three-Dimensional Magnetotelluric Response

For a 1D Earth, with an arbitrarily polarised, plane-wave inducing source-field, the impedance Z is invariant of the direction of polarisation of field: this is obviously so, as the 1D model is laterally uniform in the horizontal plane.. However, no part of Earth is exactly 1D, with conductivity varying only with depth. In practice, the horizontal components of **E** and **B** are measured in orthogonal directions. Assuming these directions are X and Y, which have arbitrary orientation with respect to the geomagnetic north and east directions, the MT impedance tensor **Z** is defined

$$E = Z.B \tag{1.70}$$

where **E** and **B** are now the vector electric and magnetic fields, and **Z** is a 2 x 2 tensor. The impedance tensor can be expressed as

$$\mathbf{Z}=\begin{bmatrix} Z_{XX} & Z_{XY} \\ Z_{YX} & Z_{YY} \end{bmatrix} \tag{1.71}$$

For a 1D structure, from eqs 1.43, 1.44, $Z_{XY} = -Z_{YX}$, and $Z_{XX} = Z_{YY} = 0$, and so Z has the form

$$\mathbf{Z}=\begin{bmatrix} 0 & Z_{1D} \\ -Z_{1D} & 0 \end{bmatrix} \tag{1.72}$$

Magnetotelluric observations over strictly 2D structure in an arbitrary coordinate system will be more complicated. However, Swift (1967) has shown that a rotation of the coordinate system to be parallel and perpendicular to the strike of the conductivity boundary results in **Z** simplifying to the form

$$\mathbf{Z}=\begin{bmatrix} 0 & Z_{12} \\ -Z_{21} & 0 \end{bmatrix} \tag{1.72}$$

The new directions of the coordinate system are defined to be the principal axes. Impedance magnitude $|Z_{12}|$ does not necessarily equal $|Z_{21}|$, so there are now two distinct values of MT impedance, corresponding to the TE mode of electric current flow parallel to the strike, and to the TM mode of magnetic field parallel to the strike. For most 3D structures, the impedance tensor will have a still more complicated form. It is usual to rotate the axes so that the off-diagonal elements of **Z** are in some sense maximised. Swift (1967) shows that maximising $|Z_{12}|^2 + |Z_{21}|^2$ is equivalent to rotating the axes through an angle of ϕ given by

$$\tan 4\phi = \frac{(Z_1 \overset{*}{Z_2} + \overset{*}{Z_1} Z_2)}{(Z_1 \overset{*}{Z_1} - \overset{*}{Z_2} Z_2)} \qquad (1.73)$$

where $Z_1 = Z_{XX} - Z_{YY}$, $Z_2 = Z_{YX} + Z_{YX}$, and the * denotes the complex conjugate. The interpretation of the 3D impedance tensor is complicated: it is often desirable to reduce the dimensionality of the problem to 2D or 1D structures. Maximising the off-diagonal elements makes the assumption that there is a predominant 2D strike, with perhaps 3D perturbations. The TE component of the 2D impedance tensor is sometimes interpreted with a 1D conductivity structure (e.g. Ferguson *et al.*, 1990), while the TM component is used in 2D interpretations (e.g. Wannamaker *et al.*, 1989b). However, various authors have shown that a simple rotation to maximise the off-diagonal elements may not recover the true impedance response of the underlying structure. Lilley (1975) uses a graphical technique to represent the impedance tensor elements, whilst Bahr (1988) and Groom & Bailey (1989) decompose the tensor into local and regional effects, to show that rotating the tensor elements by eq. 1.73 does not necessarily align the coordinate axes with the predominant 2D strike.

A measure of the dimensionality of the impedance tensor is given by the skew angle (Vozoff, 1972), defined as

$$\text{Skew} = \tan^{-1} \frac{|Z_{XX} + Z_{YY}|}{|Z_{XY} - Z_{YX}|} \qquad (1.74)$$

Although large skew angles of say > 10° are indicative of 3D conductivity structure, if the 3D structure has a high degree of symmetry, then the skew angle may be quite small. The skew angle is, of course, dependent upon rotating the impedance tensor to the principal 2D axes.

In many geological situations, near-surface perturbations of the telluric field will have a profound effect on the MT impedance tensor. The problem of static shift is due to local conductivity perturbations, which are small compared to the penetration depths, but which may change the electric field in direction and magnitude. The effect is independent of period, and is largely manifest as a change in magnitude of apparent resistivity, with little or no change in phase. Jones (1988) discusses static shift in a sedimentary basin, and the removal of such effects from observed data, using known depths to a basement layer. Another problem is that local perturbations preclude there being a coordinate direction in which the diagonal elements disappear. There are many approaches to correcting MT data for near surface heterogeneities (Berdichevsky & Dmitriev, 1976a,b). Eggers' (1982) eigenstate analysis of the impedance tensor allows for angles between the electric and magnetic fields which are not orthogonal. Various authors (Wannamaker *et al.*, 1984; Park *et al.*, 1983; Ingham, 1988) have discussed the use of impedance estimates which are invariant of the orientation of the measurement axes. For example, Ingham & Hutton (1982) modelled apparent resistivity and phase calculated from the arithmetic mean of the off-diagonal elements

$$Z = \frac{(Z_{XY} - Z_{YX})}{2} \tag{1.75}$$

Also independent of the orientation axes of measurement is the invariant impedance

$$Z = \sqrt{Z_{XX} Z_{YY} - Z_{XY} Z_{YX}} \tag{1.76}$$

defined by Ranganayaki (1984). Forward-model studies provide few general rules about the use of invariant impedance estimates. Ingham (1988) suggests that as eq. 1.76 uses all four impedance elements, it may be preferable to eq. 1.75. The problem with real observations is that as the source of perturbation is unknown, unlike that in the forward-model studies, it is difficult to guess which form of the invariant impedance estimate might be the least perturbed by local heterogeneities.

1.2.9 Geomagnetic Depth Sounding

For a uniform source-field of infinite wavelength, fluctuations in the vertical field are caused solely by the interaction of the horizontal magnetic field with lateral variations in Earth's conductivity structure. This phenomenon is used in the approach known as geomagnetic depth sounding, or GDS. The magnitude of the vertical field depends upon the proximity, form and strength of the lateral conductivity contrasts. Parkinson (1962) shows that the vertical component of the magnetic field correlates to the horizontal components of magnetic field: this can be indicated on a map by an arrow pointing in the horizontal direction that correlates with the vertical component, and whose length indicates the ratio of the magnitudes of vertical to horizontal components. These arrows are referred to in this thesis as GDS induction arrows. In a 2D situation, the GDS arrows arise from the TE mode where electric field is parallel to the strike. These arrows are therefore dependent upon the mean value of the integrated conductivity over a large vicinity of the observation site (Berdichevsky & Zhdanov, 1984). For a uniform source-field, the transfer functions A and B in

$$B_Z = A\,B_X + B\,B_Y \qquad (1.77)$$

are period dependent complex quantities, and a function of the conductivity structure. Induction arrows are formed for real and imaginary (or quadrature) parts of the transfer function by plotting arrows of magnitude l_R and l_Q

$$l_R = \sqrt{\mathrm{Re}(A)^2 + \mathrm{Re}(B)^2} \qquad (1.78)$$

$$l_Q = \sqrt{\mathrm{Im}(A)^2 + \mathrm{Im}(B)^2} \qquad (1.79)$$

with respective directions ϕ_R and ϕ_Q, given by

$$\phi_R = \tan^{-1}\frac{-\mathrm{Re}\,(B)}{-\mathrm{Re}\,(A)} \qquad (1.80)$$

$$\phi_Q = \tan^{-1}\frac{\pm\mathrm{Im}\,(B)}{\pm\mathrm{Im}\,(A)} \qquad (1.81)$$

The real part of the transfer functions A and B are reversed in sign so that the GDS real induction arrow generally 'points' towards the region of high electrical conductivity. The orientation of the quadrature part of the transfer functions is dependent upon the assumed implicit time dependence of the EM fields (Lilley & Arora, 1982). For the case studied by Lilley and Arora, a time dependence of $e^{+i\omega t}$ used in the Fourier transform will result in the quadrature arrows pointing away from the good conductor, whilst a time dependence of $e^{-i\omega t}$ will result in the arrow being orientated towards the good conductor. Whilst the period dependence will give some indication of the size and nature of an anomalous conducting body, GDS induction arrows are not particularly sensitive to the depth of the anomalous conductor.

1.2.10 Electric Field Induction Arrows

The development of seafloor electric field instrumentation, particularly by Filloux (1987), permits accurate measurements of three components of electric field. The vertical electric field is zero for induction by a uniform source-field in a layered half-space; thus an observed vertical electric field arising from lateral changes in conductivity may be regarded as anomalous. It is thus possible to construct electric field induction arrows, which for 2D structure arise from the TM mode (where electric current flows perpendicular to the conductivity boundary). Berdichevsky & Zhdanov (1984) have shown that the TM component is sensitive to the conductivity structure local to the observing site. The arrows can be formed from the transfer functions A and B, as in eqs 1.78 - 1.81, where A and B are now defined by

$$E_Z = A\,E_X + B\,E_Y \qquad (1.77)$$

By analogy with the familiar GDS arrows based on magnetic data, such electric field induction arrows may be termed 'electric depth sounding' (or EDS) arrows. Interpretation of EDS induction arrows is not entirely clear; however, they provide another measure of leakage of electric current through the seafloor.

1.3 The Principles of Electrical Conduction in Rocks and Minerals

1.3.1 Introduction

Parkinson (1983) asserts that

> "the delineation of underground electrical conductivity is little more than an elegant exercise unless the conductivity can be related to other physical variables",

however an opposing opinion is put forward by Tozer (1979):

> "when the essential scientific aim of interpreting and relating observable quantities has been achieved by the assignment of a material property, what further scientific purpose, if any, is being served by efforts to reinterpret it as the value of a function depending on an ill-defined number of unobservable quantities existing at the same point?"

While one can have some sympathy with Tozer's view, there are many reasons to undertake such a procedure. For example, it is of great value to be able to distinguish melt from solid rock, and to place bounds on the porosity of a zone of study. Such interpretation requires a clear understanding of the physics of electrical conduction in rocks and minerals, both in sub-solidus and molten forms. There are many factors which influence electrical conductivity in Earth, which act simultaneously in a complicated manner.

1.3.2 Types of Conduction

Electrical conduction occurs with the movement of electrons or ions in the response to an electric field. The electrons or ions may be bound or free. Four types of conduction occur within Earth, which are metallic, semiconductor, electrolytic and ionic. These have the following properties:

> (i) Metallic conduction is by free electrons and occurs in mineralised bodies in the crust, and in Earth's core which is predominantly Fe.
>
> (ii) In the case of semiconductors, the number of electrons in the conduction band is thermally determined, and hence conduction is a function of temperature. The existence of graphite in the lower crust, which has semiconducting properties, may account for the measured high electrical conductivities.
>
> (iii) Ions can move freely through a liquid, but the mobility of ions is much less than that of electrons, so electrolytic solutions have a conductivity less than that of semiconductors. Induced electric current flow in sea-water is by electrolytic conduction.
>
> (iv) In ionic solids, ions are bound to the crystal lattice by coulomb forces. However, thermal motions and defect make motion possible. At low temperatures, the conductivity of the common rock-forming minerals, such as silicates and carbonates is very low. The conductivity, as a function of the absolute temperature can be expressed as
>
> $$\sigma = \sigma_0 \exp\left(-\frac{A}{kT}\right) \qquad (1.78)$$
>
> where k is Boltzmann's constant, T is the absolute temperature, A is the activation energy required to produce and to move a charge carrier in the structure, and σ_0 is the conductivity of the material at very high temperatures.

1.3.3 Dependence of Conductivity on Temperature

Silicate minerals form the bulk composition of the crust, and so have a temperature dependence of the form shown in eq. 1.78. Temperature measurements of single crystals and samples of sintered olivine and orthopyroxene have been made to 1500 ° C (e.g. Duba *et al.*, 1973; Schock *et al.*, 1989; Shankland & Duba, 1990). Constable & Shankland (1991) show that the laboratory measurements are well modelled by eq. 1.78, with different low and high temperature activation energies. They also showed that three high temperature activation energies are required for the different crystallographic axes, suggesting differences in charge mobility. Constable & Shankland (1991) conclude that the activation energies are related to the location of Fe atoms in the olivine crystal lattice. Schock *et al.* (1989) show a change in sign of the thermoelectric effect in olivine at 1390° C, which reflects a change of charge carriers and of conduction mechanism. They conclude that at low temperatures, conduction is by electron holes, which are superseded by magnesium vacancies at higher temperatures.

1.3.4 Dependence of Conductivity on Crystal Defects and Impurities

Minor amounts of impurities in a mineral sample may have a marked effect on the conductivity, especially if the impurities change the activation energy E (e.g. Karato, 1990). Point defects occur in all crystals as a result of the tendency towards disorder due to thermal agitation and the presence of aliovalent impurities. Probably the most important factor controlling defects in mantle material is the oxygen fugacity, fO_2. This controls the oxidation state of iron (Fe^{2+} ferrous, or Fe^{3+} ferric) and thus the population of defects, expressed as

$$Fe^{2+} \rightleftarrows Fe^{3+} + e^{-} \qquad (1.79)$$

The oxygen fugacity is probably not important in the mantle (Duba, 1976), as it is controlled within narrow limits by the phases present; however, in the laboratory, the oxygen fugacity is an extremely important variable. Duba (1976) shows that the conductivity for olivine of interest to the upper mantle, $(Mg_{90}Fe_{10})_2SiO_4$, is four orders of magnitude less than the conductivity of pure fayalite, $(Fe_{100})_2SiO_4$,,at 800° C. Constable & Duba (1990) show that there is independence of conductivity on oxygen fugacity at low pressures, and suggest an increase of the log of conductivity with $(fO_2)^c$, where the exponent c is determined to be 1/7 experimentally and 1/5.5 theoretically.

1.3.5 Dependence of Conductivity on Composition and Grain Boundary

Polycrystalline measurements (e.g. Rai & Manghnani, 1978) are consistently higher than that of a single crystal, although the difficulties of maintaining constant laboratory conditions for a crushed and sintered mineral assemblage is considerably greater than for a single crystal. Conduction at the grain boundary may be greater than that for the single crystal measurements, due to increased defect population or impurities. Shankland & Waff (1977) attempted to account for such effects by multiplying the single olivine crystal conductivities of Duba *et al.* (1974) by a factor of 10. Constable & Duba (1990) showed that conduction in a dunite, a mono-mineralic, polycrystalline rock, composed of olivine, is indistinguishable from conduction in single olivine crystals, and hence the practice of exaggerating single crystal conductivities may not be necessary. However, this one result does not imply that grain boundary effects are unimportant, particularly where more than one phase is present.

1.3.6 Dependence of Conductivity on Pressure

It is generally accepted that the pressure effect on conductivity of olivine is small (Duba *et al.*, 1974), probably as there are two conduction mechanisms in olivine whose pressure effects oppose each other (Schock *et al.*, 1989). Omura *et al.* (1989) suggest that there is an increase of electrical conductivity in the case of high Fe content, such as a Fayalite, but for olivines representative of the mantle, with approximately 10 % Fe, there is a decrease in conductivity with pressure.

1.3.7 Dependence of Conductivity on Sub-Solidus Chemical Phase

The dominant conducting phase in the upper mantle is thought to be olivine (Duba *et al.*, 1973), and consequently, this mineral has been the focus of many laboratory experiments. Studies on orthopyroxene (Duba *et al.*, 1973) suggest comparable characteristics to olivine. There are few, if any, measurements on the other major phases in the mantle,which are clinopyroxene and garnet. There may be four orders of magnitude difference in conductivity between pure fayalite, $(Fe_{100})_2SiO_4$, at the high end of the range, and pure forsterite, $(Mg_{100})_2SiO_4$, which has much lower conductivity. An increasing amount of Fe with depth in the mantle could contribute to an increase in conductivity.

Akimoto & Fujisawa (1965) have found that there is almost two orders of magnitude change over the phase change between olivine and spinel. There is some doubt as to the reliability of the observation because of lack of control of fO_2 (Duba, 1976).

Conductivities of crustal materials have been studied by Kariya & Shankland (1983). A particular target of such studies is to identify the physical properties of the high conductivity of the lower crust. Shankland & Anders (1983) and Hyndman & Shearer (1989) consider the possibility of fluids, while Frost *et al.* (1989) examine lower crustal rocks for the presence of grain boundary graphite.

1.3.8 Dependence of Conductivity on Molten Phase

Waff & Weill (1975) show the conductivity of the melt phase of mantle minerals to be several orders of magnitude greater than the conductivity of sub-solidus olivine. This result has important consequences in explaining the presence of a high conducting layer in the mantle (Shankland & Waff, 1977; Shankland, 1981). Tyburczy & Waff (1983) investigate the conductivity of andesite and basalt melts as a function of temperature and pressure.

The conductivity of a partially molten sample is dependent upon the connectivity of the melt. Simple parallel and series mixing laws provide bounds on the conductivity (Hashin & Stricknam, 1963). For a small percentage of melt (1%), the uncertainty in the conductivity from these bounds spans an order of magnitude. Many other melt geometries have been postulated (Schmeling, 1986). Sato *et al.* (1989) discuss the problem of estimating the conductivity of melt fractions in the mantle due to unknown pressure effects, unknown frequency dependence and the unknown effect of grain boundary phases.

1.3.9 Dependence of Conductivity on Porosity and Fluids

Salt-water conductivity as a function of temperature and pressure has been measured by Quist & Marshall (1968). They show that as conduction is electrolytic, the conductivity is generally high, and not particularly sensitive to changes in temperatures and pressure. In the oceanic crust, and perhaps the top part of the upper mantle, electrical conductivity is largely controlled by pore fluids. The fluid content in the oceanic crust is thought to decrease with depth due to crack sealing, which has been verified by in-situ porosity and conductivity measurements by Becker *et al.* (1982). The problem of estimating fluid content from conductivity is again dependent upon the connectivity of the fluid. Brace *et al.* (1965) have shown that an empirically derived Archie's Law formulation is applicable to a wide range of rock types and porosities.

1.3.10 Dependence of Conductivity on Time

The factor of time is a somewhat surprising variable for laboratory electrical conductivity measurements. A phenomenon involving time is that of order-disorder in silicates: Piwinskii & Duba (1974) have shown that the conductivity of an albite increases with time, and similar characteristics may be exhibited by other crustal rocks. The age of most mantle processes is such that there is sufficient time for most chemical reactions to attain equilibrium; however, in the laboratory, the time for the experiment is of the order of hours at most. Studies in olivine below 1500° C have indicated no time dependence in conductivity; however, there is some indication that time may be a factor above 1500° C (Duba *et al.*, 1974).

1.4 Geomagnetic Studies in the Oceans

1.4.1 Introduction

Electromagnetic methods are increasingly being used to probe the sub-oceanic structures and to provide information about physical oceanographic phenomena. Developments in this area have been relatively recent, mainly as a result of improvements in instrumentation, theory and methodology. Many of the techniques under investigation are simply adaptations of terrestrial methods; others, however, are new and in a development stage. In addition to the continued expansion of seafloor MT and GDS studies of a wide range of tectonic features, controlled source-field electromagnetic (CSEM) methods have been applied with some success to mapping the conductivity structure of the upper lithosphere. The sensitivity of horizontal electric field measurements has pioneered new developments in oceanography, at much lower cost than an array of continuously operating ocean-current meters.

In this section, a brief review of the marine EM environment is given, with emphasis on the differences with terrestrial observations. Reference is made to both oceanographic and solid-Earth objectives. Comprehensive reviews of the status of EM oceanic research are given by Cox (1980), Fonarev (1982), Law (1983), and Constable (1990). Aspects of seafloor EM exploration applications are given by Chave *et al.* (1991). Filloux (1987) discuses the instrumentation developed for seafloor EM studies. However, it is worth examining here the objectives and difficulties of such studies, to indicate the motivation for the thesis research.

1.4.2 The Ocean Environment

As the terrestrial environment is in direct contact with the atmosphere, which may be considered to be an insulator, EM energy from an ionospheric source-field is propagated almost without attenuation to the surface of the crust. By contrast, measurements of the horizontal magnetic field made on the seafloor are strongly attenuated, as in Figures 1.3 and 1.4. The degree of attenuation is dependent on the period of the inducing signal, the depth of the ocean and on the underlying structure. Quist & Marshall (1968) show the conductivity of salt-water is largely a function of temperature and salinity only. To a reasonable approximation, this conductivity can be expressed as

$$\sigma(T) = 3 + \frac{T}{10} \tag{1.80}$$

where σ is the conductivity in $S.m^{-1}$ and T is the temperature in °C. Underlying the ocean may be a layer of water-saturated sediments, with conductivities approaching that of sea-water. The conductivity of the oceanic crust is largely determined by pore fluids, and at spreading ridges, the presence of magma. At the Moho, the conductivity drops considerably, as it is thought to have a low percentage of volatiles, and the temperature is too low for the conductivity to be determined by thermal processes.

Whilst the strong attenuation of the **B** through the sea-water restricts MT and GDS observations of natural source-field to periods greater than 1000 s, it results in an extremely quiet environment for CSEM experiments. At a period of 10 s, natural source **B** and **E** fields are attenuated by a factor of approximately 1000 from their surface value (Constable, 1990), so CSEM measurements are effectively screened from ionospheric contamination. Controlled source-field studies also benefit from the lack of an air wave: the first arrival at the receiver is through the seafloor, which is the target of study.

Potential electrode noise, for all types of seafloor EM experiment, is lower than experienced on land, as temperature, salinity and contact resistance are nearly constant. Electrode noise may be reduced further by the use of a water chopper (Filloux, 1987). Controlled source-field measurements may use large transmission currents because of low impedance contacts, and benefit by being constantly in electrical contact with the sea-water, so that continuous measurements are possible by dragging the transmitter and/or receiver behind a ship.

The electric fields may vary smoothly over very large distances-scales, so that the influence of local conductivity perturbations in the oceanic crust do not have such a profound consequence as similar perturbations on land. Cox (1980) found good coherence between electric field recording sites up to 100 km apart in the Atlantic Ocean.

Finally, a pervasive assumption is that the electrical structure of the oceanic lithosphere is less perturbed than that of the continental lithosphere, although this may be partly due to the paucity of seafloor EM experiments. Nevertheless, there are sound petrological grounds for believing that this may be the case in older parts of the oceanic lithosphere, and thus it may be easier to determine electrical structure beneath the ocean floor with less ambiguity than from observations on land.

1.4.3 Electromagnetic Source-Fields on the Seafloor

Seafloor EM experiments are carried out within the relatively good conductor of the salt-water, for the purpose of studying the less conductive material of the seafloor below. Furthermore, two competing sources of EM fields in the oceans are present: the ionospheric sources propagated through the ocean and the underlying lithosphere, as if the ocean were static; and secondly, the motion of sea-water through Earth's static magnetic field produces an electric field by dynamo action.

Long period EM fields in the deep ocean, from oceanic sources, are discussed by Chave & Filloux (1984, 1985), Lilley *et al.* (1986) and Chave *et al.* (1989); and for the Tasman Sea by Baines & Bell (1987). Large-scale barotropic flows, such as mesoscale eddy currents, may generate electric and magnetic fields by the dynamo process of a good conductor moving relative to a static field at periods of a few days. Chave *et al.* (1989) showed that the magnetic fields recorded on the seafloor during the EMSLAB experiment (EMSLAB group, 1988) are mainly ionospheric in origin for periods below 10 days, but that the electric fields are contaminated by oceanographic signals beyond periods of 2 to 4 days. The oceanic tides, and their harmonics, have a strong EM signature (Chave & Filloux, 1984; Bindoff, 1988; Bindoff *et al.*, 1988; see also Winch, 1981, for geomagnetic tidal analysis). Oceanic internal waves can produce a electric signature which will affect observations made at periods of 1 to 4 hours (Bindoff *et al.*, 1986). Oceanic turbulence effects have been discussed by Cox *et al.* (1978).

At periods longer than 1 day, the energy spectrum of oceanic source signals dominates the observed EM fields. As a result, MT and GDS response functions are restricted to 2 or 3 decades of period. When analysing real MT data, tidal periods are filtered out of the time domain or notched out in the frequency domain. Magnetotelluric measurements have resolution in the depth range 50 to 500 km, unattainable using other techniques. The limited magnitude of CSEM inducing fields limits mapping to the top few tens of kilometres. Thus MT and CSEM methods are complementary in their depth scales, and information of the conductivity structure of one can be used to constrain the other.

Smaller EM signals may result from short period oceanic sources. Surface gravity waves, swell and wind-driven waves produce velocity and pressure fluctuations at the seafloor which can induce temporal EM fields. Experiments and theoretical evidence for these phenomena have been reviewed by Cox *et al.* (1978).

1.4.4 Principal Objectives of Seafloor EM Studies

The prime target of most seafloor EM studies has been the conductivity structure of the sub-oceanic upper mantle, and in particular, the processes active at major tectonic zones. Many tectonic features have distinct thermal structure, and may contain regions of partial melt or fluids. Electromagnetic studies are particularly suited to examine such features: changes which produce only subtle variations in acoustic velocities generate orders of magnitude of change in electrical conductivity. Summarised below are the principal conductivity objectives of seafloor EM studies.

(i) The presence of a high conductivity layer corresponding to the seismic low-velocity zone. Partial melt, volatiles and hydrogen have been postulated as possible explanations for the low shear wave velocities: MT techniques are particularly suited to imaging such targets (Oldenburg *et al.*, 1984). There appears to be an age dependence of the depth of the high conducting layer (Law, 1983) which can be further tested by MT methods.

(ii) The mapping of ridge accretionary processes. The presence of a magma chamber at mid-oceanic ridges (MORs) is one of the prime targets in future EM studies, using both ionospheric and controlled source-fields. Magma chambers, regions of hydrothermal circulation, and the evolution of dry oceanic lithosphere may be mapped using a variety of seafloor EM techniques (Filloux, 1982; Evans *et al.*, 1991).

(iii) Imaging of fluids at subduction zones. Fluids on the upper surface of the subducting plate of the Juan de Fuca Plate have been imaged from MT and GDS observations in the EMSLAB experiment (EMSLAB group, 1988), by Wannamaker *et al.* (1989b).

(iv) The resistivity of the lithospheric mantle. The importance of the determination of the resistivity of the upper lithosphere has been detailed by Cox (1981). Controlled source-field experiments are particularly suited, as they are most sensitive to resistive structures (Cox *et al.*, 1986), but 2D MT models (Wannamaker *et al.*, 1989b) are also able to characterise the resistivity. By contrast, 1D MT interpretations cannot image a resistive lithosphere, as the MT method is not sensitive to resistive structures (Oldenburg *et al.*, 1984).

(v) Differences between oceanic and continental lithosphere. The geomagnetic coast effect has been observed on land for many years, and shown to be dependent upon the age and thickness of continental lithosphere (Constable, 1991). Seafloor MT and GDS observations may help characterise the differences (Kellett *et al.*, 1991).

(vi) Structure of hot spots. The high thermal gradients of hot spots, such as the Hawaiian chain (Larsen, 1975) and the Tasmantid Seamount Chain (Ferguson *et al.*, 1990) may have a distinct MT and GDS signature. The location and movement of molten mantle beneath active hot spots is an obvious target.

(vii) Deep conductivity structure. Magnetotelluric observations of natural source-fields have resolution over depths 50 to 500 km. A rise in conductivity at depths of approximately 400 km has been found for almost all MT interpretations (Campbell, 1987). Although the depth is at the limit of resolution, it is important to determine whether this is a global feature, both from seafloor studies, and from terrestrial measurements.

(viii) Commercial exploration. Although few commercial seafloor EM experiments have been attempted, the development of CSEM techniques has attracted interest (Chave *et al.*, 1991). Nobes *et al.* (1986a) have mapped magnesium nodules at the Juan de Fuca Ridge using seafloor EM methods.

1.4.5 Seafloor MT and GDS Instrumentation

Seafloor magnetometers are generally based on terrestrial instruments, with special adaptation of the housing required to withstand the pressures of deep ocean work. They broadly fall into two categories: those which operate by suspension and torsion principles (Filloux, 1967, 1980c, 1987) and the fluxgate units used by Law (1978), White (1979), Segawa *et al.* (1983) and Segawa (1986).

Electrometer design presents more logistical challenges, as the medium in which the electric field is measured is a relatively good conductor and the electric fields are weak by terrestrial standards. Two main types have been used. The first uses a long wire stretched out on the seafloor. The wire, which is 500 to 1000 m long, is deployed in a similar method typically used on land (Webb *et al.*, 1985). The other method is by a more sophisticated 'short-armed' device, specially developed for seafloor work, principally by J. H. Filloux from the Scripps Institution of Oceanography. This instrument measures the field between two sets of horizontal plastic arms, which are mutually perpendicular. A chopper device periodically reverses the sea-water connection, effectively reversing the direction in which the field is measured. The method obviates electrode noise by cancelling it out with this switching method (Filloux, 1987).

Chapter 2 : Seafloor Electromagnetic Experiments

2.1 Introduction

A significant number of seafloor EM studies have now been conducted using a variety of methods and in a diverse range of tectonic environments. Many of these experiments have had the principal objective of determining information about the conductivity structure of sediments, oceanic crust and upper mantle. Comparisons of interpretations have been made by Oldenburg (1981), Oldenburg *et al.* (1984), Law (1983) and Campbell (1987); all have indicated that there is a distinct EM response from the sub-oceanic lithosphere and upper mantle. A significant advantage for later seafloor EM studies is that parameters derived from these previous experiments act as a data base against which new interpretations may be judged.

In this chapter, two seafloor array experiments are described, with emphasis on the distinct tectonic environment of each region. Interpretation of the MT and GDS observations from these experiments has formed the motivation for much of the research in this thesis. The Tasman Project of Seafloor Magnetotelluric Exploration (TPSME) and has been extensively studied by the group led by F. E. M. Lilley at the Australian National University. In chapter 7 below, 3D modelling techniques are applied to the Tasman Sea to analyse EM induction effects in the ocean; the results are compared with the Tasman Sea MT and GDS data published by Lilley *et al.* (1989) and Ferguson *et al.* (1990).

The second experiment is EMRIDGE, an EM exploration of a mid-oceanic ridge (MOR). A detailed report on the experiment is given, with emphasis on the tectonic nature of the Juan de Fuca Ridge, and the principal EM objectives. Also included is a preliminary analysis of the experimental data, to indicate the methods of data processing, and some simple conclusions: in chapter 6, GDS and MT data are interpreted and compared to theoretical predictions from 2D and 3D ridge-transform -models.

Finally, a brief overview of the developments of seafloor EM studies is presented in two tables: the first is a summary of experiments aimed at determining the conductivity of deep upper mantle structure, and the second reviews experiments which examine the conductivity of shallow upper mantle, crust and sediment structures. Also, seafloor MT data from the experiments are reviewed with 1D inversions of the observed data.

2.2 Tasman Project of Seafloor Magnetotelluric Exploration

2.2.1 Introduction

The Tasman Project of Seafloor Magnetotelluric Exploration (TPSME) took place between early December 1983 and late March 1984: a detailed account of the experimental details is presented by Filloux *et al.* (1985), Ferguson *et al.* (1985), Ferguson (1988), Lilley *et al.* (1989) and Ferguson *et al.* (1990), so a brief outline only will be presented here. Figure 2.1 illustrates the distribution of recording sites, both on the seafloor and on the adjacent coast and continental regions of Australia and New Zealand. Previous work on land (Tammemagi & Lilley, 1971; Bennett & Lilley, 1974; Woods & Lilley, 1980) determined a strong coast effect which was modelled as being not only the result from the effect of highly conducting sea-water in contact with the much more resistive continental crustal material, but also deep electrical conductivity contrasts beneath the continent-ocean margin.

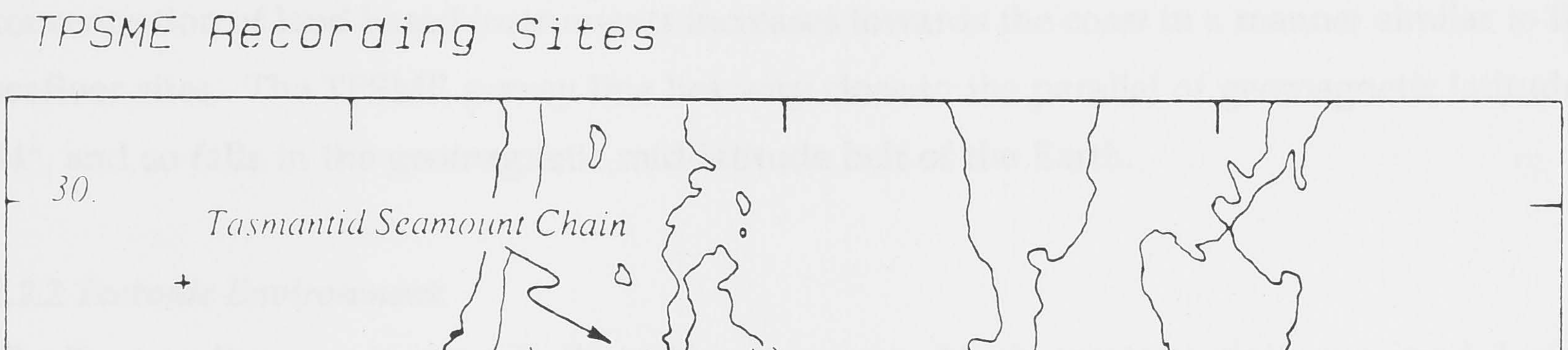

Figure 2.1 Recording sites for the Tasman Project of Seafloor Magnetotelluric Exploration, and location of major tectonic features.

The line of seafloor sites across the Tasman Sea was carefully chosen to span a number of major tectonic features. The experiment was partly designed to consider the geomagnetic coast effect, by having the sites spaced in an exponentially increasing distance away from the coast, along a survey line perpendicular to it. The site TP1 was on the Lord Howe Rise, an area of submerged continental crust. Site TP4 lies close to both the fossil spreading ridge and Mount Gascoigne, which is part of the Tasmantid Seamount Chain.

In 1986, a further three magnetometers observed on the continental shelf and slope close to the coastline of N.S.W., along the TPSME survey line. This latter experiment is known as the Continental Slope Experiment (CSE), and details of it may be found in Kellett *et al.* (1988), Kellett (1989), White *et al.* (1989) and Kellett *et al.* (1991).

For both the TPSME and CSE experiments, observations were made with a number of land-based instruments, and records were obtained from the Canberra Magnetic Observatory (CMO) in Australia and the Eyrewell Magnetic Observatory (EYR) in New Zealand. The concentration of land based instruments increases towards the coast in a manner similar to the seafloor sites. The TPSME survey line lies very close to the parallel of geomagnetic latitude -44°, and so falls in the geomagnetic mid-latitude belt of the Earth.

2.2.2 Tectonic Environment

The Tasman Sea area is tectonically stable at present. Much greater activity occurred during a period of seafloor spreading which terminated approximately 55 Ma ago: TPSME recording sites thus lie on lithosphere formed between 82 and 60 Ma (Weissel & Hayes, 1977). The spreading ridge is offset by a number of fracture zones, and is now characterised by a shallowing of the seafloor and a basement ridge (e.g. Hayes & Ringis, 1973). During this period of tectonic activity, the Lord Howe Rise rotated anticlockwise in an eastwards direction away from Australia. It is believed that the Lord Howe Rise comprises altered continental crust (e.g. Frey, 1985; Shor *et al.*, 1971), which submerged to its present depth of 750 - 2000 m sometime between the end of seafloor spreading and 55 Ma (McDougall & van der Lingen, 1974; Schubert & Sandwell, 1989). Using the detachment-fault model of passive margin evolution (Lister *et al.*, 1986) the Lord Howe Rise would compose the lower plate margin while southeast Australia represents the upper plate margin (Kellett *et al.*, 1991).

The Tasmantid Seamount Chain is associated with Tertiary to Recent volcanic activity, and the hot spot trace charts the movement of the Indo-Australian plate in a northwards direction (McDougall & Duncan, 1988). At the head of the chain, the youngest of the seamounts is the Gascoigne Seamount which is dated by McDougall & Duncan (1988) as being of age 5 Ma; TPSME site TP4 lies approximately 50 km to the south. There is an age progression of the seamounts southwards at a rate of approximately 6.4 km.Ma^{-1}, which is comparable to the plate velocity north. The predicted location of the present hot spot is marked by a region of increased seismicity (Denham, 1985).

Except for localised features, such as seamounts, the bathymetry of the Tasman Sea is close to that predicted by the cooling plate model of Parsons & Sclater (1977). The ridge crest has been observed at depths of 4500 to 5200 m, and the basement depths for the oldest ocean floor are 6000 m near the Australian continent and 5500 m near the base of the Lord Howe Rise (Hayes & Ringis, 1973).

The limited number of heat-flow data (e.g. Grim, 1969; Morin & Von Herzen, 1986) from the Tasman Sea floor and Lord Howe Rise are in agreement with heat flow data from lithosphere of comparable age (Parsons & Sclater, 1977). However, observed heat flow values in southeast Australia are anomalously high (Cull, 1982). O'Reilly & Griffin (1985) construct a geotherm from the equilibration temperatures from mantle-derived xenoliths of garnet websterite, and show that high temperature gradients at depths of 10 - 100 km characterise much of southeast Australia, and are closely associated with the tectonics of the opening of the Tasman Sea and crustal extension.

A blanket of sediment covers much of the Tasman abyssal plain, derived from the terrestrial erosion of east Australia. Sediment thicknesses reported in Ferguson (1988) range from 1250 m close to the coastline of southeast Australia, to less than 400 m on the Lord Howe Rise. The oceanic crust is estimated from seismic results (Shor *et al.*, 1971) to be approximately 10 km thick.

The deep structure of the Tasman Sea has been examined by seismic surface wave analysis (Sundaralingam & Denham, 1987). By examining Rayleigh waves and fixing shear wave velocities to the global PREM model (Dziewonski & Anderson, 1981), Sundaralingam & Denham determined a low-velocity zone at a depth of 65 km, which is consistent with the depth to the low-velocity zone calculated by Forsyth (1977) for lithosphere of age greater than 30 Ma.

From global tomographic inversions of free-Earth oscillation data and seismic surface wave analysis Woodhouse & Dziewonski (1984) and Dziewonski (1984) suggest that there are systematic differences in velocity structure across the Tasman Sea, southeast Australia and central Australia. Such differences extend to depths of 400 km, and although the depths of shear wave variations are not well resolved, a maximum difference of 4 % is postulated between shield areas and the sub-oceanic upper mantle. Low shear wave velocities may be indicative of high temperatures in the sub-oceanic upper mantle, consistent with the result of

O'Reilly & Griffin (1985) for the southeast Australian continental lithosphere. The resolution from the tomographic inversion is of scale-distance approximately 2000 km, so lateral variations in velocity structure across the Tasman Sea are not resolved.

Observations of the seismic Sn phase also suggest that the lithosphere of the Tasman Sea is anomalous (Molnar & Oliver, 1969). There appears to be strong attenuation of the Sn phase across the Tasman Sea, but there is some doubt as to the interpretation (Bennett, 1972).

2.2.3 *Instrumentation*

Seafloor EM array experiments, such as the TPSME, have become feasible over the last ten years due mainly to the design of very accurate seafloor instruments. The instruments deployed at the seafloor sites were developed at the Scripps Institution of Oceanography (SIO) (Filloux, 1987). The complementary CSE used magnetometers designed at the Flinders University of South Australia (White, 1979). The land-based Gough-Reitzel magnetometers were built at the Australian National University (ANU) (Lilley *et al.*, 1975). Table 2.1 describes the location and nature of the recording sites.

2.2.4 *Experimental Aims*

The main objective of the TPSME was to probe Earth's deep electrical conductivity structure and relate it to the major tectonic framework of the Tasman Sea region. By the nature of seafloor observations of natural fluctuations in Earth's **E** and **B** fields, only the large scale of the lithosphere and asthenosphere structures could be probed: little or no crustal information can be resolved, although the presence of sediments may profoundly alter interpretations. The resolution of a partial melt layer coincident with the seismic low-velocity zone is of great interest, particularly in relation to the position and age of the fossil spreading ridge (Ferguson, 1988; Ferguson *et al.*, 1990).

Another objective was to determine lateral changes in electrical conductivity from continental to oceanic lithosphere. Previous GDS studies on land suggested that differences in the geomagnetic coast effect may be correlated to the age and tectonic structure of the continental margin (Everett & Hyndman, 1967). The spacing of the TPSME sites on land and along the seafloor, and the latter deployment of three additional magnetometers along the continental shelf, have been used by Kellett (1988) and Kellett *et al.* (1991) to determine a distinct, but poorly resolved, difference in conductivity beneath the Tasman Sea and continental Australia.

Table 2.1 Location and origin of instruments used in TPSME (after Ferguson ,1988).

Site	Location	Geographical Coordinates		Institution	Instrument
	/ Depth (m)	Latitude (N)	Longitude (W)		
MYL	Meryula	31° 32'	146° 08'	A.N.U.	G
GNS	Ivanhoe	33° 16'	143° 56'	A.N.U.	G
BLN	Barellan	34° 19'	146° 37'	A.N.U.	G
CLC	Coolac	34° 59'	148° 16'	A.N.U.	G
BKM	Black Mt.	35° 16'	149° 06'	A.N.U.	G
CMO	Mag. Obs.	35° 19'	149° 22'	B.M.R	PPM
BBB	Bombay Bridge	35° 25'	149° 43'	A.N.U.	G
CDM	Clyde Mt.	35° 33'	149° 59'	A.N.U.	G
DRS	Durras	35° 40'	150° 17'	A.N.U.	G
TP8	4850	35° 49'	151° 08'	S.I.O	M,H
TP9	4850	35° 55'	151° 22'	S.I.O.	M
TP7	4850	36° 00'	151° 36'	S.I.O.	M,H,V
TP6	4836	36° 14'	152° 15'	S.I.O.	M,H
TP5	4660	36° 43'	153° 35'	S.I.O.	M,H
TP4	4460	37° 33'	155° 58'	S.I.O.	M,H
TP3	4980	38° 54'	159° 50'	S.I.O.	M,H
TP2	4800	38° 30'	162° 38'	S.I.O.	M,P
TP1	2550	38° 13'	166° 11'	S.I.O.	M,H
EYR	Eyrewell			NZ DSIR	PPM

G - Gough-Reitzel magnetometer, PPM - proton precession magnetometer at magnetic observatories, M - Filloux magnetometer, H - Filloux horizontal electric field instrument, P - Filloux seafloor pressure records, V - Filloux vertical electric field instrument. A recording oceanographic current meter was operated near the seafloor site at TP9.

BMR - Bureau of Mineral Resources, NZ DSIR - New Zealand Department of Science and Industrial Research.

Another important aim of the TPSME was to examine large scale oceanographic flows. Near the Australian coast, the observation line traverses the Eastern Australian Current which is a western boundary intensification for the south Pacific gyre. Between latitudes 30° S and 34° S (Godfrey *et al.*, 1980) this current may break into warm core rings. The density of instruments close to the coast allows a careful study of the associated EM effects due to a large body of highly conducting sea-water moving relative to a stationary magnetic field. The electric field observations have been analysed to isolate the motion of a mesoscale eddy (Bindoff *et al.*, 1986; Lilley *et al.*, 1986; Bindoff, 1988). Recent evidence by Lilley *et al.* (1991) shows that there is also a magnetic signature from the mesoscale eddy, and that approximately 6 % of the return electric current induced in the sea-water leaks through the seabed; such estimates may lead to an estimate of the conductance of the sediment layer. Traditional oceanographic measures of barotropic velocity are compared to EM observations by Mulhearn *et al.* (1988).

Site TP4 was located approximately 50 km south of Mount Gascoigne. The high heat-flow associated with the Tertiary volcanics may still have a distinct EM signature. Ferguson (1988) points out that MT and GDS soundings are suited to investigating the different plausible mechanisms proposed for the source of the seamount chain.

2.3 EMRIDGE : the Electromagnetic Exploration of the Juan de Fuca Ridge

2.3.1 Introduction

Mid-oceanic ridge (MOR) systems provide the key to understanding how Earth's oceanic lithosphere is generated. At these spreading centres, upwelling mantle partially melts as a result of pressure relief, and this melt migrates and solidifies to create new oceanic crust. Fractures in the upper crust result in hydrothermal circulation, which decreases with depth as porosity falls due to crack closure and sealing. Electromagnetic techniques are admirably suited to the study of hydrothermal circulation, migration and accumulation of melt, and the thermal evolution of dry lithosphere, as they have great sensitivity to the physical properties under consideration.

To date, the relatively few EM experiments which have been conducted in MOR environments have not detected any continuous conductive zones along ridge axes (Law & Greenhouse, 1981; Filloux, 1982b; Wannamaker *et al.*, 1989a, Evans *et al.*, 1991). These results may be profoundly important to the understanding of the processes of magma separation and migration.

This section reports on a new EM project, EMRIDGE (Electromagnetic study of the Juan de Fuca Ridge) designed to investigate the processes active in the generation of new oceanic crust. An array of EM apparatus was deployed within a small region centred on the southern-most segment of the Juan de Fuca Ridge in the northeast Pacific Ocean, shown in Figure 2.2 and in more detail in Figure 2.3. EMRIDGE was designed to complement the earlier large EM array study known as EMSLAB (Electromagnetic Sounding of the Lithosphere and Beyond), which spanned the entire Juan de Fuca Plate, from the ridge axis to the subduction zone beneath the Cascade Mountain belt in the states of California, Oregon and Washington, U.S.A., and British Columbia, Canada (EMSLAB Group, 1988; Filloux *et al.*, 1989; *J. Geophys. Res.* Special Issue, 1989). The principal objective of EMSLAB was to examine the size and nature of the resistive lithospheric slab, from ridge accretionary processes to the subduction zone and beyond; also important oceanographic information was observed (Filloux *et al.*, 1989; Chave *et al.*, 1989). Despite the high percentage of the world's existing seafloor apparatus which was employed for offshore EMSLAB (Filloux *et al.*, 1989), the number of instruments was not sufficient for the detailed study of the ridge area. EMRIDGE was subsequently proposed by J. H. Filloux to realise this objective, by deploying an array of instruments close to the ridge accretionary zone.

2.3.2 Tectonics

The Juan de Fuca Ridge, shown in Figures 2.2 and 2.3, marks the boundary between the Pacific and Juan de Fuca Plates, and has a spreading half-rate of 29 $\mathrm{km.Ma^{-1}}$ (Blackman & Forsyth, 1989). Understanding of the processes active at the Juan de Fuca Ridge has been improved dramatically by a series of geophysical and geological investigations, such as high-resolution swath mapping by SEABEAM, SeaMARC and GLORIA (USGS Juan de Fuca study group, 1986), submersible diving programs and closely spaced magnetic surveys. These have revealed that the Juan de Fuca Ridge is divided into at least six segments, each 50 to 150 km long (Johnson & Holmes, 1990), consistent with patterns observed at the East Pacific Rise (Macdonald *et al.*, 1988) and the Mid-Atlantic Ridge (Sempéré *et al.*, 1990). Gravity data from the Mid-Atlantic Ridge (Lin *et al.*, 1990) suggest that accretion of magma at a MOR is focused in each segment, which agrees with laboratory studies and with the fluid dynamic properties of melt (Whitehead *et al.*, 1984). Seismic refraction studies show that fast-spreading ridges have a nearly continuous axial magma chamber, about 2 km below the seafloor and with width 2 - 3 km (Detrick *et al.*, 1980; Mutter *et al.*, 1988), but a re-interpretation of East Pacific Rise data (Kent *et al.*, 1990) restricts the size of magma chamber to only a thin lens of melt at a depth of 1 km. Further evidence from a recent 3D seismic experiment also suggests that only a narrow (about 1km) section of the upper surface of the chamber has the unusually low velocities associated with mostly molten rock, but low velocities on the flanks infer a wider region of hot, mostly solid rock (Toomey *et al.*, 1990). At the northern end of the Juan de Fuca Ridge, a medium-spreading centre, a seismic refraction study (White & Clowes, 1990) has been inconclusive in delineating a shallow magma chamber.

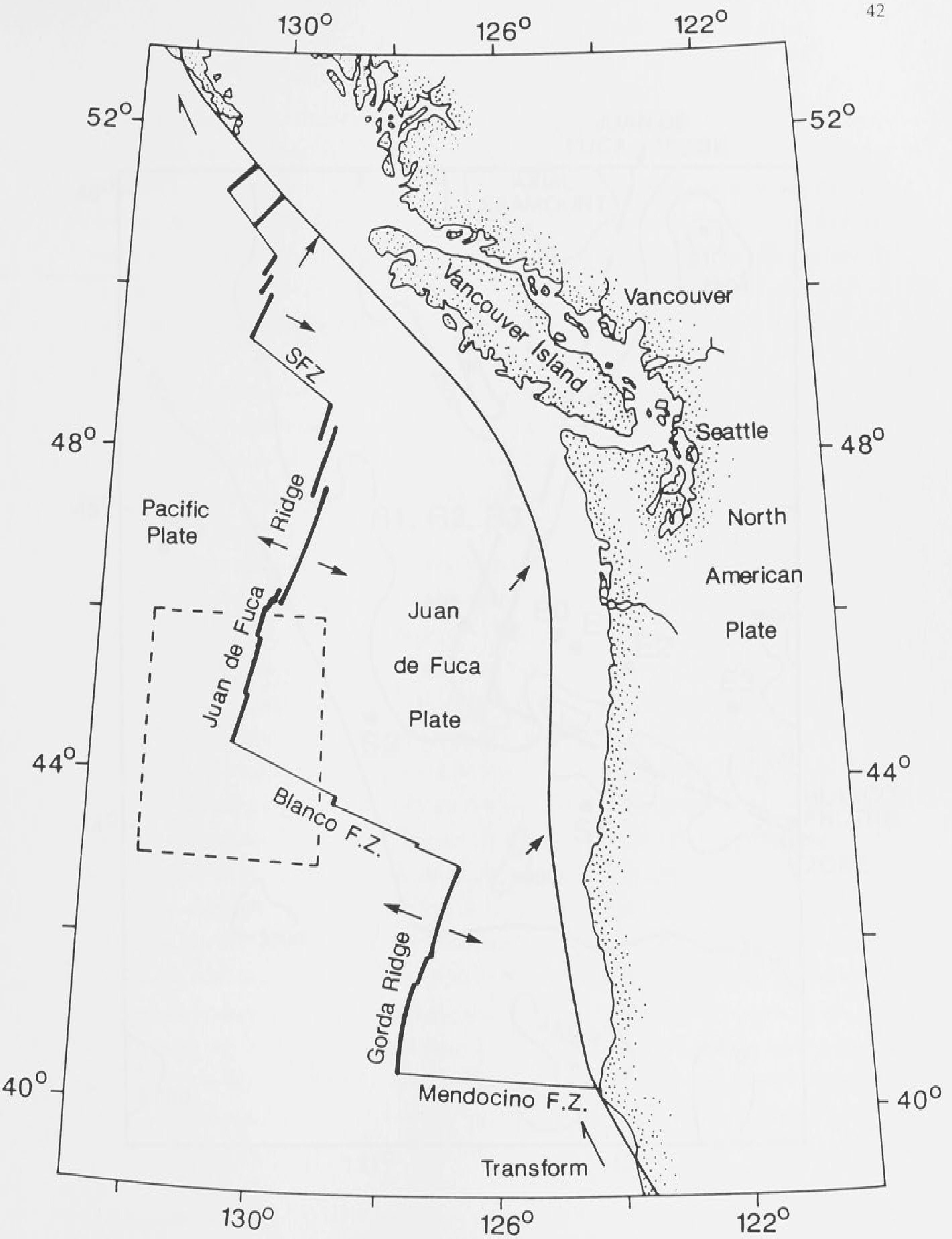

Figure 2.2 Location of the Juan de Fuca Ridge in the northeast Pacific Ocean. The dashed box is centred over the EMRIDGE study area shown in Figure 2.3.

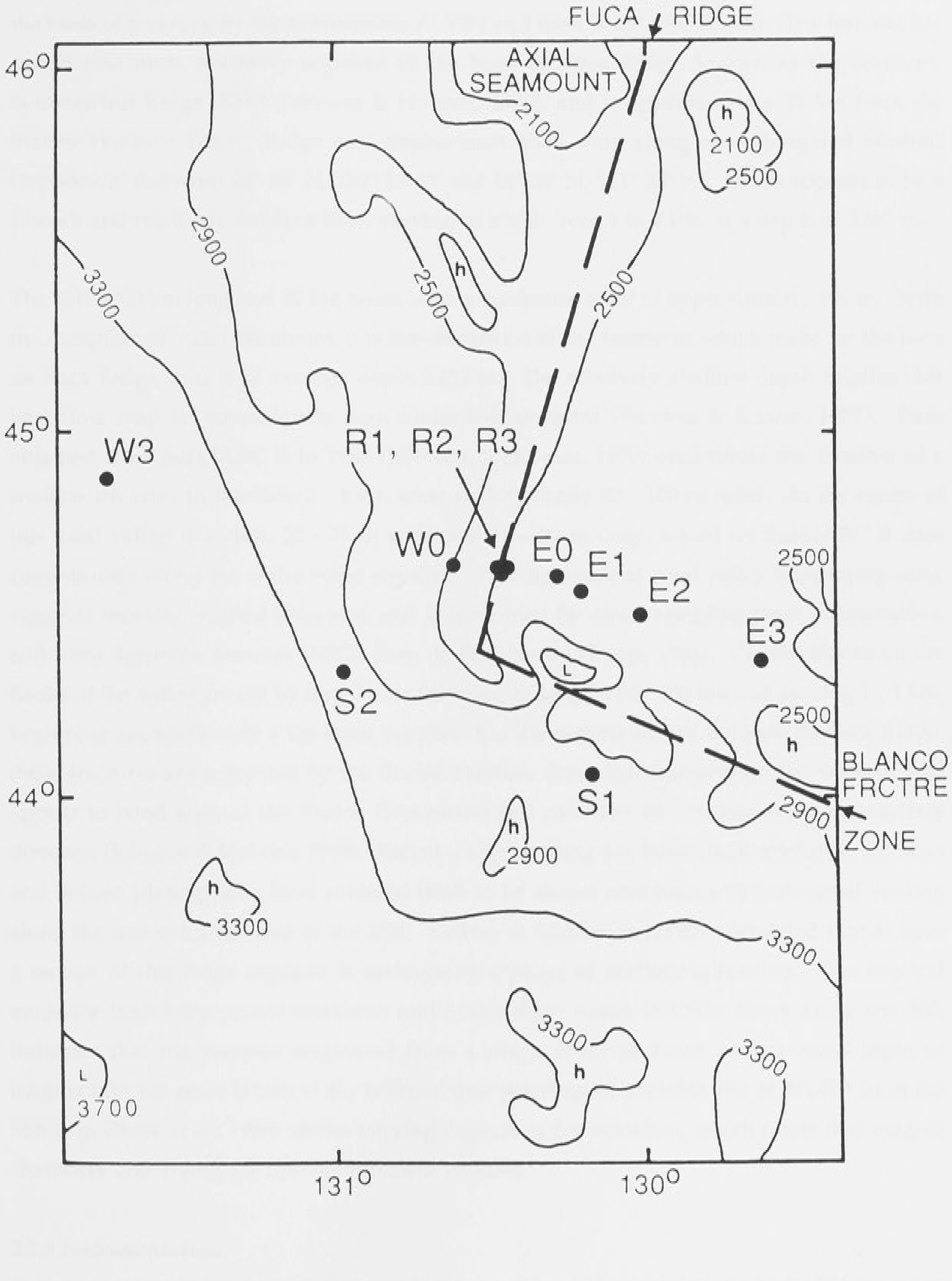

Figure 2.3 Bathymetry of the southern symmetrical segment of the Juan de Fuca Ridge and the Blanco Fracture Zone. EMRIDGE observation sites are indicated by solid circles and codes.

Deployment sites for the EMRIDGE seafloor instruments, shown in Figure 2.3, were chosen on the basis of a survey by the submersible ALVIN and from SeaMARC II data. The transect lies across that most southerly segment of the Juan de Fuca Ridge, known as the Southern Symmetrical Ridge (SSR) (Johnson & Holmes, 1990), and is approximately 37 km from the Blanco Fracture Zone. Ridge axis deployment sites were along the 'Elongated Summit Depression' (between 44° 38' N, 130° 23' W and 44° 35' N, 131° 24' W), which appears to be a smooth and relatively flat lava flow, varying in width from 1 to 2 km, at a depth of 2240 m.

The SSR is 60 km long and 20 km wide, with a maximum relief of approximately 200 m. With the exception of Axial Seamount, it is the shallowest of the segments which make up the Juan de Fuca Ridge, and is of average depth 2250 m. The relatively shallow depth implies that heat flow may be anomalously high under this segment (Parsons & Sclater, 1977). Data obtained from SeaMARC II in 1983 (Johnson & Holmes, 1990) established the location of a shallow rift zone in the SSR, 2 - 3 km wide with typically 80 - 100 m relief. At the centre of this axial valley is a cleft, 50 - 75 m wide and 10 - 30 m deep, traced by SeaMARC II data continuously along the entire ridge segment. This signature of axial valley floor topography suggests recently erupted volcanics, and is confirmed by direct sampling from submersibles, and from deep-tow cameras (USGS Juan de Fuca Study Group, 1986). Crustal blocks on the flanks of the valley are cut by long linear fractures, of lengths 80 - 100 km and spacing 1 - 3 km, beginning approximately 4 km from the axis. On the eastern side of the Juan de Fuca Ridge, these fractures are truncated by the Blanco Fracture Zone, but fractures on the western side appear to bend around the Blanco Depression and continue 40 - 50 km in a southeasterly direction (Johnson & Holmes, 1990). Recent mapping using Sea Beam, high resolution sidescan and bottom photography have revealed there to be almost continuous hydrothermal venting along the neo-volcanic zone of the SSR. Embley & Chadwick (1990) postulated that at least a section of this ridge segment is undergoing a phase of seafloor spreading. Geochemical evidence from very recent extensive mid-ocean ridge basalt (MORB) flows along the SSR indicates that the samples originated from a single eruptive event, with a rapid input of magma into the crust (Perfit *et al.*, 1989). Other petrological examination of MORB from the SSR (e.g. Dixon *et al.*, 1986) shows varying degrees of fractionation, which infers that magma chambers underlying the SSR are transient features.

2.3.3 Instrumentation

Collaboration between groups from institutions in Japan, Canada and Australia led to eleven instruments being placed on the seafloor, from July to November, 1988. Deployment took place from the Research Vessel Hakhuomaru, operated by the University of Tokyo (EMRIDGE Cruise Report, 1988). A precision depth-recorder and a small air-gun towed behind the ship helped locate seafloor sediment pockets, which were sought as deployment sites on both sides of the Juan de Fuca Ridge and to the south of the Blanco Fracture Zone. A detailed survey of the ridge axis was made to identify relatively flat areas, and a transect across the ridge was chosen. Three instruments were deployed at the ridge axis, six on the ridge flanks, and two to the south of the transform fault. At the end of the experiment, all eleven instruments were successfully recovered by the Canadian Research Vessel Parizeau. The global positioning system (GPS) provided precise navigation and recovery was aided by a radio-transmitter and flashing-Xenon beacons attached to the instruments. More information is provided in Table 2.2.

Table 2.2 Location, origin and data quality of instruments used in EMRIDGE.

Site Code	Sea Depth (m)	Geographical Coordinates Latitude (N)	Longitude (W)	Instrument (Institution)	Data Quality
W3	3662	44° 52.50'	131° 40.50'	PGC#1 (Pac. Geosc. Centre)	VG
W0	2658	44° 39.15'	130° 32.87'	OBM-S1 (Univ. of Tokyo)	VG
R1	2232	44° 37.20'	130° 22.70'	OBM-F2 (Flinders Univ.)	P
R2	2239	44° 36.19'	130° 23.44'	OBM-S5 (Univ. of Tokyo)	VG
R3	2234	44° 36.90'	130° 23.30'	OBEM-1 (Univ.of Tokyo)	ND
E0	2644	44° 36.88'	130° 12.46'	OBM-F4 (Flinders Univ.)	G
E1	2798	44° 34.60'	130° 07.50'	OBM-F3 (Flinders Univ.)	P
E2	2795	44° 31.40'	129° 57.70'	OBM-F1 (Flinders Univ.)	P
E2	2795	44° 31.40'	129° 57.70'	OBE (Univ. of Tokyo)	G
E3	2807	44° 23.02'	129° 32.95'	OBM-S3 (Univ. of Tokyo)	P
S1	3212	44° 05.70'	130° 08.20'	PGC#2 (Pac. Geosc. Centre)	VG
S2	3268	44° 20.19'	130° 55.20'	PGC#3 (Pac. Geosc. Centre)	G

OBM - Ocean Bottom Magnetometer, OBE - Ocean Bottom Electrometer, PGC - Ocean Bottom Magnetometer, OBEM - Ocean Bottom Electrometer and Magnetometer.
VG - Very Good, G - Good, P - Poor, ND - No Data

The seafloor instruments comprised seven three-component magnetometers, one horizontal field electrometer, and one combined magnetometer-electrometer. All were 'free-fall' in design, and at the end of recording returned to the sea-surface by buoyancy, after a timed or triggered release of ballast. Data sampling intervals were one-minute for the Australian magnetometers (White, 1979), two- and three-minutes for the Japanese magnetometers (Segawa *et al.*, 1983) and electrometers, and five-minutes for the Canadian magnetometers (Law, 1978). Instrument resolution was in the range 0.1 - 1 nT. Simultaneous land-based magnetic data were recorded at the Victoria Magnetic Observatory (VMO) of the Geological Survey of Canada, and at a site in Oregon U.S.A., arranged by H. S. Waff and J. R. Booker. Data sampling rates were one-minute and sixteen-seconds respectively, with corresponding least counts of 1 nT and 0.25 nT.

2.3.4 EMRIDGE Seafloor and Land Electromagnetic Data

The duration and quality of the data of the seafloor array varied considerably, as shown in Table 2.2. This thesis uses seafloor records recovered from six magnetometers, and from the electrometer at the site 35 km to the east of the ridge axis (Figure 2.3); further processing may produce good sections of data from two of the remaining magnetometers. All data sets required cleaning to remove spikes and jumps, by linear interpolation between successive uncorrupted data points, and long-period drift apparent on many records was removed by subtracting a low-order Chebyshev polynomial , fitted by least squares (Chave *et al.*, 1981). The order of such a polynomial was based on root mean square (RMS) error; the polynomial chosen was one for which the RMS error showed little improvement, typically less than 1% change, for any higher order of fit. For most of the magnetic field records a first or second order polynomial was sufficient to remove the mean and any linear or quadratic trend. The electric field observations exhibited larger drifts, particularly over the first few days, and for these records higher-order polynomials were found to be required.

Each data set was reformatted to a two-minute sample interval. For observations with a longer sampling interval, cubic-spline fits were applied, and the time series was then oversampled to produce pseudo two-minute values. Instruments with a sample rate of one-minute or less were averaged into two-minute values. Some high-frequency information is discarded in this process; however as high-frequency signals are strongly attenuated with depth in the ocean, little of value is lost for data with a least count of 1 nT.

Figures 2.4 (a and b) show magnetic and electric field data plotted over twenty-four hour periods (U.T.) on the 11th September (day 255) and 10th October (day 284). These two days were the most geomagnetically active of the three-month period. In both figures the uppermost traces are the seafloor magnetic components, with their respective site identifiers. Plotted below are the magnetic components for the land-based sites and, in Figure 2.4 a, the electric field recorded close to the ridge axis. The components of magnetic field shown are those of geomagnetic north (H), geomagnetic east (D) and vertical (Z), with the corresponding induced electric fields in geomagnetic orientation: east (Ed) and north (Eh).

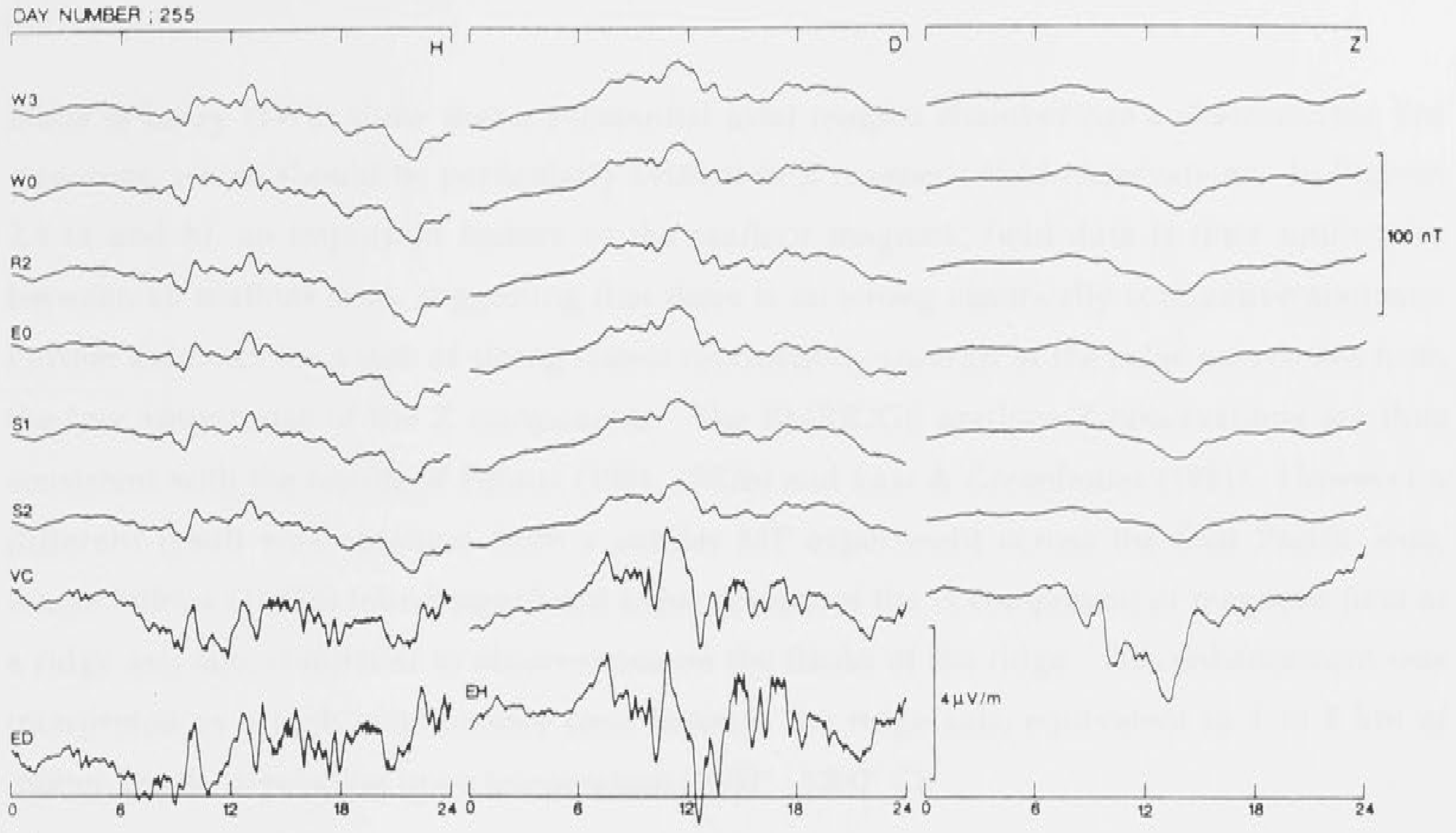

(a)

Figure 2.4 (a) Magnetic and electric field data from the seafloor sites (W3 - E0) and land site (VC) for 11 September 1988 (UT) over 24 hours. Shown are the geomagnetic north (H), geomagnetic east (D) and vertical components (Z) of magnetic field, and the electric field in the geomagnetic east (Ed) and geomagnetic north (Eh) directions. Note that Eh has been plotted reversed in sign to show its coherence with D.

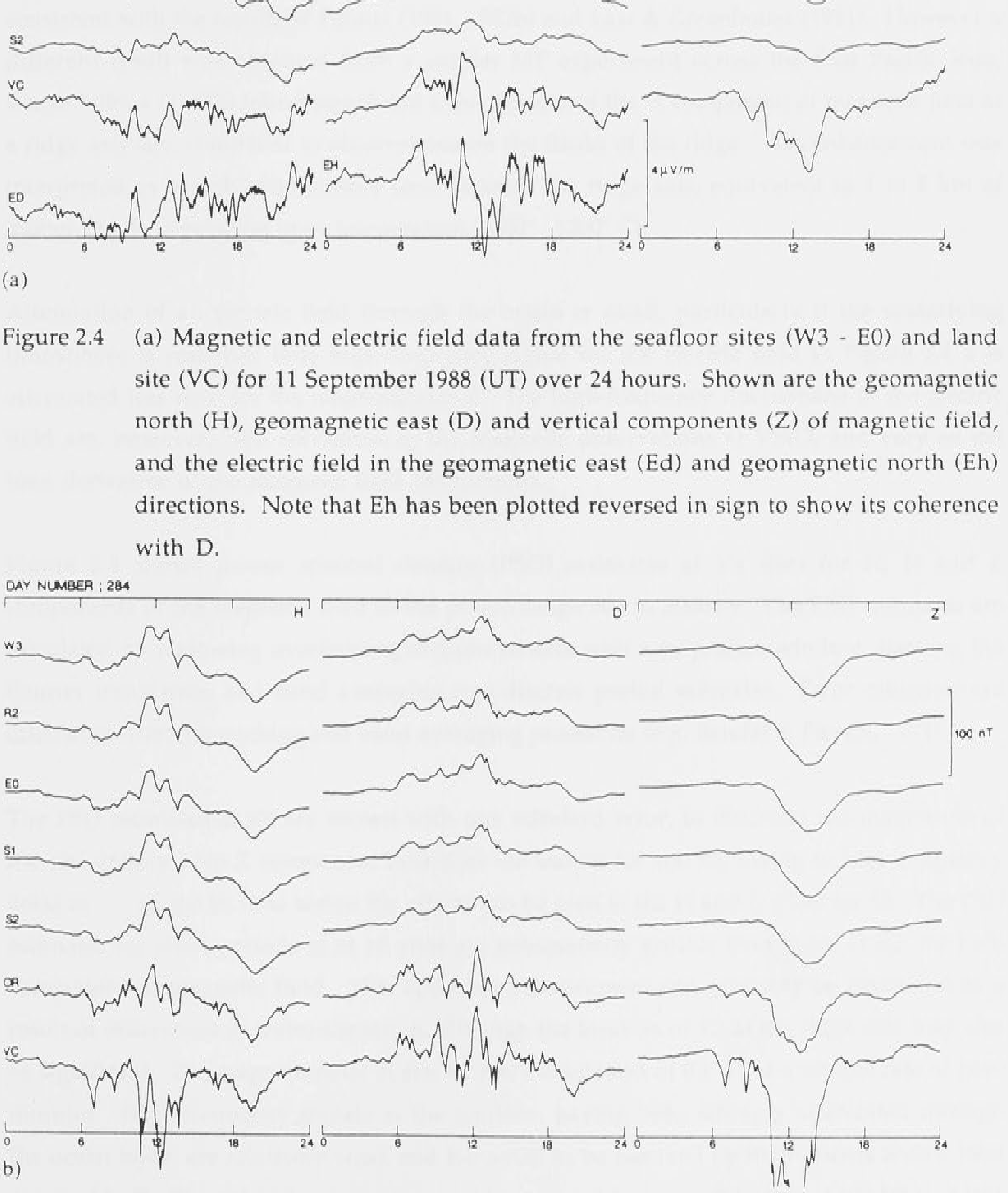

(b)

Figure 2.4 (b) Magnetic field data from seafloor sites (W3-E0) and land sites (OR-VC) on 10 October 1988 (UT) over 24 hours.

Duba & Lilley (1972) show that a substantial axial magma chamber has a characteristic EM signature, which should be particularly evident in Z magnetic field observations. In Figures 2.4 (a and b), an important feature of the seafloor magnetic field data is their uniformity between all seafloor sites, suggesting that there is no strong electrically conductive anomaly. Further evidence for a lack of strong lateral conductivity contrast at the ridge axis comes from the low amplitudes of the Z components. The EMRIDGE seafloor Z observations are thus consistent with the results of Filloux (1981, 1982b) and Law & Greenhouse (1981). However a different result was obtained from a similar MT experiment across the East Pacific Rise, where Filloux (1982b) found significant enhancement of the H component of magnetic field at a ridge axis site, compared to observations on the flanks of the ridge. This enhancement was interpreted as a high conductance zone beneath the ridge axis, equivalent to 1 to 8 km of molten basalt, depending upon temperature (1000° - 1200° C).

Attenuation of an electric field through the ocean is small, particularly if the underlying lithosphere is resistive; thus high-frequency signal for the electric field in Figure 2.4 a is attenuated less than for the magnetic signal. The high-frequency fluctuations in the electric field are, however, well correlated to the magnetic observations at VMO, and vary as the time derivative of the magnetic field fluctuations.

Figure 2.5 shows power spectral density (PSD) estimates at six sites for H, D and Z components of the magnetic field in the period range 300 to 30000 s. The PSD estimates are calculated by widowing overlapping sections of data with a 4π prolate window, stacking the Fourier transforms, and band averaging into discrete period estimates. Error estimates are calculated from the stacking and band averaging procedure (e.g. Bendat & Piersol, 1971)

The PSD estimates at R2 are shown with one standard error, to illustrate the magnitude of the uncertainty. No Z component estimates are shown for site S2, owing to high frequency noise in all the S2 time series; the effects can be seen in the H and D plots for S2. The PSD estimates for short periods at at all sites are substantially greater than those at R2, for each component of magnetic field. This apparent enhancement can probably be explained as a result of differences in instrumentation, although the location of R2 at the ridge axis may also be significant. The magnetometer at site R2 has a resolution of 0.1 nT at a sample rate of two-minutes. High-frequency signals at the seafloor, having been strongly attenuated through the ocean layer, are relatively weak and too small to be resolved by instruments with a least count of 1 nT. The only other instrument with comparable accuracy to that at site R2 is at W0, however the sample interval is longer than for the magnetometer at R2.

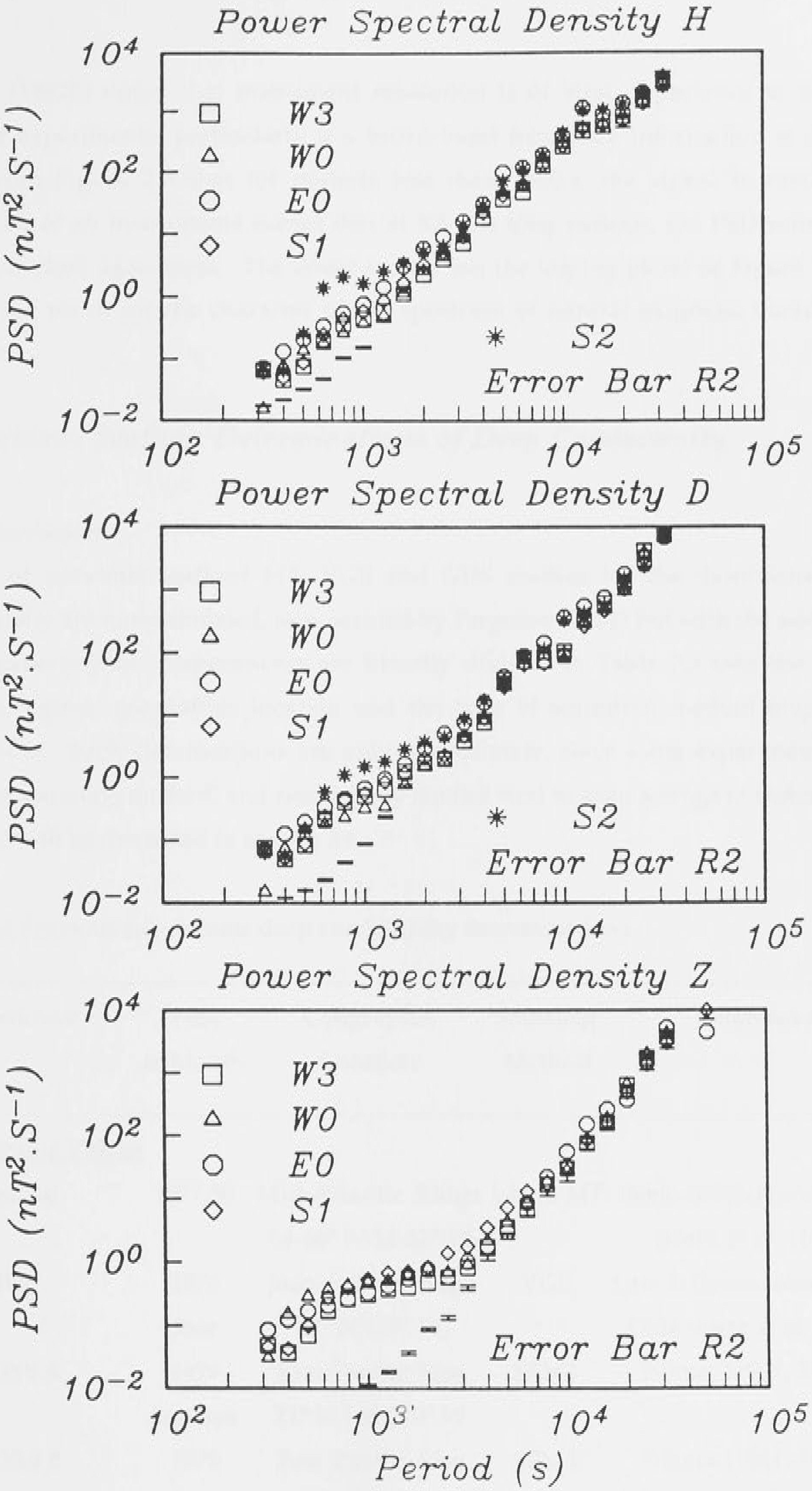

Figure 2.5 Power spectral density (PSD) estimates for magnetic field data at sites W3, W0, R2, E0, S1 and S2, for the geomagnetic north (H), geomagnetic east (D) and vertical components, respectively. The PSD estimates for R2 are shown with one standard deviation error bars. No Z component PSD estimates are shown for S2 due to high frequency noise in the observations.

Filloux (1982b) noted that instrument resolution is of vital importance to the success of seafloor experiments, particularly if a broad-band frequency information is desired. It is clear from Figure 2.5 that for periods less than 1500 s, the signal is smaller than the resolution of all instruments except that at R2. At long periods, the PSD estimates at each site show close agreement. The linear nature (on the log-log plots) of Figure 2.5 is also an interesting result for the character of the spectrum of natural magnetic fluctuations at the seafloor.

2.4 Previous Seafloor Determinations of Deep Conductivity

2.4.1 Introduction

Details of previous seafloor MT, VGS and GDS studies for the determination of deep conductivity are now tabulated, as presented by Ferguson (1988) but with the addition of more recent experiments. Experiments are broadly divided in Table 2.3 into the categories of tectonic regime, geographic location and the type of sounding method employed in the experiment. Such classifications are only approximate, since some experiments used more than one sounding method, and recent array studies tend to span a range of tectonic structures. Table 2.3 will be discussed in section 2.6.

Table 2.3 Previous sub-oceanic deep conductivity determinations.

Experiment	Year & Month	Geographic Location	Sounding Method	References
Mid-Oceanic Ridges				
Iceland	1977,80	Mid-Atlantic Ridge 64-66° N 14-22° W	Island MT	Beblo & Bjornsson (1980) Beblo *et al.* (1983)
JDF	1978 June	Juan de Fuca Ridge 47° N 129° W	VGS	Law & Greenhouse (1981) Oldenburg *et al.* (1984)
ROSE A	1979 Jan-Apr	East Pacific Rise 21° N 108-110° W	SFMT	Filloux (1981, 1982b)
ROSE B	1979 Feb	East Pacific Rise 12° N 102-103° W	SFMT	Filloux (1981, 1982b)
EMSLAB	1985 Aug-Sep	Juan de Fuca Ridge 44-46° N 125-131° W	SFMT	Filloux *et al.* (1989) Wannamaker *et al.* (1989a,b)
EMRIDGE	1988 Jul-Nov	Juan De Fuca Ridge 44-45° N 129-132° W	SFMT	(This chapter)

Experiment	Year & Month	Geographic Location	Sounding Method	References
Normal Sub-Oceanic Lithosphere				
SF (30 Ma)	1965 May	NE Pacific 33° N 127° W	SFMT	Cox *et al.* (1971)
MODE (130 Ma)	1973 Mar-Jul	NW Atlantic 27° N 70° W	VGS	Poehls & Von Herzen (1976)
MODE (130 Ma)	1973 Mar-Jul	NW Atlantic 27° N 70° W	SFMT	Cox *et al.* (1980)
AGGY I & II (50 Ma)	1976 Aug-Sep	N Central Pacific 27° N 150° W	SFMT	Chave *et al.* (1981)
NCP (72 Ma)	1976 Aug-Sep	N Central Pacific 27° N 151° W	SFMT	Filloux (1977, 1980b)
CAL (30 Ma)	1977 May-Jun	NE Pacific 31° N 128° W	SFMT	Filloux (1980b)
Murray	1979-80 Oct-Jan	N central Pacific 32° N 128° W	SFMT	
California	1983 Dec	California, U.S.A. 37° N 121° W	Land MT	Mackie *et al.* (1988)
TPSME (85-55 Ma)	1983-84 Dec-Apr	Tasman Sea 31-39° S 142-167° E	SFMT & VGS	Lilley *et al.* (1989) Ferguson *et al.* (1990)
EMSLAB (0-20 Ma)	1985 Aug-Sep	NE Pacific 44-46° N 125-131° W	SFMT	Filloux *et al.* (1989) Wannamaker *et al.* (1989a,b)
BEMPEX	1986-87 Aug-Aug	N Central Pacific 42° N 163° W	SFMT	Luther *et al.* (1987) Chave *et al.* (1990)
Aegean Sea	1989	Mediterranean Sea 35-40° N 10-30° E	VGS	Palshin *et al.* (1990)
Kerguelen	1989-90	S Indian Ocean 50° S 70° E	Island MT	Jouanne *et al.* (1990)

Experiment	Year & Month	Geographic Location	Sounding Method	References
Subduction Zones				
Marianas	1978 Sep-Dec	Marianas trough 18° N 144-146° E	SFMT	Filloux (1982c)
Japan	1981 Jul-Sep	Japan trough 39° N 142-150° E	SFMT	Yukutake *et al.* (1983)
New Zealand	1982	SW Pacific 35° S 180° W	SFMT	
EMSLAB	1985 Aug-Sep	Juan de Fuca Plate 44-46° N 125-131° W	SFMT	Filloux *et al.* (1989) Wannamaker *et al.* (1989a,b)

Experiment	Year & Month	Geographic Location	Sounding Method	References
Hot spots and seamount chains				
SF	1965 May	NE Pacific 33° N 127° W	SFMT	Cox *et al.* (1971)
Hawaii	1969-71	N Central Pacific 21° N 158° W	Island MT	Larsen (1975) Parker & Whaler (1981)
Hawaii	1969-71	N Central Pacific 21° N 158° W	Island GDS	Klein & Larsen (1978)
Hawaii	1978 Jun-Aug	N Central Pacific 18° N 150° W	SFMT	Tarits *et al.* (1986)
TPSME	1983-84 Dec-Apr	Tasman Sea 31-39° S 142-167° E	SFMT	Lilley *et al.* (1989) Ferguson *et al.* (1990)
Tahiti	1989 Mar-Jun	S Pacific 17° N 149° W	SFMT	Tarits *et al.* (1990)

Experiment	Year & Month	Geographic Location	Sounding Method	References
Geomagnetic Coast Effect				
ROBE 1	1976 Nov	S. Australia 37° S 139° E	GDS	White & Polatajko (1978)
Japan	1981 Jul-Sep	N Japan 39° N 142-150° E	GDS	Yukutake *et al.* (1983)
Vancouver Is.	1980 Jul-Aug	B.C., Canada 47-49° N 125-128° W	GDS	DeLaurier *et al.* (1983)
CSE	1986 Jul-Oct	SE Australia 36° S 151° E	GDS	Kellett *et al.* (1991)
ROBE 2	1989 Jan-Mar	S Australia 37° S 139° E	GDS	

Experiment	Year & Month	Geographic Location	Sounding Method	References
Arctic Ocean Studies				
Gakkel Ridge	?	E Arctic 82° N 100° E	Ice MT	Trofimov & Fonarev (1976) Fonarev (1982)
Haeckel Ridge	?	E Arctic ?	Ice MT	Trofimov & Fonarev (1976)
Podvodniki Basin	?	E Arctic 82° N 140° E	Ice MT	Trofimov & Fonarev (1976)
Lomonosov Ridge	?	C Arctic 84° N 120° E	Ice MT	Trofimov & Fonarev (1976)
Chukchi Plateau	?	W Arctic 78° N 165° W	Ice MT	Trofimov & Fonarev (1976)
Canadian Basin	1976-77	W Arctic 83-84° N 120-140° W	Ice MT	Trofimov (1979)
Medeleiev Ridge	?	W Arctic 82-83° N 175° W	Ice MT	Fonarev (1982)
Alpha Ridge	1983	W Arctic 85° N 100° W	Ice MT	Niblett *et al.* (1987)

2.5 Previous Seafloor Determinations of Shallow Conductivity

2.5.1 Introduction

This section is complementary to the previous one, and tabulates seafloor EM experiments used to determine sediment, crustal and uppermost mantle conductivities. A significant difference to the deep conductivity interpretations is that in-situ measurements have been made for sediment and crustal conductivities. Controlled source-field methods have the ability to bridge the gap between boreholes a kilometre or so deep and MT soundings, which on the seafloor are not sensitive to structure shallower than about 50 km. Experiments are tabulated in Table 2.4 by technique, rather than by tectonic regime, as few experiments have been conducted to date; this subject, however, is now one of growth in marine geophysics, particularly with the increased interest of commercial exploration of the continental shelves and mid-oceanic ridges.

Table 2.4 Previous sub-oceanic shallow conductivity determinations.

Experiment	Year & Month	Geographic Location	Tectonic Setting	References
Controlled Source EM Experiments				
RISE	?	East Pacific Rise 21* N 109° W	Spreading Ridge	Young & Cox (1981)
25 Ma Seafloor	1984 Aug	NE Pacific 28° N 122° W	Normal Lithosphere	Cox *et al.* (1986)
45 Ma Seafloor	1988 Nov	NE Pacific	Normal Lithosphere	Constable (1990)
MOSES	?	B.C., Canada 50° N 125° W		Edwards *et al.* (1985)
MOSES	1984 Jul	Juan de Fuca Ridge 48° N 128° W	Spreading Ridge	Nobes *et al.* (1986a,b)
East Pacific Rise	1984 Mar	E Pacific 12° N 103° W	Spreading Ridge	Francis (1985)
East Pacific Rise	1989 Jun	E Pacific 13° N	Spreading Ridge	Evans *et al.* (1991)

Experiment	Year & Month	Geographic Location	Tectonic Setting	References
Conductance of Seafloor from Oceanic Source-Fields				
BEMPEX	1986-87	N Pacific	Normal	Luther *et al.* (1987)
	Aug-Aug	42° N 163° W	Lithosphere	
TPSME	1983-84	Tasman Sea	Normal	Bindoff *et al.* (1988)
	Dec-Apr	31-39° S 142-167° E	Lith.	Lilley *et al.* (1991)

Experiment	Year & Month	Geographic Location	Tectonic Setting	References
Conductivity of Sediments and Crust From In-Situ Measurements				
108 Ma	?	?	Normal Lithosphere	Salisbury *et al.* (1980)
6.2 Ma	1981-82	E Pacific	Normal	Von Herzen *et al.* (1983)
	Nov-Jan	1° N 84° W	Lithosphere	Becker *et al.* (1982)
0 Ma	?	?	Spreading Ridge	Hyndman & Salisbury (1984)

2.6 *Seafloor Magnetotelluric Data*

2.6.1 Introduction

Magnetotelluric data are published in a wide variety of formats, and it is a useful exercise to present reformatted data, and to examine the consistency between MT estimates in different tectonic settings. In this section, published seafloor MT estimates are re-examined using the same interpretational techniques. The geographical distribution of past experiments in the north Pacific Ocean, shown in Figure 2.6, reflects the location of the principal institutions involved in such studies. However, experiments have been conducted over a wide range of tectonic environments, and on all ages of seafloor.

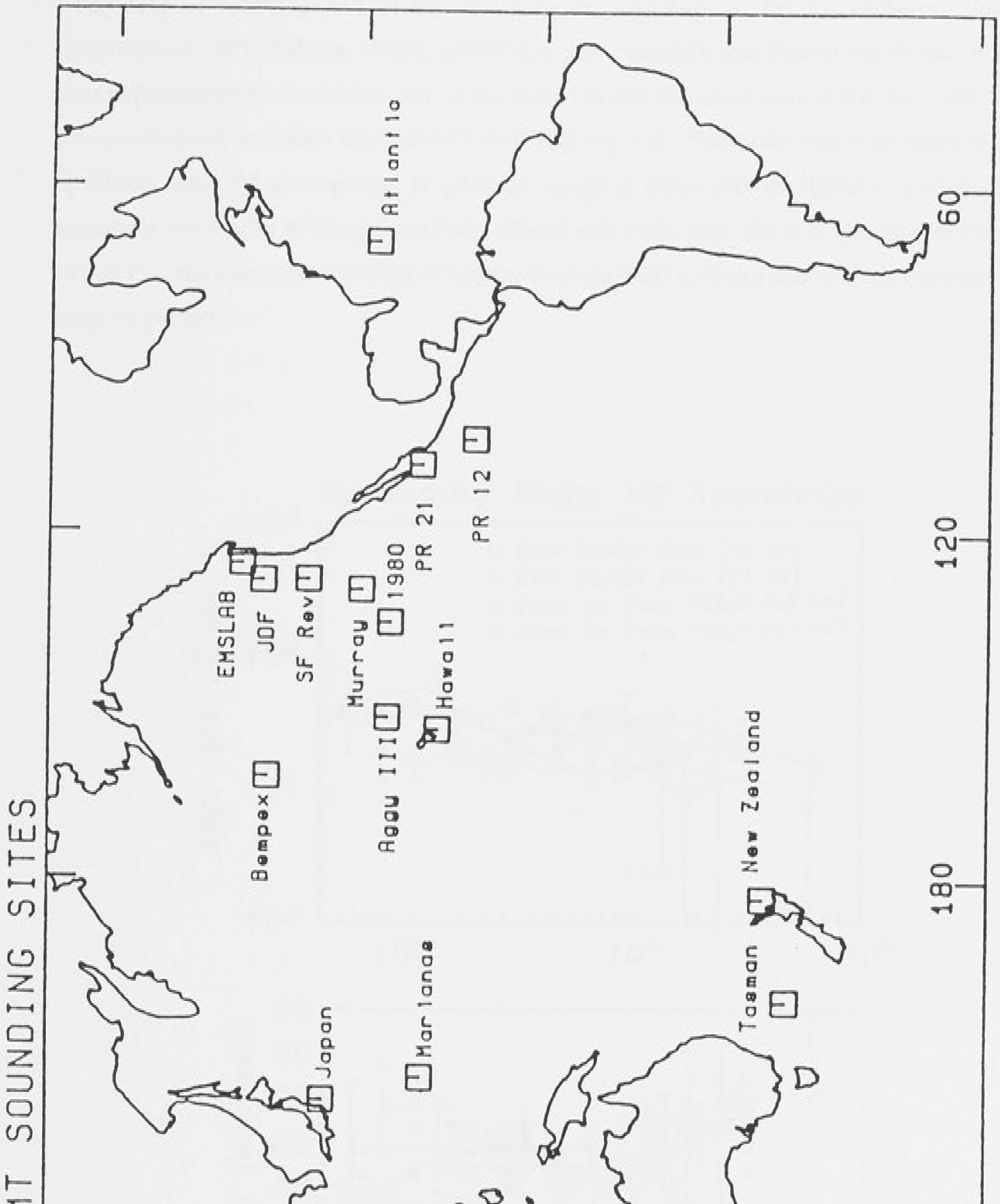

Figure 2.6 Location of seafloor MT experiments in the north Pacific Ocean, Atlantic Ocean and Tasman Sea (from Ferguson, 1988).

2.6.2 Magnetotelluric Observations at Spreading Ridges

Four sets of seafloor MT estimates from experiments at MORs (Filloux, 1981; Law & Greenhouse, 1981; Filloux, 1982b; EMRIDGE, see chapter 6 this thesis) are shown in Figure 2.7; two experiment were carried out at the East Pacific Rise and two at the Juan de Fuca Ridge. The consistency between seafloor MT data sets is good. The main characteristics are a uniform apparent resistivity response at periods ranging from 500 to 10000 s, and a decrease in apparent resistivity at longer periods. Phase estimates also show close agreement: the phase drops to a minimum at a period of approximately 5000 s, then rises to a maximum value at the longest period.

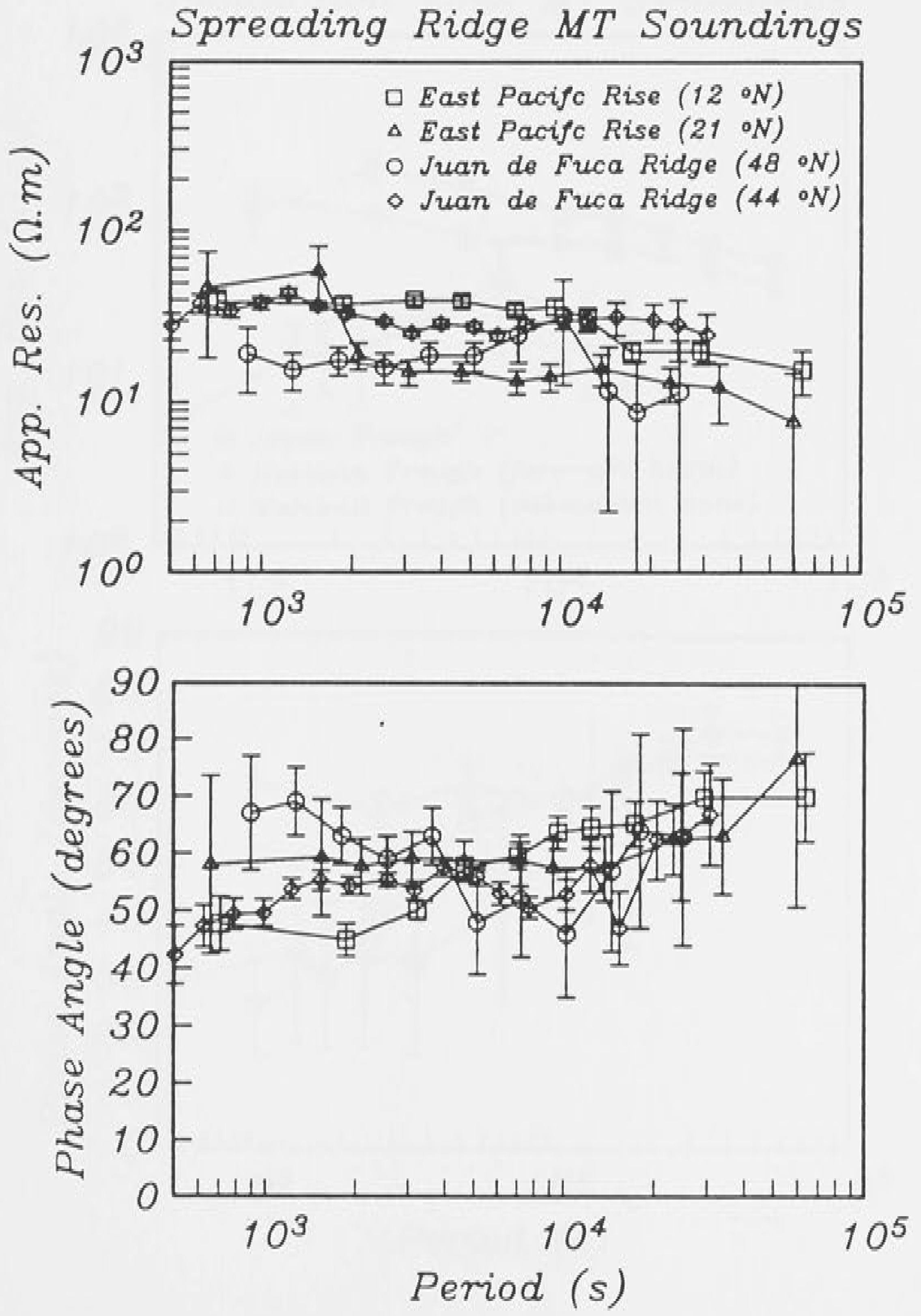

Figure 2.7 Seafloor MT soundings on mid-oceanic ridges. Apparent resistivity and phase data are shown with one standard deviation error.

2.6.3 Magnetotelluric Observations at Subduction Zones

Figure 2.8 shows three sets of MT sounding data made in the vicinity of a subduction zone (Filloux, 1982c; Yukutake *et al.*, 1983). The MT estimates in Figure 2.8 are less consistent than above MORs, however this may be expected as the sites are located on both sides of the subduction zone and at various distances from the trench. At long periods, all three curves have similar decreasing apparent resistivity and increasing phase, which suggests that the deepest structure is common to all sites. At short periods two of the MT soundings have small apparent resistivity and phase estimates, which are most probably due to electric current channelling along the thick wedge of sediments at the subduction zones. The MT site at the Mariana Fore-arc basin spreading-ridge is further from the subduction zone, and shows monotonically increasing apparent resistivity and large phase angles with decreasing period. The MT estimates from this site suggests the presence of a resistive upper lithosphere.

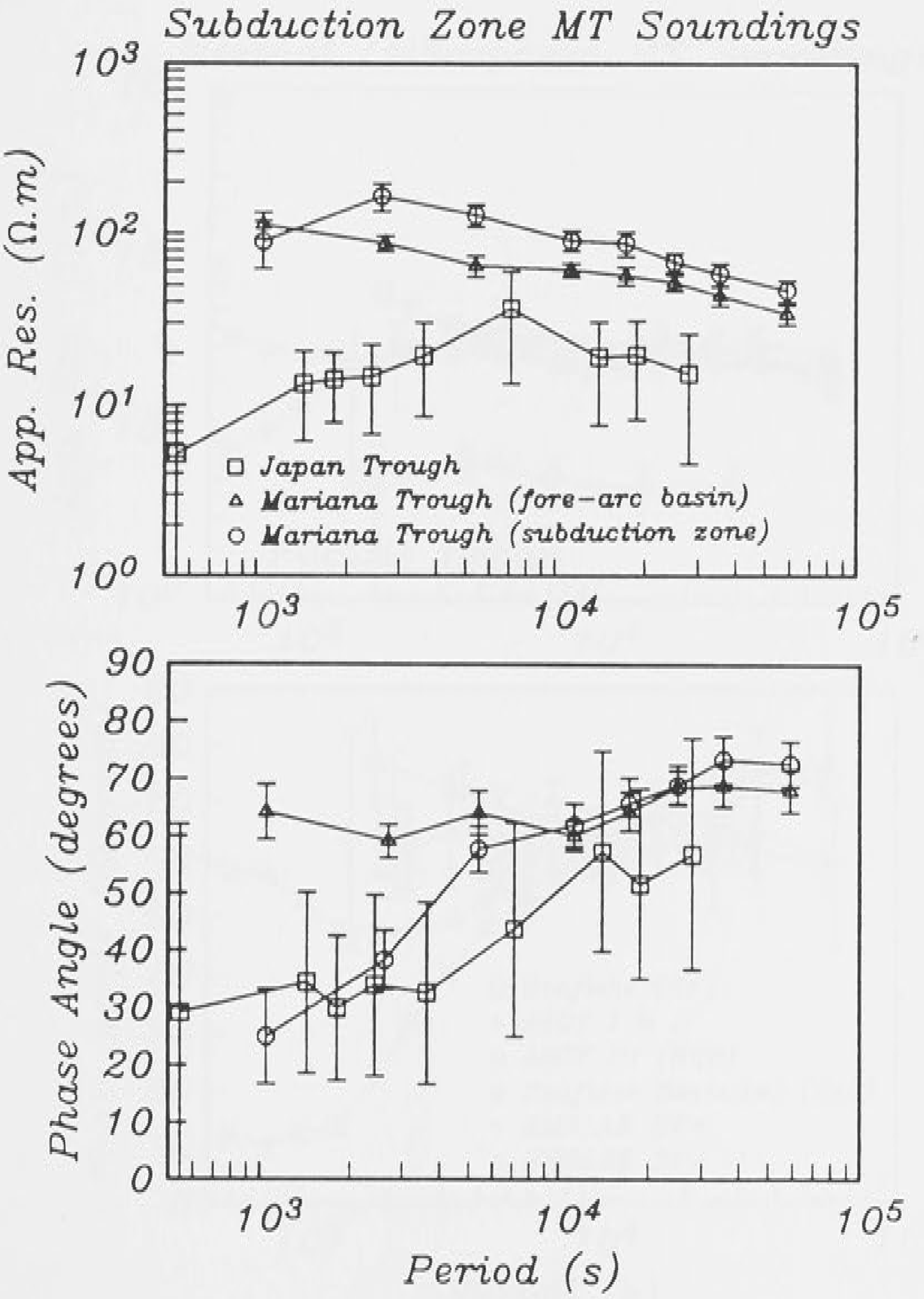

Figure 2.8 As for Figure 2.7, but seafloor MT soundings in close proximity to subduction zones.

2.6.4 Magnetotelluric Observations on 'Normal' Oceanic Lithosphere

'Normal' lithosphere constitutes seafloor from active tectonic regions (such as spreading ridges, subduction zones and hot spots). Magnetotelluric soundings on normal lithosphere span a wide range of seafloor age, and so the predicted age dependence (e.g. Law, 1983) due to the cooling of lithosphere away from the ridge and drop in asthenosphere melt fraction may be examined. Experimental seafloor MT estimates from the north Pacific Ocean, shown in Figure 2.9, are published by Cox *et al.* (1971), Chave *et al.* (1981), Filloux (1977, 1980b, 1982a) and Wannamaker *et al.* (1989a). There is good agreement, particularly over periods 1000 to 10000 s, between apparent resistivity and phase estimates at all sites (given that Seafloor Revisited should be regarded as revising SF; Filloux, 1980b). At longer periods, there is a consistent drop in apparent resistivity at most sites. Short period MT estimates show the greatest disparity between observations, which may be the result of different sediment thicknesses.

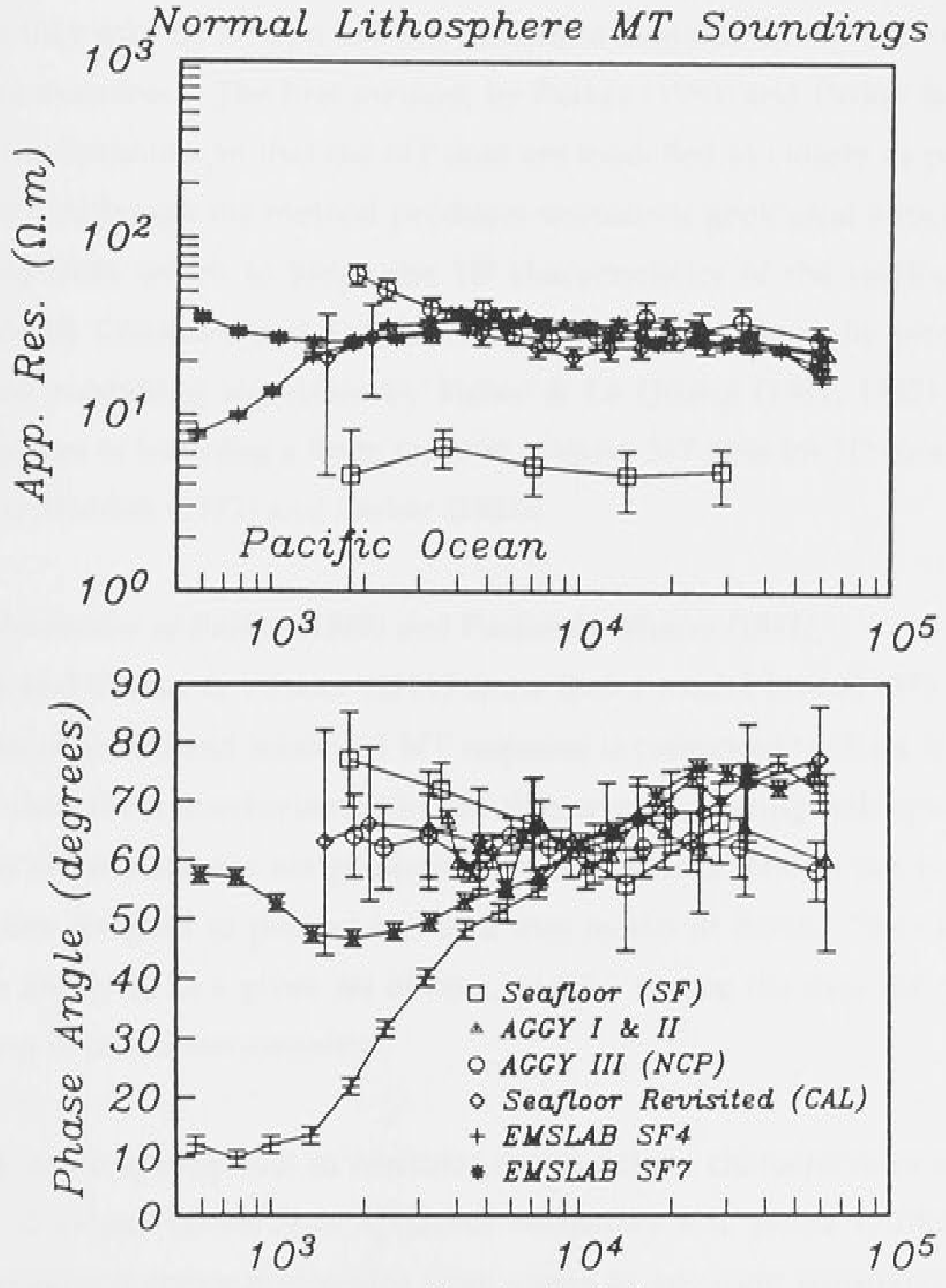

Figure 2.9 As for Figure 2.7, but seafloor MT soundings on 'normal' oceanic lithosphere in the Pacific Ocean.

2.7 One-Dimensional Interpretations

2.7.1 Introduction

Although 3D induction effects in the ocean basins are observed in the non-zero diagonal impedance tensor elements (e.g. Ferguson, 1988) it is not obvious how 3D induction may distort the 1D MT response of the underlying structure. If the 1D signature of the underlying upper mantle dominates the 3D induction effects in the ocean, then a 1D inversion of the data is valid. However, if the converse is true, a 1D inversion of seafloor MT data will not recover the underlying conductivity structure. Single-site MT data interpretations have favoured the former argument, as anisotropy of the off-diagonal impedance elements is generally small; and 1D inversions appear to be consistent with the observed MT data.

An advantage of collating seafloor MT data sets from previous experiments in a standard format is that they may be interpreted in a consistent manner. In this section, three inversion techniques are examined. The first method, by Parker (1980) and Parker & Whaler (1981), is in some regards optimum, in that the MT data are modelled as closely as possible (in a least-squares sense). Although the method produces unrealistic geological structure, it provides a statistical base from which to judge the 1D characteristics of the seafloor MT data. The second method by Constable *et al.* (1987) produces smooth conductivity profiles; and finally a simple layered modelling algorithm by Fisher & Le Quang (1981, 1982) is applied to the data. The problem of inverting a finite number of noisy MT data for 1D conductivity structure is reviewed by Weidelt (1972) and Parker (1983).

2.7.2 D-Plus Inversion of Parker (1980) and Parker & Whaler (1981)

Parker (1980) and Parker & Whaler (1981) show that a model (called D^+) which minimises misfit between observed and modelled MT response is composed of delta functions of infinite conductivity (but finite conductance) in an otherwise insulating half-space. It is perhaps fortunate that D^+ models are not geologically reasonable (although not impossible), and so no-one has been tempted to present one as a true model of Earth. The utility of D^+ lies in bounding the ability to fit a given set of data, and for testing the data for compatibility with the assumption of one-dimensionality.

It is probably more appropriate to consider the statistical characteristics of the MT data as Schmucker's **c** values rather than apparent resistivity and phase (Parker, 1983), but the problem of assigning errors to **c** values from errors in apparent resistivity and phase is not straightforward. Parker and Whaler's algorithm uses the errors on apparent resistivity magnitude and phase to generate equal errors on real and imaginary components of **c**, which would have been the error partitioning for the time series analysis of the original data.

However, in this section the apparent resistivity and phase are considered as independent variables; although for a perfectly 1D structure apparent resistivity and phase are not independent in practice, the presence of 3D induction effects causes them to effectively be so.

A measure of the misfit of model response to data is the chi-squared (χ^2) misfit of the weighted residuals (Parker & Whaler, 1981). The misfit between model response and data, on the assumption of independent and Gaussian errors, is $\chi^2 = N$ at the expected value, and $\chi^2 = N + 2\sqrt{2N}$ at the 95 % confidence level, for N independent estimates. The χ^2 statistic is therefore dependent upon the number of data used: to compare misfits from two or more sets of MT estimates, the root mean square (RMS) misfit is useful. The RMS misfit is the square root of the χ^2 misfit divided by the number of data; hence, for a χ^2 misfit at the expected value, the RMS misfit is unity. In modelling or inverting MT data, a generally accepted criterion for one-dimensionality is a misfit less than or equal to the expected value of unity, although some authors (Oldenburg *et al.*, 1984; Smith & Booker, 1988) prefer the 95 % confidence limit.

Parker and Whaler's D^+ inversions were applied to 20 of the sets of seafloor MT data listed in Table 2.3. Fourteen sets of MT estimates have RMS < 1, which suggest that these MT data are each compatible with a 1D conductivity structure. The remaining sets of MT data have misfits spaced almost equally between RMS = 1 and RMS = 4. This distribution is not unreasonable for model RMS misfits; objective statistical guide-lines for data analysis will be appropriate only on average, and even perfect 1D data with random zero-mean Gaussian errors will have RMS misfit > 1 occasionally. It is pertinent to note, however, that five of the MT data sets which fail to satisfy the χ^2 criterion for a 1D Earth are from the most recent experiments of the Tasman Project (Ferguson *et al.*, 1990) and EMSLAB (Wannamaker *et al.*, 1989a), in which time series processing techniques are most advanced, using robust analysis and/or remote-reference techniques to reduce biases and error magnitudes. Thus, small RMS misfits may result from large error estimates on the MT data, and not necessarily from any intrinsic 1D property of the data (which casts doubt on the use of the RMS misfit as the sole criterion of one-dimensionality).

However, the RMS criterion of one-dimensionality is based on the premise that the residuals between model response and data will have a Gaussian distribution, with zero mean. To examine the significance of the residuals computed for the data sets, it is useful to generate comparable statistics synthetically. Thus, 80 sets of synthetic MT data were generated for a model ocean structure, by taking the 1D forward-model response and adding random Gaussian errors. The 80 data sets comprised 20 different realisations of 2 %, 5 %, 10 % and 20 % errors, respectively, comparable to the errors of observed seafloor data. These synthetic data sets were inverted using D^+.

If the D$^+$ inversions from the 80 synthetic data sets are examined for RMS misfit, 61 have misfit less than the expected value (of unity), 18 have misfit between the expected value and the 95 % confidence limit, and 1 data set (with 5 % Gaussian error) has misfit greater than the 95 % confidence limit. Table 2.5 gives the mean misfit of each group of 20 in the 80 synthetic data sets; and also the standard deviation of the mean. Table 2.5 shows that the mean RMS misfits are less than the expected value (of unity), and appear independent of the level of Gaussian noise.

Table 2.5 Mean RMS misfits from D$^+$ inversion of 4 groups of 20 sets of synthetic 1D MT data.

Gaussian noise (%)	Mean RMS Misfit	Standard Deviation of Mean
2	0.746	0.151
5	0.863	0.236
10	0.916	0.158
20	0.816	0.203
Mean	0.835	0.187

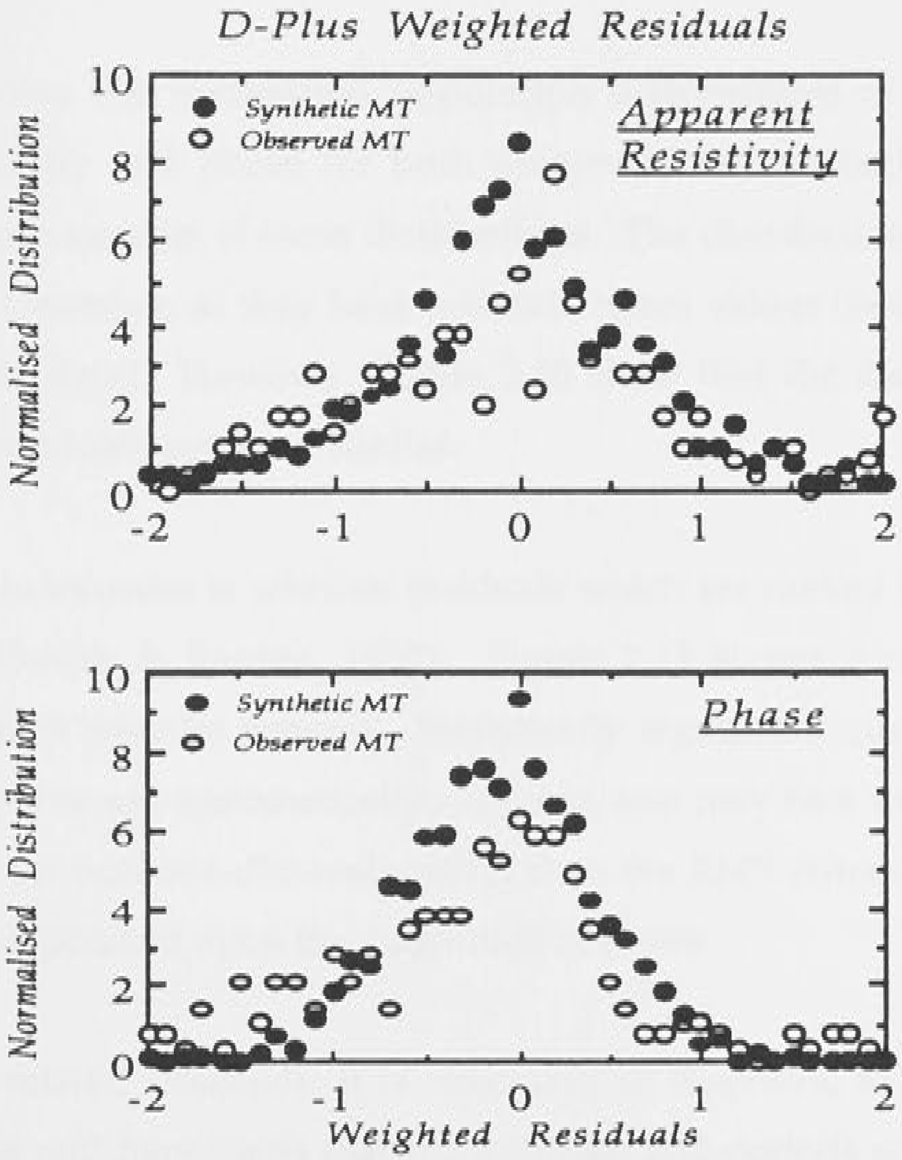

Figure 2.10 Normalised population distributions of weighted MT residuals (defined as D$^+$ response minus data, weighted by the error), for 20 sets of seafloor data and of 80 sets of synthetic data.

Table 2.6 Statistical moments of the distributions of the weighted residuals from D^+ inversion of observed and synthetic seafloor MT data.

(a) Observed Seafloor MT Data

Apparent Resistivity		Phase	
Number of data	288	Number of data	288
Mean	-0.193	Mean	-0.461
Standard deviation	1.108	Standard deviation	1.706
Skewness	-0.096	Skewness	-0.601

(b) Synthetic MT Data

Apparent Resistivity		Phase	
Number of data	880	Number of data	880
Mean	0.009	Mean	0.001
Standard deviation	0.699	Standard deviation	0.505
Skewness	0.173	Skewness	-0.172

Figure 2.10 shows the normalised population distributions of the weighted residuals of apparent resistivity and phase for both observed and synthetic data, and Table 2.6 lists simple statistical moments of these distributions. The distributions for the observed residuals are not strictly Gaussian, as they have non-zero mean values (note these values are near zero for the synthetic data). However, Figure 2.10 show that the distributions for the observed and synthetic residuals are very similar.

The next point to examine is whether residuals which are ranked by period may be correlated in some way (Smith & Booker, 1988). Figure 2.11 shows a schematic representation of correlations which may be present. Statistically significant correlations indicate that data and model response are systematically different, and may be a more robust indicator of one-dimensionality (or non one-dimensionality) than the RMS criterion; for such correlations are not necessarily dependent upon the magnitude of errors.

To test for correlated residuals, it is necessary to disprove, to a certain required level of significance, the null hypothesis that the residuals and periods are uncorrelated. A common technique is to measure non-parametric (or rank) correlation, given by Spearman's rank-order correlation coefficient (r_s) and Kendall's tau (τ).

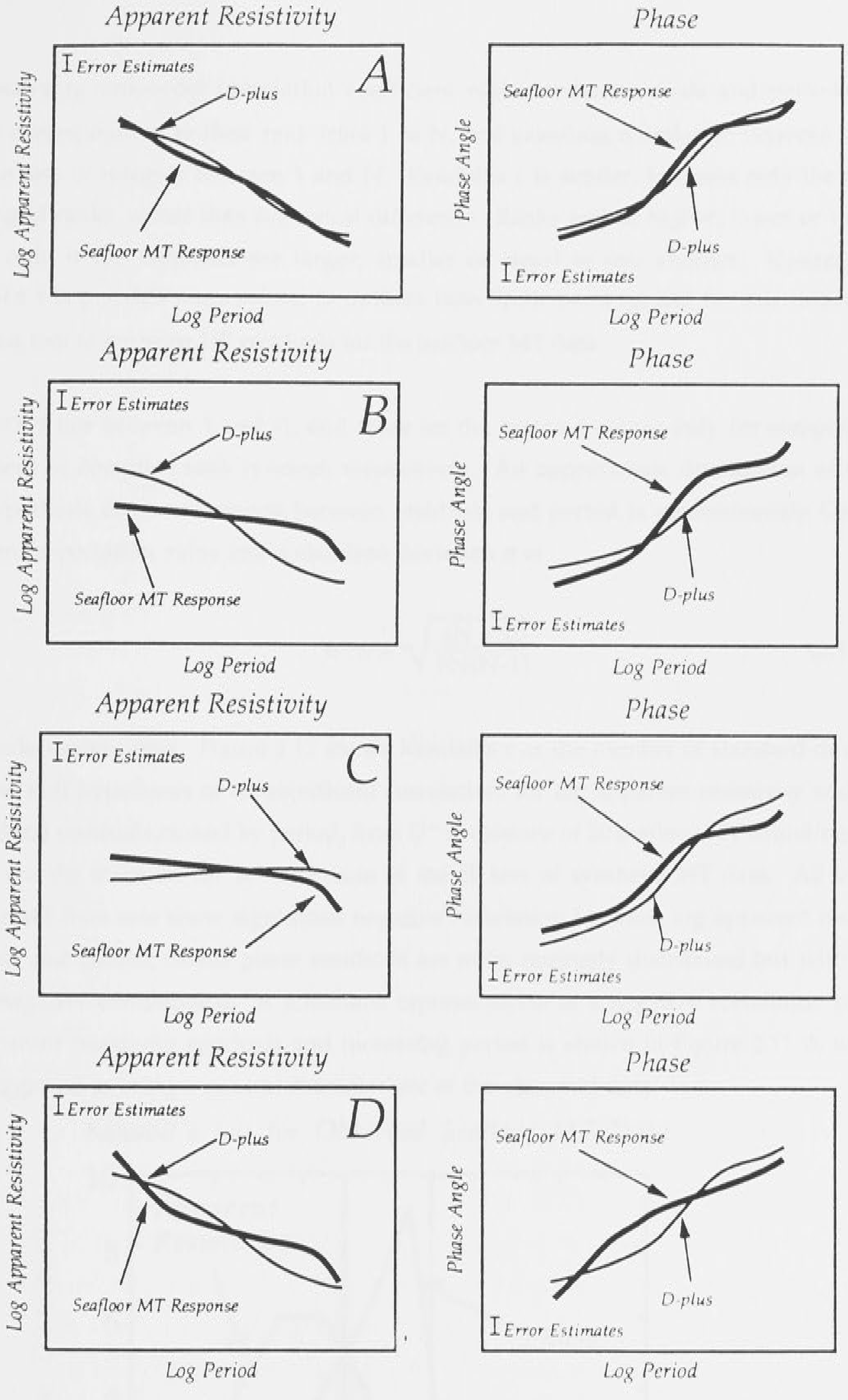

Figure 2.11 Schematic illustration of possible correlations between the D^+ response and data. (A) Residuals (defined as the D^+ response minus the data) are uncorrelated with period. (B) Residuals have negative correlation with increasing period. (C) Residuals have positive correlation with increasing period. (D) Residuals are serially (but not linearly) correlated with increasing period.

Spearman's r_S rank-order correlation coefficient replaces the residuals and periods by an integer corresponding to their rank from 1 to N, and examines correlation between the two uniform sets of integers between 1 and N. Kendall's τ is similar, but uses only the relative ordering of ranks, rather than numerical difference. Ranks will be higher, lower or the same if and only if the residuals are larger, smaller or equal to one another. Consequently, Kendall's τ is perhaps more robust to outliers than Spearman's r_S, and for this reason is the favoured tool to examine D^+ residuals for the seafloor MT data.

Kendall's τ lies between 1 and -1, and takes on the extreme values only for complete rank agreement or complete rank reversal, respectively. An approximate distribution of τ in the null hypothesis of no association between residuals and period is approximately Gaussian, with zero expectation value and a standard deviation σ of

$$\sigma(\tau) = \sqrt{\frac{4N + 10}{9N(N-1)}} \tag{2.1}$$

for N independent data. Figure 2.12 shows Kendall's τ as the number of standard deviations from the null hypothesis of no significant correlation, for log apparent resistivity and phase unweighted residuals ranked by period, from D^+ inversions of 20 seafloor MT soundings. Also shown are the statistics for D^+ inversion of the 80 sets of synthetic MT data. All but four seafloor MT data sets show significant negative correlation between log apparent resistivity residuals and period, (while phase residuals are more normally distributed but with a long tail of negative correlations). A schematic representation of a negative correlation between log apparent resistivity residuals and increasing period is shown in Figure 2.11 B; which is thus suggested as being a general characteristic of the observed data.

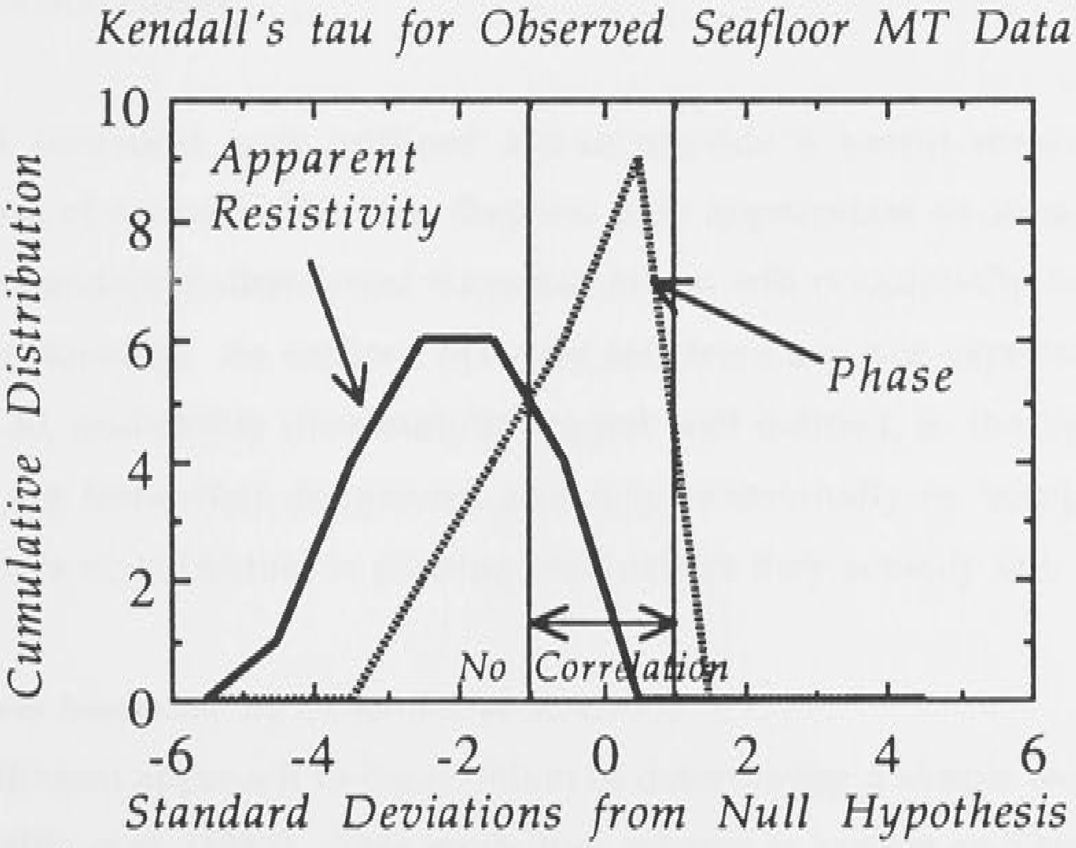

Figure 2.12 (a) Kendall's τ for D^+ inversions of 20 sets of seafloor data. (b) for D^+ inversions of 80 sets of synthetic data.

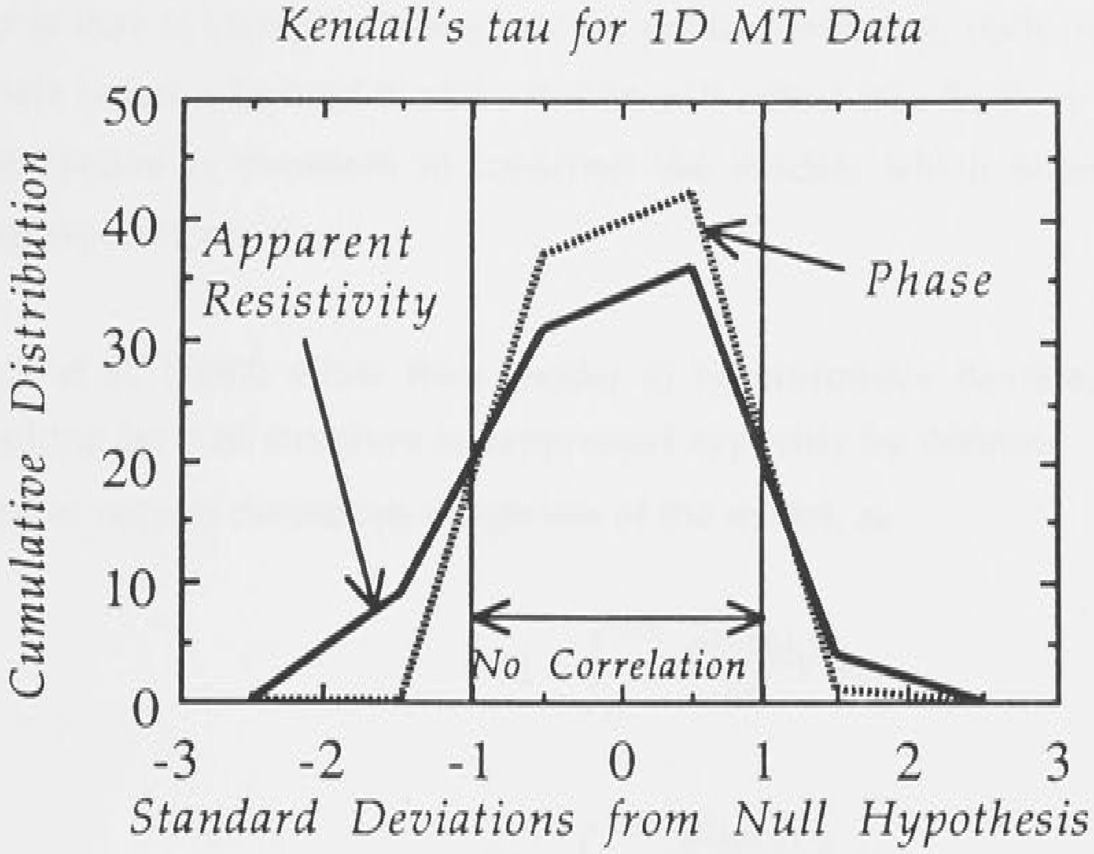

The difference between the observed-data apparent resistivity and phase curves in Figure 2.12 is important, and shows that D^+ is unable to fit both apparent resistivity and phase simultaneously. The significance of the negative correlation will be discussed later in terms of general 3D induction effects in a closed or partially closed ocean basin.

The linear and rank correlation techniques described are appropriate for correlations over the entire MT data set, but are not suitable if residuals have serial, but non-linear, correlation, as shown in Figure 2.11 D. Several tests of the serial correlation exist between successive data but have not been applied to seafloor MT data. Strong serial correlation may indicate that 3D induction effects are present, but may also result from correlated errors due to side-band leakage of noise at some period into a neighbouring bandwidth; it may be difficult to isolate the two possibilities. A rank-order correlation can be considered more unambiguously in terms of 3D induction effects.

Although statistical tests outlined above provide a useful means of characterising the distribution of errors in 1D data, they are only appropriate *on average*, and even perfect 1D data with randomly distributed Gaussian errors will occasionally fail the statistical tests of one-dimensionality. As seafloor MT data sets from any one experiment are small, typically less than 30, probability distributions are not well defined, so the interpretation of the error statistics are somewhat dangerous, and may occasionally be inappropriate. With so few data, there is no substitute to plotting residuals as they actually are.

2.7.3 *Occam Inversion by Constable et al. (1987)*

A very different approach to the problem of determining a simple model has been developed by Constable *et al.* (1987). This modelling scheme is known as 'Occam inversion', after the William of Occam ideal of simplicity, expressed as Occam's razor. The line of thought followed is that as layered models rely on parameterisation, such parameterisation must be appropriate before a layered-model solution will reflect true Earth structure. The objective of Occam inversion is therefore to construct the models which reflect the limitation of the observing experiment.

Constable *et al.* (1987) allow their model to be arbitrarily flexible, but the complexity of their resulting layered structure is suppressed explicitly by defining terms R_1 or R_2, known as the first or second derivative roughness of the model, as

$$R_1 = \int_0^{+\infty} \left(\frac{\partial m(z)}{\partial z}\right)^2 dz \tag{2.3}$$

$$R_2 = \int_0^{+\infty} \left(\frac{\partial^2 m(z)}{\partial z^2}\right)^2 dz \tag{2.4}$$

where m(z) is the electrical resistivity or its logarithm, and z is the depth. These roughness parameters are defined as the depth-integrated first or second derivative of the gradient modelled resistivity with depth. With a model composed of a discrete number of layers, the integrals in eqs 2.3 and 2.4 are replaced by summation over the number of layers, and the first and second derivatives are in turn replaced by finite difference formulas. The strategy is to find the solution agreeing with the measurements, to some desired degree of accuracy, which has a minimum roughness, either in R_1 or R_2; this is a procedure of regularisation which is common in solution of ill-posed problems.

The desired RMS misfit is defined in terms of least-squares misfit between model response and data. The minimum desired RMS misfit possible is obtained with a D^+ inversion: for a finite number of discrete layers, the model approaches a D^+ structure, but does not quite achieve the minimum misfit. At the other extreme, if the desired misfit is set arbitrarily large, the roughness parameters R_1 and R_2 tend to zero. The resulting conductivity structure for first derivative roughness R_1 is a uniform half-space (as the gradient of conductivity with depth must be zero), and for second derivative roughness R_2 the conductivity structure can be uniformly increasing, decreasing or constant with depth (as the gradient of conductivity with depth must be a constant). The Occam model falls arbitrarily between the two extremes of D^+ and zero roughness.

Figure 2.13 shows Occam inversion models for an observed set of seafloor MT data, for varying levels of desired misfit. Relaxing the desired level of misfit from the D^+ minimum of RMS = 1 by 40 % to RMS = 1.4 removes nearly all structural features from the conductivity profile, except a slight rise in conductivity with depth at 60 km. As the desired misfit is reduced, the size and position of the conductivity peaks also changes. It is usual practice to define a desired level of misfit in terms of the observational error; however, this is not necessarily the optimum method, as it depends on the assumption that the data are 1D, and that error estimates are appropriate for the actual noise levels in MT data.

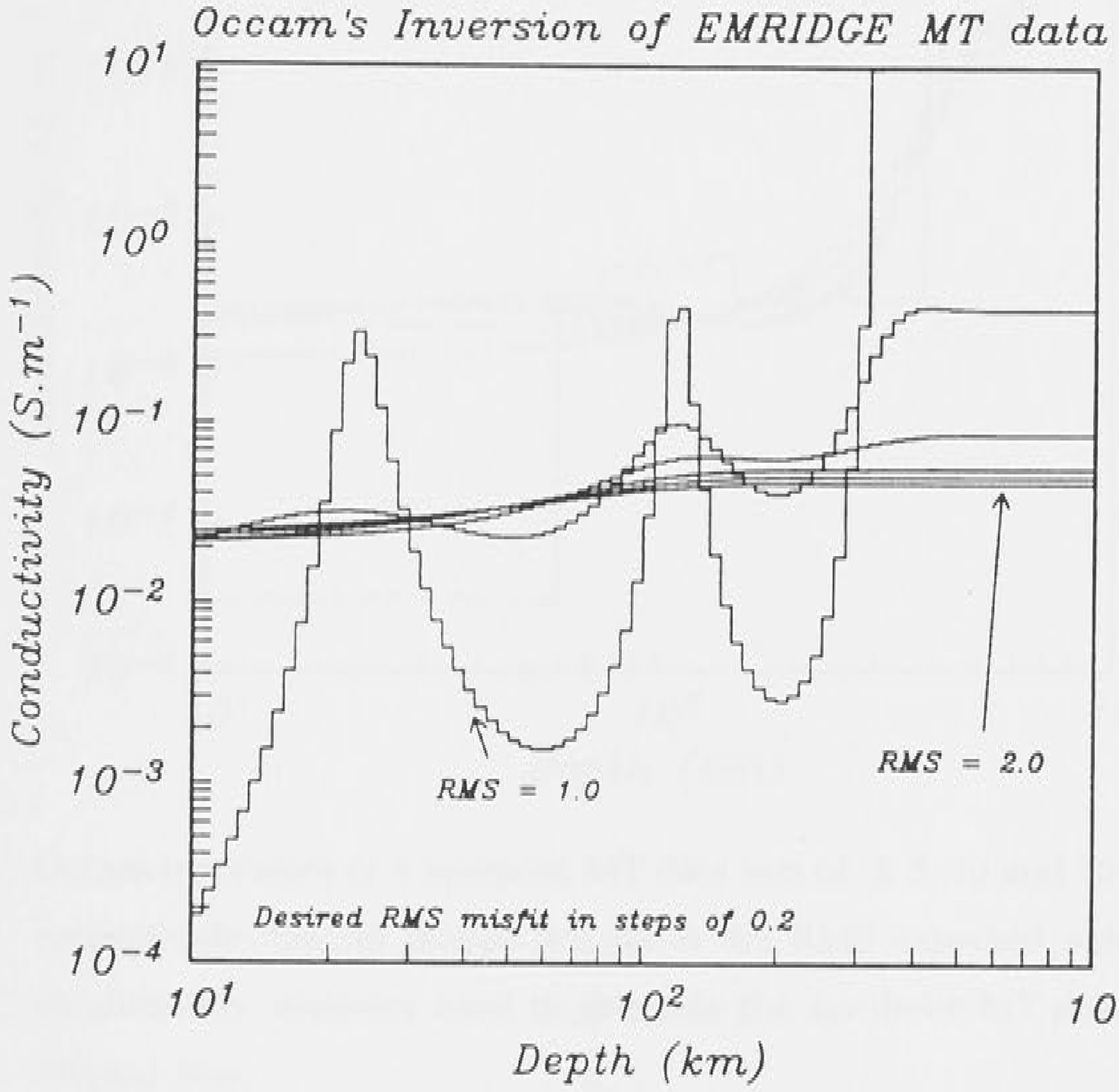

Figure 2.13 Occam inversions of a set of seafloor MT data at various levels of desired RMS misfit. Minimum RMS misfit obtained is 1 (the expected value), and desired misfit is relaxed in steps of 0.2 until structure almost disappears at RMS = 2.

For an Occam inversion of the synthetic MT data, an appropriate level of RMS misfit would be that of unity (as expected, on average, for inversions generally). Figure 2.14 shows Occam inversions (with an RMS misfit of unity) for 4 of the 80 synthetic MT data sets; of 2, 5, 10 and 20 % Gaussian noise respectively. (The 4 sets were chosen for their D^+ misfits of approximately 0.8, the mean from Table 2.5). The smooth models in Figure 2.14 resolve the major changes in conductivity structure with depth, although resolution of the asthenosphere and deep structure is poor.

A difficulty arises in deciding the appropriate level of Occam misfit for data of D^+ misfit significantly different from the expected value (Constable *pers. comm.*, 1990). For example, Ferguson *et al.* (1990) discuss inverting seafloor MT data with a D^+ RMS misfit of 3.04. As D^+ is independent of error magnitude, it may be better to define the desired Occam misfits in terms of the D^+ RMS misfit.

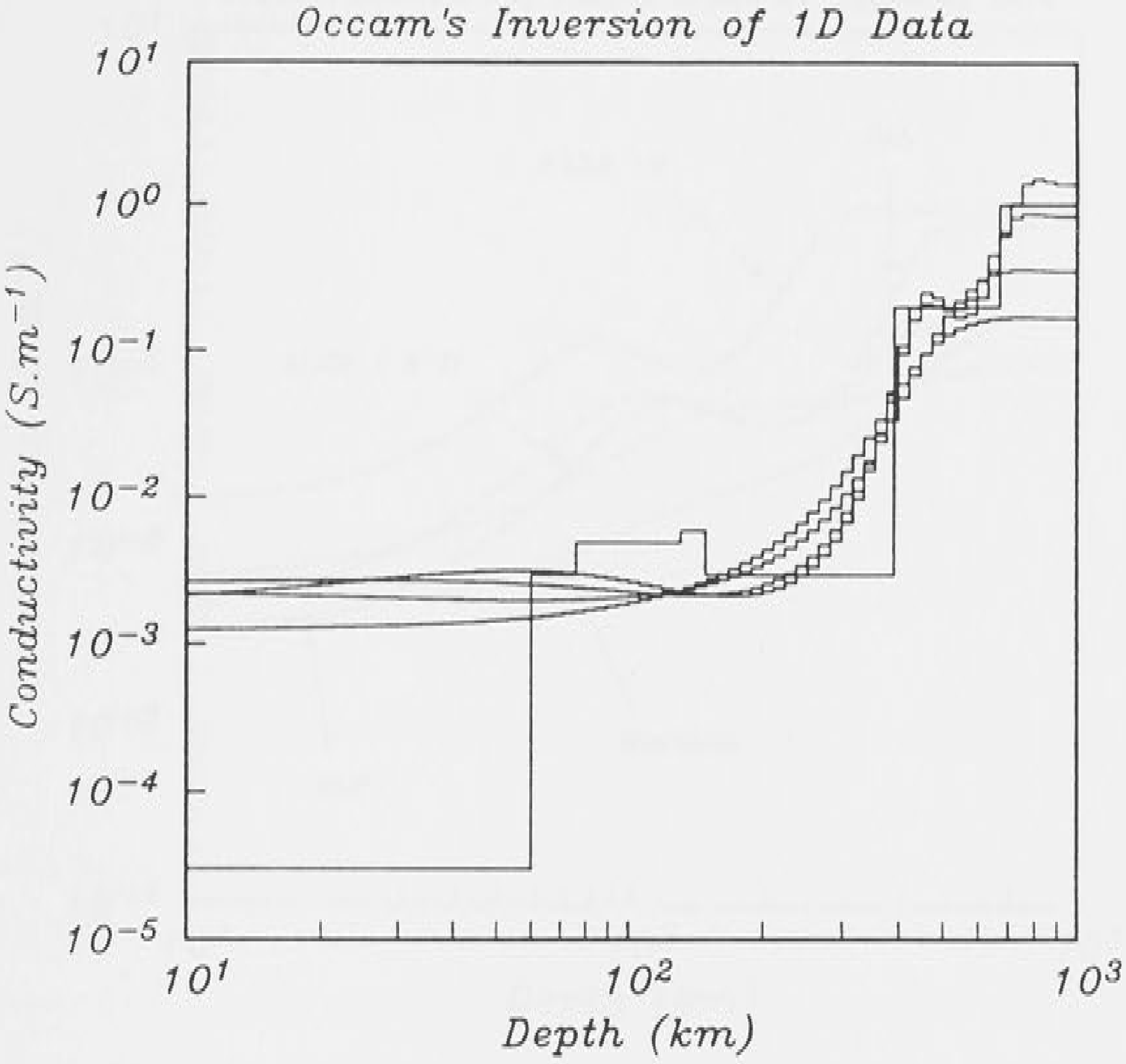

Figure 2.14 Occam inversions of 4 synthetic MT data sets of 2, 5, 10 and 20 % Gaussian noise respectively: Occam misfits are set at the RMS expected value of unity. The conductivity structure used to generate the synthetic MT data is shown by the stepped line.

D^+ inversion 'overfits' synthetic MT data (on average) to RMS = 0.8, so an RMS misfit for Occam inversion can be set a factor of $(0.8)^{-1}$ = 1.25 greater than the D^+ RMS misfit. Then the RMS misfit for an Occam inversion will be, on average, at the expected value of RMS = 1, (but may be larger or smaller, depending on the D^+ misfit). By defining an 'Occam desired RMS misfit' in terms of the D^+ RMS misfit, the distribution of D^+ residuals, rather than the error estimates themselves, are used to define the optimum fitting level.

Figure 2.15 shows first derivative Occam inversions for the Pacific Ocean, from the data sets of Filloux (1982a). The sites of the seafloor MT soundings range from the 1 Ma lithosphere near the East Pacific Rise to the subducting Pacific Plate at the Mariana Trough, and were selected as being least distorted by 3D induction effects and sediments. There is a significant decrease in the uppermost 200 km conductance, with increasing distance from the ridge axis. Such a decrease is consistent with the cooling lithospheric slab model of Parsons & Sclater (1977). Figures 2.16 and 2.17 show plots of the conductance over depths 10 to 100 km (lithosphere) and 70 to 200 km (asthenosphere) with square root of age for twelve seafloor MT soundings. The trend with age is very clearly defined, particularly for the lithosphere.

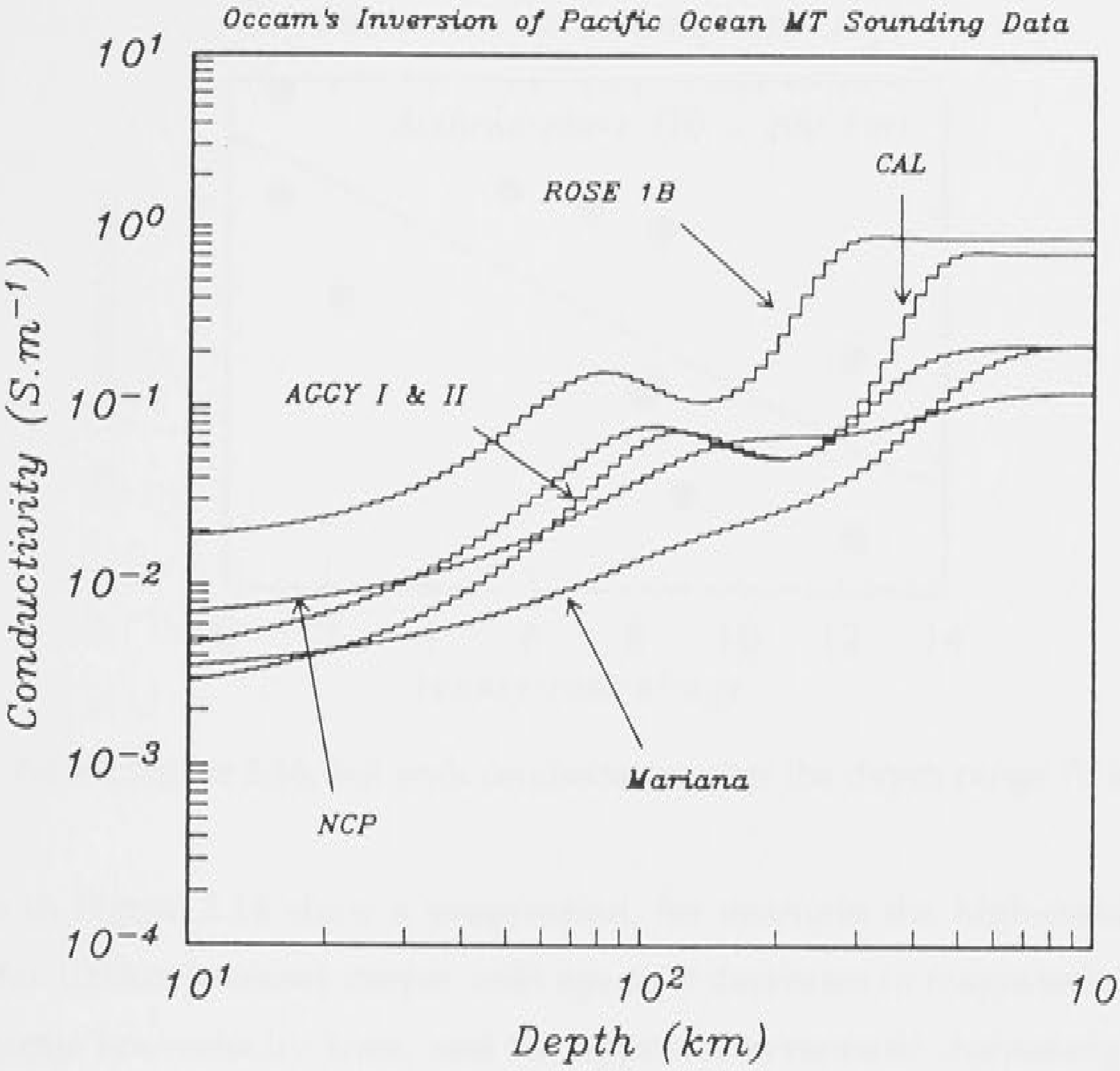

Figure 2.15 Comparison of first derivative Occam inversions for five sets of Pacific Ocean seafloor MT data. Ages range from 1 Ma for the East Pacific Rise (ROSE 1B), 30 Ma for CAL, 50 Ma for AGGY I & II, 72 Ma for NCP and > 100 Ma for the Mariana Fore-arc basin. There appears to be a strong age dependence in lithosphere conductance, depth and magnitude of high-conductivity layer at ~100 km, and depth to the deep conductive structure at ~300 km.

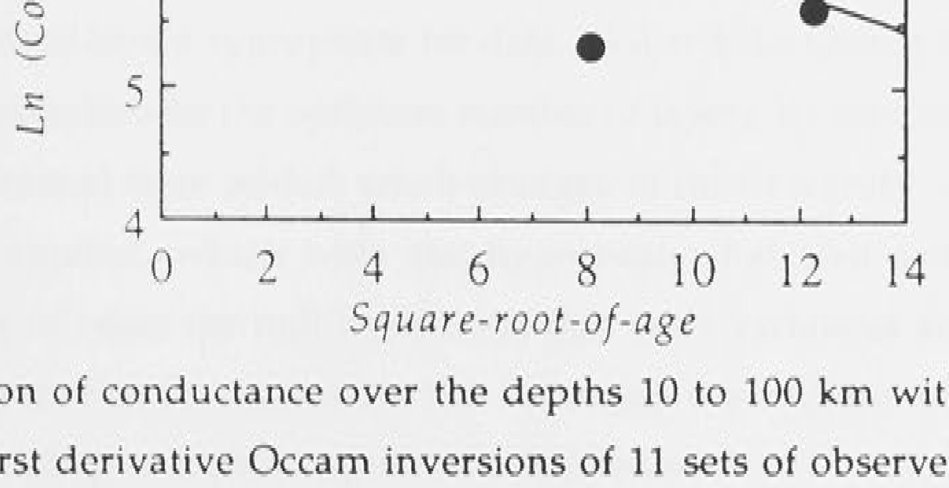

Figure 2.16 Variation of conductance over the depths 10 to 100 km with age of lithosphere, from first derivative Occam inversions of 11 sets of observed seafloor data. The best fit linear relationship between log conductance and square root of age is aslo shown.

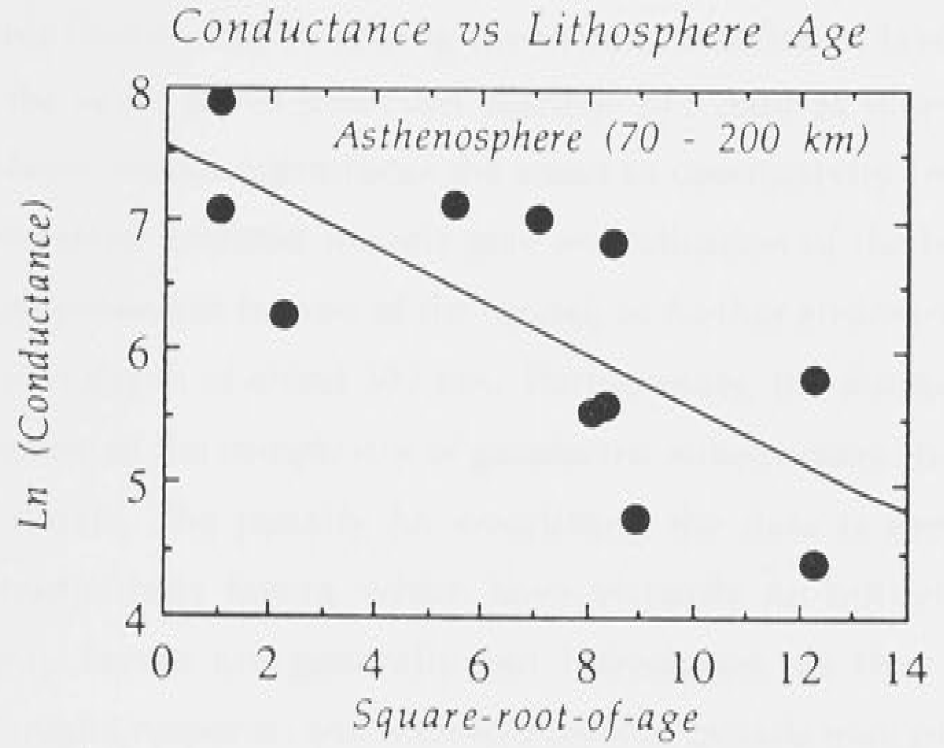

Figure 2.17 As for Figure 2.16, but with conductance over the depth range 70 to 200 km.

The profiles in Figure 2.16 show a progression: for example the high-conductivity layer at depth of order 100 km becomes deeper with age, and decreases in magnitude. The coincidence with the seismic low-velocity zone, and the apparent systematic deepening with age, imply that such a feature is real. The deep rise in conductivity at depths greater than 200 km also shows an indication of age dependence.

2.7.4 Layered Models by Fischer & Le Quang (1981, 1982)

A layered model is most useful where Earth approaches a layered configuration, such as a sedimentary basin, but can also be applied to characterise the principal conductivity changes of a structure which is smoothly varying. Whereas smooth modelling approaches the non-uniqueness problem by over-parameterising the conductivity structure, but explicitly restricting the complexity, layered models seek the most simple under-parameterised model which is consistent with the data. The principal problem encountered in smooth models (of designating a satisfactory misfit) is avoided; Fisher & Le Quang (1981, 1982) use a ridge-regression method to obtain a layered structure which minimises in a least-squares sense the misfit between model response and data. A more straightforward problem remains, of choosing the number of layers appropriate for data. Fisher & Le Quang (1981, 1982) propose a systematic search procedure for the optimum number of layers, by considering improvement in misfit for each additional layer added: small changes in misfit signify unnecessary structure. An F-test can be applied, which tests the hypothesis that two samples have different variances by trying to reject the null hypothesis that their variances are actually consistent. The optimum number of layers required is that for which the addition of further layers would result in the F-test failing to a show significant difference.

Figure 2.18 shows Fischer and Le Quang inversions, in terms of layered models of increasing complexity, of the same set of observed seafloor MT data as inverted in Figure 2.13. The optimum three-layer model reproduces the trend in conductivity increase with depth shown from Occam inversion. Layered models give an indication of the best resolved conductivity features: the most persistent feature of the model, as further structure is introduced, is the rise in conductivity at a depth of about 300 km. Furthermore, the number of layers supported by the data is a measure of the complexity of geoelectric substructure (but is also dependent upon the number of data). The penalty for overfitting the data is seen as the introduction of spurious low conductivity layers, which have virtually no influence on the MT response. High-conductivity layers are generally not introduced, as they have a more profound influence on the model response; and therefore layered models may provide an upper-bound on the conductivity structure beneath the observation site.

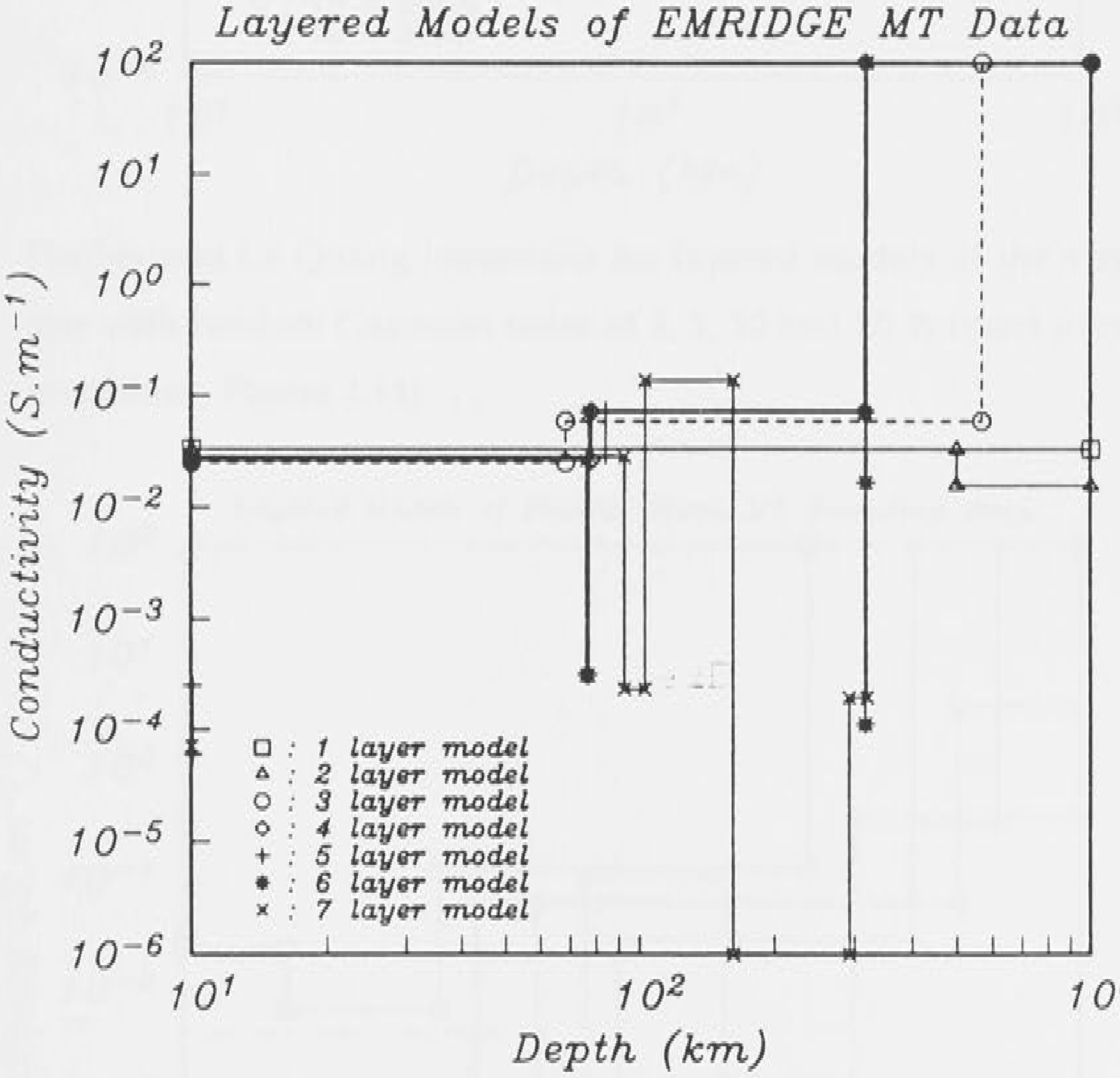

Figure 2.18 Fischer and Le Quang inversions, in terms of layered models of increasing complexity, for the same set of observed seafloor MT data as inverted in Figure 2.13: the optimum number of layers is 3, indicated by the dashed line.

Figure 2.19 shows similar Fischer and Le Quang inversions of 4 sets of the synthetic MT data, for comparison with Figure 2.14. Also, layered inversions of the Pacific Ocean data are shown in Figure 2.20, for comparison with Figure 2.15. In the latter, the decrease in conductance with age and the increasing conductivity with depth are consistent with the Occam inversions.

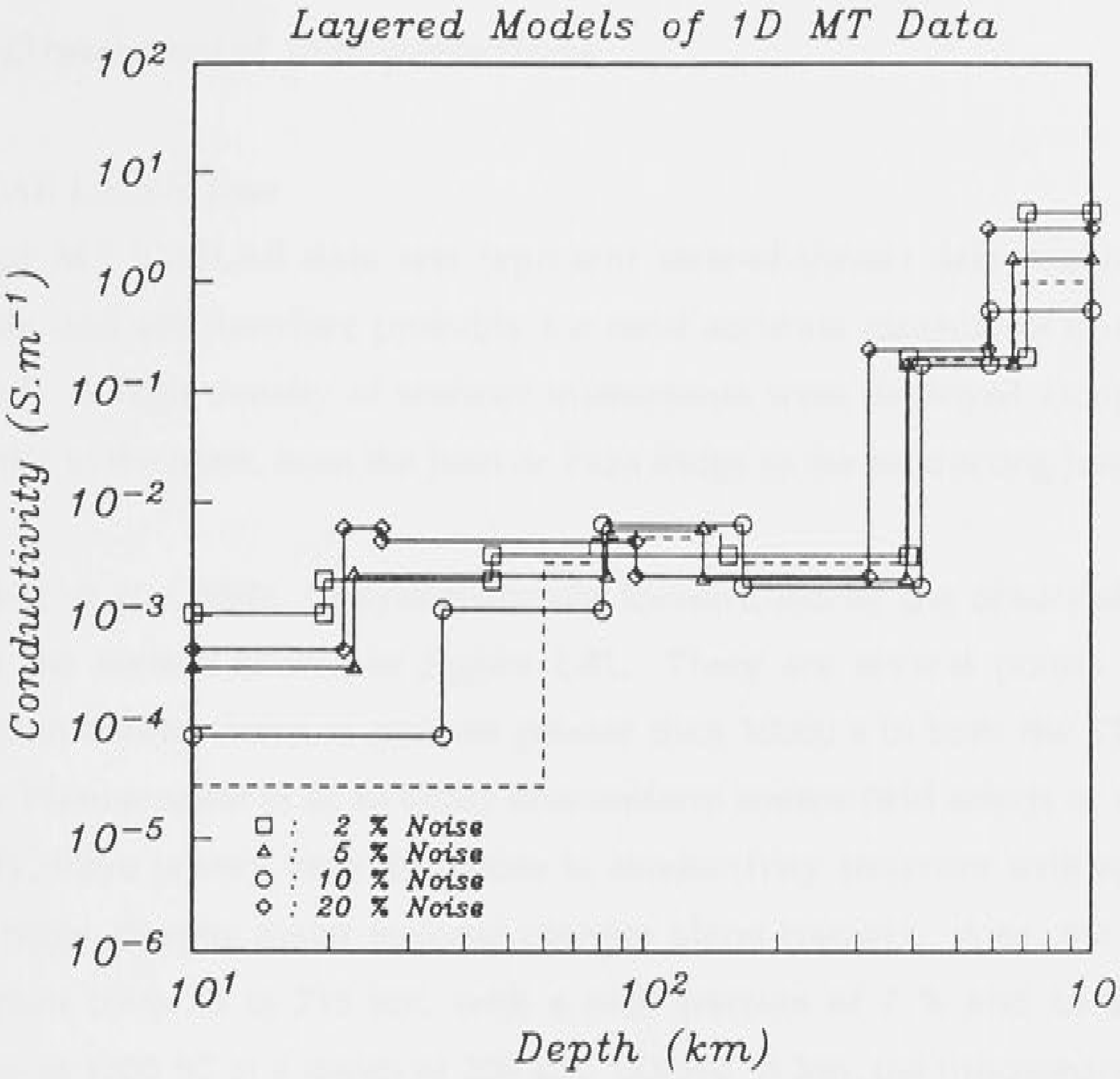

Figure 2.19 Fischer and Le Quang inversions for layered models of the 4 synthetic MT data sets with random Gaussian noise of 2, 5, 10 and 20 % (used previously in Occam inversions, Figure 2.14).

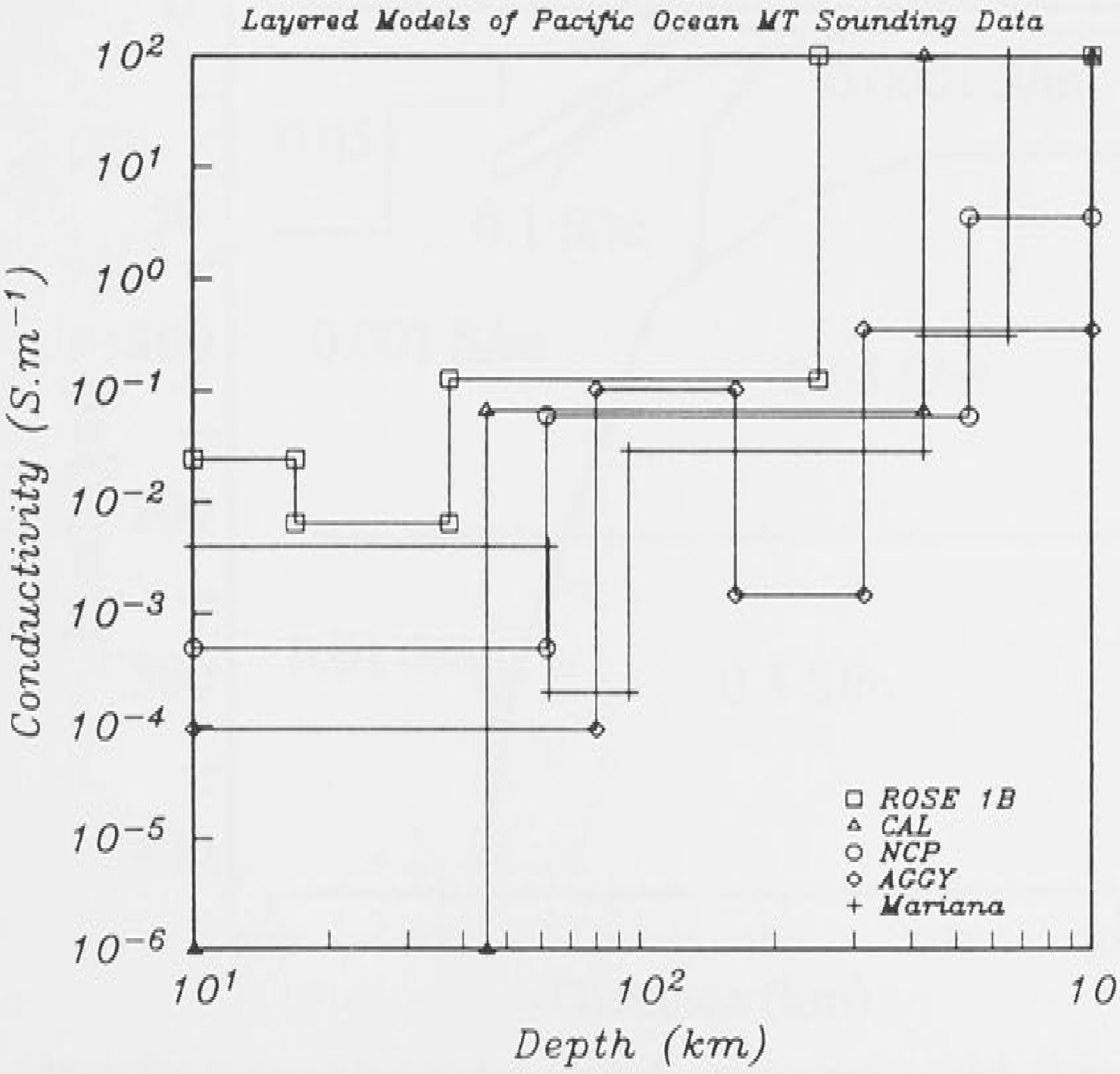

Figure 2.20 Fischer and Le Quang inversions for layered models observed seafloor data from the Pacific Ocean, (used previously in Occam inversions, Figure 2.15).

2.8 Two-Dimensional Interpretations

2.8.1 EMSLAB Lincoln Line

The seafloor MT EMSLAB data sets represent state-of-the-art data acquisition, processing and analysis, and are therefore probably the most accurate measure of oceanic conductivity yet acquired. A high density of seafloor instruments were deployed along the Lincoln line perpendicular to the coast, from the Juan de Fuca Ridge to the subducting Juan de Fuca Plate.

Wannamaker *et al.* (1989a, b) systematically forward-model the observed EM data in 2D, arriving at the section shown in Figure 2.21. There are several points to note. The 2D approximation breaks down at periods greater than 10000 s in both the TE and TM modes, ascribed by Wannamaker et al. to either non-uniform source-field effects or oceanic induction. Surprisingly, there is very little difference in conductivity structure with age away from the spreading ridge, despite major tectonic changes along transect. Also, the model requires a region of melt from 35 to 215 km, with a melt fraction of 7 % and an anomalously high temperature of 1700 °C at a depth of 200 km. Above 35 km, the lithosphere is very resistive, with an implied compensation distance of approximately 1300 km. Below 215 km, the upper mantle has a conductivity of 1 S.m^{-1}.

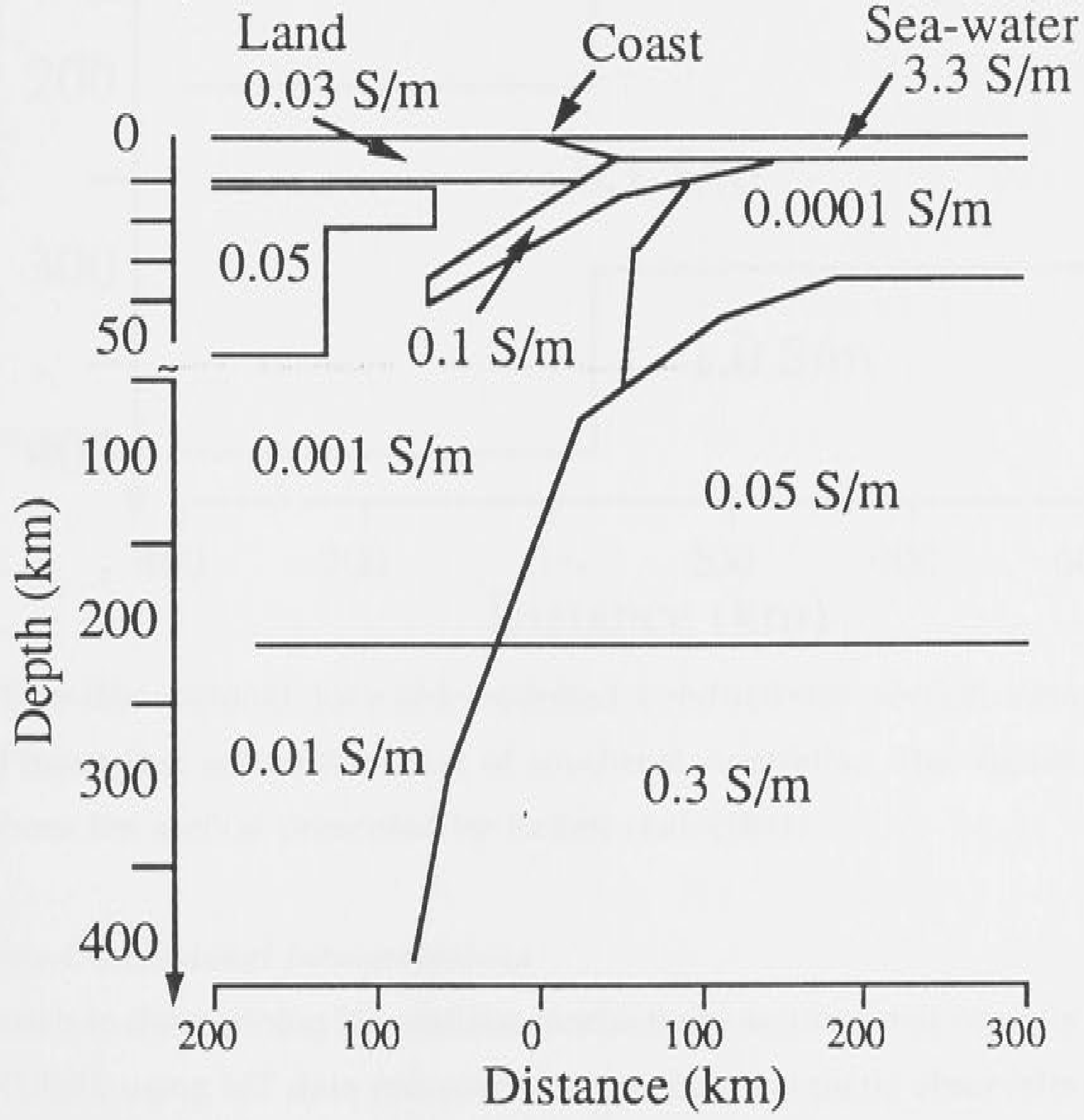

Figure 2.21 Two-dimensional forward-modelled conductivity section along the Lincoln Line across the northwest coast of America. Adapted from the resistivity section presented by Wannamaker *et al.* (1989b).

2.8.2 *Tasman Project Transect*

In contrast to the EMSLAB transect across young, and tectonically active oceanic crust, the Tasman Project took place on old, stable oceanic lithosphere. Two-dimensional modelling by Kellett *et al.* (1991) from Tasman Project data and Continental Slope Experiment data reveal a conductivity contrast between continental and oceanic lithosphere at the coastline of southeast Australia. Figure 2.22 shows the 2D profile of Kellett *et al.* (1991). The conductivity structure determined by Kellett *et al.* (1991) is more conductive than Wannamaker *et al.*'s (1989b) 2D profile.

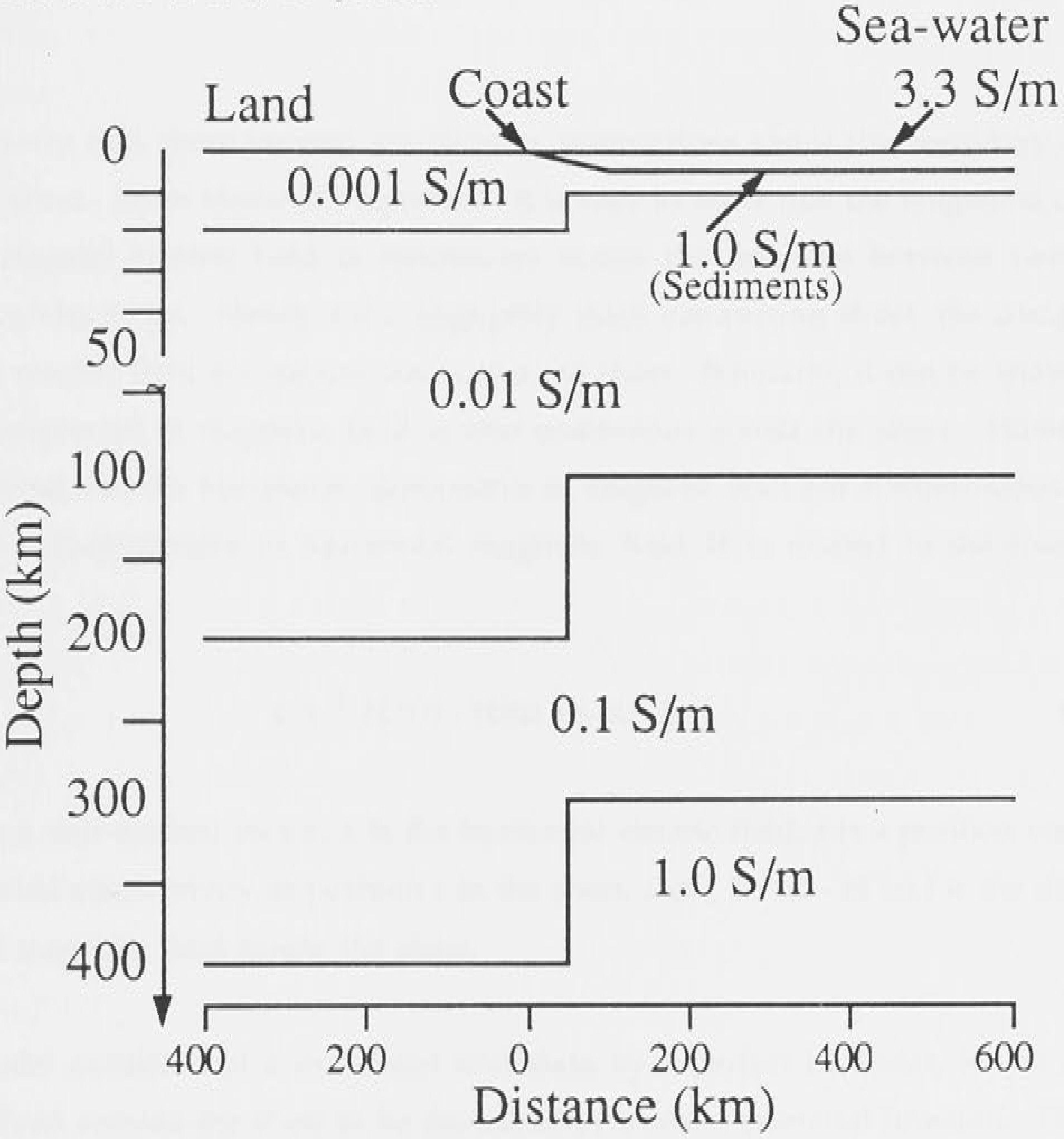

Figure 2.22 Two-dimensional forward-modelled conductivity section along the Tasman Project line across the coast of southeast Australia. This figure is reproduced from the section presented by Kellett *et al.* (1991).

2.8.3 *Other Two-Dimensional Interpretations*

A novel approach to determining 2D seafloor conductivity sections was recently undertaken by Mackie *et al.* (1988), using MT data recorded at a coastline magnetic observatory. They found that a resistive oceanic lithosphere of resistance-thickness product greater than 10^9 $\Omega.m^2$ was required to reproduce observed anisotropy in recorded data. A similar result was obtained from inversions of MT data from the Tuscon observatory in New Mexico, many hundreds of kilometres from the coastline of southern California (Egbert *pers. comm.*, 1990).

Chapter 3 : The Thin-Sheet Electromagnetic Approximation

3.1 Thin-Sheet Modelling Theory

3.1.1 Introduction

Price (1949) developed the idea of a geoelectric thin-sheet approximation to model such effects in the low-frequency limit when the depth of penetration of the waves is much greater than the thickness of the sheet, so that the sheet can be considered to have negligible thickness.

An electrically thin sheet permits simplifying assumptions about the boundary conditions across the sheet. From Maxwell's equations, it is easy to show that the tangential component of the horizontal electric field is continuous across the interface between two layers of different conductivity. Hence, for a negligibly thick conducting sheet, the components of horizontal electric field are continuous across the sheet. Similarly, it can be shown that the vertical component of magnetic field is also continuous across the sheet. However, Price (1949) showed that the horizontal components of magnetic field are discontinuous across the sheet. The discontinuity in horizontal magnetic field **H** is related to the sheet current-density as

$$\mathbf{z} \times \left[\mathbf{H}^{+}(\mathbf{r}) - \mathbf{H}^{-}(\mathbf{r}) \right] = \tau(\mathbf{r})\, \mathbf{E}(\mathbf{r}) \qquad (3.1)$$

where **z** is a unit vertical vector, **E** is the horizontal electric field, **r** is a position vector, $\tau(\mathbf{r})$ is the integrated conductivity at position **r** in the sheet, and $[\, \mathbf{H}^{+}(\mathbf{r}) - \mathbf{H}^{-}(\mathbf{r})\,]$ is the difference in horizontal magnetic field across the sheet.

Price's model consisted of a thin-sheet underlain by a perfect insulator, which allows the magnetic field outside the sheet to be described by a scalar potential function. The effect of Earth's conductivity was later introduced in the form of a perfect conductor at some depth below the thin-sheet. A review of such models and practical computational techniques is given by Bullard & Parker (1970). One serious limitation of such models is that they do not allow for current flow into or out of the thin-sheet, which is physically unrealistic. Earth's lithosphere is generally a poor conductor, but not poor enough to prevent resistive coupling between the surface and the more conductive parts of the mantle.

A better representation of Earth's conductivity structure is to allow general layered media below the sheet, which can be related to the thin-sheet by impedance boundary conditions: several authors have developed this approach. Vasseur & Weidelt (1977), following from the work of Weidelt (1975), have formulated the 3D problem in the thin-sheet in terms of a surface-integral equation for the electric field. Such a solution requires that the anomalous field vanishes at infinity, hence the region of anomalous conductance must be surrounded by uniform structure. Thus, it is computationally efficient, since the integral equation need only be solved in the anomalous region. However, it cannot examine strictly 2D problems, such as a single coastline.

Ranganayaki & Madden (1980) developed a generalised thin-sheet method which is essentially equivalent to a conductive layer overlying a resistive layer. Although their approach was different from that taken by Vasseur & Weidelt, by considering the total rather than the anomalous field, Ranganayaki & Madden's method appears to be restricted in practice to models in which the anomalous region is of finite extent. Such an approach has been extended by Park *et al.* (1983), Park (1985) and Park & Livelybrooks (1989), to model 3D structures by stacking many non-uniform layers.

A group led by J. T. Weaver, at the University of Victoria, Canada developed in a series of papers, 2D and 3D thin-sheet models underlain by a half-space of uniform conductivity (Green & Weaver, 1978; Dawson & Weaver, 1979), and a layered half-space (McKirdy & Weaver, 1984; McKirdy *et al.*, 1985). The methods do not require the fields to be separated into normal and anomalous parts, nor is it necessary to assume that an anomalous region is surrounded by a uniform structure. Thus, models may approach either a TE or TM configuration at infinity. This technique can be used to examine strictly 2D problems, and consequently may be compared with more accurate 2D modelling algorithms.

The thin-sheet algorithms described above are formulated for an external magnetic field which is uniform and horizontal. Thus, they are well suited to model MT and GDS problems which use natural sources of EM induction, for which the ionospheric source is approximately uniform. However, thin-sheet techniques can also be applied to exploration problems with a controlled source-field of known dimensionality. Conductive overburdens commonly have lateral variations in either conductance or thickness, such as a weathered layer or salt lake. Smith & West (1987) extend Price's (1949) analysis to arbitrary 3D sources, for a thin-sheet which is electrically isolated.

Electromagnetic experiments are often carried out in environments where a highly conductive layer, varying in lateral conductance, masks the EM response of the underlying structure. In the oceans, seafloor MT soundings using natural source-fields are profoundly influenced by EM induction in the highly conducting salt-water. Lateral changes in the depth-integrated conductivity of the oceans, due to both changes in seafloor topography and the coastlines, distort the EM signature of the underlying crust and upper mantle. Geomagnetic array studies close to the coastline suggest that the influence of EM induction effects in the ocean may stretch several hundred kilometres inland. A recent paper by Chamalaun & Barton (1990) has shown from a Australia-wide array of magnetometers (AWAGS) that sedimentary basins with high porosity also influence the pattern of EM induction within the Australian lithosphere. Woods & Lilley (1980) show that anomalous geomagnetic variations in southwest Queensland, Australia, can largely be accounted for by EM induction in the conductive sediments.

The thin-sheet approximation is well suited to modelling the effects of anomalous surface conductors: various authors have applied this technique to a wide range of geophysical problems. These have included the analysis of geomagnetic fields in relation to a continent-ocean boundary (Green & Weaver, 1978; Dawson & Weaver, 1979; Ranganyaki & Madden, 1980; McKirdy *et al.*, 1985) and comparisons with observations to discriminate the presence of anomalous conductors from the geomagnetic coast effect (e.g. Weaver, 1982; Mareschal *et al.*, 1987; Agarwal & Weaver, 1990). Thin-sheet techniques have been applied to theoretical studies of current channelling phenomena (Vasseur & Weidelt, 1977; McKirdy & Weaver, 1983). Heinson & Lilley (1989, 1991) have compared the thin-sheet calculations to seafloor MT observations in the Tasman Sea, to assess the influence of electric charge accumulation at the coastlines, and Heinson *et al.* (1991) have calculated the effect of seafloor topography on MT and GDS observations. Park *et al.* (1983), Park (1985) and Park & Livelybrooks (1989) have calculated the effects of 3D structure on MT sounding curves, and investigated the use of rotationally invariant MT parameters. Smith & West (1987) modelled controlled source-field data, to assess whether variations in conductance of the overburden could account for the anomalous response seen in field measurements.

3.1.2 Thin-Sheet Algorithm of McKirdy et al. (1985)

The modelling algorithm used in this thesis was developed at the University of Victoria, Canada, by a group led by J. T. Weaver. Instead of using a Dirichlet boundary condition of vanishing anomalous field at infinity, the total field is required to have a Neumann boundary condition of vanishing outward gradient at infinity. Under this boundary condition the model may approach a 2D configuration at infinity. Surface-integral formulae above and below the sheet are derived so that the magnetic field is expressed as the convolution of an admittance tensor with the electric field within the sheet. Analytical solutions for magnetic fields above and below the non-uniform sheet are known, leaving only the sheet itself as the region where numerical methods must be applied. A brief outline is now given of the theory presented by McKirdy *et al.* (1985).

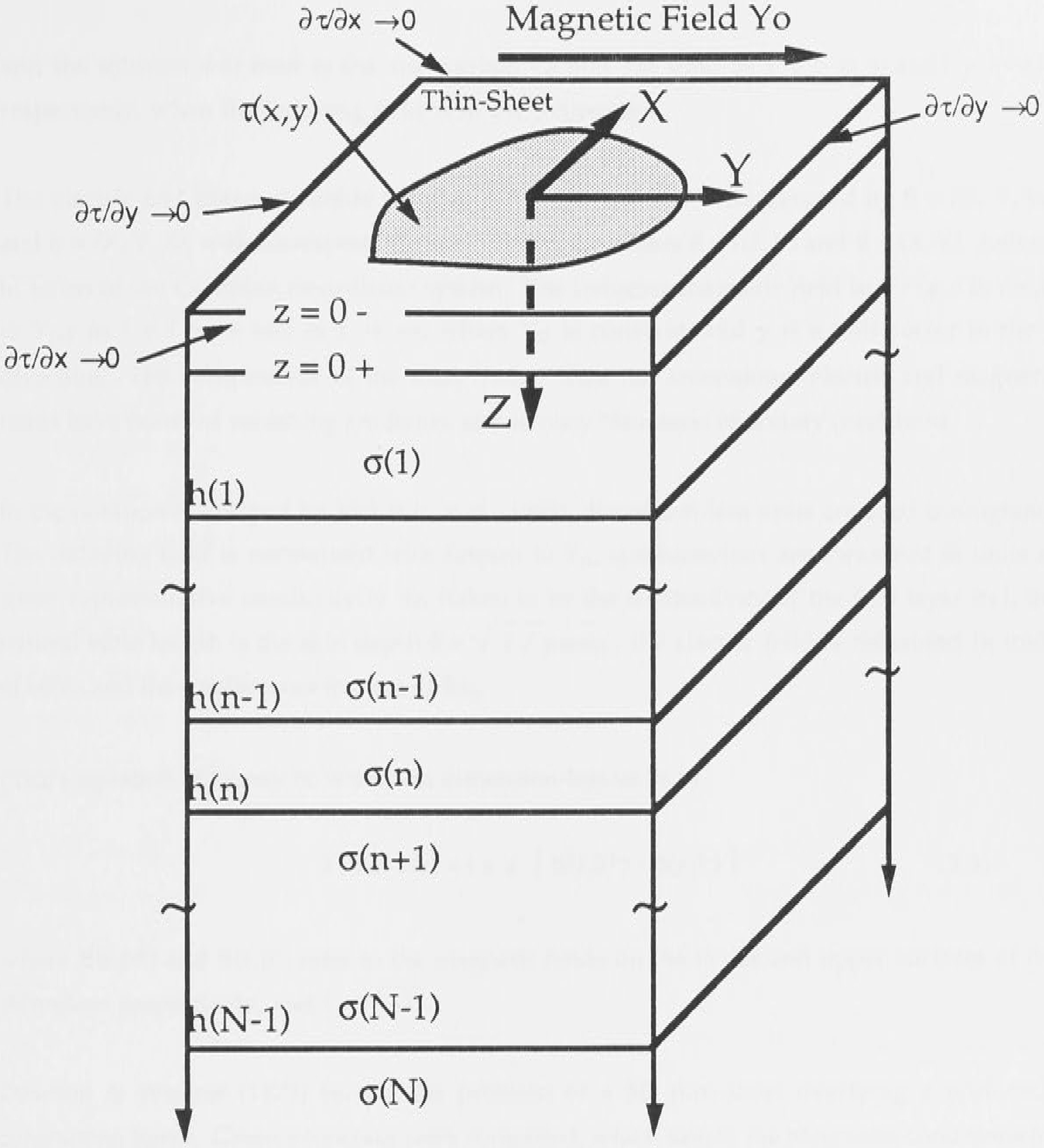

Figure 3.1 A schematic illustration of a thin-sheet model. The external magnetic field may be aligned with the y-axis as shown for the D-polarisation case, or aligned with the x-axis for the H-polarisation case.

Figure 3.1 illustrates the type of model under consideration. The n^{th} layer has conductivity σ_n and lies between depths $z = h_{n-1}$ and $z = h_n$; the N^{th} layer extends to $z = \infty$. The thin surface sheet has conductance $\tau(\mathbf{r}) = \tau(x,y)$, where x and y are Cartesian co-ordinates in the horizontal plain, and conductance variations within the sheet are required to approach a 2D configuration at infinity. Thus

$$\frac{\partial\tau}{\partial x} \rightarrow 0 \text{ as } |x| \rightarrow \infty \text{ and } \frac{\partial\tau}{\partial y} \rightarrow 0 \text{ as } |y| \rightarrow \infty \qquad (3.2)$$

and the solution will tend to the appropriate TE and TM limit as $| x | \rightarrow \infty$ and $| y | \rightarrow \infty$ respectively, when the inducing field is in the y-direction.

The electric and magnetic fields $E(\mathbf{r},z)\, e^{+i\omega t}$ and $B(\mathbf{r},z)\, e^{+i\omega t}$ are denoted by E = (U, V, W) and B = (X, Y, Z), with corresponding horizontal components **E** = (U, V) and **B** = (X, Y), defined in terms of the Cartesian co-ordinate system. The inducing magnetic field in air ($z < 0$) tends to $Y_0\mathbf{y}$ as $| y | \rightarrow \infty$ and as $z \rightarrow -\infty$, where Y_0 is constant, and **y** is a unit vector in the y direction. The components of the total (rather than the anomalous) electric and magnetic fields have outward vanishing gradients, and so obey Neumann boundary conditions.

In the notation developed by McKirdy *et al.* (1985), dimension-less units are used throughout. The inducing field is normalised with respect to Y_0, conductivities are measured in units of some representative conductivity σ_0 (taken to be the conductivity of the first layer σ_1), the natural scale length is the skin depth $\delta = \sqrt{2 / \mu\omega\sigma_0}$, the electric field is measured in units of $\omega\delta Y_0$ and the conductance in units of $\delta\sigma_0$.

Price's equation (3.1) may be written in dimension-less units as

$$2\, i\, \tau(\mathbf{r})\, \mathbf{E}(\mathbf{r}) = i\, \mathbf{z} \times \left[\, \mathbf{B}(\mathbf{r},0^+) - \mathbf{B}(\mathbf{r},0^-) \,\right] \qquad (3.3)$$

where $\mathbf{B}(\mathbf{r},0^+)$ and $\mathbf{B}(\mathbf{r},0^-)$ refer to the magnetic fields on the lower and upper surfaces of the thin-sheet respectively, and $i = \sqrt{-1}$.

Dawson & Weaver (1979) solved the problem of a 3D thin-sheet overlying a uniformly conducting Earth. Green's function were computed, which satisfy the Neumann conditions for the total electric and magnetic fields in a grid of discrete nodes. Hence, a Green's tensor was constructed, which generates the kernel of the vector integral equation, satisfied by the horizontal components of the total electric field on the top surface of the sheet. As infinity is approached in directions respectively parallel and perpendicular to the direction of the inducing magnetic field, the vector integral equation reduces to the distinct TM and TE polarisation integral equations derived by Green & Weaver (1978) for the 2D algorithm. The half-space preserves electrical contact with the sheet, which permits vertical flow of currents from the non-uniform sheet into the conducting region below, in addition to the horizontal flow of currents in the sheet itself. These two types of flow correspond to the poloidal and toroidal currents.

The magnetic field $\mathbf{B}(\mathbf{r},0^-)$ on the top surface of the sheet in contact with the insulating half-space, can be related to the horizontal electric field $\mathbf{E}(\mathbf{r})$ within the sheet by the following expression

$$-\mathbf{i}\,\mathbf{z} \times \mathbf{B}(\mathbf{r},0^-) = \mathbf{i}\,\mathbf{x} + \frac{1}{2\pi}\int_{-\infty}^{+\infty} \mathbf{M}(\mathbf{s}-\mathbf{r}) \,.\, \{\, \mathbf{E}(\mathbf{s}) - \mathbf{E}(\mathbf{r}) \,\}\, ds \qquad (3.4)$$

where $\mathbf{s}$ is a vector position in the sheet, and the tensor $\mathbf{M}$ is the insulating half-space admittance kernel.

Equation 3.4 is not altered by the inclusion of layers in the model. The relationship between $\mathbf{B}(\mathbf{r},0^+)$ and $\mathbf{E}(\mathbf{r})$ calculated by Dawson & Weaver (1979) will, however, be affected by the more complex geoelectric structure. The Green's function approach could be extended to deal with layered sub-strata, but McKirdy *et al.* (1985) found it simpler to develop the analysis in Fourier transform space, resolving the electric and magnetic fields in terms of the toroidal and poloidal scalar functions. This formulation was developed by Vasseur & Weidelt (1977), and the term bi-modal induction is used for studies of this type. In the limit $y \to \infty$ and $x \to \infty$, the problem may approach a 2D configuration, which takes the form of the integral relationships derived by McKirdy & Weaver (1984).

An expression for $\mathbf{B}(\mathbf{r},0^+)$ can be divided into a half-space solution $\mathbf{B}_H(\mathbf{r},0^+)$, and a layered half-space perturbation of the half-space solution, $\mathbf{B}_L(\mathbf{r},0^+)$. The half-space term can be written as

$$\mathbf{i}\,\mathbf{z} \times \mathbf{B}_H(\mathbf{r},0^+) = -k_1\, \mathbf{E}(\mathbf{r}) + \frac{1}{2\pi}\int_{-\infty}^{+\infty} \mathbf{L}(\mathbf{s}-\mathbf{r}) \,.\, \{\, \mathbf{E}(\mathbf{s}) - \mathbf{E}(\mathbf{r}) \,\}\, ds \qquad (3.5)$$

where $k_1 = \sqrt{2\, i\, \sigma_1}$ and the tensor $\mathbf{L}(\mathbf{r})$ is the half-space admittance kernel. The layered half-space perturbation to the half-space solution is given by

$$\mathbf{i}\,\mathbf{z} \times \mathbf{B}_L(\mathbf{r},0^+) = \frac{1}{2\pi}\int_{-\infty}^{+\infty} \mathbf{Lg}(\mathbf{r}-\mathbf{s}) \,.\, \mathbf{E}(\mathbf{s})\, ds \qquad (3.6)$$

where $\mathbf{Lg}(\mathbf{r})$ is the layered half-space admittance kernel, which is a function of the 0^{th} and 2^{nd} order Hankel transforms of the toroidal and poloidal inductive scale lengths, defined by Schmucker (1970).

When expressions for $\mathbf{B}(\mathbf{r},0^+)$ from eqs 3.5 and 3.6, and $\mathbf{B}(\mathbf{r},0^-)$ from eq. 3.4 are substituted into the boundary condition equation eq. 3.3, an integral equation expression for the horizontal electric field is

$$c(\mathbf{r})\,\mathbf{E}(\mathbf{r}) = 2\pi i\mathbf{x} + \int_{-\infty}^{+\infty} \mathbf{K}(\mathbf{s}-\mathbf{r}) \,.\, \{\, \mathbf{E}(\mathbf{s}) - \mathbf{E}(\mathbf{r}) \,\}\, d\mathbf{s} + \int_{-\infty}^{+\infty} \mathbf{L}g(\mathbf{s}-\mathbf{r}) \,.\, \mathbf{E}(\mathbf{s})\, d\mathbf{s} \quad (3.7)$$

where $c(\mathbf{r}) = 2\pi\,[\,k_1 + 2i\tau(\mathbf{r})]$ and $\mathbf{K} = \mathbf{L} + \mathbf{M}$. The horizontal electric field at a point $\mathbf{r}$ in the thin-sheet is related to the integral sum of the electric fields at all the other points within the thin-sheet.

Once the solution of $\mathbf{E}(\mathbf{r})$ has been obtained, it is a straightforward matter to compute the other components of the surface EM fields from the appropriate integral formulae that define it in terms of $\mathbf{E}(\mathbf{r})$. Thus the horizontal components of the magnetic field can be calculated from eq. 3.4 for $\mathbf{B}(\mathbf{r},0^-)$ and from eqs 3.5 and 3.6 for $\mathbf{B}(\mathbf{r},0^+)$. Integral expressions for the vertical magnetic field across the sheet and the vertical electric field on the underside of the sheet can be derived from the toroidal and poloidal transfer functions respectively (Vasseur & Weidelt, 1977). The vertical magnetic field is given by

$$Z(\mathbf{r},0) = \frac{1}{2\pi}\int_{-\infty}^{+\infty} \{\, (\mathbf{s}-\mathbf{r}) \,.\, \mathbf{B}(\mathbf{s},0^+) \,\}\, Q(\,|\mathbf{s}-\mathbf{r}|\,)\, d\mathbf{s} \; - \\ \frac{1}{2\pi}\int_{-\infty}^{+\infty} \frac{\{\, (\mathbf{s}-\mathbf{r}) \,.\, \mathbf{B}(\mathbf{s},0^+) \,\}}{|\mathbf{s}-\mathbf{r}|}\, \chi_z(\,|\mathbf{s}-\mathbf{r}|\,)\, d\mathbf{s} \quad (3.8)$$

where

$$Q(r) = \frac{(\,1 + k_1 r\,)}{r}\, \exp(-k_1 r\,) \quad (3.9)$$

and $\chi_z(\mathbf{r})$ is a toroidal correction term for the underlying layered half-space. A similar approach for the vertical electric field on the underside of the sheet gives the following expression

$$W(\mathbf{r},0^+) = \frac{1}{2\pi}\int_{-\infty}^{+\infty} \{\, (\mathbf{s}-\mathbf{r}) \,.\, \mathbf{E}(\mathbf{s}) \,\}\, Q(\,|\mathbf{s}-\mathbf{r}|\,)\, d\mathbf{s} \; - \\ \frac{1}{2\pi k_1}\int_{-\infty}^{+\infty} \frac{\{\, (\mathbf{s}-\mathbf{r}) \,.\, \mathbf{E}(\mathbf{s}) \,\}}{|\mathbf{s}-\mathbf{r}|}\, \chi_p(\,|\mathbf{s}-\mathbf{r}|\,)\, d\mathbf{s} \quad (3.10)$$

where $\chi_p(\mathbf{r})$ is a poloidal correction term for the underlying structure.

3.1.3 *Numerical Thin-Sheet Modelling*

Equation 3.7 cannot be solved by analytic methods, except in trivial cases, so numerical methods are employed. A square N x N grid is set up on the surface $z = 0$, with nodes at $r_{lm} = (x_l, y_m)$, ($l = 1,\ldots,N$; $m = 1,\ldots,N$) spaced at equal intervals (Figure 3.2). The electric field is now defined at the finite N^2 number of grid-nodes. Consider a point $\mathbf{r} = (l, m)$ to be within the grid, i.e. not on a boundary. The electric field at this point **E(r)** is defined in terms of the electric field values at all other points **s** = (λ, μ) given by **E(s)**. Special boundary conditions apply when the point in question is on the edge of the grid. A detailed explanation of the numerical calculation for the first integral in eq. 3.7 is given by Dawson & Weaver (1979).

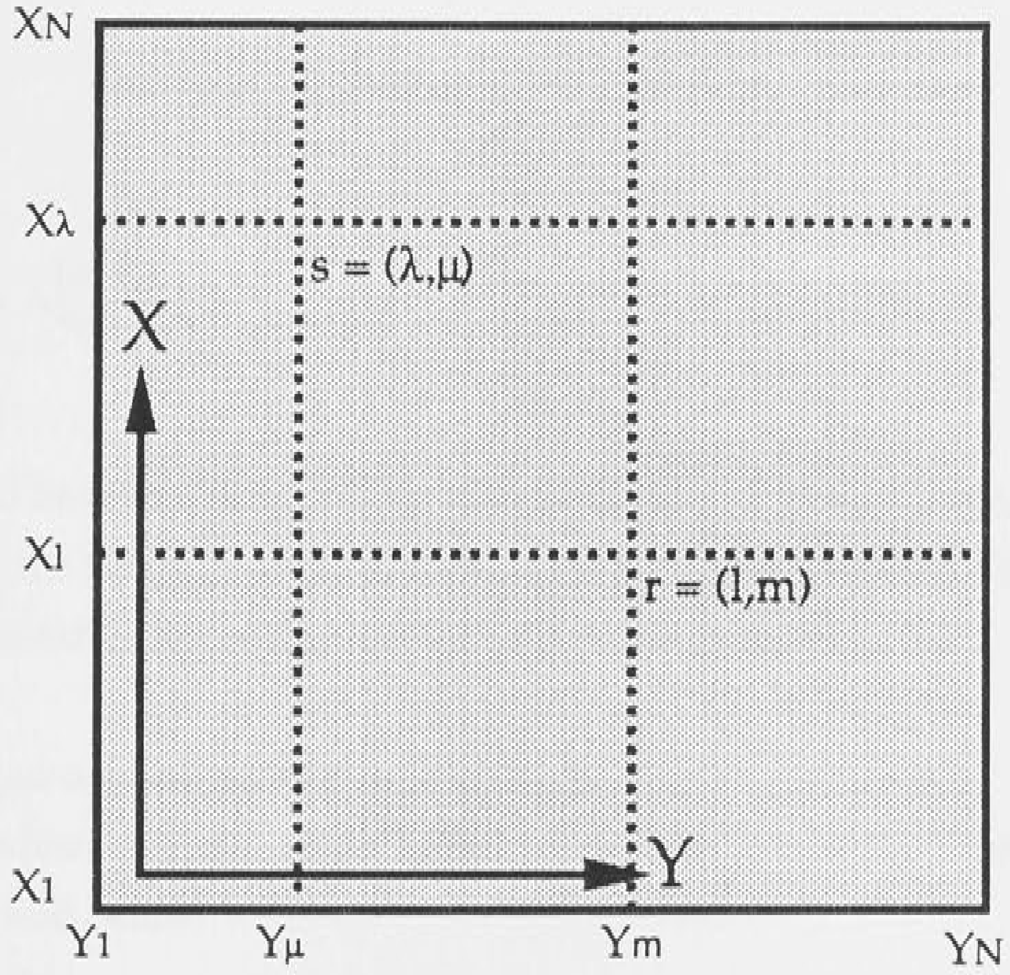

Figure 3.2 The numerical grid defined for the thin-sheet. The conductance at each grid node is defined by the integrated conductivity through the sheet.

Within each cell, the electric field is approximated by a bi-linear function, except in the four cells surrounding the singular point **s** = **r** where it is necessary to use a bi-quadratic approximation. Basic integrals in each cell are calculated, and when combined with the admittance kernel coefficients used to approximate **E(s)**, the tensor $\mathbf{T}_{\lambda\mu}^{lm}$ can be constructed for a half-space (**Lg** = 0). In the discrete form

$$c_{\lambda\mu}\, \mathbf{E}_{\lambda\mu} = 2\pi i x + \sum_{l=1}^{N} \sum_{m=1}^{N} \mathbf{T}_{\lambda\mu}^{lm}\, \mathbf{E}_{lm} \qquad (3.11)$$

A similar approach is used for the second integral in eq. 3.7. A fast Hankel transform (FHT) routine (Johansen & Sørensen, 1979) is used to calculate the tensor elements of **Lg(r)**. McKirdy *et al.* (1985) show that the components of the kernel **Lg(r)** are reasonably well behaved so that further refinement to the FHT is not required. Another tensor $\mathbf{A}_{\lambda\mu}^{lm}$ may be constructed in a similar manner as those for the half-space calculation, so that

$$c_{\lambda\mu}\, E_{\lambda\mu} = \sum_{l=1}^{N} \sum_{m=1}^{N} A_{\lambda\mu}^{lm}\, E_{lm} \qquad (3.12)$$

Equations 3.11 and 3.12 may be combined and the full solution is given by

$$c_{\lambda\mu}\, E_{\lambda\mu} = 2\pi i x + \sum_{l=1}^{N} \sum_{m=1}^{N} C_{\lambda\mu}^{lm}\, E_{lm} \qquad (3.13)$$

where $C_{\lambda\mu}^{lm} = T_{\lambda\mu}^{lm} + A_{\lambda\mu}^{lm}$.

Equation 3.13 could be solved as N^2 simultaneous equations, however it is much more efficient and quicker to use the Jacobi iterative procedure, as described in Dawson & Weaver (1979) or the Gauss-Seidel iterative approach, developed in Weaver (1982).

3.1.4 Thin-Sheet Approximations and Assumptions

Weaver (1982) reviews the conditions under which the thin-sheet approximation holds, which are summarised below:

(a) The thin-sheet thickness must be small in comparison with the skin depth in the half-space or layer directly beneath it. Weaver (1982) suggested the thickness should be less than 15 % of the skin depth δ in the underlying layer.

(b) The attenuation of the electric field through a surface layer is given by Weaver (1973). For the thin-sheet approximation to be satisfied, the electric field must be nearly constant within the sheet, i.e there is no attenuation. It is easy to show that for this to be the case

$$(h / \eta)^2 \ll 1 \qquad (3.14)$$

where h is the thickness of the thin-sheet, and η is the skin depth for the conductors within the sheet.

(c) The grid-node spacing must be small in comparison to the skin depth in the underlying layer. The spacing should be less than 25 % of this skin depth. This acts as a high-frequency (or short period) limit for calculations.

(d) Sharp conductivity changes parallel to a grid boundary should, if possible, be well away from the grid edge. Changes perpendicular to the boundary are, of course, permitted. This provides a low-frequency (or long period) limit for calculations.

(e) Conductance values present on the grid boundaries are assumed to continue to infinity, perpendicularly to the grid edge.

A significant advantage of the thin-sheet algorithm of McKirdy *et al.* (1985) over those which have anomalous conductance surrounded by normal structure, is that comparisons can be made with 2D analytical solutions, and with accurate 2D modelling programs. A 2D analytic solution exists for the TM polarisation case (Nicoll & Weaver, 1977), however, the model is unrealistic and the extreme contrasts would be difficult to reproduce with the coarse grid used in thin-sheet modelling. McKirdy *et al.* (1985, Figures 2,3 and 4) make a comparison with the 2D integral equation method of McKirdy & Weaver (1984) of a single discontinuity in a surface sheet, underlain by a two-layer Earth, which has been shown to give excellent agreement with finite-difference solutions.

The agreement between thin-sheet and finite-difference solutions are excellent, except where the thin-sheet grid lacks resolution at the discontinuity in the surface sheet. The anomalous field components are smoothed out on a 3D grid of regular grid-node spacing; this is particularly apparent in the vertical field, which should become very large at the discontinuity. In section 5.1, another analytical technique is described, to examine the numerical accuracy of the thin-sheet algorithm.

3.1.5 Source-Field and Flat Earth Approximations

The thin-sheet algorithm of McKirdy *et al.* (1985) requires that the external inducing field is uniform and horizontal. Three-dimensional source-fields have been applied to thin-sheet problems (Smith & West, 1987), but the solution is limited to that of an electrically isolated sheet.

Natural source-fields used for seafloor EM observations at mid-latitudes are uniform over many thousands of kilometres. Chave *et al.* (1981) estimate that source-field wavelengths at mid-latitudes are approximately 5000 km. Ferguson *et al.* (1990) show that over a distance of 1000 km, the finite source-field wavelength of 5000 km will cause at most a 5 % difference in the amplitude of the horizontal magnetic field. At high latitudes, source-field scale lengths are smaller, due to anisotropic polar ionospheric currents (Parkinson, 1983), and close to the geomagnetic equator, the equatorial ring-current produces a non-uniform source-field (Oni & Agunloye, 1974). All thin-sheet models presented in this thesis have lateral dimensions equal to or less than the source-field wavelength of 5000 km. Both the Tasman Sea and northeast Pacific are at mid-latitudes, so thin-sheet models of infinite wavelength source-fields are applicable. It is assumed that all synthetic ocean basin models are also at mid-latitudes, so that an assumption of uniform source-field is again valid. A grid of lateral dimensions 5000 km subtends an angle of approximately 45° over Earth's surface. Inevitably, the grid may cover areas for which a uniform source-field approximation is not valid. It is therefore prudent to carefully consider the extent of the anomalous conductor, and ensure that the condition of uniform source-field is applicable for the thin-sheet model.

The thin-sheet approximation can be applied to the case of a spherical conducting sheet, electrically isolated from a perfect spherical conductor, which approximates the high conductivity of the lower mantle. Solutions for arbitrarily shaped oceans of variable depth are derived by Beamish *et al.* (1983) and references therein. A similar approach has been made by Hobbs & Brignall (1976) and Hobbs & Dawes (1979). Such solutions do not allow any current flow into or out of the sheet; no published solution exists for the case of a spherical conducting sheet which is in electrical contact with the resistive lithosphere. However, there exists an analytical solution in terms of Bessel functions for a uniform conducting sphere, and a numerical solution for a spherically-layered sphere (Srivastava, 1966). As Price's equation applies across the spherical thin-shell, it seems probable that a thin-sheet solution could be formulated.

Srivastava (1966) showed that a flat-Earth approximation is valid for periods less than about one day. This period is at the upper limit used in seafloor MT, so that a flat thin-sheet model of an ocean basin is justified.

3.2 Electromagnetic Induction Parameters

3.2.1 Introduction

Thin-sheet calculations of the EM fields are made with two orthogonal polarisations of inducing magnetic field. These polarisations are denoted H-polarisation, for the field in the x-direction, and D-polarisation for the field aligned with the y-direction, and are equivalent to B- and E-polarisations defined by Weaver (1982). The H and D directions refer to the geomagnetic north and geomagnetic east directions respectively, although the thin-sheet grid may not necessarily be aligned with geomagnetic co-ordinates. The notation of Weaver (1982) is not used as the terms E- and B-polarisation are often applied to MT parameters rotated to the directions parallel and perpendicular to the predominant 2D strike.

Although the computed electric and magnetic fields for the H- and D-polarisations of inducing magnetic field contain all the information required to calculate the 3D response of the thin-sheet model, it is often more illuminating to express the results in terms of induction parameters which are usually used to present field data. The electric and magnetic field components may be related to each other by transfer functions at any point within the grid, or at grid points on opposite sides of the sheet, to simulate experimental techniques.

Furthermore, it is important to be able to relate electric and magnetic field components at an arbitrary point within the thin-sheet to any other arbitrary point on either surface of the sheet. There are many experimental case studies in which two or more sets of observations at different locations are combined (e.g. Law & Greenhouse, 1981): thin-sheet methods can be used to reproduce experimental procedures, and so test the assumptions implicit in many such techniques.

3.2.2 Thin-Sheet MT Response Functions

To determine the MT response of the thin-sheet model at each grid-node, the method formulated by Weaver (1982) is used. The two directions of regional magnetic field are defined to be D- and H-polarisation, parallel to the y- and x-axes respectively. Two MT equations orientated to the y- and x-axes can be expressed as

$$U^D = Z_{xx} X^D + Z_{xy} Y^D, \qquad V^D = Z_{yx} X^D + Z_{yy} Y^D \tag{3.15}$$

$$U^H = Z_{xx} X^H + Z_{xy} Y^H, \qquad V^H = Z_{yx} X^H + Z_{yy} Y^H \tag{3.16}$$

where the electric field **E** = (U, V) and the magnetic field **B** = (X, Y), the subscripts D and H refer to the polarisation of the inducing field, and **Z** is the impedance tensor in eq. 1.43. The impedance tensor **Z**, defined with respect to the co-ordinate system of the grid, is invariant to the orientation of the source-field, and so eqs 3.15 and 3.16 can be solved simultaneously. The dimension-less value of **Z** can be converted to SI units of impedance by multiplying by $\omega\delta\mu_0$. Magnetotelluric parameters can be derived for both the top and bottom of the thin-sheet surface, using the appropriate components of calculated magnetic field, $\mathbf{B}(\mathbf{r},0^-)$ and $\mathbf{B}(\mathbf{r},0^+)$.

The impedance tensors may be interpreted by a number of techniques of tensor decomposition and invariant parameter estimation. Weaver (1982) shows how the tensor may be rotated by the method of Swift (1967), so that two (dimension-less) apparent resistivities are defined.

3.2.3 Thin-Sheet VGS Response Functions

The VGS method, derived in chapter 1, is an important new technique for seafloor MT and GDS experiments, and elegantly demonstrates how the seafloor environment generates new processing and interpretation developments. Such theory is easy to adapt to thin-sheet models, as the horizontal magnetic field components are calculated at the top and bottom of the thin-sheet. The method follows the theory outlined in Poehls & Von Herzen (1976) in that a tensor **R** is defined as the transfer function between the horizontal magnetic field components above and below the surfaces of the thin-sheet. Using the same notation as defined for thin-sheet MT parameters, the tensor R can be defined as

$$X(r,0^+)^D = R_{xx}\,X(r,0^-)^D + R_{xy}\,Y(r,0^-)^D \qquad (3.17a)$$

$$Y(r,0^+)^D = Ryx\,X(r,0^-)^D + Ryy\,Y(r,0^-)^D \qquad (3.17b)$$

$$X(r,0^+)^H = R_{xx}\,X(r,0^-)^H + R_{xy}\,Y(r,0^-)^H \qquad (3.18a)$$

$$Y(r,0^+)^H = Ryx\,X(r,0^-)^H + Ryy\,Y(r,0^-)^H \qquad (3.18b)$$

The components of the tensor **R**, which are a ratio of horizontal magnetic fields, are related to the impedance **Z** at each interface of the sheet by eq. 1.57.

Schmucker's (1970) recursive equation can also be used to determine a relationship between the impedance at the top of one layer to the impedance at the top of the layer above or below. Thin-sheet EM fields are calculated at the top or bottom of the sheet, however, it is sometimes necessary that MT and GDS parameters are derived at some point within the sheet. Although the sheet is approximated as being infinitely thin, conductances are derived from a finite thickness of anomalous conductor; for example, when modelling ocean basins, it is often desirable to include both sea-water and a layer of sediments into the thin-sheet, while the lithosphere and upper mantle are modelled by a layered structure. Thus, eq. 1.55 can be used to calculate the MT response at the top of the sediments from the thin-sheet EM fields at the base of the sediments.

3.2.4 Thin-Sheet GDS Induction Arrows

The GDS induction arrow is perhaps the most commonly employed graphical means of displaying field data collected at a single station (Parkinsons, 1962). The vertical field within the thin-sheet is related to the horizontal components of magnetic fields, by an assumed linear relationship. Weaver (1982) shows for the thin-sheet grid that

$$Z^D = A\,X^D + B\,Y^D \qquad (3.19)$$

$$Z^H = A\,X^H + B\,Y^H \qquad (3.20)$$

using the notation of this chapter. Equations 3.19 and 3.20 can be solved simultaneously for the transfer functions A and B, and the magnitudes and directions of GDS arrows are determined as in section 1.2.9. The GDS induction arrows may be determined on either side of the sheet, using the corresponding horizontal magnetic fields $X(r,0^-)$ and $Y(r,0^-)$, or $X(r,0^+)$ and $Y(r,0^+)$.

Equations 3.19 and 3.20 use the total field in the computation of the induction arrows. A more general assertion is that the internal anomalous field is linearly dependent on the regional field, the assumption being that Z is largely anomalous, whilst X and Y are largely normal (Banks, 1973). It is a straightforward matter to use the regional fields, instead of the total fields, which are unity and in the y-direction for the D-polarisation, and in the x-direction for the H-polarisation.

3.2.5 Thin-Sheet Channelling of Induced Electric Currents

McKirdy & Weaver (1983) show that the derivatives of the surface current-density $\partial J/\partial x$ and $\partial J/\partial y$ can be found at the middle of a cell in the grid (Figure 3.2), whose bottom left hand corner is at node (l,m), by the central difference formulae

$$\frac{\partial J_x}{\partial x} = \frac{J_{l+1\,m+1} + J_{l+1\,m} - J_{l\,m+1} - J_{l\,m}}{2h} \tag{3.21}$$

$$\frac{\partial J_y}{\partial y} = \frac{J_{l+1\,m+1} - J_{l+1\,m} + J_{l\,m+1} - J_{l\,m}}{2h} \tag{3.22}$$

which are obtained by neglecting terms in h^3 and higher, where h is the distance between grid-nodes in the sheet. Weaver (1982) and McKirdy & Weaver (1983) suggest that a measure of channelling and leakage of electric current is provided by the 2D divergence of the surface current-density **J**, as detailed in section 1.2.7. McKirdy & Weaver (1983) also define anomalous electric current and anomalous magnetic field vectors, as the vector difference between the calculated surface current-density and magnetic fields, at some grid location in the region of anomalous conductance, and the 'normal' field components, defined from a grid location well away from anomalous structure. The regional magnetic field and associated induced electric field could also be used as the reference from which to define anomalous field vectors.

Leakage of electrical current from the lower thin-sheet surface can also be defined with an electric field (EDS) induction arrow, see section 1.2.10. Such an arrow may be determined from thin-sheet calculations as

$$W^D = A\,U^D + B\,V^D \tag{3.23}$$

$$W^H = A\,U^H + B\,V^H \tag{3.24}$$

using the notation of this chapter. The magnitude and direction of the electric field induction arrows may be determined in a similar manner as described for the GDS induction arrows.

3.3 Computer Adaptation at the Australian National University

3.3.1 Introduction

In this section, brief notes as to the adaptation of the computer code to the computer facilities at the Australian National University are provided. It should be mentioned that the code worked admirably well on a whole range of machines, with very few modifications required for different computers. No bugs were found in the code, and the iterative procedure proved to be robust to extreme model configurations, only occasionally failing to converge. Overflow errors in the Fast Hankel Transform occurred for layered models with large discontinuities; however, these could be overcome with no serious repercussions using Fortran compiling options. The main problem encountered was the large disk storage space required for the tensor coefficients, shown in eqs 3.11 - 3.13.

3.3.2 Computer Code

The code was supplied in Fortran, and consisted of five sets of routines. These were used to calculate the half-space coefficients **M** and **L**, the layered half-space perturbation correction coefficient **Lg**, a routine to combine these coefficients together, and two final programs to solve by iterative procedures either the thin-sheet problem for the half-space or the layered half-space. Minor modifications were made to combine these separate routines together into one program, which was run using some form of command file. The original code was run on an IBM 4341 at the University of Victoria, using job control language files. The code was adapted at the ANU to run on a FACOM M360 with a Fujitsu OSIV/F4 operating system (similar to IBM's operating system), and was also run on the FACOM VP-100 supercomputer. The most satisfactory mode of operation was found to be on a VAX 8700, with VMS operating system. The code was also adapted to run on a Macintosh SE/30, with 200 Mbyte hard disk.

3.3.3 C.P.U. Times

McKirdy *et al.* (1985) report that for a layered half-space model, the calculation of all tensor elements took 23 minutes on an IBM 4341. The time for computation increases as the dimension-less grid-node separation decreases, and for an increase in the number of grid-nodes. On the VAX 8700, the time for calculation of the tensor coefficients varied from 8.6 minutes for a dimension-less grid-node spacing of 0.18, and 20 minutes for a grid-node spacing of 0.04, with a 22 x 22 grid. For the Tasman Sea model, each thin-sheet iteration took, on average, 21 seconds, and the number of iterations required varied from approximately 50 to the maximum number of 150. The number of iterations required increased with a decrease in the dimension-less grid-node separation. Thus, for 150 iterations, with two polarisations of the inducing field, the total c.p.u. time for a thin-sheet model calculation is of the order of 2 hours, which makes computation of many models impractical. Furthermore, the computation time for each forward-calculation probably excludes it from being used as the basis of an iterative inversion method (Fisher *et al.*, 1981; Fischer & Le Quang, 1981, 1982), as an entire forward-calculation is required for each change in the sub-structure.

3.3.4 Disk Storage Requirements

The disk storage requirement is the most restrictive feature of the forward-modelling algorithm. In the final chapter, suggestions are made in which the code may be modified to take advantage of new developments in computer technology, and as the tensor coefficients are symmetrical in a square grid, changes are also suggested so that only a fraction of the number coefficients actually need be stored on disk.

At each grid-node in an N x N grid, there are 25 x N^2 tensor elements stored, so for the entire grid, the number of stored coefficients are 25 x N^4. The original version of the code had all variables stored as complex double precision; the storage space in bytes is 16 x 25 x N^4. Thus disk storage requirements increase as the fourth power of the number of grid nodes, whilst the c.p.u. time increases by less than the second power. For a 15 x 15 grid, the disk storage requirements are 21 Mbytes, whilst for a 30 x 30 grid, this increases to 324 Mbytes. Clearly, it is impractical to compute models with too many grid-nodes. In practice, it was found that it was satisfactory to store coefficients in single precision format, which halved the storage requirements.

Chapter 4 : The Conductivity of the Oceanic Upper Mantle: Forward-Calculations From Laboratory Data

4.1 Introduction

Estimates of upper mantle conductivity based on laboratory data are important in the interpretation of electrical soundings for three reasons:

Firstly, in the ideal case where the electrical conductivity structure of the upper mantle can be determined uniquely from the EM sounding data, the laboratory data can be used to infer the physical properties of the upper mantle. More realistically, bounds on conductivity can be converted to bounds on physical properties.

The second reason arises from the non-uniqueness of the EM inversion problem. The decisions as to what models are geologically realistic are often carried out in an ad hoc manner. For example, 1D inversion of MT data may result in conductivity structures which are entirely consistent with the observations, but which are geologically unlikely, such as the discrete finite conductance delta functions of Parker's (1980) D^+ model. Few researchers would accept this as a geologically reasonable model of the earth, yet are less critical in accepting the output from other modelling schemes. Apart from providing an indication of the geological feasibility of models generated to fit sounding data, the inclusion of laboratory information can be used to reduce the non-uniqueness of the problem. For example, in a marine controlled source-field sounding, Cox *et al.* (1986) constrained conductivity below 20 km depth using laboratory measurements of olivine conductivity in order to obtain better resolution above 20 km.

Finally, EM sounding data can be used to test the hypotheses generated by the laboratory experiments. That is, the EM response of the laboratory generated conductivity models of the upper mantle may be tested for compatibility with the sounding data. Alternatively, a class of inversion methods exist which generate the model closest to the a priori model and which is compatible with the data (e.g. Parker *et al.*, 1987).

This chapter presents an attempt at determining realistic models of the conductivity structure of the sub-oceanic upper mantle independently of EM sounding data, by using other geophysical and petrological information. Although the uncertainty in the range of petrological models is large, the differences between models of chemical composition of the upper mantle are not a major factor in determining the conductivity structure. Of far greater importance is the presence of a region of partial melt or volatiles which has been used to explain the seismic low-velocity zone / high-conductivity zone. Most geothermal models of the sub-oceanic lithosphere (e.g. Parsons & Sclater, 1977) are shown to be consistent with a region of partial melt, where the width of the zone is a function of age of the sub-oceanic lithosphere, but the fraction of partial melt is less well constrained.

4.2 Geothermal Models

The construction of suitable geotherms for Earth is not straightforward, as Earth's thermal structure is poorly understood. In this analysis, simple modelling procedures are used, dividing the upper mantle into a non-viscous thermal lithosphere, in which the dominant mode of heat-flow is conduction, and a convective region extending beneath the thermal lithosphere into Earth.

Simple cooling models (Parker & Oldenburg, 1973) and of a rigid plate (McKenzie, 1967; Parsons & Sclater, 1977) have been advanced to explain the approximately linear relationship between the ocean depth and the square root of the age, for seafloor ages less than 70 Ma. For older seafloor, the depth and the heat-flow observations appears to decay exponentially to constant values (Parsons & Sclater, 1977), for which the plate model is better suited. However, recent re-interpretation of a much larger data set by Marty & Cazenave (1989) indicates that the plate model is too simple, and that the square root of age dependence may in fact be extended out to seafloor of age 80 to 100 Ma and possibly beyond. While there is little evidence to support a thermal boundary zone at a depth of approximately 131 km (taken from the plate thickness plus the ocean depth), and furthermore, the model has the physically unrealistic characteristic of infinite heat-flow at the ridge-axis, Parsons & Sclater show there to be good agreement with bathymetry and, to a lesser extent, heat-flow observations for a wide range of seafloor ages. The method described by Parsons & Sclater also has the advantage that it permits an inversion of bathymetry data to give the model parameters of plate thickness, the temperature at the base of the plate and thermal expansion coefficient. Calculation of these parameters for the north Pacific and the north Atlantic agree within one standard error, and are listed in Table 4.1. The temperature distribution may be calculated using a 1D heat-flow approximation, given by Parsons & Sclater (1977) and Carslaw & Jaeger (1959), using the resulting best fit parameters from the north Pacific, for ages of sub-oceanic lithosphere ranging from 10 to 100 Ma. These are shown in Figure 4.1.

Beneath the thermal lithosphere, convection is the dominant method of heat transfer through Earth (Stacey, 1977a). The physics of a very large, slowly convecting fluid system places a lower-bound on the temperature gradient, which is the the adiabat.

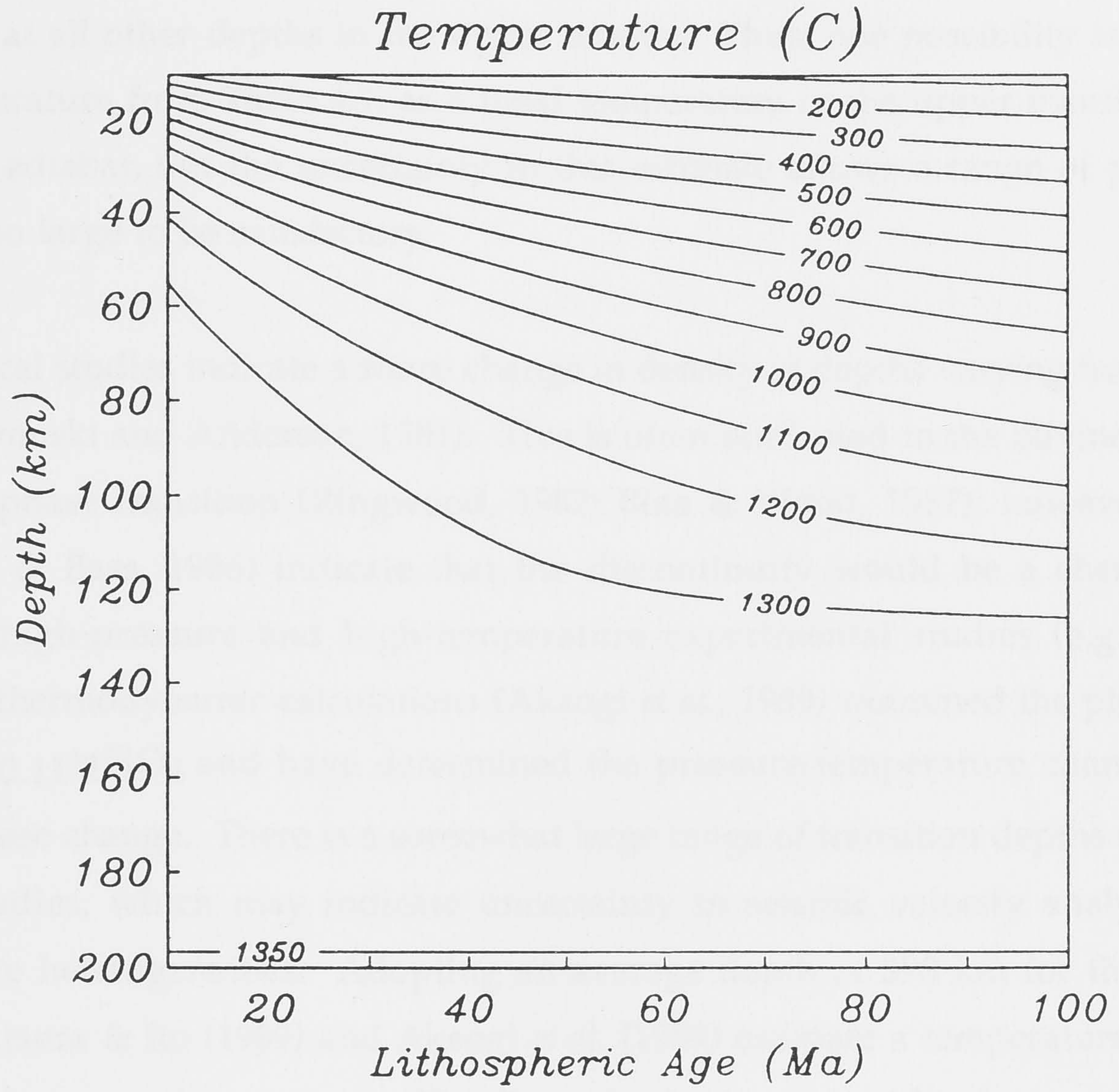

Figure 4.1 Isotherms calculated from Parsons & Sclater (1977) for sub-oceanic lithosphere ranging in age from 10 to 100 Ma over depths of 10 to 200 km. A reference depth of ocean for 120 Ma crust of 6400 m depth is used in the calculation. The temperature gradient from 131 km to 200 km is approximately adiabatic.

Table 4.1 Plate Model Parameters for north Pacific and north Atlantic from an inversion of Bathymetrical Data

	Plate Thickness (km)	Plate Base Temperature (°C)	Thermal Expansion Coefficient (°C^{-1})
North Pacific	125 ±10	1333 ± 274	(3.28 ± 1.19)x10^{-5}
North Atlantic	128±10	1365 ± 276	(3.10 ± 1.11)x10^{-5}

Stacey (1977a; page 195) shows that the temperature and density of an adiabatic system are simply related by the Grüneisen parameter, and suggested values of 0.8 and 1.0 for the upper and lower mantle. The density-depth relationship for sub-oceanic lithosphere can be derived from the PEM model of Earth (Dziewonski *et al.*, 1975). If the temperature at one point in

Earth can be determined, the adiabatic temperature equation allows the temperature to be calculated at all other depths in the upper mantle. Thus, one possibility is to use the plate base temperature from Table 4.1, as a fixed temperature in the upper mantle from which to define the adiabat, but the uncertainty in this estimate allows a range of possible adiabats which is too large to be satisfactory.

Seismological studies indicate a sharp change in density at depths varying from 370 to 420 km (e.g. Dziewonski and Anderson, 1981). This is often attributed to the olivine (α) to modified spinel (β) phase transition (Ringwood, 1982; Bina & Wood, 1987); however other authors (Anderson & Bass, 1986) indicate that the discontinuity would be a chemical boundary. Extensive high-pressure and high-temperature experimental studies (e.g. Katsura & Ito, 1989) and thermodynamic calculations (Akaogi *et al.*, 1989) examined the phase transition in $(Mg_{0.89}Fe_{0.11})_2SiO_4$ and have determined the pressure-temperature characteristics of the $\alpha \rightarrow \alpha+\beta$ phase change. There is a somewhat large range of transition depths determined from seismic studies, which may indicate uncertainty in seismic velocity analysis, or possible temperature heterogeneities. Adopting an average depth of 390 km for the $\alpha \rightarrow \alpha+\beta$ phase change, Katsura & Ito (1989) and Akaogi *et al.* (1989) estimate a temperature of ~1400 °C for the phase change at this pressure. The discontinuity is estimated to have a width of about 18 ± 5 km. Navrotsky & Akaogi (1984) argue that over this transition there will be a temperature rise of 50 °C due to the latent heat of phase transition, superimposed on the adiabatic gradient, which results in an overall rise in temperature of approximately 55 °C.

If a geotherm is taken between the plate base temperature of 1333 °C (see Table 4.1) and the temperature of 1400 °C at the $\alpha \rightarrow \alpha+\beta$ transition at 390 km then the temperature gradient of 0.25 $°C.km^{-1}$ is approximately adiabatic; it is greater than the adiabatic gradient of Stacey but less than the value of 0.3 $°C.km^{-1}$ calculated by Turcotte & Schubert (1982).

The resulting geotherms are indicative of geophysically reasonable temperature gradients. There is good agreement with other geothermal models calculated from seismic parameters (Brown & Shankland, 1981; Sato *et al.*, 1988), geochemical studies on equilibration temperatures of mantle xenoliths (Mercier & Carter, 1975), high-pressure and high-temperature studies (Presnall, 1980) and equations of state (Stacey, 1977b; Habese *et al.*, 1970). The temperature distributions calculated by Oldenburg (1981) and Oldenburg *et al.* (1984), determined from conductivity profiles on various ages of seafloor, show temperatures that are consistently greater than the model, particularly at depths less than 80 km, where the temperature is higher by several hundred degrees. It is worth noting that the adiabat represents a lower-bound on the temperature gradient. Parsons & Sclater (1977) state that a mechanism is required to supply heat to the base of the plate, which implies that the temperature gradient in the upper mantle must be greater than the adiabat. If the temperature associated with the $\alpha \rightarrow \alpha+\beta$ phase transition is considered to be well determined, then the modelled geotherms in Figure 4.1 represent an upper-bound on the temperature distribution in Earth, between the extremes of 0 °C at 0 km and 1400 °C at 390 km.

4.3 Mantle Composition and Mantle Solidus Determination

The chemical composition of the upper mantle has been the subject of intense investigation. To account for the seismic low-velocity zone (Forsyth, 1977), a region of partial melt has been postulated. Such melts are thought to be rich in water and carbonates, and to be similar in composition to kimberlite and potassium-rich magmas (McKenzie, 1989). In this analysis, the 'pyrolite' model of Earth's mantle is adopted (Ringwood, 1975, 1982) although the eclogite model of Anderson (1982) is not substantially different below 220 km and it will be demonstrated later that the differences between the pyrolite model and the eclogite model are not sufficient to change the conductivity structure in a profound way.

Experimental evidence from Takahashi (1986) and Scarfe & Takahashi (1986) on a spinel lherzolite and garnet peridotite respectively indicate that the 'dry' (i.e. no H_2O or CO_2) solidus is at a considerably higher temperature than the geotherms shown in Figure 4.1. Sato *et al.* (1989) argue that a dry upper mantle is supported by seismic evidence and thus the geotherm will remain lower than the solidus for ages of sub-oceanic lithosphere greater than 40 Ma. If small fractions of H_2O and CO_2 are present, the position of the mantle solidus can vary greatly. There is little agreement amongst petrologists as to the exact proportion of volatiles, however the percentages are likely to be small, of the order of 0.5 % or less. The reader is referred to the work of Kushiro *et al.* (1968), Green & Liebermann (1976) and Ringwood (1975) for a full discussion. Delaney *et al.* (1978) and Muenow *et al.* (1979) infer that the mantle source region of Hawaiian tholeiites is nearly anhydrous. They conclude that the oceanic mantle contains on the order of 0.02 to 0.1 % CO_2, and a negligible amount of H_2O. Ringwood (1975) argues for 0.1 % H_2O, with an uncertainty of a factor of 2; this value is used here, for the important reason that the partial melt fractions are given as a function of pressure and temperature. Figure 4.2 illustrates the form of the 'wet' solidus for the mantle, reproduced from Ringwood (1975, page 155), and the lower-bound 'wet' solidus for a mantle containing excess H_2O, from Kushiro *et al.* (1968), superimposed on the mantle geotherms shown in Figure 4.1. The abrupt drop in the wet solidus from Ringwood (1975) at a depth of approximately 85 km is associated with the hydration of amphiboles. Presnall *et al.* (1979) and Presnall (1980) take the results of Delaney *et al.* (1979) and Muenow *et al.* (1979) to infer that the mantle solidus would be very close to the pure CO_2-saturated mantle solidus (Wyllie, 1977), which is also shown in Figure 4.2. Presnall (1980) concludes that the low-velocity zone would not be the result of the breakdown of amphiboles (Ringwood, 1975), but rather the result of a deep low-temperature cusp in the mantle solidus caused by a carbonation reaction.

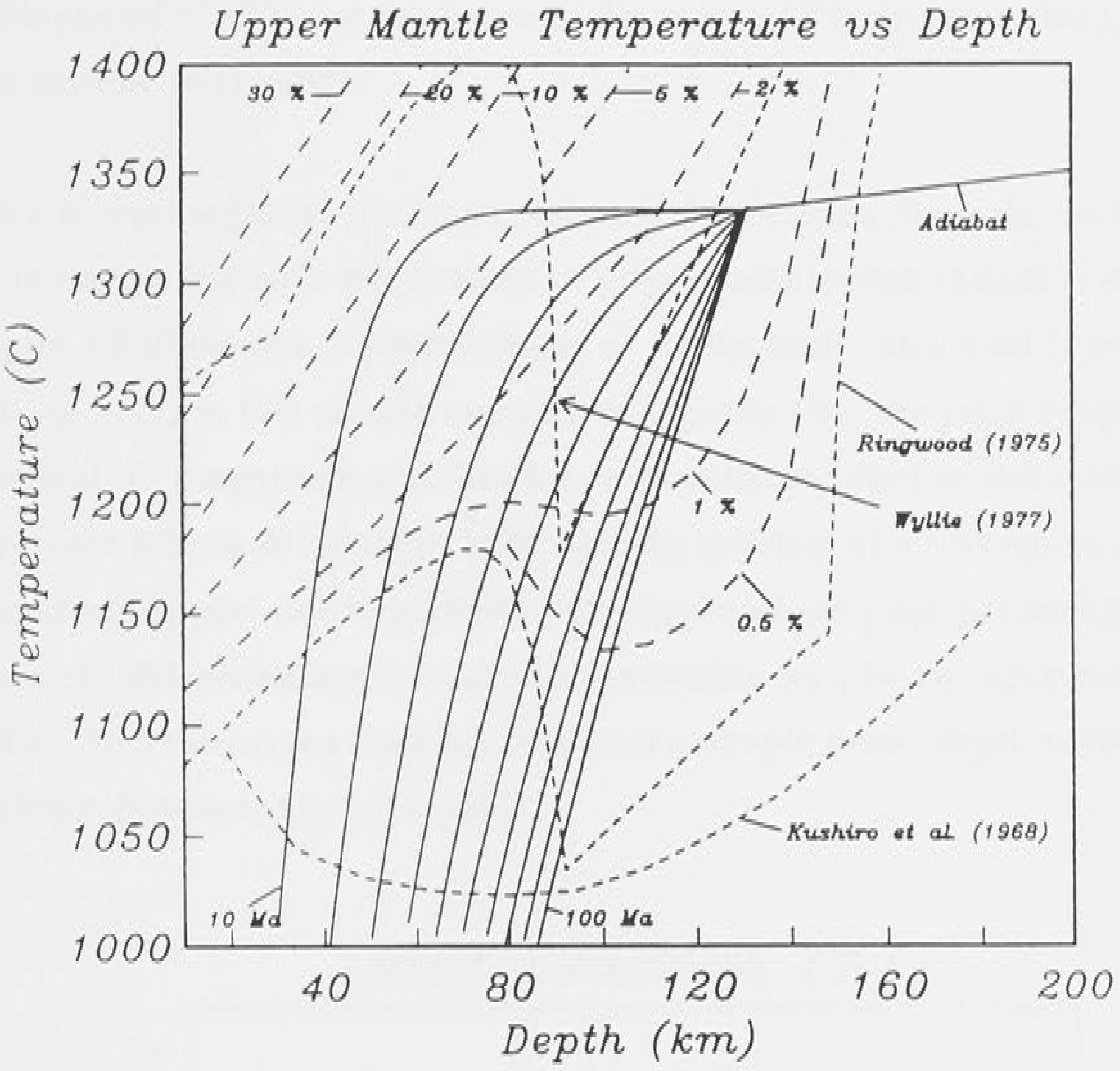

Figure 4.2 The wet solidus curve (light dashed line) for 0.1 % H_2O from Ringwood (1975, page 155), with partial melt fractions (heavy dashed lines) as a function of temperature and depth. Also shown is the saturated CO_2 solidus curve (light dashed line) of Wyllie (1977) and the wet solidus curve (light dashed line) of Kushiro *et al.* (1968) for excess H_2O in the mantle, which represents a lower-bound. Geotherms (solid lines) from Figure 4.1 are superimposed on the solidus curves.

The most striking features shown in Figure 4.2 are the intersections of the geotherms with the mantle solidus at depths ranging from 40 km to 90 km for sub-oceanic lithosphere ranging from 10 to 100 Ma. This phenomenon is also observed when the wet solidus of Green and Liebermann (1976) is used (Forsyth, 1977). If the geotherm of Habese *et al.* (1970) is used instead of the Parsons and Sclater curves, then it does not intersect the wet solidus curves of Ringwood (1975), Wyllie (1977), or the lower-bound wet solidus of Kushiro *et al.* (1968). From this, Liu (1989) argues that the low-velocity zone results from a fraction of free H_2O between the water line at a depth of 250 km and the stability field of amphibole in the sub-oceanic mantle. Another alternative hypothesis by Green & Gueguen (1974) attributes seismic attenuation to bubbles of a CO_2 rich fluid phase. Recently, Karato (1990) has argued that hydrogen dissolved in the olivine lattice may increase the plasticity of the asthenosphere by a factor of 1.5 to 3. The eclogite model of Anderson (1982) differs little from the pyrolite model of Ringwood (1975) over the low-velocity zone, and incipient melting is again used to explain the seismic attenuation.

If Figure 4.2 is representative of the partial melt distribution, then the width of the partial melt zone is compatible with calculations of seismic attenuation (Leeds *et al.*, 1974; Forsyth, 1977). Figure 4.3 illustrates the percentages of partial melt calculated from Figure 4.2 as a function of age. From this simple analysis, it appears that the peak percentage of partial melt varies both in magnitude and location with different ages of sub-oceanic lithosphere. Seismic evidence (Canas & Mitchell, 1978) and the conductivity inversions of (Oldenburg *et al.*, 1984) tend to support this hypothesis. The depth of the peak percentage of partial melt as a function of lithospheric age is modelled reasonably well by an exponential curve, shown in Figure 4.4. Also shown is a least squares fit of a simple linear depth versus square root of age dependence, postulated by Law (1983).

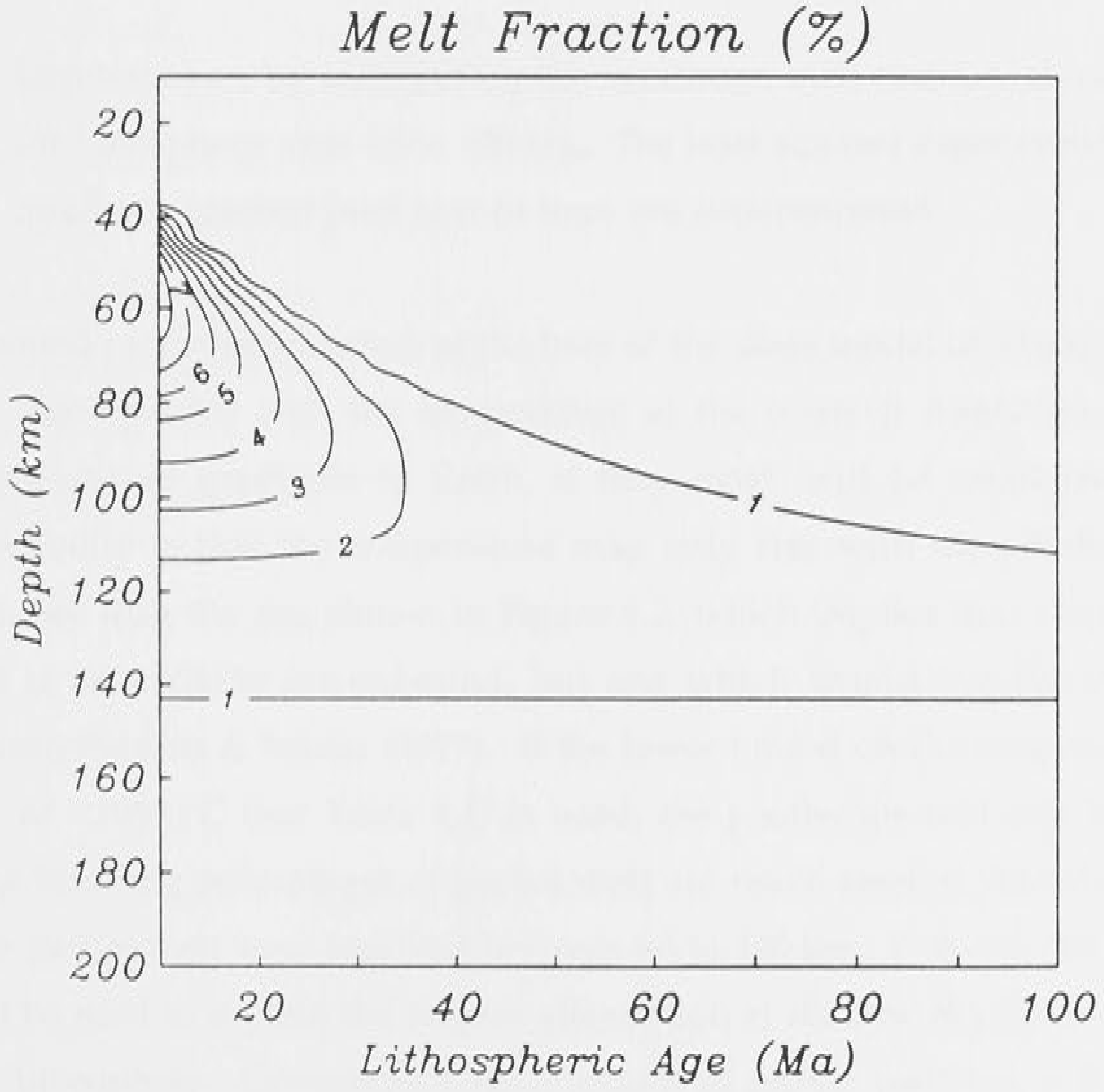

Figure 4.3 Percentages of partial melt obtained from Parsons & Sclater's (1977) 10 Ma to 100 Ma geotherms intersecting a 'wet' solidus for 0.1 % H_2O (Ringwood, 1975).

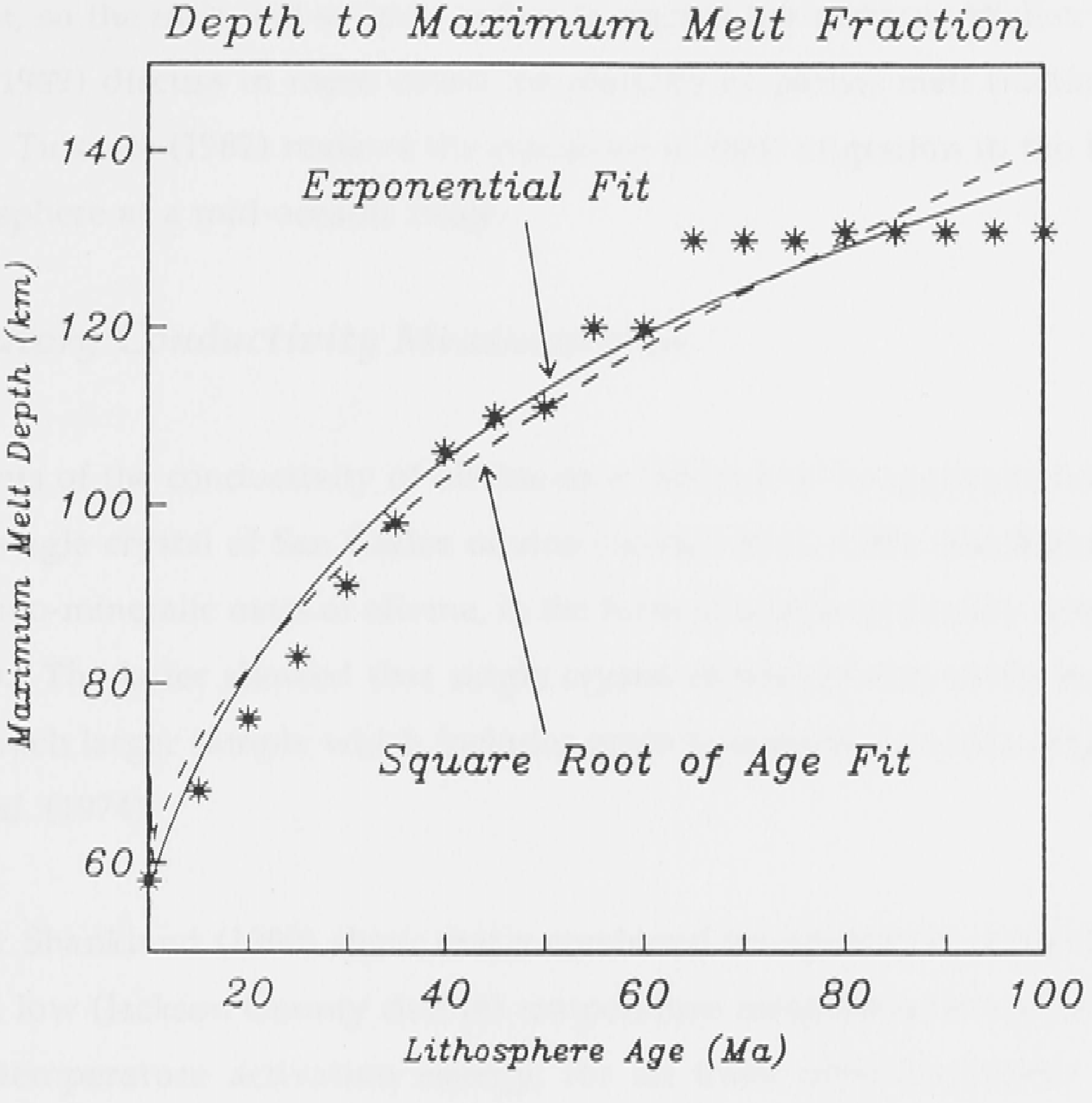

Figure 4.4 Depth (shown by asterisks) to the maximum melt fraction, shown in Figure 4.3, for lithospheric ages 10 to 100 Ma. The least squares exponential (solid line) and quadratic (dashed line) best fit lines are superimposed.

The upper-bound on the temperature at the base of the plate model of ~1600 C (see Table 4.1) is probably incompatible with the temperature at the $\alpha \rightarrow \alpha+\beta$ transition, providing that negative temperature gradients in Earth, if they exist, will be small (Anderson, 1982). Another possibility is that the temperature may only rise with the adiabat in the partial melt zone rather than the rise shown in Figure 4.2, which implies that convection is taking place. This is an unlikely lower-bound, but one which would invalidate the geotherms calculated from Parsons & Sclater (1977). If the lower-bound on the temperature at the base of the plate of ~1050 °C (see Table 4.1) is used, the geotherms will still intersect the wet solidus. The resulting percentages of partial melt are much smaller, less than 1 % , and the width of the partial melt zone confined between 90 to 140 km. If this is the case, then other factors must be used to explain the seismic attenuation at shallow depths in relatively young sub-oceanic lithosphere. Generating large fractions of partial melt (i.e. > 5 %) as shown in Figure 4.3, raises associated problems, such as the contradiction between this relatively high permeability and the low permeability required for geologically significant residence times. McKenzie (1989) argues that small melt fractions will separate from the matrix when there is more than 10^{-3} % melt present if their viscosity is 0.1 Pa s. Such melt movement cannot transfer heat, so the melt will solidify before it reaches the surface. Walker *et al.* (1978) and McKenzie (1989) discuss in more detail the stability of partial melt fractions in the upper mantle, and Turcotte (1982) reviews the processes of melt migration in the lithosphere from the asthenosphere at a mid-oceanic ridge.

4.4 Laboratory Conductivity Measurements

Measurements of the conductivity of olivine as a function of temperature have recently been made on a single crystal of San Carlos olivine (Schock *et al.*, 1989; Shankland & Duba, 1990) and on a mono-mineralic mass of olivine, in the form of a Jackson County dunite (Constable & Duba, 1990). The latter showed that single crystal measurements could be extrapolated to those of a much larger sample which includes grain boundaries, an idea originally suggested by Duba *et al.* (1974).

Constable & Shankland (1990) show that a combined interpretation of the high (San Carlos olivine) and low (Jackson County dunite) temperature measurements indicate that there is a single low-temperature activation energy, for all three crystallographic axes directions. This activation energy is fixed at 1.58 eV, which is a weighted average of the Red Sea Peridot and Jackson County Dunite fits published by Constable & Duba (1990). This activation compares favourably with a value of 1.49 eV obtained by Tyburczy & Roberts (1990) for sintered, polycrystalline San Carlos olivine, particularly when considering the alteration associated with the sintering process and the necessity to remove the resulting grain boundary conduction before an estimate can be made. Using a linear iterative Marquardt modelling method to determine the high temperature activation energy and coefficients (see eq. 1.78), the geometric mean of the conductivity in the three directions is approximately

$$\sigma = 10^{2.335}\, e^{-1.58\mathrm{eV}/kT} + 10^{9.10}\, e^{-4.19\mathrm{eV}/kT} \tag{4.1}$$

shown in Figure 4.5.

The conductivity of olivine is dependent upon iron content (e.g. Constable & Duba 1990). San Carlos olivine, which is the basis of Constable & Shankland's (1991) model, has an iron content of approximately 8.9 %. There is little compelling evidence to suggest that the fraction of iron varies much in the pyrolite upper mantle: Ringwood (1982) estimates fractions of 10.4 % for pyrolite and 8.8 % for harzburgite. Given the uncertainty in the iron content from petrological studies and that San Carlos olivine is a mantle derived material, no correction to the San Carlos olivine conductivities has been made.

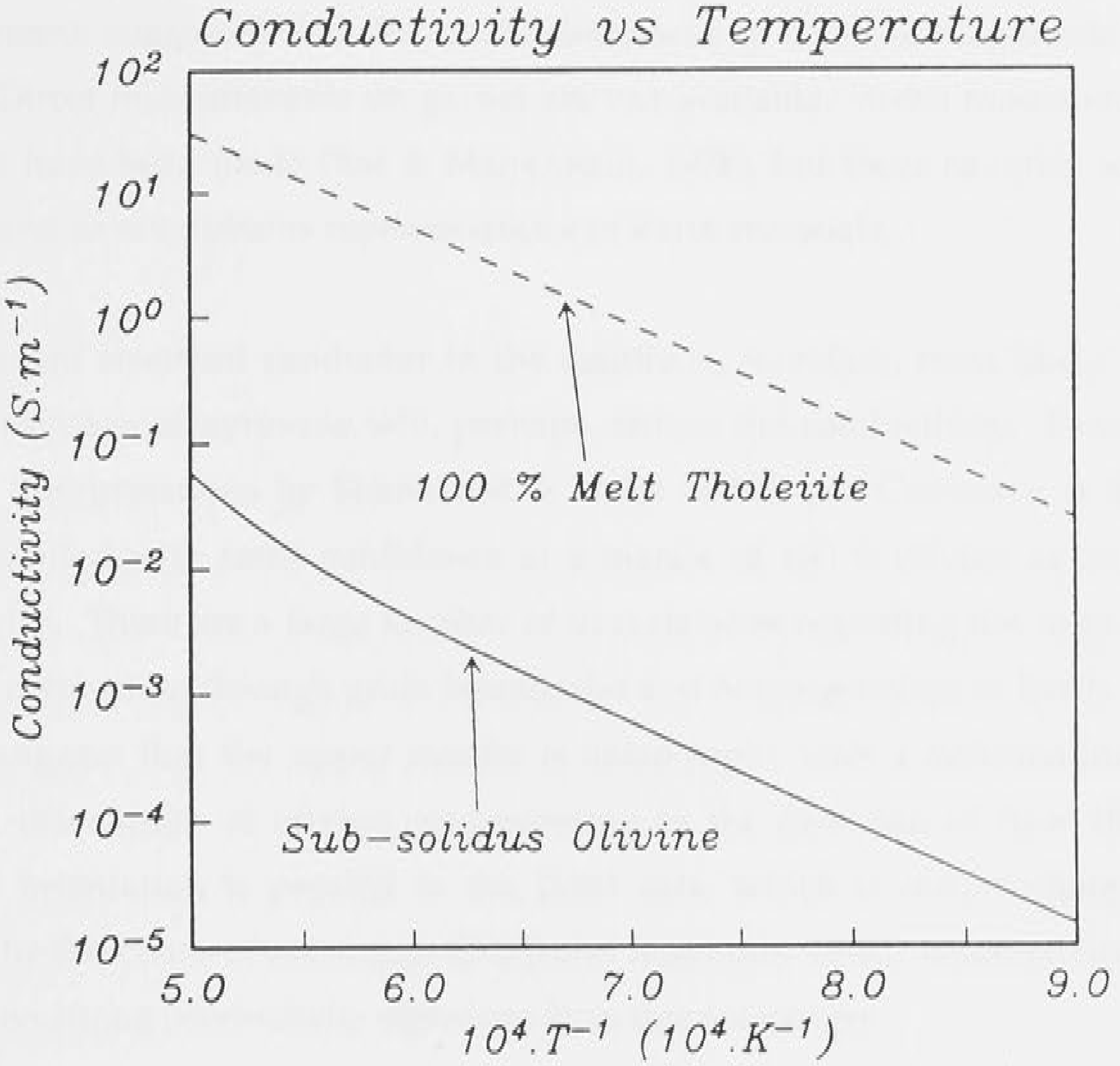

Figure 4.5 The conductivity of an isotropic polymorphic olivine based on the geometric mean of the fits to the three crystalline axes directions, from Constable & Shankland (1991) and a the conductivity of a tholeiite melt from Tyburczy & Waff (1983). The temperature ranges from 2000 °C to 1111 °C along the x-axis.

With the adopted pyrolite model of the mantle, petrological constraints allow estimates of the percentage of olivine ranging from 78 % for the residual harzburgite from 6 - 30 km depth, 65 % for the residual lherzolite from 30 to 40 km, and 57 % for the depleted pyrolite to the 400 km discontinuity (Ringwood, 1982). The principal accompanying minerals are orthopyroxene with smaller proportion of clinopyroxene and garnet. A high proportion of olivine has also been proposed by Bina & Wood (1987), who argue that an upper mantle containing 70 % olivine is required to satisfy P and S wave velocities at the 400 km discontinuity. The eclogite model of Anderson (1982) is not substantially different from the pyrolite model to a depth of 220 km. From 220 to 400 km, Anderson argues that eclogite must be present to account for seismic and free-Earth oscillation observations. Duffy & Anderson (1989) calculate percentages of olivine to be 40 % in the upper mantle, with 37 % clinopyroxene, 13 % garnet and 10 % orthopyroxene. The percentages of garnet and clinopyroxene are much higher than in the pyrolite model in the eclogite layer.

Little is known about the conductivity of pyroxene. Measurements by Duba *et al.* (1973) on an orthopyroxene suggested that the conductivity was an order of magnitude less than that of olivine. Direct measurements on garnet are not available. Some measurements of a garnet peridotite have been made (Rai & Manghnani, 1978), but these samples were crushed and sintered, and so are dubious representations of Earth materials.

The dominant electrical conductor in the mantle is, therefore, most likely to be olivine. A minor percentage of pyroxene will, perhaps, reduce the conductivity. Parameter estimation from the interpretations by Shankland & Duba (1990) and Constable & Shankland (1990) may be applied with some confidence to a mantle of 100 % olivine as an upper-bound of conductivity. There are a large number of uncertainties regarding the roles of the secondary minerals, conduction through grain boundaries and heterogeneities in Earth. Seismic velocity analysis suggest that the upper mantle is anisotropic, with a deformation-induced lattice preferred orientation of olivine concentrating in the direction of flow (Ribe, 1989). The preferred orientation is parallel to the [100] axis, which is intermediate in conductivity between the directions of maximum ([001]) and minimum ([010]) conductivity. Thus, there is probably no strong conductivity signature from this anisotropy.

Whilst the conductivity of olivine is strongly dependent upon temperature, another significant factor is the presence of partial melt (Shankland & Waff, 1977; Sato *et al.*, 1989). Figure 4.3 suggests that a small amount of partial melting of the Earth's mantle will occur, even allowing for a drop in temperature at the base on the plate model.

A tholeiite is not an unreasonable representative of partial melt in Earth's upper mantle, since this is in fact its origin. Tyburczy & Waff (1983) have measured the conductivity of a molten tholeiite to pressures equivalent to depths of 80 km. The dependence upon pressure drops rapidly above pressures of 10 kbars (40 km) above which the conductivity is primarily a function of temperature. The conductivity of tholeiitic melt above pressures of 9 kbars can be modelled reasonably well by an equation of the form (shown in Figure 4.5):

$$\sigma = 10^{5.332}\, e^{-1.533\mathrm{eV}/kT} \tag{4.2}$$

Experimental and theoretical thermodynamics, as well as petrological observations provide only limited constraints on the melt geometry in partially molten rocks. Many researchers choose the Hashin & Stricknam (1962) bounds for totally isolated and totally connected melt fractions (Waff, 1974; Shankland & Waff, 1977; Oldenburg *et al.*, 1984), but there is little compelling evidence to suggest that either of these geometries is feasible in a state of equilibrium. Schmeling (1986) provides a good overview of the variety of mixing formulations which have been postulated by various authors. Two models of melt geometry, which give possibly more realistic bounds on the conductivity, are now considered. The tube model of Grant & West (1965) is based upon a system containing fluid filled tubes along grain boundaries. This has a similar form to Waff's (1974) model for complete grain boundary wetting. For small amounts of melt ($b \leq 15$ %), the conductivity is given by:

$$\sigma = \frac{1}{3} b \, \sigma_m + (1 - b) \, \sigma_s \tag{4.3}$$

where σ_m and σ_s are the melt and solid phase conductivities respectively and b is the fraction of partial melt. This tube model is based on parallel mixing laws and its total interconnection of melt makes it analogous to the upper-bound of Hashin & Stricknam. However, interconnected tubes are probably more realistic than total grain wetting models, particularly for hydrostatic rather than lithostatic fluid pressure.

Another common formulation is based on Archie's Law, which was later modified by Hermance (1979) to account for the finite conductivity of the sub-solidus phase of olivine at mantle temperatures:

$$\sigma = \sigma_s + (\sigma_m - \sigma_s) \, b^{\dagger} \tag{4.4}$$

The exponent ($\dagger$) has been demonstrated to be ~2 for a wide variety of rock types and porosities (Brace *et al.*, 1965). Archie's Law is applicable to fluids which are only partly interconnected; modifications invariably improve the efficiency of conduction, and so Archie's Law with an exponent of 2 is probably a realistic lower-bound on conductivity for a given porosity. Calculations by Madden (1976) indicate that the conductance of the interconnected pores will increases with decreasing pressure at upper mantle pressures. An exponent of 1.5 in eq. 4.4 is suggested as an appropriate estimate for conductivity of a partial melt zone in the upper mantle. Figure 4.6 shows the variations in conductivity as a function of partial melt fraction, for olivine at a temperature of 1200 °C, using the Hashin & Stricknam bounds, the complete grain boundary wetting model, the tube model (eq. 4.3), and Archie's Law formulations (eq. 4.4) with exponents of 1.5 and 2. Sub-solidus and melt conductivities are given in eqs 4.1 and 4.2. The curves for the tube melt and complete grain boundary wetting model are only applicable for melt fractions less than 15 %.

Karato (1990) argues that a high conductivity layer in the asthenosphere can be attributed to solid-state conductivity in olivine, if there is a small amount of hydrogen present. Hydrogen would enhance the upper mantle conductivity without causing extensive melting in much of the asthenosphere. As hydrogen is mobile in the [100] axis in olivine, only a modest amount of hydrogen, with H/Si content between 200 and 2000 parts per million (p.p.m.), would be sufficient to account for conductivities in the asthenosphere of 0.1 and 0.01 $S.m^{-1}$.

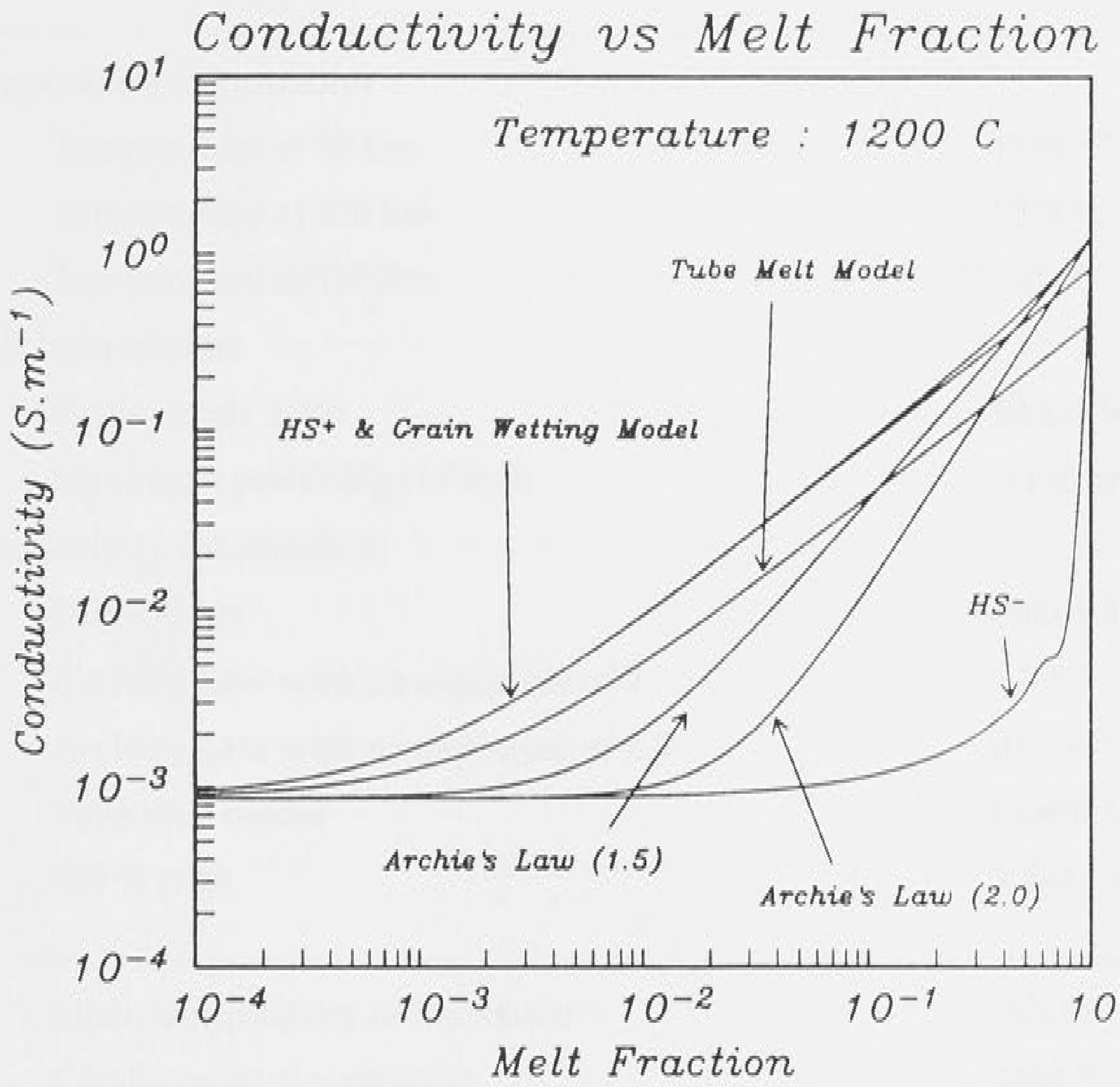

Figure 4.6 The electrical conductivity of a partial melt, based on the conductivities of sub-solidus olivine and tholeiite melt at 1200 °C, using different assumed melt geometries. For less than 5 % melt (melt fraction 5×10^{-2}), Archie's Law with an exponent of 2 and the tube model are proposed as being more reliable bounds on the electrical conductivity than the Hashin & Stricknam bounds HS^+ and HS^-.

Such amounts of hydrogen are below that which would cause extensive partial melting, and avoid the mechanical and petrological stability problems associated with interconnected fluid phases maintained over large distances in the upper mantle for long geological times. A review of the evidence for hydrogen enhanced conductivity is given by Hirsch (1990).

Table 4.2 lists the difference in conductivity over the partial melt zone for 20 Ma sub-oceanic lithosphere. If the model of Liu (1989) is used in which the low-velocity zone represents a region of free H_2O, the conductivity would still show a rapid increase, as the conductivity of water is comparable to that of partially molten tholeiite. Liu (1989) estimates a percentage of H_2O of less than 0.5 %, and it is likely to have the same effect on electrical conductivity as the fraction of partial melt calculated from Parson & Sclater's curves.

Table 4.2 Temperature, conductivity and melt parameters for 20 Ma lithosphere

20 Ma Lithosphere	
Temperature Information	
Temperature at 50 km	1128 °C
Temperature at 100 km	1328 °C
Temperature at 150 km	1337 °C
Melt Information	
Partial melt zone	53 to 154 km
Maximum percentage of melt	4.4 % at 75 km
Conductivity Information	
Sub-solidus	0.0019 $S.m^{-1}$ at 75 km
Archie's Law with an exponent of 2	0.0071 $S.m^{-1}$ at 75 km
Archie's Law with an exponent of 1.5	0.0265 $S.m^{-1}$ at 75 km
Tube melt model	0.0407 $S.m^{-1}$ at 75 km
100 % melt	2.6262 $S.m^{-1}$ at 75 km
Mean conductivity of melt zone	0.0147 $S.m^{-1}$
Conductance of melt zone	1494.5 S

Piwinskii & Duba (1974) observe that if a sodium-rich feldspar is kept just below its melting point for a sufficiently long time, the conductivity increases to that of the melt. If minerals more representative of Earth's deep interior exhibit the same characteristics, then a sub-solidus mantle may have the high conductivities observed by Oldenburg (1981), without the presence of melt or volatiles. However, Duba & Shankland (1990) report that a single crystal of San Carlos olivine held at 1200 °C and 1500 °C for 12 hours and 2 hours respectively show insignificant changes in conductivity with time. The temperature of the low-velocity zone is between 1100 and 1300 °C, so it appears that this hypothesis for the high conductivities is unsupported.

It is not really possible to estimate uncertainties caused by mantle pressures on the conductivity of olivine. Dvorak (1973) and Duba *et al.* (1974) conclude that the pressure effects are small, probably because there are two conduction mechanisms in olivine whose pressure effects oppose each other. Omura *et al.* (1989) report that measurements at constant temperatures and various pressures show a decrease in conductivity for sintered olivine samples of Fe percentages 10.4 %, representative of a pyrolite mantle

4.5 The Conductivity Structure of the Upper Mantle

A best estimate of the conductivity structure beneath the seafloor as a function of age is shown in Figure 4.7. Based on a sub-solidus olivine mantle, the calculations predict conductivities of less than 10^{-6} $S.m^{-1}$ for the cooler, uppermost mantle. One would not expect such low conductivities to be obtained in real Earth, but rather limited by trace amounts of H_2O or other phases. The upper part of the lithosphere was estimated by Cox *et al.* (1986) to have a resistivity-thickness product of the order of 10^9 $\Omega.m^2$, from controlled source experiments on 25 Ma seafloor, with a maximum conductivity of 3×10^{-5} $S.m^{-1}$. Cox *et al.* (1986) use this conductivity to argue for the presence of volatiles, inferring a volatiles content of $\leq$ 0.1 %. Such a percentage of volatiles is consistent with most petrological estimates (Ringwood, 1975). Thermally activated mineral conduction of olivine begins to dominate at depths varying from 30 to 90 km, implying a resistivity-thickness product ranging from 9.0×10^8 $\Omega.m^2$ and 2.7×10^9 $\Omega.m^2$ for sub-oceanic lithosphere of age 10 Ma to 100 Ma (Table 4.3).

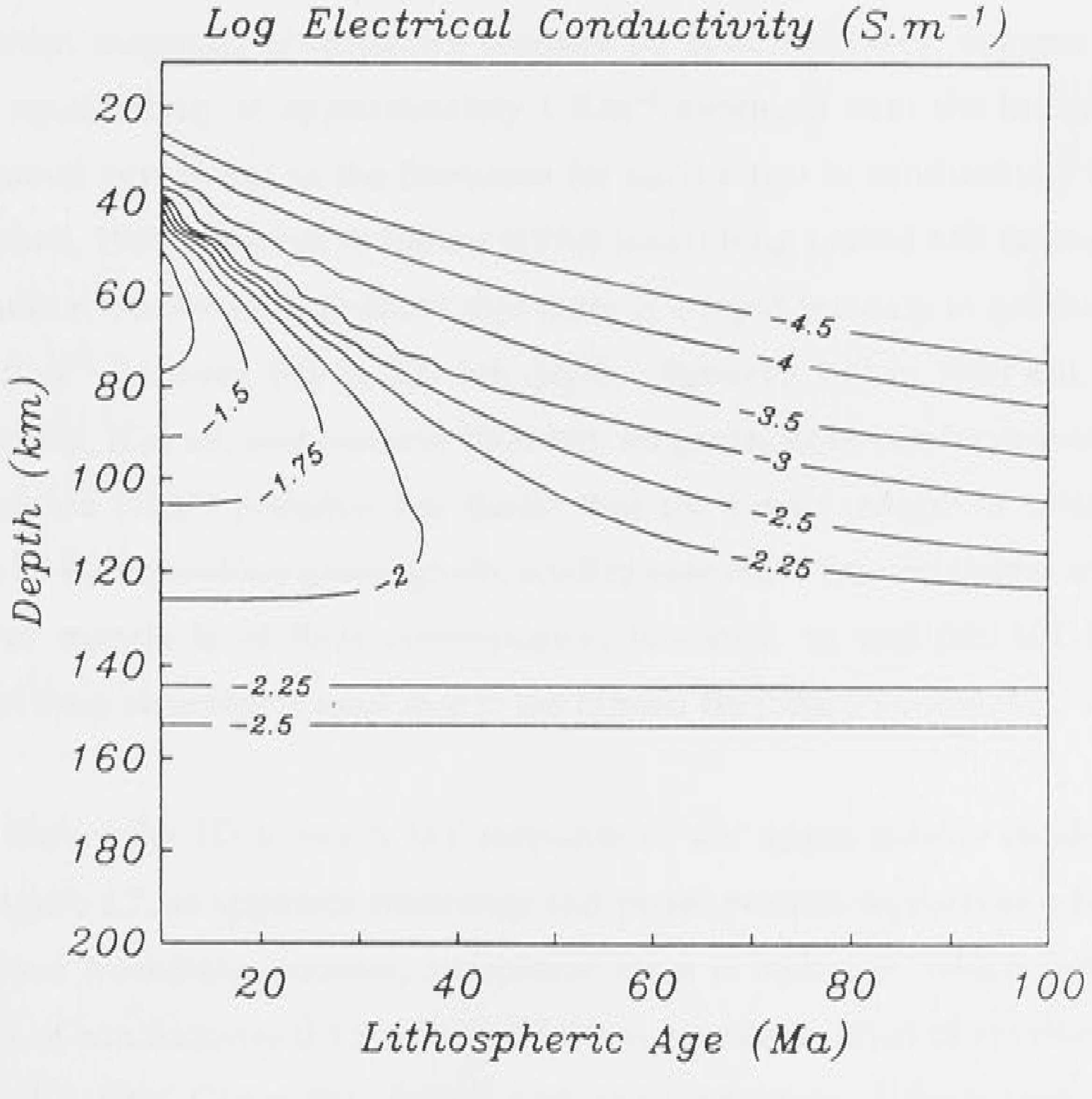

Figure 4.7 Proposed conductivity structure of the upper mantle from laboratory data, using Archie's Law with an exponent of 1.5 for the partial melt zone. The uppermost lithosphere has a conductivity set at 3×10^{-5} $S.m^{-1}$, which corresponds with a Log_{10} conductivity of ~-4.5, or equivalently $\leq$ 0.1 % volatiles content (Cox *et al.*, 1986)

Table 4.3 Resistivity-thickness product for sub-oceanic lithosphere 10 to 100 Ma

Age (Ma)	RT ($\Omega.m^2$)	Age (Ma)	RT ($\Omega.m^2$)
10	5.1×10^8	60	1.63×10^9
20	8.3×10^8	70	1.78×10^9
30	1.07×10^9	80	1.91×10^9
40	1.28×10^9	90	2.02×10^9
50	1.46×10^9	100	2.12×10^9

Below the partial melt zone, the conductivity is lower, and rises gently with the adiabat to the $\alpha\rightarrow\alpha+\beta$ transition zone beginning at 390 km, where an increase in temperature due to latent heat of phase change superimposed on the adiabat would occur. Experimental measurements have been made on the conductivity of spinel (Akimoto & Fujisawa, 1965), but the results are probably not reliable (Duba, 1976). The recent inversions of equivalent MT estimates from magnetic observatory records by Schultz (1990), suggest that there is an increase in conductivity to approximately 1 $S.m^{-1}$ averaged over the interval 400 to 670 km. There is general agreement in the literature for such a rise in conductivity (e.g. Banks, 1969, 1972; Campbell, 1987). Booker & Egbert (1990) invert long period MT estimates (10^4 to 10^7 s) from the Tuscon Observatory to show that there is a rapid increase in conductivity from < 0.1 $S.m^{-1}$ to 1 $S.m^{-1}$ between 600 to 900 km depth. Between 900 to 1500 km, the conductivity increases slowly, if at all, and beneath 1500 km, no conclusions can be drawn. A recent paper by Li & Jeanloz (1987) presents the thesis that the lower mantle is relatively insulating, much more so than previous geomagnetic studies suggest. The uncertainty in the conductivity of the lower mantle is of little consequence, however, to seafloor MT estimates, as the resolution of deep structure is poor due to the limited frequency bandwidth.

Figure 4.8 shows the 1D forward MT response of the upper mantle conductivity structure shown in Figure 4.7, as apparent resistivity and phase pseudo-sections as a function of period. In the forward modelling exercise, an oceanic crust is included, which consists of 600 m of pillow lavas of conductivity 0.1 $S.m^{-1}$ and 5400 m of oceanic crust of conductivity 0.001 $S.m^{-1}$ (Becker *et al.*, 1982; Constable, 1990), and the uppermost lithosphere has a minimum conductivity of 3×10^{-5} $S.m^{-1}$. These are not true 2D pseudo-sections, as they are compiled from contoured 1D profiles, however they clearly illustrate the changes in MT parameters with age.

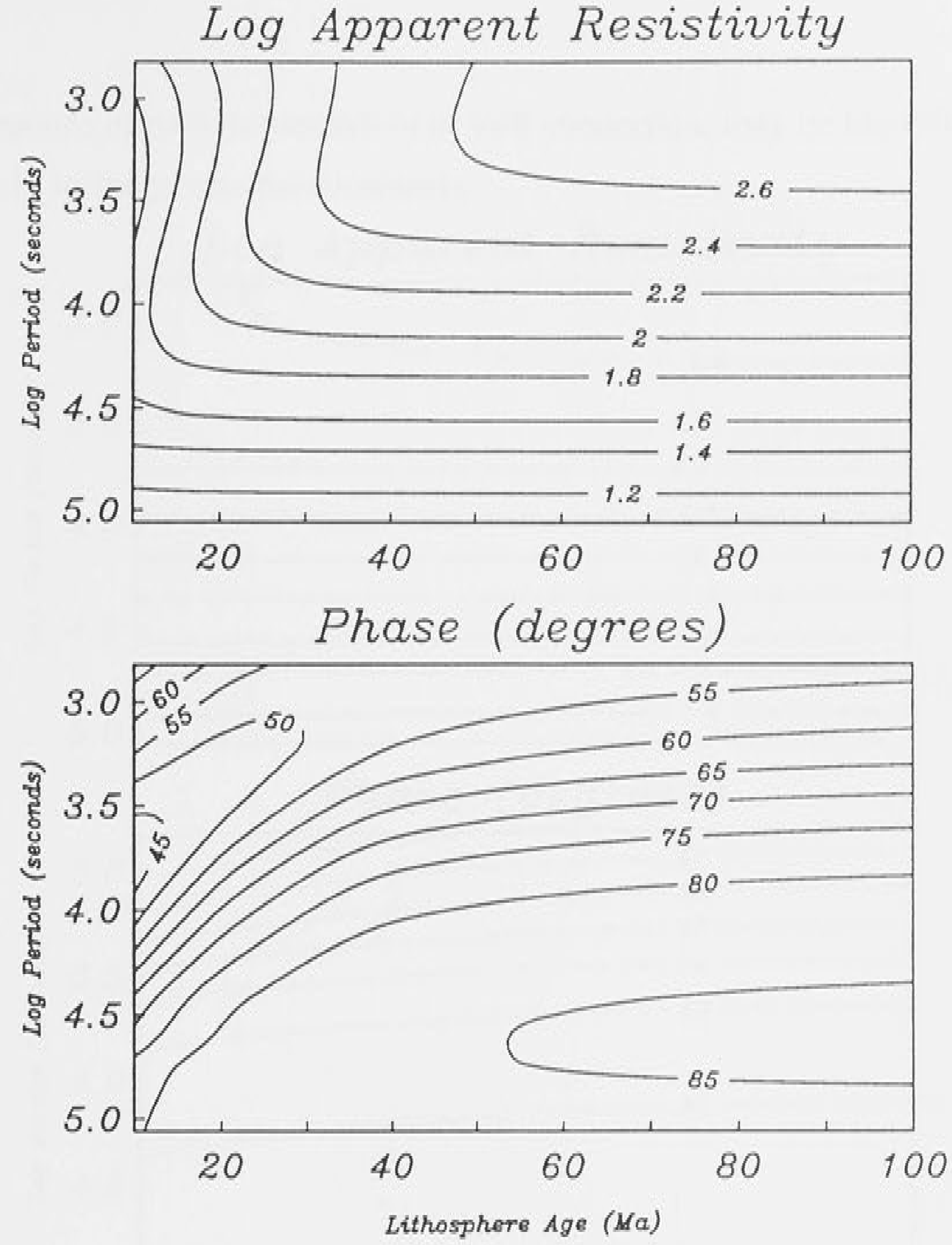

Figure 4.8 Pseudo-sections of apparent resistivity and phase as a function of period, from 1000 to 100000 s, for ages of lithosphere ranging from 10 to 100 Ma. The pseudo-sections are constructed from the forward modelled 1D response of the upper mantle structures shown in Figure 4.7, with a 5.4 km thick oceanic crust of sheeted dykes ($\sigma = 0.001$ S.m^{-1}) and 600 m of pillow lavas ($\sigma = 0.1$ S.m^{-1}).

It is worth remarking that for lithosphere of age greater than 40 Ma, the differences between the forward MT responses are only noticeable at the shortest periods of less one hour (Log period = 3.55), and indeed would probably not be resolved with real seafloor data with errors of the order of 5%.

Figure 4.9 shows pseudo-sections of apparent resistivity and phase, constructed in the manner described above, for a model of the conductivity in which there is no partial melt zone. By comparing Figures 4.8 and 4.9, it is apparent that the presence of a small fraction of poorly connected melt cannot be determined unambiguously for lithosphere older than 40 Ma *from this particular conductivity model* except for MT estimates at periods less than one hour. However, if the melt is connected along grain boundaries, small fractions may be detected for all ages of seafloor and at much longer periods than one hour. For lithosphere younger than

40 Ma, the presence of melt, independent of melt connection, may be identified from seafloor MT, particularly in the phase measurements.

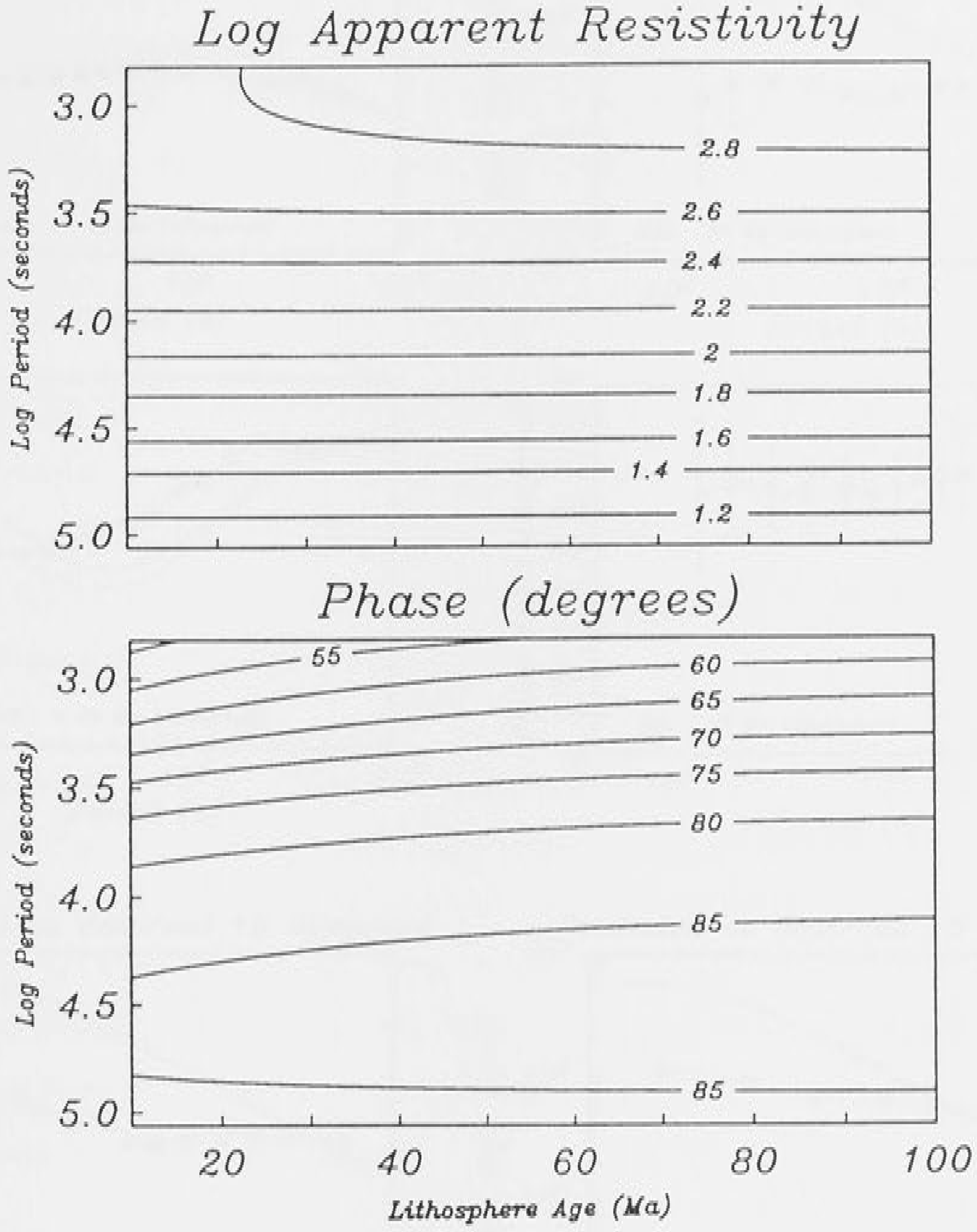

Figure 4.9 Similar pseudo-sections as constructed for Figure 4.8, however it is now assumed that the upper mantle is 'dry', and that the geotherms do not intersect the 'dry' mantle solidus of Takahashi (1986), so there is no melt generated.

4.6 Comparison of Seafloor MT Data and Predicted MT Response

Many authors have calculated, albeit with caution, fractions of partial melt and temperatures from MT sounding data (e.g. Oldenburg *et al.*, 1984; Law & Greenhouse, 1981; Wannamaker *et al.*, 1989b) which are often larger than predicted by the laboratory derived profiles, and also larger than can be supported by other geophysical techniques, particularly seismic velocity analysis (Sato *et al.*, 1989). Secondary conduction mechanisms at grain boundaries (Shankland & Duba, 1977), volatiles (Tarits, 1986) and hydrogen ions (Karato, 1990) in a sub-solidus mantle have been advanced as possible explanations to account for the differences.

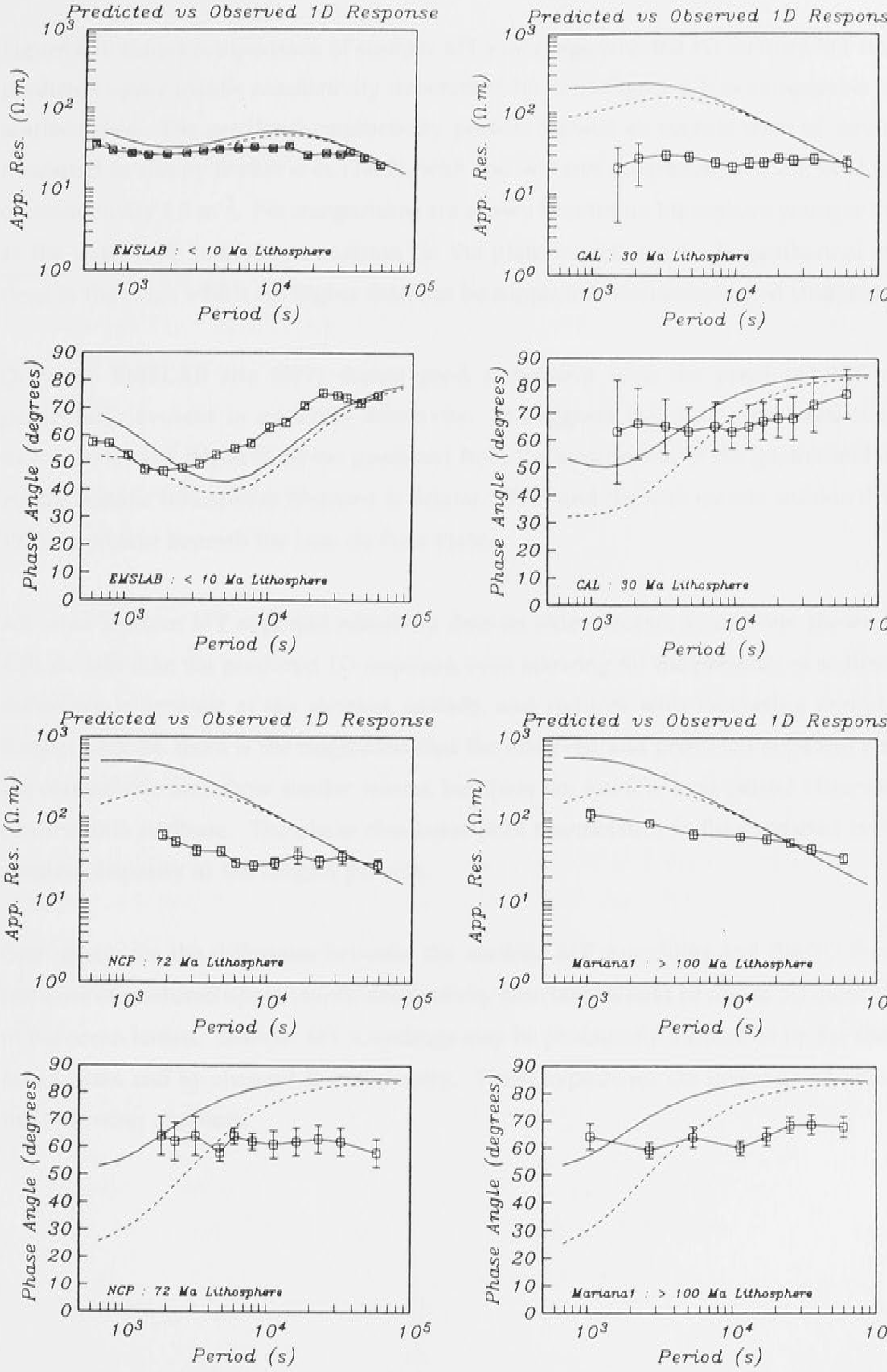

Figure 4.10 Comparison between (a) EMSLAB site SF7 (< 10 Ma), (b) CAL (30 Ma) (c) NCP (72 Ma) and (d) Mariana Fore-arc basin (> 100 Ma) apparent resistivity and phase data and predicted 1D response above oceanic upper mantle without any sediments (solid line) and with 500 m sediments (dashed line).

Figure 4.10 shows comparisons of seafloor MT soundings with the 1D forward MT response of predicted upper mantle conductivity structures (shown in Figure 4.7) of comparable age to the seafloor sites. The predicted conductivity profiles include an oceanic crust of conductivities measured *in situ* by Becker *et al.* (1982), with and without the presence of 500 m of sediments of conductivity 1 $S.m^{-1}$. No comparisons are shown for sites on lithosphere younger than 5 Ma, as the unrealistic boundary condition (in the plate model) results in geothermal structures close to the ridge which are higher than can be supported from petrological studies of MORB.

Only the EMSLAB site (SF7) shows good agreement with the predicted MT response, particularly evident in apparent resistivity. It suggests that the large fraction of partial melt (~10 %) at a depth of 60 km predicted from the intersection of the geothermal models of young oceanic lithosphere (Parsons & Sclater, 1977) and the wet mantle solidus (Ringwood, 1975) is present beneath the Juan de Fuca Plate.

All other seafloor MT apparent resistivity data on older oceanic lithosphere shown in Figure 4.10 are less than the predicted 1D response, even allowing for the presence of sediments. The difference is greatest at the shortest periods, and reduces with increasing period. At the longest periods, there is the suggestion that the observed and predicted apparent resistivities are comparable and show similar trends, but there are too few long period observed data to confirm this attribute. The phase also bears little resemblance to the predicted curves, with greatest disparity at the longest periods.

One reason for the difference between the seafloor MT soundings and the 1D forward MT response of predicted upper mantle conductivity structures would be due to 3D induction effects in the ocean basins. Seafloor MT soundings may be profoundly influenced by the shape of the ocean basin and by changes in bathymetry. These hypotheses are investigated more fully in the following chapters.

Chapter 5 : Thin-Sheet Modelling of Coastlines, Ocean Basins and Seafloor Topography

5.1 Numerical Modelling Approximations

5.1.1 Introduction

Attention now turns to the construction of suitable thin-sheet models for Earth's ocean basins. The thin-sheet approximations listed in section 3.4 must be fulfilled, to satisfy both the sheet boundary conditions, and the approximations which result from representing surface conductors by a grid of discrete conductance values. These conditions can be examined separately: the former are defined by analytical expressions, which must be satisfied for the thin-sheet approximation to be valid; while the latter are more qualitative in nature, and require analysis of forward model studies.

5.1.2 Thin-Sheet Electromagnetic Boundary Conditions

Price's (1950) equation is at the heart of the thin-sheet approximation, and must be satisfied for the method to be applicable. This condition is satisfied by ensuring that the sheet has negligible thickness in comparison to the skin depth in the underlying layer or half-space, and also negligible thickness compared to the skin depth within the sheet itself.

The electrical conductivity of sea-water is several orders of magnitude greater than typical estimates of lithosphere conductivity, and seafloor EM observations of natural source-fields are typically in the period range 1000 to 100000 s. Table 5.1 shows skin depths in salt water and in the lithosphere, for external plane-wave source-fields of periods 1000, 10000 and 100000 s.

Table 5.1 Skin depth calculations for sea-water, sediments, oceanic crust and upper mantle.

Layer	Thickness (m)	Conductivity ($S.m^{-1}$)	Skin Depth (km) 1000 s	10000 s	100000 s
Sea-water	5000.	3.3	8.7	27.5	87.0
Sediments	1000.	1.0	15.8	50.0	158.1
Pillow Lava	600.	0.1	50.0	158.1	500.0
Sheeted Dykes	5400.	0.001	500.0	1581.1	5000.0
Upper Mantle	-	~0.00001	5000.0	15811.4	50000.0

Thin-sheet conductance, τ(r), is defined as the integrated conductivity across the thickness of the sheet, expressed as

$$\tau(\mathbf{r}) = \lim_{\delta \to +0} \int_{-0}^{\delta} \sigma(\mathbf{r},z)\, dz \tag{5.1}$$

where $\sigma(\mathbf{r},z)$ is the conductivity in the sheet for $0 < z < \delta$. In the case of a thin-sheet ocean, the conductivity $\sigma(\mathbf{r},z)$ is almost constant, but the ocean has variable depth. In such cases, the integrated conductivity is calculated from the formula

$$\tau(\mathbf{r}) = \sigma\, d(\mathbf{r}) \tag{5.2}$$

where $d(\mathbf{r})$ is the depth of the ocean at position $\mathbf{r}$, and σ is the conductivity of sea-water. Thus, the thickness of the sheet is determined by the depth of the ocean. Parsons & Sclater (1977) show that in the north Pacific and north Atlantic, ocean depths are generally less than 6 km, except at subduction zones, where the ocean depth may approach 11 km. If sediments, or both sediments and an oceanic crust, are included in the sheet, they will increase the sheet thickness.

At an inducing period of 1000 s, the skin depth in sediments is 16 km, while the thickness of an ocean thin-sheet is at most 6 km; in such cases, the thin-sheet approximation is not satisfied, as the sheet thickness is 38 % of the skin depth, whereas Weaver (1982) recommends a maximum of 15 %. However, if sediments are included in the thin-sheet, then the approximation is satisfied. The skin depth in pillow lavas is 50 km at a period of 1000 s, which is almost an order of magnitude greater than the thickness of the sheet. Furthermore, if the entire oceanic crust is also included within the thin-sheet, the skin depth within the upper mantle is two to three orders of magnitude greater than the thickness of the thin-sheet.

The skin depth within the thin-sheet for sea-water is 8.7 km at a periods of 1000 s, and the maximum ocean depth is approximately 6 km. For the thin-sheet approximation to be justified, the square of the skin depth in sea-water must be substantially greater than the square of the thickness of the sheet (eq. 3.14). This condition is just satisfied with these parameters, although such parameters represent an upper-bound on the ratio of sheet thickness to skin depth. At longer periods, and for shallower oceans, the thin-sheet approximation is appropriate. If sediments are included within the sheet, then the sheet thickness may be greater than the skin depth of sea-water at the shortest periods, invalidating the thin-sheet approximation. However, few areas of seafloor actually approach conditions that do not satisfy the thin-sheet approximation at the periods appropriate for seafloor EM observations. Table 5.2 shows the mean depth and sediment thickness, as a function of age, for profiles in the north Atlantic Ocean, south of 34° N, taken from Parsons & Sclater (1977).

Table 5.2 Mean depth and sediment thickness versus lithospheric age in the north Atlantic Ocean, south of 34° N.

Age (Ma)	Mean Depth (m)	Mean Sediment Thickness (m)	Age (Ma)	Mean Depth (m)	Mean Sediment Thickness (m)
0	2582	-	90	5409	280
10	3395	40	101	5442	388
38	4500	95	109	5427	410
53	4889	121	117	5340	587
63	5118	143	137	5333	806
72	5298	199	143	5371	817
82	5331	225	153	5389	1172

5.1.3 Finite Grid Approximations

A limit of 30 x 30 grid-nodes for a thin-sheet model is imposed by computer resources. The distance between adjacent nodes must be considerably less than the skin depth in the underlying layer: Weaver (1982) suggests that the grid spacing should be less than 33 % of the skin depth. Ocean basins are of distance-scales of several thousand kilometres; thus, spacing between grid-nodes is usually of order several hundred kilometres and therefore skin depths must be three or more times larger. Skin depths in sediments are of order tens of kilometres, so clearly cannot be included in the layered half-space beneath the thin-sheet. Furthermore, the skin depth in the oceanic crust is too small at periods less than 10000 s. The large skin depths required to satisfy this criterion imply that for almost all thin-sheet models of ocean basins, the layered half-space can be composed only of the mantle. Omission of oceanic crust from a thin-sheet model of an ocean basin is not of major significance, as it has similar conductivity to the upper part of the mantle. In contrast, sediments have a conductivity approaching that of sea-water, and may profoundly distort the MT response on the seafloor at short periods. The conductance of sediments can be incorporated into the sheet, but this procedure has the disadvantage that the EM fields are then calculated at the base of the sediments, rather than at the seafloor.

Sharp conductance contrasts in the sheet parallel to the grid margins, such as an ocean - continent boundary, should be kept well away from the edges of the grid. Conductance changes in the sheet perpendicular to the grid margins are, of course, permitted, as the solution at the grid edge may approach the 2D TE and TM solution, given by McKirdy & Weaver (1984). This criterion is the most difficult to satisfy, as grid edge effects depend upon how rapidly anomalous fields perpendicular to the coastline attain a uniform gradient, to satisfy the Neumann boundary conditions of vanishing outward gradient on the grid boundary. Agarwal & Weaver (1990) suggest that a skin depth or more away from the edge of the grid is required, which implies that for ocean basin models, there should be several thousand kilometres of land or ocean between the grid edge and the coastline.

5.1.4 Thin-Sheet Model Construction

Thin-sheet models are constructed to calculate the forward response of simple 1D and 2D ocean - continent geometries. Whilst it is advantageous to examine a wide range of thin-sheet models at different inducing periods to check numerical accuracy, in practice the computation time restricts examination to models which are relevant to seafloor EM studies.

The basic thin-sheet model used in testing 1D and 2D structures is defined as follows. The inducing magnetic field **B** at the interface between the thin-sheet surface and the insulating half-space is of infinite wavelength, sinusoidal with period 10000 s, and with maximum amplitude 100 nT. As seafloor EM observations of natural source-fields have a bandwidth of approximately 1000 to 100000 s, the period 10000 s falls about midway on the log scale. In general, seafloor MT estimates at this period are well resolved, as signal is well above noise level and oceanic source-fields are relatively small. The basic thin-sheet model has grid-node spacing of 200 km, so that a grid of 15 x 15 nodes covers an area of 8×10^6 km^2.

In these model studies, emphasis is placed on the EM induction effects at passive margins, as the layered half-space must extend beneath both oceanic and continental crusts. The age of the oceanic crust at passive margins is generally older than 40 Ma; Figure 4.7 shows that the conductivity structure is not substantially different for lithosphere older than this. A layered half-space, listed in Table 5.3, is derived from the model of conductivity structure for 70 Ma oceanic lithosphere shown in Figure 4.7. In the testing of 1D and 2D structures, this layered model forms the half-space beneath the 1D or 2D thin-sheet. Also listed in Table 5.3 are approximate bounds placed on the conductivity from interpretation of observed EM data on land and seafloor, and from the uncertainty of the parameters used to construct the model in chapter 4.

Table 5.3 Parameters for an Earth conductivity profile below lithosphere of age 70 Ma.

Description	Conductivity ($S.m^{-1}$)	Uncertainty Range ($S.m^{-1}$)	Thickness (m)	Depth to Base (m)
Surface Thin-Sheet:				
Continental crust	0.001	$1x10^{-1}$ to $1x10^{-5}$	5000	5000
Sea-water	3.3	5.0 to 3.2	5000	5000
Layered Half-Space:				
Upper lithosphere	0.00003	$3x10^{-3}$ to $3x10^{-6}$	58000	63000
Lithosphere	0.003	?	16000	79000
Asthenosphere	0.005	$3x10^{-3}$ to $1x10^{-1}$	52000	131000
Upper mantle (adiabatic)	0.003	?	254000	385000
Upper mantle (transition zone)	0.2	?	280000	665000
Lower Mantle	1.0	$5x10^{-1}$ to $5x10^{+0}$	∞	∞

5.1.5 One-Dimensional Model Analysis

As shown in chapter 1, the forward 1D EM induction problem has an analytical solution, from which the attenuation of electric and magnetic fields through the layered half-space can be calculated. A 1D thin-sheet model is simple to construct, by specifying a sheet of uniform conductivity, and thus forward-modelled EM fields at the top and bottom of the thin-sheet may be compared with the analytical response for the same structure.

The conductivity of the upper lithosphere has profound consequences for the interpretation of seafloor EM data (Cox, 1981): estimates from previous seafloor and coastal studies have ranged from greater than 10^{-3} $S.m^{-1}$ to less than 10^{-5} $S.m^{-1}$. Thin-sheet modelling can be used to forward model such hypotheses; however, it is also important to consider systematic errors which may arise from numerical inaccuracies. Four models are now considered, with upper lithosphere conductivities of $3x10^{-3}$ $S.m^{-1}$ to $3x10^{-6}$ $S.m^{-1}$, covering the range of observed estimates. Figure 5.1 shows the attenuation of the horizontal magnetic field **B** through an ocean of depth 5 km, underlain by a layered electrical structure representative of 70 Ma lithosphere, as tabulated in Table 5.3. Figure 5.2 shows similar calculations for the thin-sheet forward models with the same electrical structure.

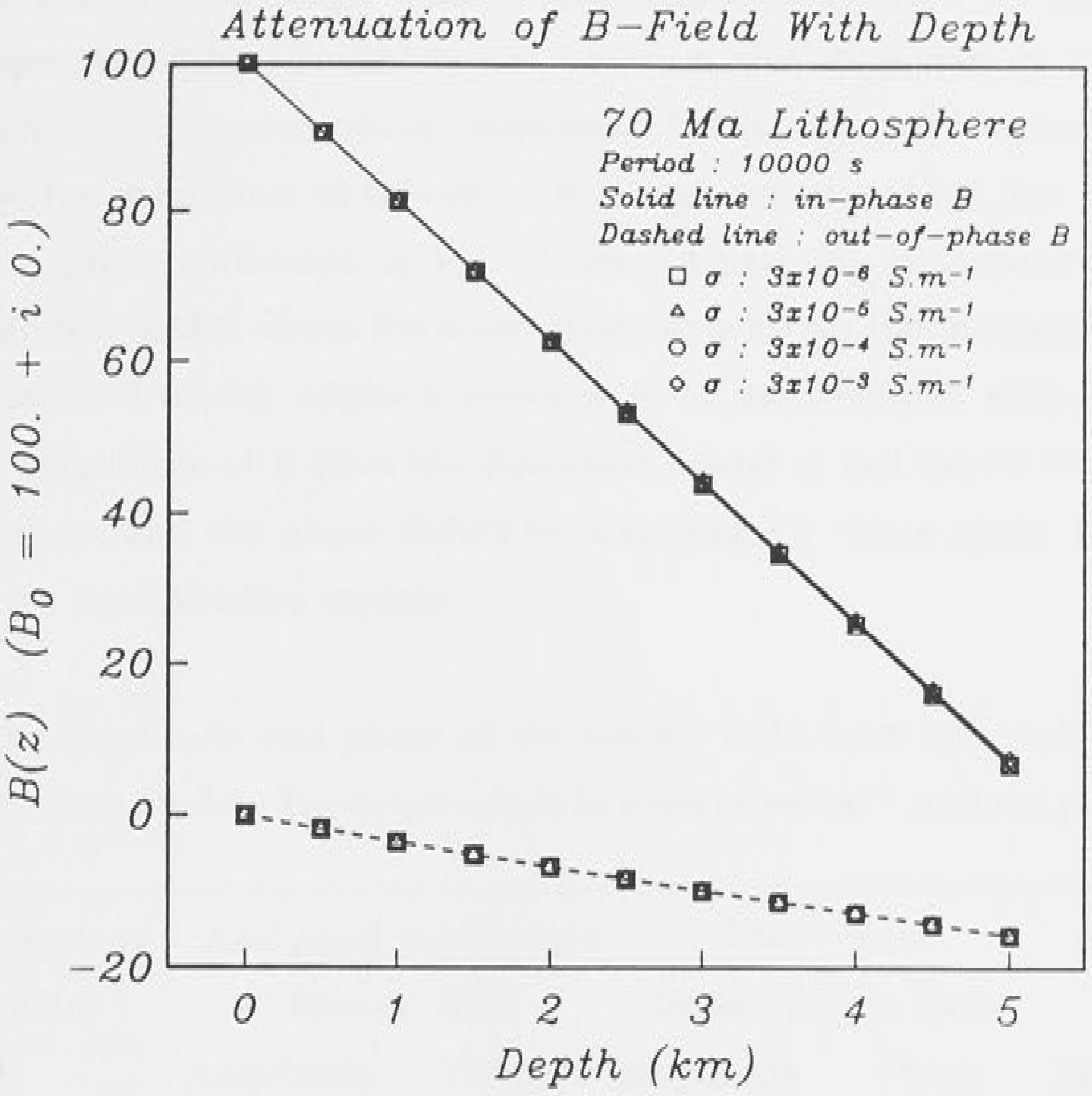

Figure 5.1 Analytic calculation of the attenuation of horizontal magnetic field **B** from a surface amplitude 100 nT through an ocean of depth 5 km, for four cases of upper lithospheric conductivity in a layered Earth.

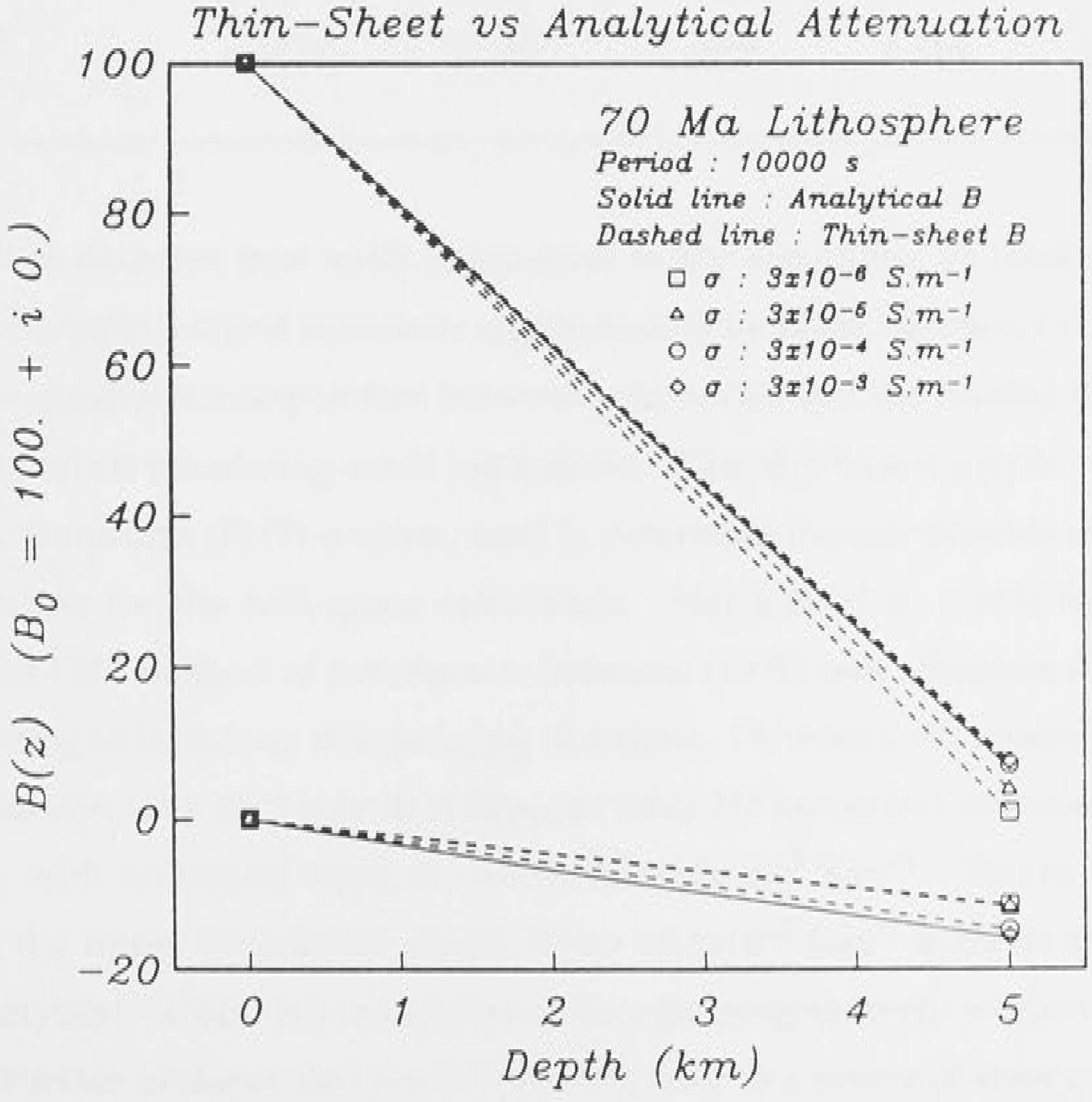

Figure 5.2 Thin-sheet results for comparison with the analytic calculations of Figure 5.1.

The analytical calculations show there is little difference between the attenuation of **B** for different upper lithosphere conductivities, however, thin-sheet models show an increasing systematic error as the conductivity decreases. For an upper lithosphere of $3\text{x}10^{-6}$ S.m^{-1} conductivity, the magnitude of thin-sheet **B** is approximately 33 % less than the analytical value, with a phase difference of 18°. Table 5.4 lists the magnitude and phase of the horizontal electric field **E** across the ocean layer from the analytical model, and **E** calculated from the thin-sheet model, which is assumed to be unattenuated with depth through the ocean. The magnitude of **E** from the thin-sheet model is less than 5 % different from the analytical values, and the phase differs by less than 4°. Once again, the differences are greatest for the most resistive models.

Table 5.4 The amplitude and phase of the electric field from analytical calculations, and from the thin-sheet model. The amplitude is in units of mV.m^{-1}, and the phase is in degrees.

Upper Lithosphere Conductivity (S.m^{-1})	Analytical Sea-Surface Electric Field		Thin-Sheet Ocean Electric Field		Analytical Seafloor Electric Field	
	Amplitude	Phase	Amplitude	Phase	Amplitude	Phase
$3\text{x}10^{-6}$	4.5916	10.87	4.7675	6.535	4.5377	8.85
$3\text{x}10^{-5}$	4.5912	10.87	4.6378	6.885	4.5373	8.85
$3\text{x}10^{-4}$	4.5877	10.86	4.4989	8.977	4.5339	8.84
$3\text{x}10^{-3}$	4.5527	10.83	4.4827	9.515	4.4992	8.78

It is difficult to examine how such errors arise in the algorithm, as there are many possible sources; for example integral equations approximated by finite Simpson's rule summations, bi-linear and bi-quadratic interpolation between grid-nodes and the limited numerical precision of computers when calculating small parameters. One significant source of error may be the Fast Hankel Transform (FHT) routine, used to determine the components of the layered space correction terms for the half-space calculation. McKirdy *et al.* (1985) found that a simple version of the FHT method of Johansen & Sørensen (1979) was adequate for a 2D test model, without needing to introduce interpolating functions. However, the model configuration used in the comparison with McKirdy & Weaver's (1984) 2D numerical solution comprised a two-layer Earth, with an upper layer of conductivity $8\text{x}10^{-3}$ S.m^{-1}. Figure 5.2 shows that the model with the upper lithosphere conductivity of $3\text{x}10^{-3}$ S.m^{-1} exhibits excellent agreement with the analytical values, but comparisons become progressively worse with more resistive structures. Further evidence that the FHT routine may be a source of error comes from 1D thin-sheet models which have a uniform half-space beneath the sheet. In such cases, no Hankel transforms need to be calculated, and the analytical and thin-sheet **E** and **B** fields at the top and bottom of the ocean show good agreement, independent of the resistivity of the half-space.

The errors in **E** and **B** at the base of the thin-sheet are also dependent upon the period of the magnetic field. Figure 5.3 shows the correction-factors, as a function of period, for five models of lithosphere conductivity. A complex correction-factor, $Z^{\text{Correction}}$, is defined as

$$Z^{\text{Correction}} = \frac{Z^{1D}}{Z^{\text{Thin-sheet}}} \tag{5.3}$$

where Z^{1D} is the analytically derived 1D impedance at the seafloor, and $Z^{\text{Thin-sheet}}$ is the corresponding thin-sheet impedance for the same 1D model, at the base of the thin-sheet: if no distortion is present, the correction-factor is real and of unit magnitude. Figure 5.3 shows that the distortion is greatest at the longest periods, and for the most resistive structures. The phase of the distortion is small, as the imaginary parts of the correction-factor have magnitude less than 0.1. Although there are distinct trends in the real part of the correction-factor, there appear to be no systematic changes in the imaginary part, either with period or upper lithosphere conductivity, which suggests that the imaginary part of the correction-factor is not significant.

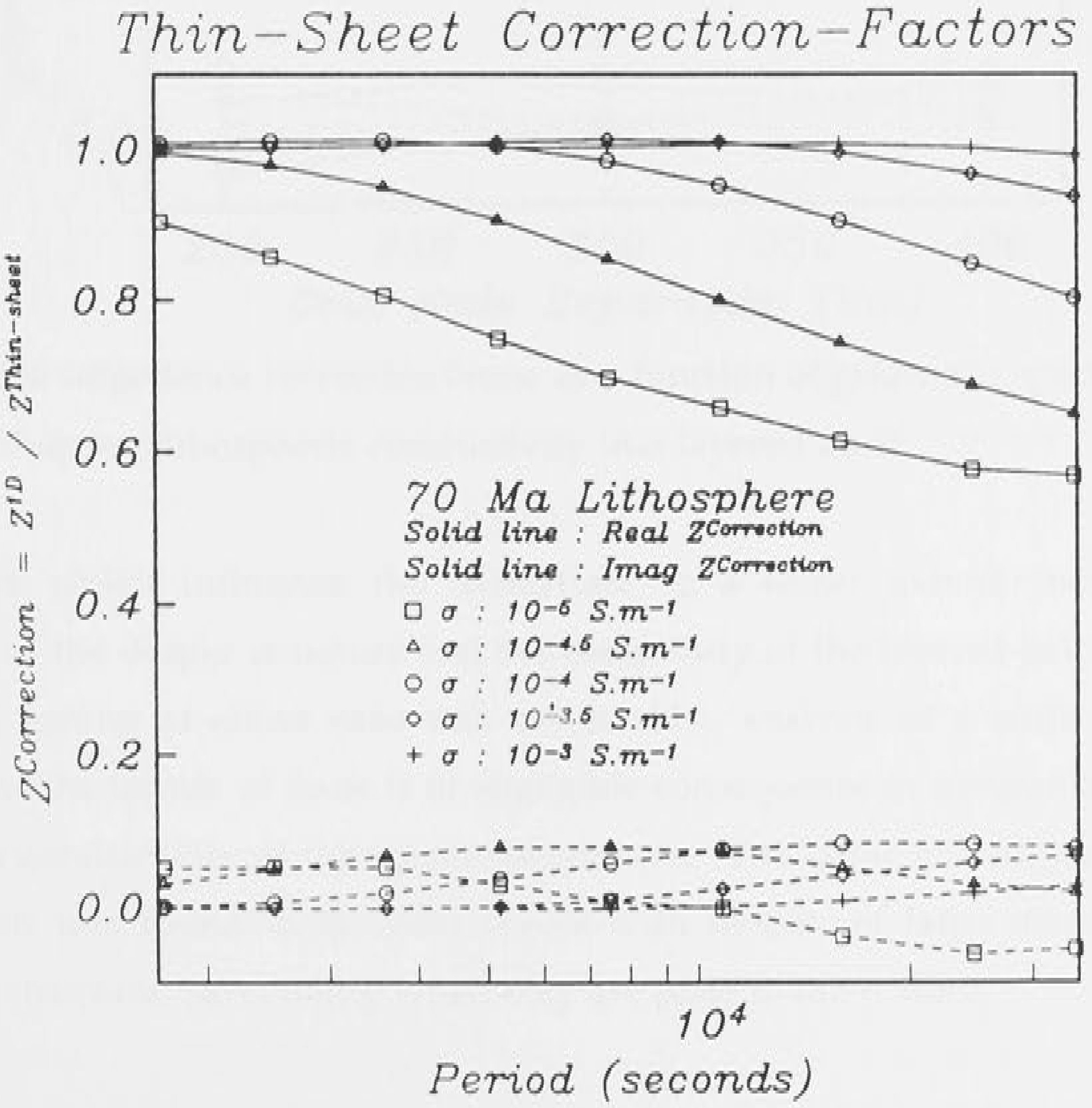

Figure 5.3 The impedance correction factor (at the bottom of the thin-sheet) as a function of period, for five cases of upper lithospheric conductivity in a layered Earth.

This distortion in the thin-sheet impedance is also dependent upon the spacing between grid-nodes in the thin-sheet. Figure 5.4 shows a comparison between the correction-factors for 1D models with variable upper lithosphere conductivity, and grid-node spacing of 200, 300 and 400 km, at an inducing period of 7500 s. The distortion is most severe for models with closely spaced grid-nodes. In the thin-sheet algorithm, the grid-node spacing is normalised with respect to the skin depth in the underlying layer, to give a dimension-less value. The skin depth is a function of both period and conductivity; thus it appears that the systematic error increases as the dimension-less grid-node spacing decreases.

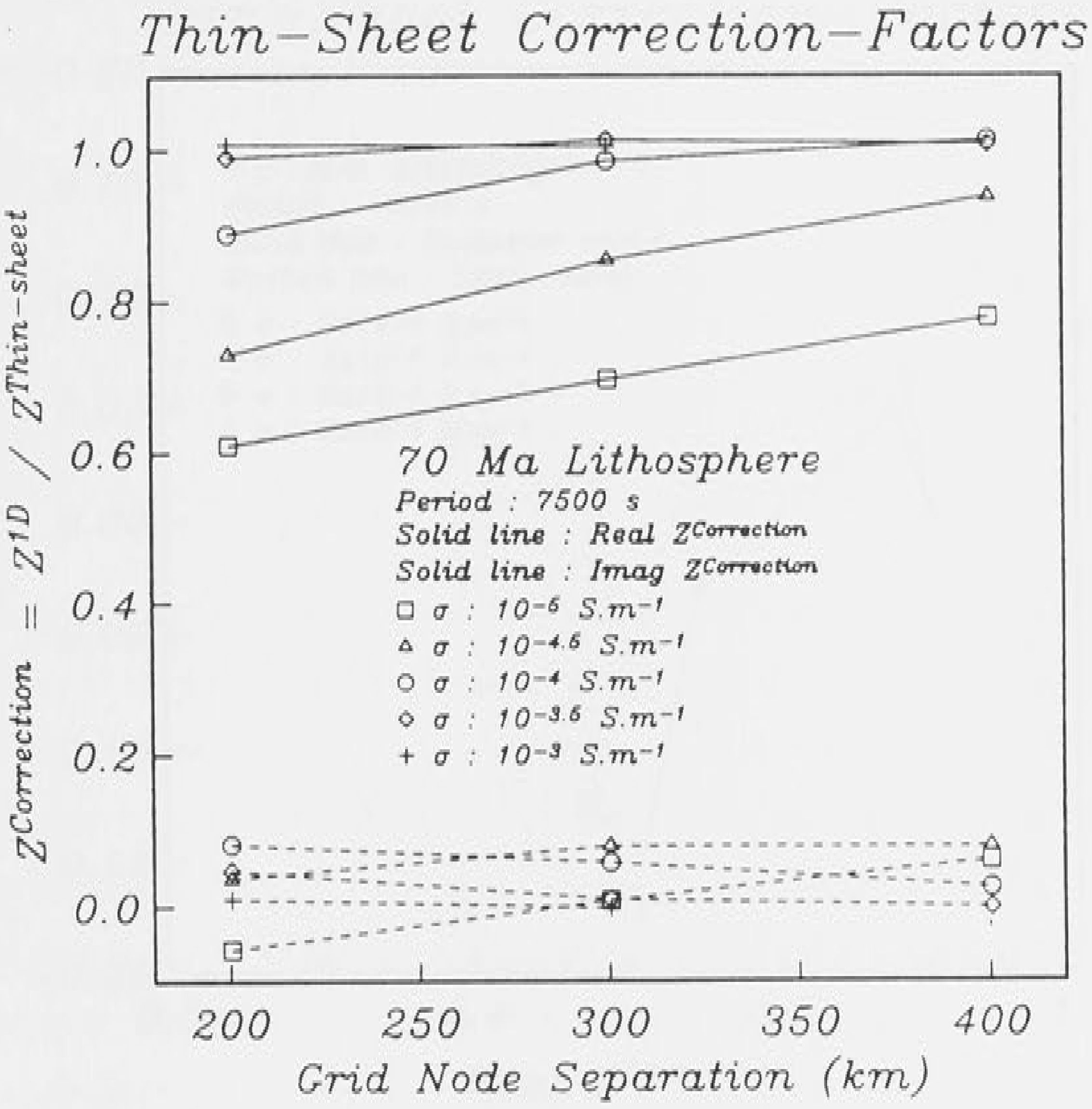

Figure 5.4 The impedance correction factor as a function of grid-node spacing, for five cases of upper lithospheric conductivity in a layered Earth.

Other factors which influence the distortion, to a lesser extent, include changes in conductivity of the deeper structure and the complexity of the layered half-space. Although no thorough testing of either case was undertaken, analysis of a wide range of models suggested that the former of these is of negligible consequence in comparison to the effect of changing the conductivity of the upper lithosphere. The latter was of greater significance, and distortion was found to be most severe with models of large discontinuities in the conductivity structure, particularly when they are close to the surface.

Finally, all of the above models have examined the attenuation of **E** and **B** from 1D ocean thin-sheet models, as a principal objective of the thin-sheet modelling exercise is to examine

3D induction effects within the ocean. However, it is important to consider the correction-factor for a thin-sheet model in which the sheet is composed of homogeneous continental crust, rather than sea-water. Analytically derived impedances, Z^{1D}, at the base of the sheet, are independent of the conductivity of the overlying homogeneous thin-sheet. Figure 5.5 shows a comparison between the correction-factors for sea-water and land 1D thin-sheets, using four values of upper lithosphere conductivity, at an inducing period of 10000 s. Table 5.5 lists the magnitude and phase of such correction-factors: there is agreement for the most conductive lithosphere, but differences increase with decreasing conductivity.

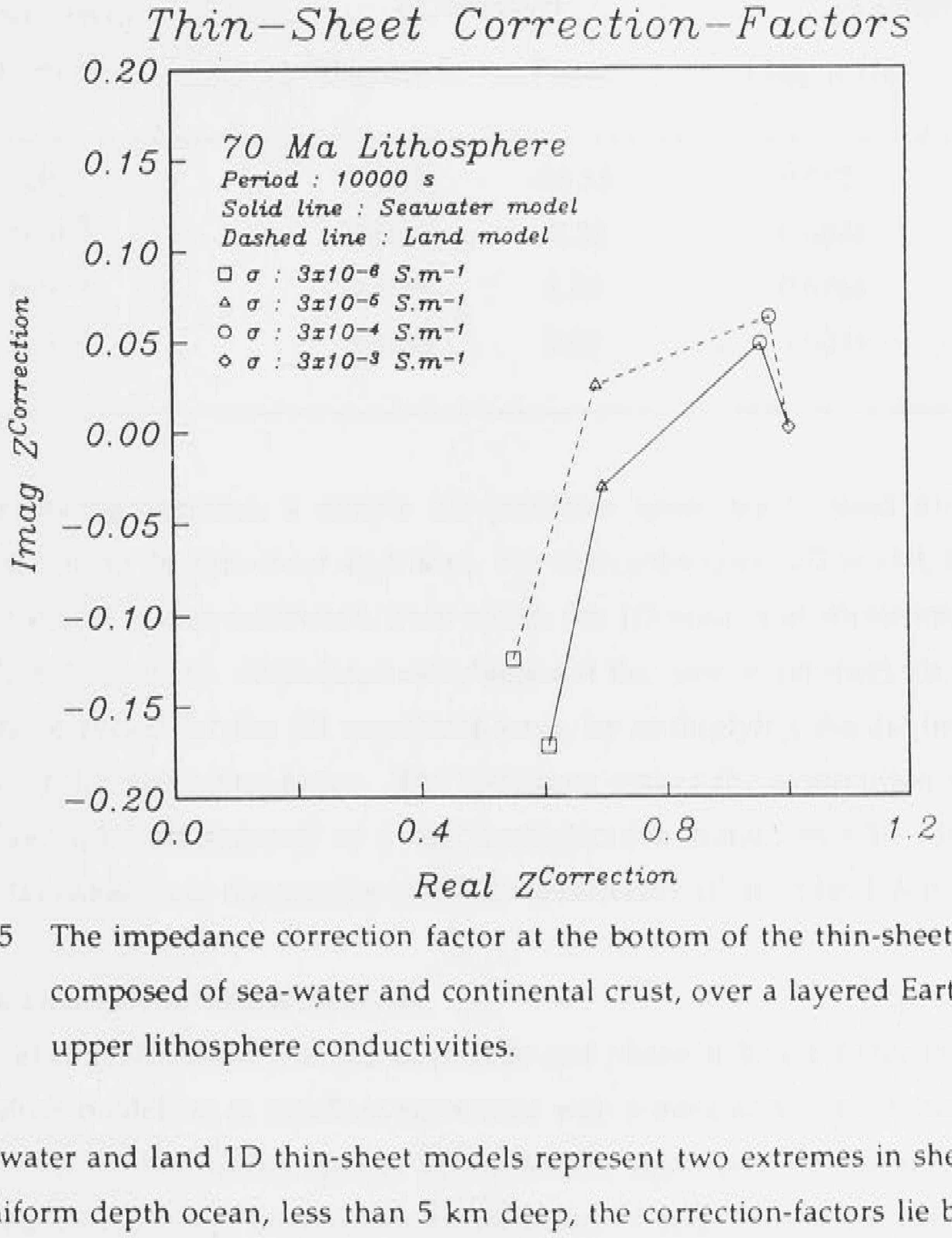

Figure 5.5 The impedance correction factor at the bottom of the thin-sheet, for thin-sheets composed of sea-water and continental crust, over a layered Earth with different upper lithosphere conductivities.

The sea-water and land 1D thin-sheet models represent two extremes in sheet conductance. For a uniform depth ocean, less than 5 km deep, the correction-factors lie between the two curves shown in Figure 5.5, and furthermore, are not substantially different from the correction-factors for the 5 km 1D ocean thin-sheet model. This is a consequence of the high conductivity of the sea-water compared to that of the continental crust. In general, a thin-sheet model of a real ocean basin will include ocean of variable depth and continental crust. It is not practical to compute separate 1D thin-sheet models, at each period, for homogeneous continental crust and for each ocean depth included in the ocean basin, to calculate the correction-factor as a function of both conductance and frequency. Instead, only correction-factors from 5 km ocean 1D thin-sheet models are used in this thesis.

Table 5.5 The magnitude and phase of the correction-factors, calculated as the ratio of the analytical impedance for the layered half-space and thin-sheet impedance, for a sheet composed of sea-water and of continental crust.

Upper Lithosphere Conductivity (S.m^{-1})	Sea-Water Thin-Sheet Model $Z^{Correction}$		Land Thin-Sheet Model $Z^{Correction}$	
	Magnitude	Phase	Magnitude	Phase
3x10^{-6}	0.6297	-15.85	0.5627	-12.73
3x10^{-5}	0.6972	-2.53	0.6874	2.09
3x10^{-4}	0.9585	2.88	0.9744	3.70
3x10^{-3}	1.0033	0.09	1.0033	0.09

In the following sections, a simple 2D coastline geometry is used to test numerical approximations in the thin-sheet algorithm. For each subsequent 2D model, a 5 km 1D ocean thin-sheet model is also calculated, from which the 1D numerical correction-factor, defined in eq. 5.3, is determined. Impedance calculations at the base of the sheet for the 2D coastline model are corrected for the 1D numerical error, by multiplying the 2D impedance tensor elements by this correction-factor. The technique makes the assumption that 1D and 2D effects de-couple; the removal of a real multiplicative factor from 2D impedance tensor elements is analogous to the practice of MT static shift correction on land (Jones, 1983).

5.1.6 Two-Dimensional Model Analysis

McKirdy *et al.* (1985) show that the amplitude and phase of **E** and **B** from (the surface of) a 2D thin-sheet model are in excellent agreement with a more accurate 2D numerical solution. In this thesis, further testing against 2D numerical algorithms or analytical solutions was considered unnecessary: instead, an examination of self-consistency between models of variable grid-node spacing and different locations of the coastline within the grid, are shown to give a reliable check on numerical accuracy.

However, a simple order of magnitude check on the 2D EM parameters can be made by comparisons with the compensation distance of Cox (1980) and Ranganayaki & Madden (1980). A 2D coastline model is set up, consisting of a thin-sheet with 1300 km of continental crust and 1500 km of 5000 m depth ocean, underlain by a 70 Ma lithosphere, as defined in

Table 5.3. Lithosphere conductivities in the range 3×10^{-3} to 3×10^{-6} S.m^{-1}, over a depth of 58 km, have corresponding compensation distances of 565 to 17861 km. Table 5.6 shows a comparison between the compensation distances in the oceans, calculated from the formulation given by Cox (1980), and that obtained on the ocean side of the 2D thin-sheet model. Thin-sheet compensation distances are calculated from an exponential expression for the seafloor impedance polarised in a direction perpendicular to the coastline, given by Lilley *et al.* (1989).

Table 5.6 Compensation distances calculated from the expression given by Cox (1980), and from the 2D thin-sheet models, for an inducing period of 10000 s.

Upper Lithosphere Conductivity (S.m^{-1})	Correction Distance From $L = \sqrt{ST}$ (km)	Correction Distance From 2D Thin-Sheet Model (km)
3×10^{-6}	17860	8579 ± 502
3×10^{-5}	5648	6067 ± 187
3×10^{-4}	1786	2485 ± 113
3×10^{-3}	565	1211 ± 109

There is an order of magnitude agreement between the two calculations of the compensation distance. The thin-sheet compensation distances are smaller if impedances are calculated using the sea-surface **B**. The derivation by Cox (1980) assumes that the integrated leakage current through the sea-bed is of the same order as the surface current-density J, which implies that there is no channelling of electric current within the ocean, and also that there is no flow of induced electric current across the resistive continental boundary. A consequence of this is that the gradient of the surface current density, $\partial J/\partial y$, in the direction y perpendicular to the coast, is infinite at the coastline.

Leakage of electric current into the lithosphere can be quantified by considering the 2D divergence of the surface current-density J in the thin-sheet (Weaver, 1982; McKirdy & Weaver, 1983). Figure 5.6 shows the divergence of J, which is equivalent to the vertical volume current density across the interface between the sheet and upper lithosphere, for a 2D coastline thin-sheet model with an external inducing magnetic field polarised parallel to the coastline. As would be expected, leakage is a maximum close to the coastline.

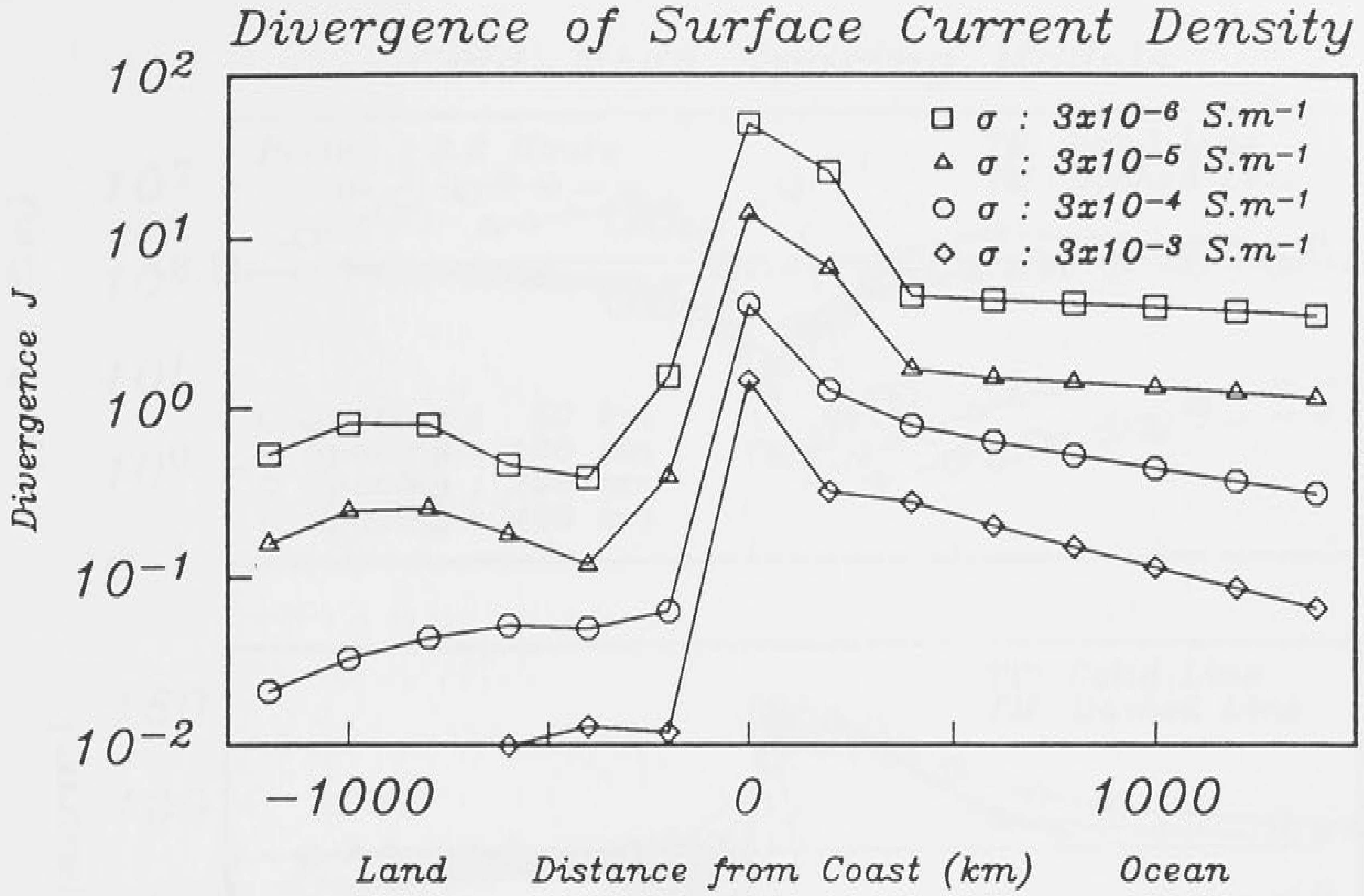

Figure 5.6 The 2D divergence of the dimensionless surface current-density J, along a transect perpendicular to the coastline, for four cases of upper lithospheric conductivity.

Thin-sheet compensation distances are dependent upon the grid-node spacing. Table 5.7 shows the compensation distances for 2D thin-sheet coastline models, with an upper lithosphere of conductivity 3×10^{-5} $S.m^{-1}$, and with spacing of grid-nodes varying from 50 to 400 km. As all models are identical, except for the area covered by the grid, the compensation distances should be in close agreement, but Table 5.7 shows that this is far from the case. Figure 5.7 shows the MT apparent resistivity and phase curves at the base of the thin-sheet, for a transect perpendicular to the coastline. Consistent with notation developed in chapter 1, the TE polarisation is parallel to the coastline, while the TM polarisation is perpendicular. Although the MT parameters on the land side of the model are calculated at the base of the sheet, the resistivity of the continental crust ensures that the horizontal magnetic field is nearly unattenuated through the sheet, which implies that the MT parameters are almost the same on both top and bottom of the sheet. Thus, sub-sheet land MT parameters are taken to be equivalent to the land surface MT. The differences between the TM apparent resistivities for different grid-node separations are obvious. Such differences may possibly be due to the proximity of the coastline to the grid boundary, which varies from 375 to 3000 km on the ocean side and from 325 to 2600 km of land, so that EM boundary conditions at the grid margin are not satisfied.

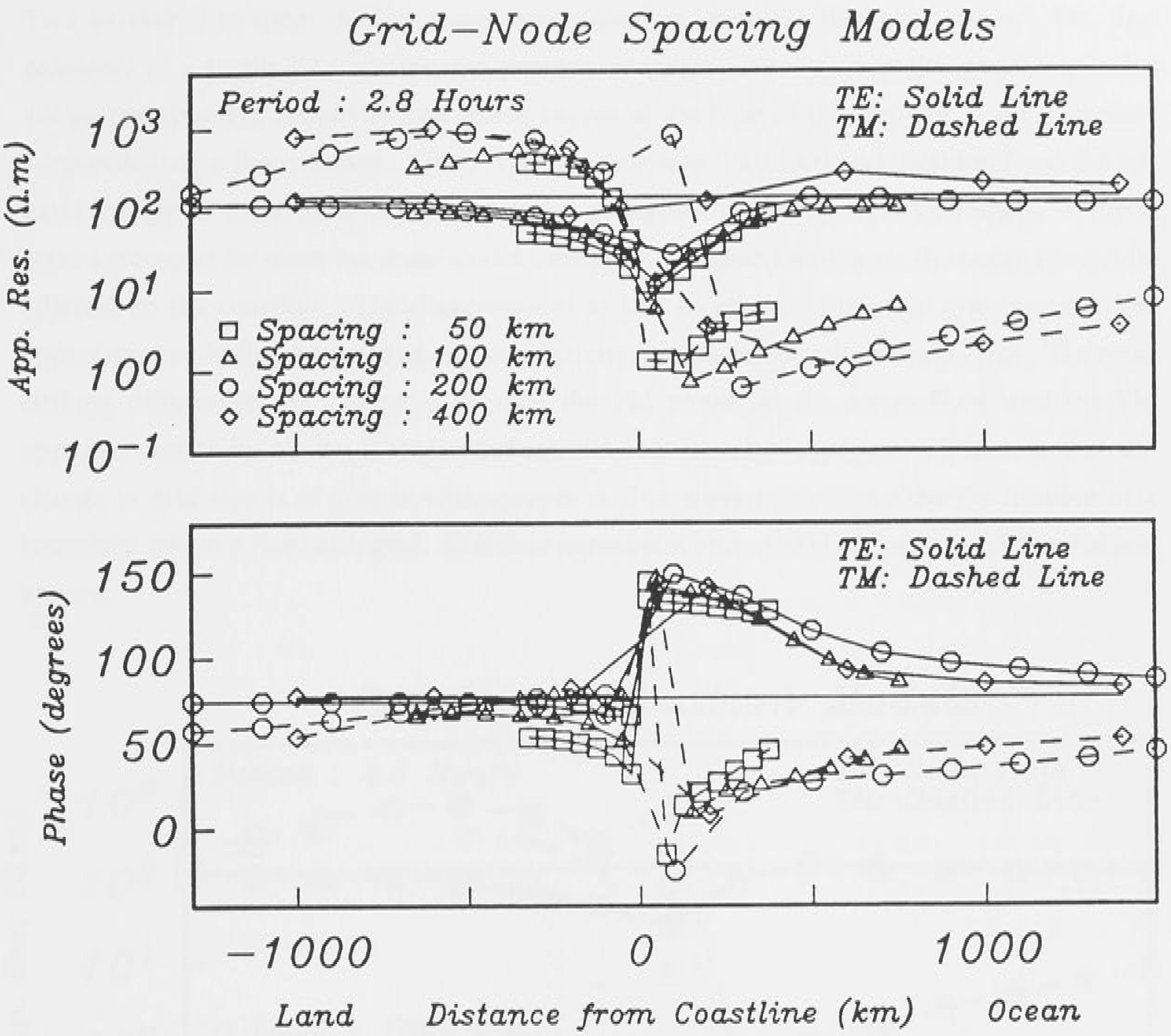

Figure 5.7 The effect of changing the grid-node spacing on MT apparent resistivity and phase at the base of the thin-sheet, along a transect perpendicular to the 2D coastline. The MT parameters are polarised parallel (TE) and perpendicular (TM) to the coastline, over a 70 Ma lithosphere.

Table 5.7 Correction distances calculated from the 2D thin-sheet models at an inducing period of 10000 s and a lithosphere of 3×10^{-5} $S.m^{-1}$, for four different grid-node spacings.

Grid-Node Spacing (km)	Correction Distance From $L = \sqrt{ST}$ (km)	Correction Distance From 2D Thin-Sheet Model (km)
50	5648	1509 ± 151
100	5648	3136 ± 160
200	5648	6067 ± 187
400	5648	8004 ± 299

Two further thin-sheet models were constructed to consider this hypothesis. The first consisted of a single 2D coastline, the position of which was varied in the grid. Figure 5.8 shows the apparent resistivity and phase curves at the base of the thin-sheet, for a transect perpendicular to the coastline. Three coastline locations 500, 1300 and 2300 km from the left hand margin of the grid, which is composed of continental crust, were examined. There is good agreement between the three models, except at the grid location on the ocean floor side, adjacent to the coastline. The disagreement at this location is probably due to numerical approximation at the sharp change in conductivity, and so is not a significant error. The most striking differences are shown to be with the TM phase on the ocean floor, and the TM apparent resistivity on land. Nevertheless, the high level of agreement indicates that the change in grid size is of greater consequence in thin-sheet modelling than the location of a boundary within a fixed size grid. Excellent agreement also exists between the GDS induction arrows.

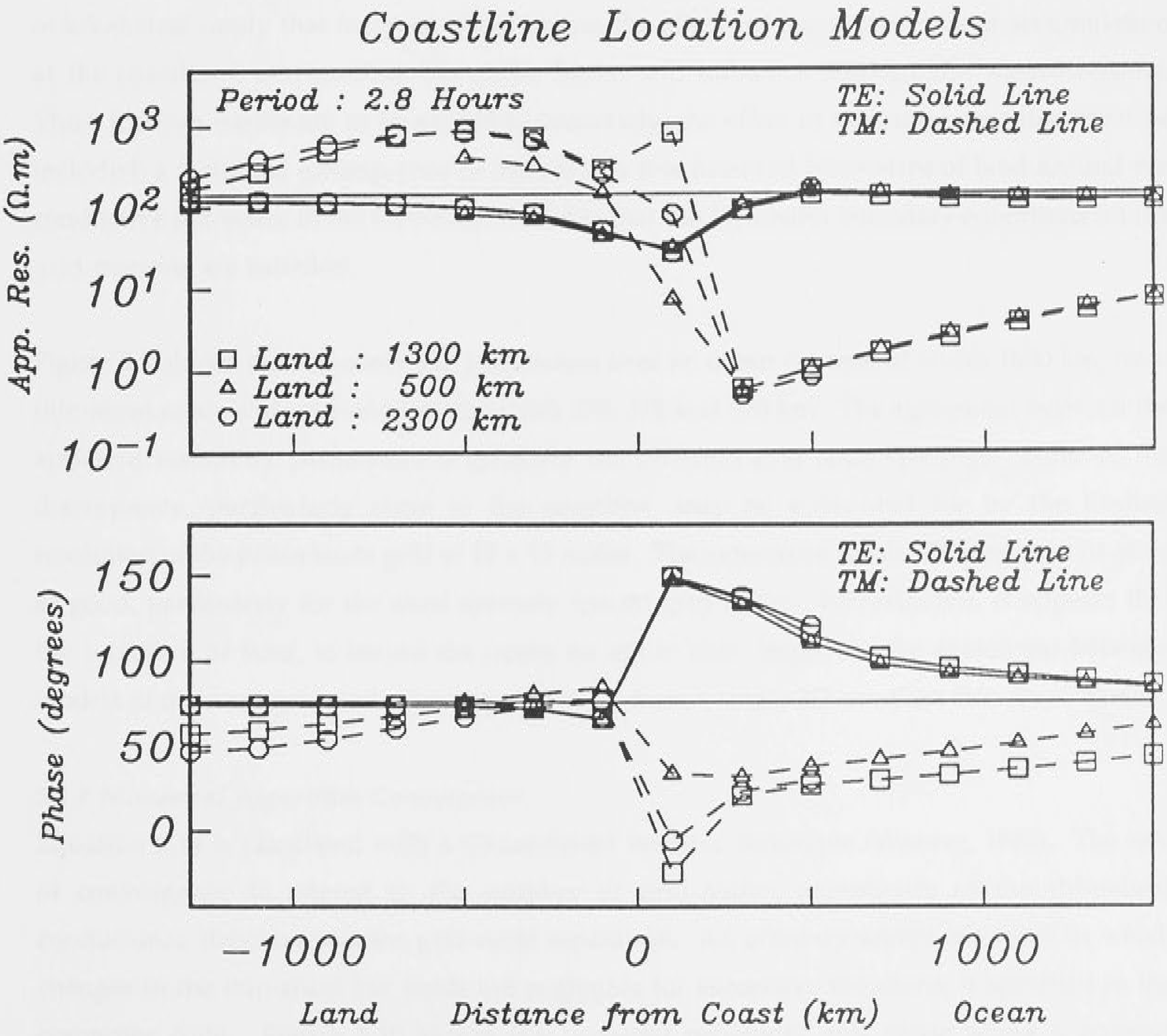

Figure 5.8 As for Figure 5.7, but changing the location of the coastline (with constant grid-node spacing).

The effect of the changing the grid-node separation has a more profound consequence on the ocean floor side than on land, as shown by the MT parameters in Figure 5.7. Magnetotelluric apparent resistivity and phase, at the base of the thin-sheet, approach the 1D layered half-space response over a distance of the order of a few hundred kilometres on land, whereas, on the ocean floor, compensation distances are several thousand kilometres. Ranganayaki & Madden (1980) derive a solution for E, polarised perpendicularly to the coastline, for both land and ocean sides of a 2D model. The compensation distance on land is less than that for the ocean, by a factor which is dependent upon the square root of the ratio of the conductivity of sea-water to that of continental crust. Seafloor MT calculations for a thin-sheet model of a single coastline may thus be inaccurate: this inaccuracy restricts the use of thin-sheet models for ocean floor EM analysis. It is probable that the large compensation distances for the resistive upper lithosphere mean that the Neumann boundary conditions at the edge of the grid are not satisfied on the ocean side of a single coastline model, if the grid size is less than the compensation distance. However, such compensation distances of the order of thousands of kilometres imply that for most ocean basins, the effects of the electric charge accumulation at the coastlines, surrounding the entire basin, will influence seafloor EM measurements. Thus, if ocean basins are to be modelled accurately, the effect of the entire coastline must be included; a fortunate consequence of including a few hundred kilometres of land around the conductive sea-water in the thin-sheet model is that the Neumann boundary conditions on the grid margins are satisfied.

Figure 5.9 shows the sub-sheet MT parameters over an ocean channel of width 1890 km, from thin-sheet models of grid-node spacing 210, 270, 378 and 630 km. The agreement between the apparent resistivity parameters is good for the different grid-node spacings. Some of the discrepancy, particularly close to the coastline, may be accounted for by the limited resolution of the ocean basin grid of 15 x 15 nodes. The agreement for the TE phase is not quite as good, particularly for the most sparsely spaced grid-nodes. Nevertheless, it appears that the inclusion of land, to bound the ocean on either side, improves the agreement between models of different grid-node spacing over those from a single 2D coastline thin-sheet model.

5.1.7 Numerical Algorithm Convergence

Equation 3.13 is calculated with a Gauss-Seidel iterative technique (Weaver, 1982). The rate of convergence is related to the number of grid-nodes, complexity of the thin-sheet conductance structure and the grid-node separation. An arbitrary acceptable level, at which changes in the thin-sheet EM fields are negligible for successive iterations, is specified in the computer code. Figure 5.10 shows the apparent resistivity and phase along a transect perpendicular to a 2D coastline thin-sheet model after 1, 5, 20 and 100 iterations. It shows that the TE parameters are virtually unchanged after 2 iterations; however the TM

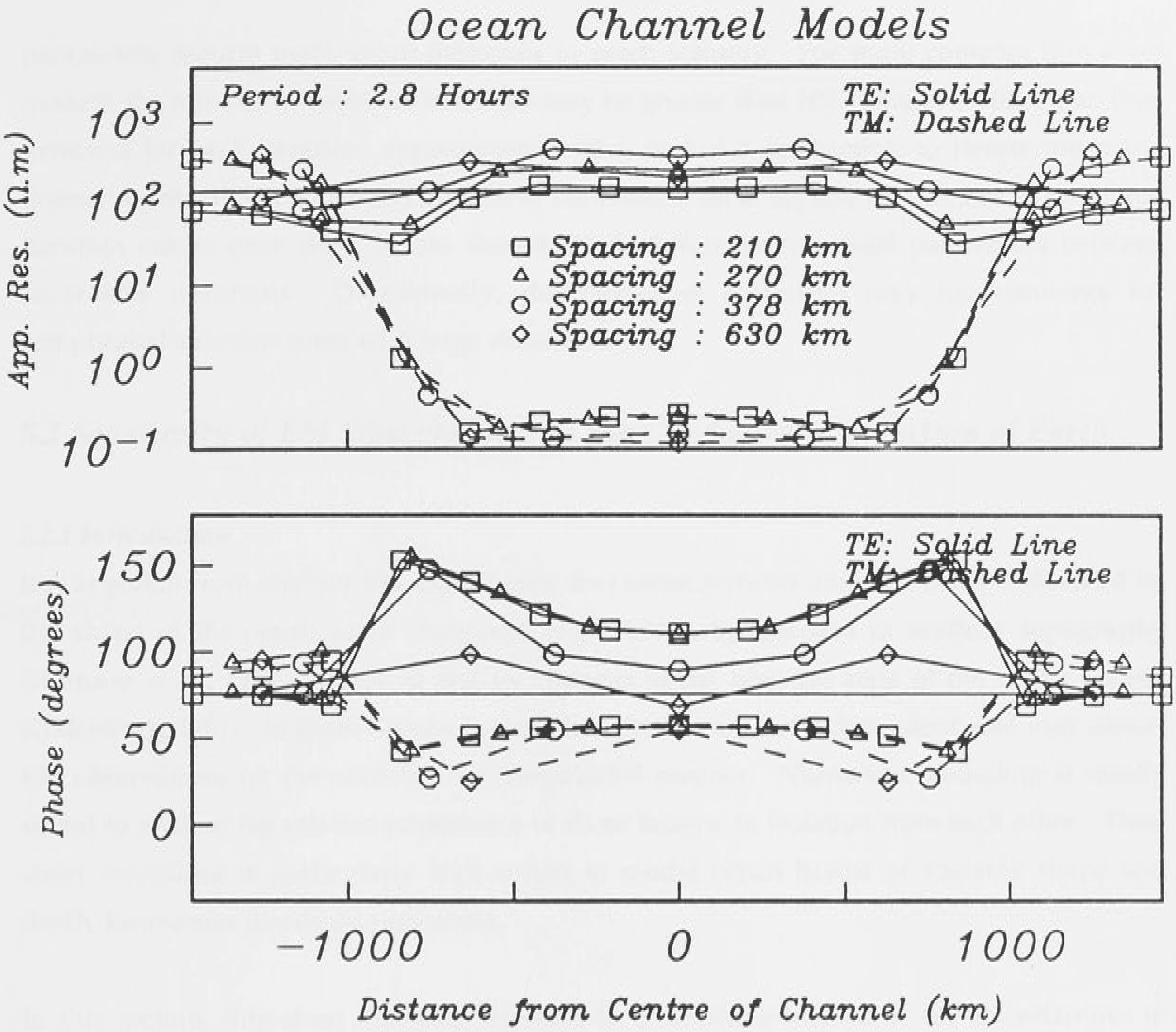

Figure 5.9 As for Figure 5.7, but for a 2D ocean channel of width 1890 km.

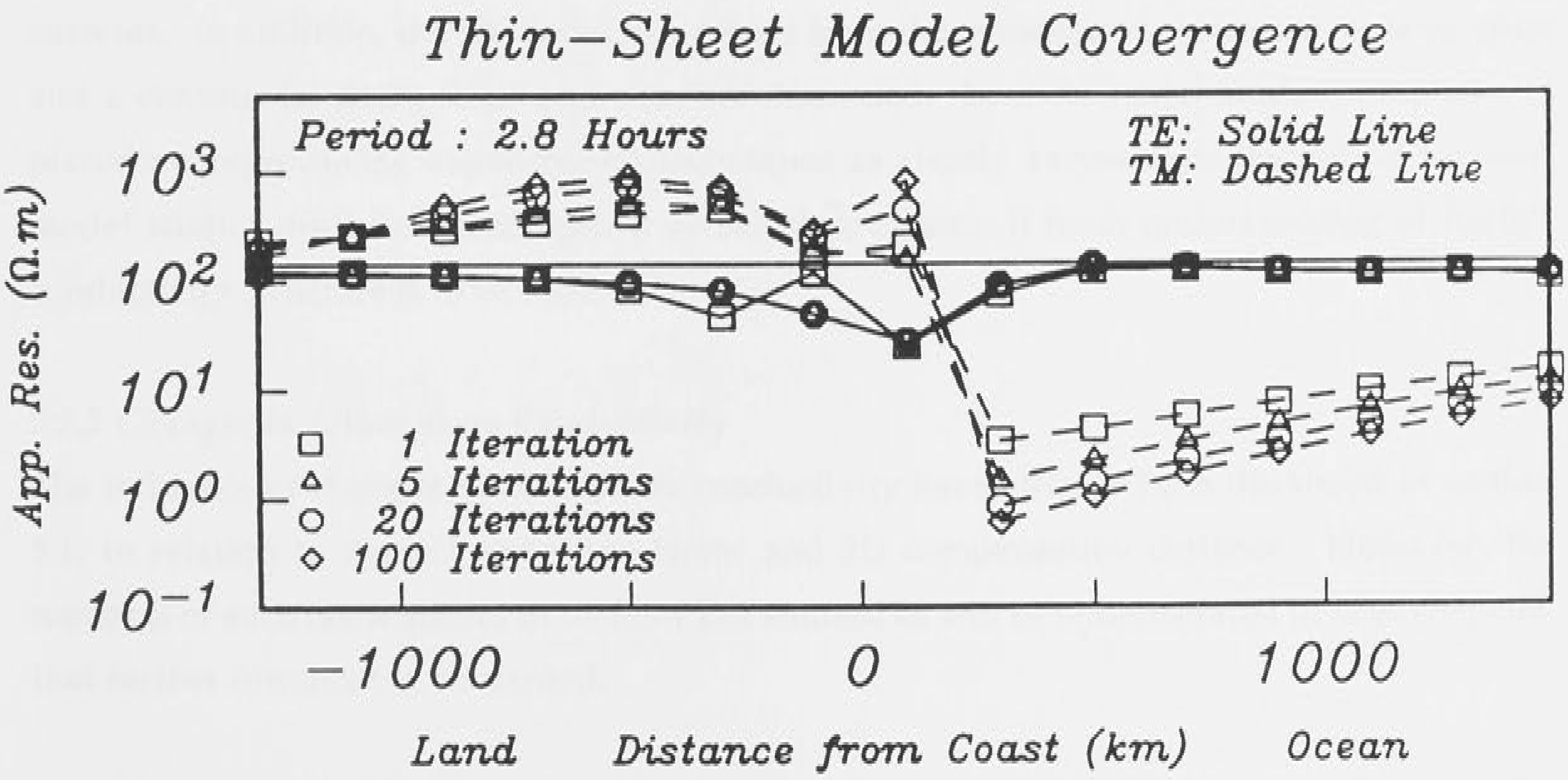

Figure 5.10 As for Figure 5.7, but changing the number of completed iterations.

parameters require many more iterations to reach stability. For more complex thin-sheet models, the number of required iterations may be greater than 100. However, the c.p.u. time involved for each iteration, approximately 20 s, makes it impractical to iterate too many times. In general, the maximum number of iterations is set at 50, and a parameter is set so that iteration ceases once there is less than 0.005 % difference in model parameters between successive iterations. Occasionally, the thin-sheet algorithm may not converge for complicated sub-structures with large discontinuities.

5.2 Sensitivity of EM Observations to the Conductivity Structure of Earth

5.2.1 Introduction

It is apparent from seafloor EM experiments that measurements are profoundly influenced by the shape of the ocean basin (Ferguson *et al.*, 1990), by changes in seafloor topography (Heinson *et al.*, 1991; chapter 6) and by changes in the physical state of the upper mantle (Oldenburg, 1981). In Earth's ocean basins, these factors are not independent, and may distort EM observations on the seafloor in a complicated manner. Numerical modelling is ideally suited to analyse the relative importance of these factors, in isolation from each other. Thin-sheet modelling is particularly well suited to model ocean basins of variable shape and depth, for reasons discussed previously.

In this section, thin-sheet methods are used to assess the influence of the uncertainties in electrical conductivity of the continental crust and upper mantle, listed in Table 5.3, on synthetic MT, VGS, GDS parameters, and on the channelling and leakage of induced electric currents. In addition, the EM induction effects from the presence of sediments, oceanic crust and a continental shelf, slope and rise, are discussed. In such model studies, emphasis is placed on reproducing experimental techniques as closely as possible: theoretical forward model studies must be tested against actual observations, if fresh understanding of Earth's conductivity structure is to be achieved.

5.2.2 Changes in Lithosphere Conductivity

The influence of changes in lithosphere conductivity have already been discussed in section 5.1, in relation to the 1D correction-factor and 2D compensation distance. However, the matter is of such consequence to seafloor EM studies, as will be demonstrated in later chapters, that further comment is warranted.

Figure 5.11 shows MT apparent resistivity and phase, at the base of the thin-sheet, for the models of varying upper lithosphere conductivity listed in Table 5.3. Also shown is the 1D forward MT response for the layered half-space. The ratio of the TE to TM apparent resistivity on the ocean side, defined as the anisotropy in apparent resistivity, is correlated to the conductivity of the lithosphere. On the ocean floor, the most resistive lithosphere has the smallest TM apparent resistivity. By contrast, the TE apparent resistivity is close to the 1D MT response at all ocean floor grid-nodes, except for the model with upper lithosphere conductivity 3x10^{-6} S.m^{-1}, which asymptotes to a value less than the 1D MT response. On land, the differences are less pronounced. The TE apparent resistivity approaches the 1D MT response away from the coastline over a short distance, but the TM response is up to an order of magnitude greater, at a distances of several hundred kilometres away from the coastline. Indeed, the magnitude and distance inland at which this peak arises is a function of the conductivity of the lithosphere. Phase angle calculations for the two polarisations have similar morphology to the apparent resistivity curves on the ocean side, with the TM phase rising from a minimum, and the TE phase dropping from a maximum value at the coast, to approach the 1D MT response. On the land side, both polarisations of phase are close to the 1D forward modelled response, although the TM phase values tend to be slightly lower.

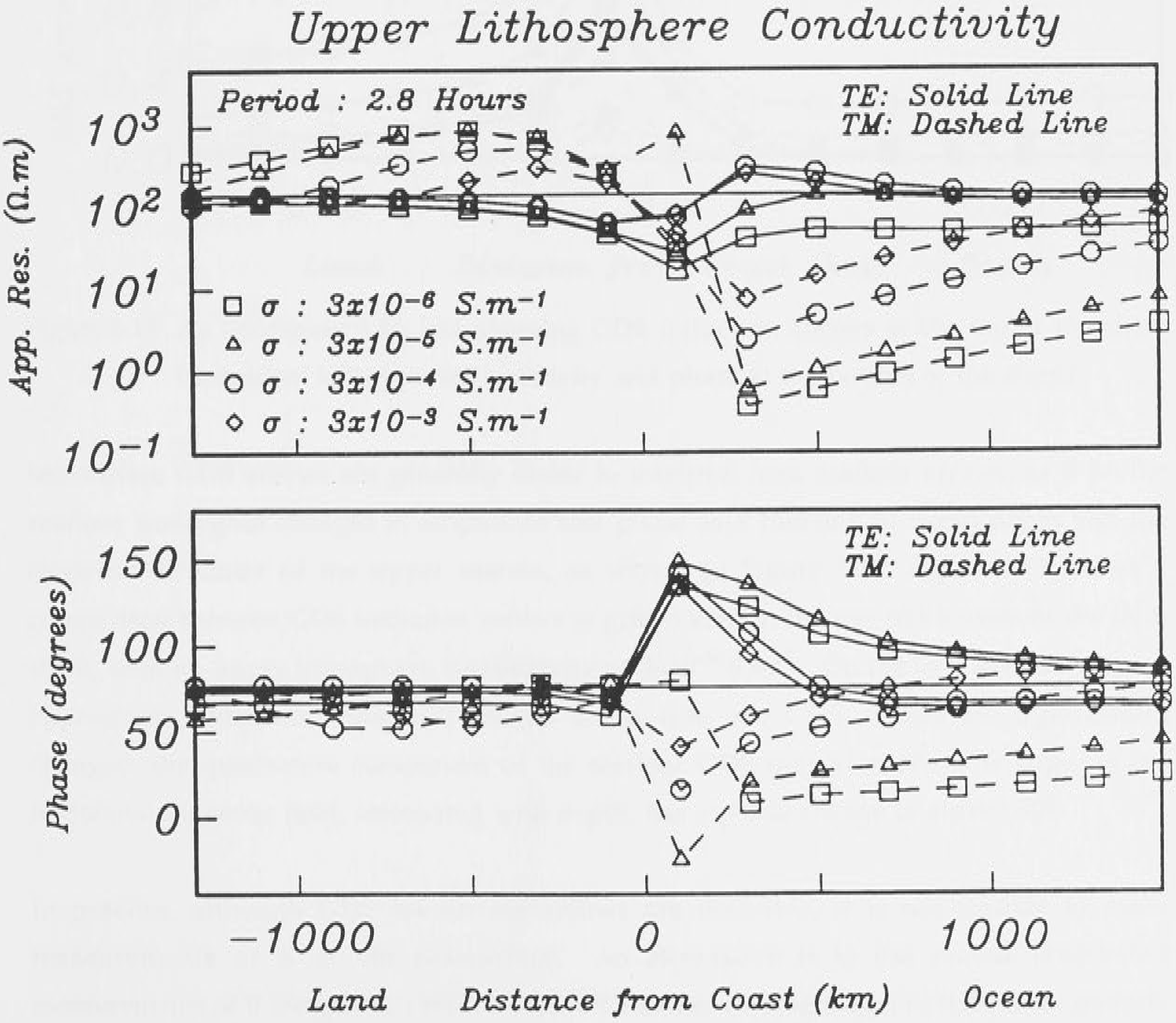

Figure 5.11 As for Figure 5.7, but changing the conductivity of the upper lithosphere.

GDS induction arrows are shown in Figure 5.12, calculated on the top of the thin-sheet. Once again, the magnitudes of the real GDS induction arrows are dependent upon the lithosphere conductivity: there is a factor of 2 between the induction arrows at the coastline for the most conductive and most resistive lithospheres. The absolute magnitudes of the arrows must be viewed with caution: McKirdy *et al.* (1985) have shown that the anomalous field, and hence the amplitude of the vertical magnetic field Z, is smoothed out with a fixed grid-node spacing. The amplitude of Z, and consequently of the GDS induction arrows, increases with finer grid resolution over sharp conductivity contrasts.

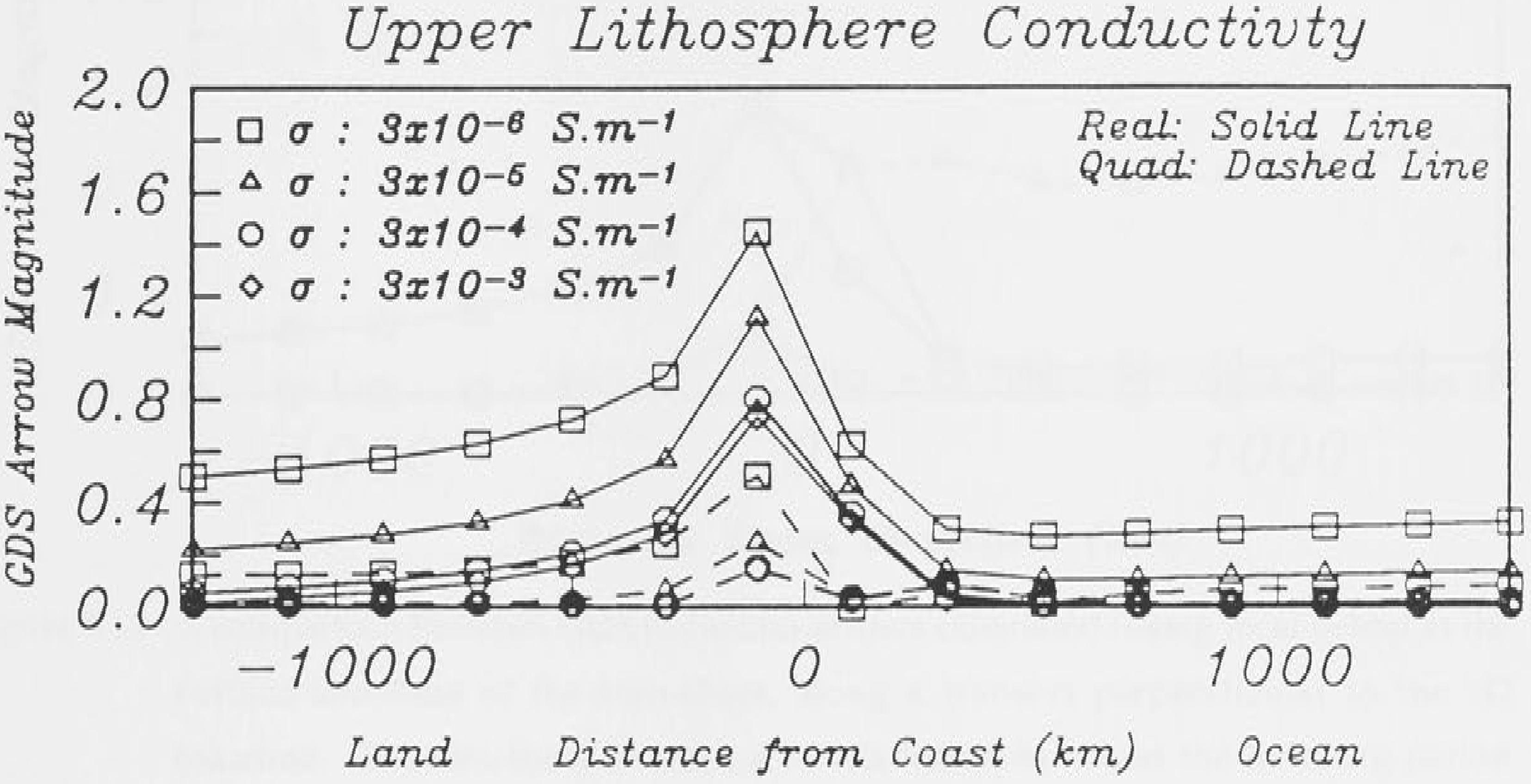

Figure 5.12 As for Figure 5.11, but showing GDS induction arrows at the top of the sheet (instead of MT apparent resistivity and phase at the bottom of the sheet).

Sea-surface GDS arrows are generally easier to interpret than seafloor arrows, as **B** on the seafloor undergoes changes in amplitude and phase as a function of ocean depth and the electrical structure of the upper mantle, as shown in Figure 5.1. Figure 5.13 shows a comparison between GDS induction arrows at grid-nodes on the top and bottom of the thin-sheet, with an upper lithosphere conductivity of 3x10^{-5} S.m^{-1}. On the land side, there is no appreciable difference; however, on the ocean side, the GDS arrows are significantly changed: the quadrature component of the seafloor GDS induction arrow is large, as the horizontal magnetic field, attenuated with depth, has a phase change of almost 90°.

In practice, although GDS sea-surface arrows are desirable, it is not feasible to make measurements of **B** on the sea-surface. An alternative is to use remote land-based measurements of **B** (Ferguson, 1988). However, the time-varying magnetic field is not uniform over land and sea: Figure 5.14 shows variations of **B** over the top of the thin-sheet, for D- and H-polarisations of the regional fields. For a 2D coastline, the magnitude of the GDS induction arrow is given by Z / Y, where Z is the vertical magnetic field, and Y is the component of **B** perpendicular to the coastline. As Y is smaller over land than over the sea-surface, GDS induction arrows calculated from a remote land source will be larger than those using sea-surface magnetic fields. An illustration of this is shown in Figure 5.15, for GDS arrows calculated at various distances seaward from the coastline using remote land **B**.

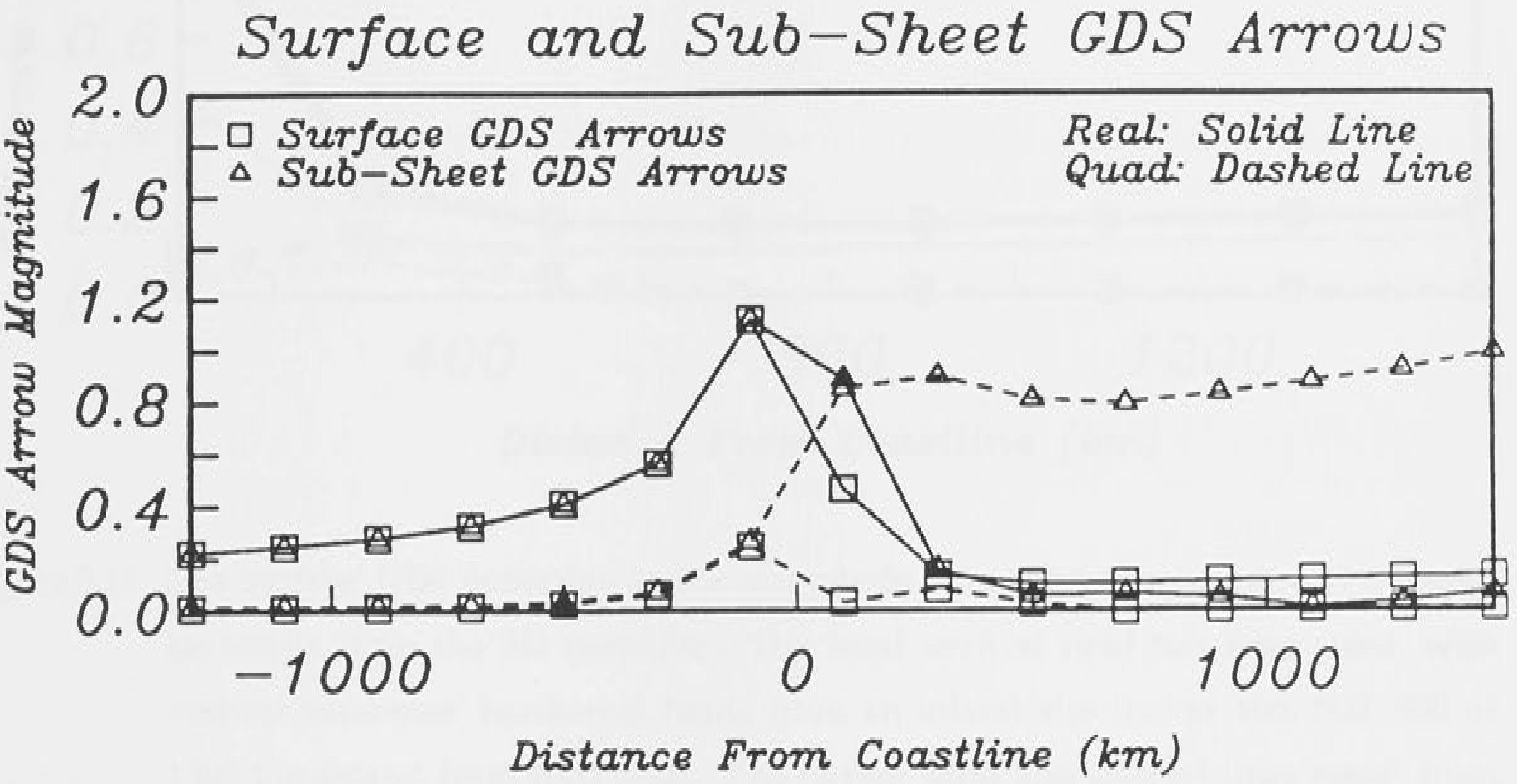

Figure 5.13 A comparison between GDS induction arrows calculated (using local fields) at the surface and base of the thin-sheet, along a transect perpendicular to the 2D coastline. The thin-sheet overlies a 70 Ma lithosphere and the inducing period is 10000 s (2.8 hrs).

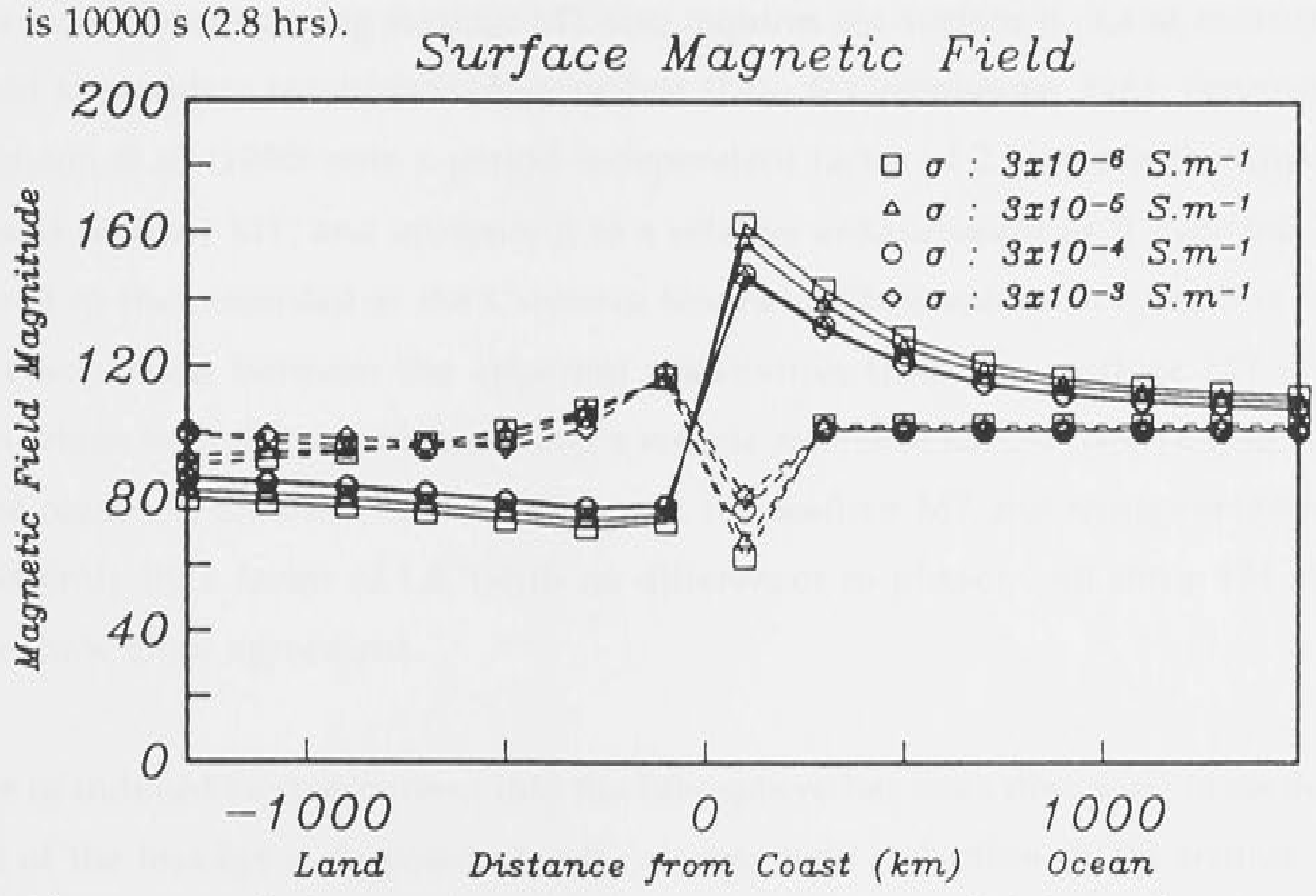

Figure 5.14 Variation of the surface horizontal magnetic field **B** along a transect perpendicular to the 2D coastline, for four cases of upper lithospheric conductivity. The TE and TM modes are shown by solid and dashed lines respectively.

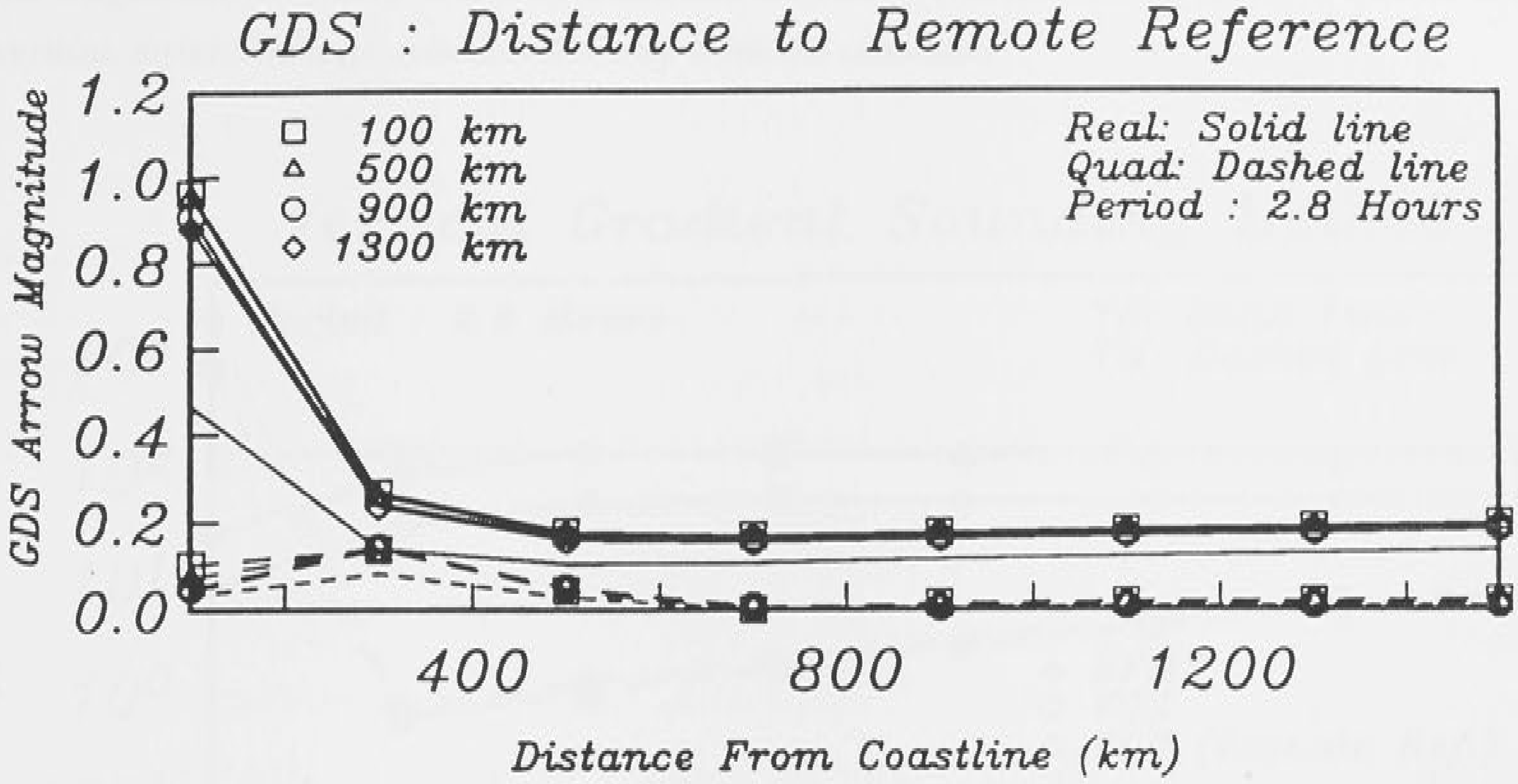

Figure 5.15 'Sea surface' GDS induction arrow magnitude calculated as a function of distance seawards from the 2D coastline. The local vertical field has been used, with 'remote reference' horizontal fields from an inland site (either 100, 500, 900 or 1300 km inland from the coast). The lighter solid and dashed lines result from using the local sea-surface horizontal magnetic fields, instead of an inland remote reference.

The VGS method of determining seafloor MT also requires sea-surface **B**. Land measurements of **B** are used to simulate sea-surface observations (Law & Greenhouse, 1981; Ferguson *et al.*, 1990). Ferguson *et al.* (1990) note a period independent factor of 2 between the impedances from VGS and seafloor MT, and attribute it to a relative enhancement of **B** over the Tasman Sea compared to that recorded at the Canberra Magnetic Observatory. Figure 5.16 shows a calculated comparison between the apparent resistivities from the seafloor MT and VGS methods, in which both the sea-surface **B** and a remote-reference land **B** (from a grid-node 300 km from the coastline) are used. For the TE mode, the seafloor MT and remote-reference VGS differ consistently by a factor of 1.5, (with no differences in phase). All three TM apparent resistivities show close agreement.

The leakage of induced electric current into the lithosphere has been discussed in section 1.2.7. A measure of the leakage is demonstrated by electric field induction (EDS) arrows: Figure 5.17 shows such induction arrows across the coastline. With three orders of magnitude difference in lithosphere conductivity, the induction arrows vary over three orders of magnitude, and are largest close to the coastline. Away from the coastline, on the ocean side, the magnitude of the electric field induction arrows decreases slowly, which indicates that vertical current leakage occurs well away from the coastline.

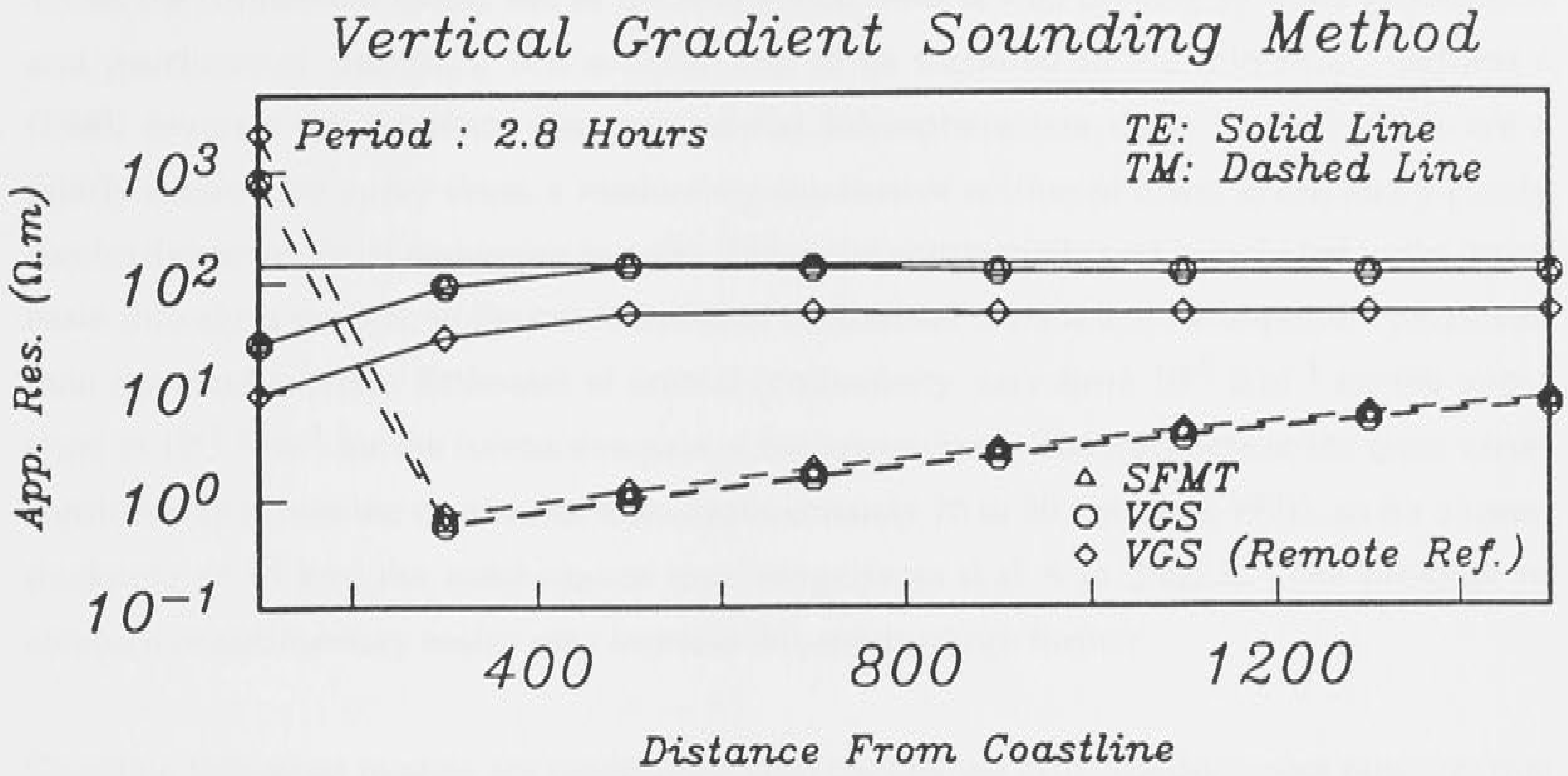

Figure 5.16 'Seafloor' MT apparent resistivity as a function of distance seawards from the 2D coastline. The solid line shows the 1D response for the layered structure. Also shown are two sets VGS apparent resistivities: one calculated using seafloor and sea-surface fields and the other using seafloor fields and 'remote-reference' horizontal fields from an inland site (300 km inland from the coast).

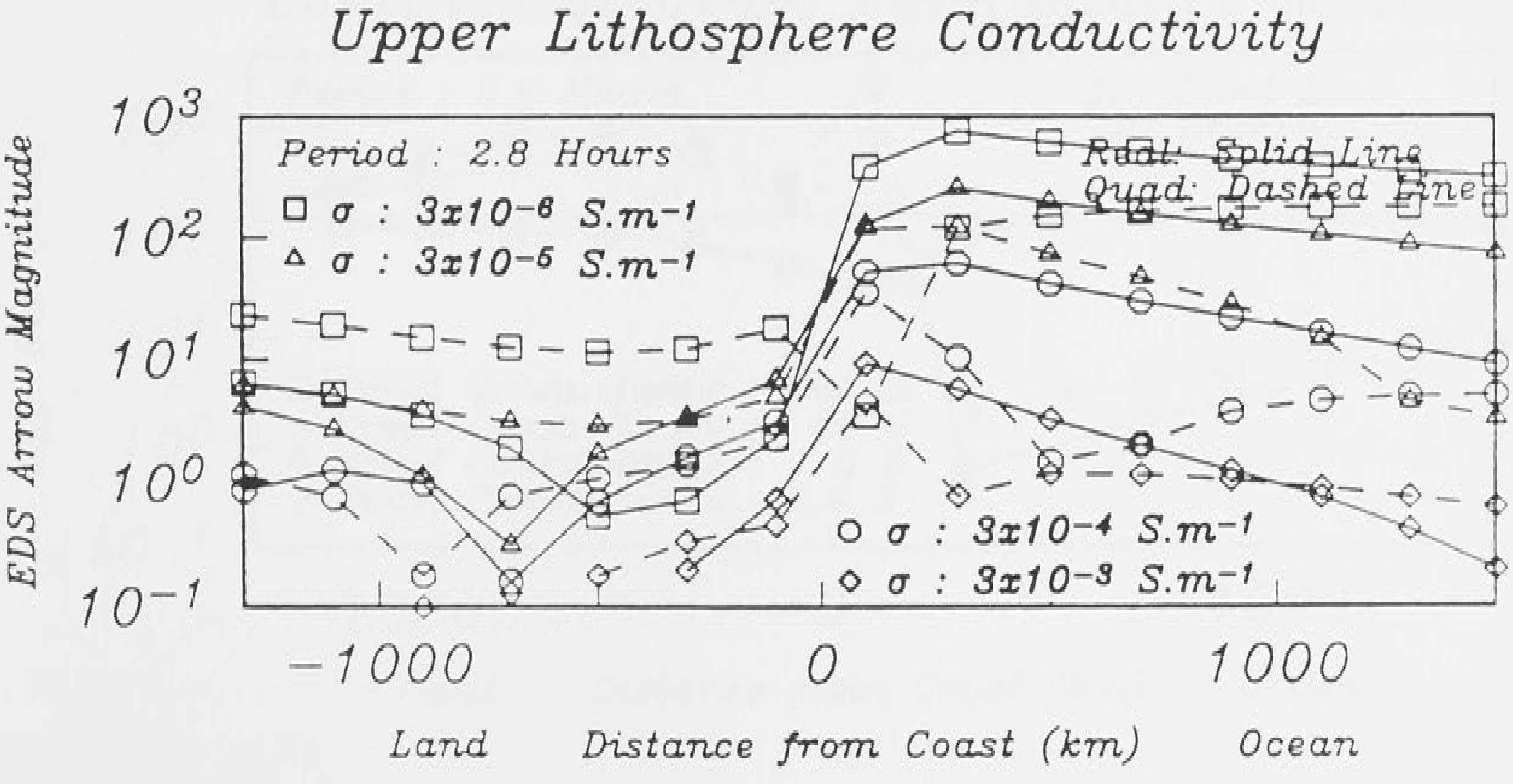

Figure 5.17 As for Figure 5.12, but showing EDS induction arrows at the bottom of the sheet.

5.2.3 Changes in Continental Crust Conductance

Jones (1982) has suggested that there is no large electrical conductivity contrast vertically across the continental Moho, but as the continental crust is well defined by other geophysical and geochemical studies, it is a suitable unit to be included in the thin-sheet. Schwarz (1990) reviews the evidence that continental lithosphere has three layers, which are a poorly conductive upper crust, a moderately conductive section of lower crust, and a poorly conductive lower crust and upper mantle. The entire continental crust is included in the ocean basin thin-sheet models, so the conductance of continental crust is a more important parameter than the conductivity. Estimates of crustal conductivity vary from 10^{-5} S.m^{-1} for the upper crust to 10^{-1} S.m^{-1} for the conductive part of the lower crust. The thickness of the crust varies considerably across the continents, from approximately 20 to 50 km (Bott, 1971), so for a mean thickness of 35 km, the conductance may range from 0.35 S to 3500 S. The presence of conductive sedimentary basins may increase this conductance further.

Coastline thin-sheet models are constructed with continental crust conductances ranging from 0.5 to 500 S, which equate to mean conductivities over a 35 km thick crust of $1.4\text{x}10^{-5}$ to $1.4\text{x}10^{-2}$ S.m^{-1}. Apparent resistivity values across the coastline are shown in Figure 5.18. There are no significant differences between the TE parameters from different models. A similar agreement exists between the GDS induction arrows across the coastline. TM parameters are more sensitive to the changes, but, for conductances less than 50 S, the differences are not significant.

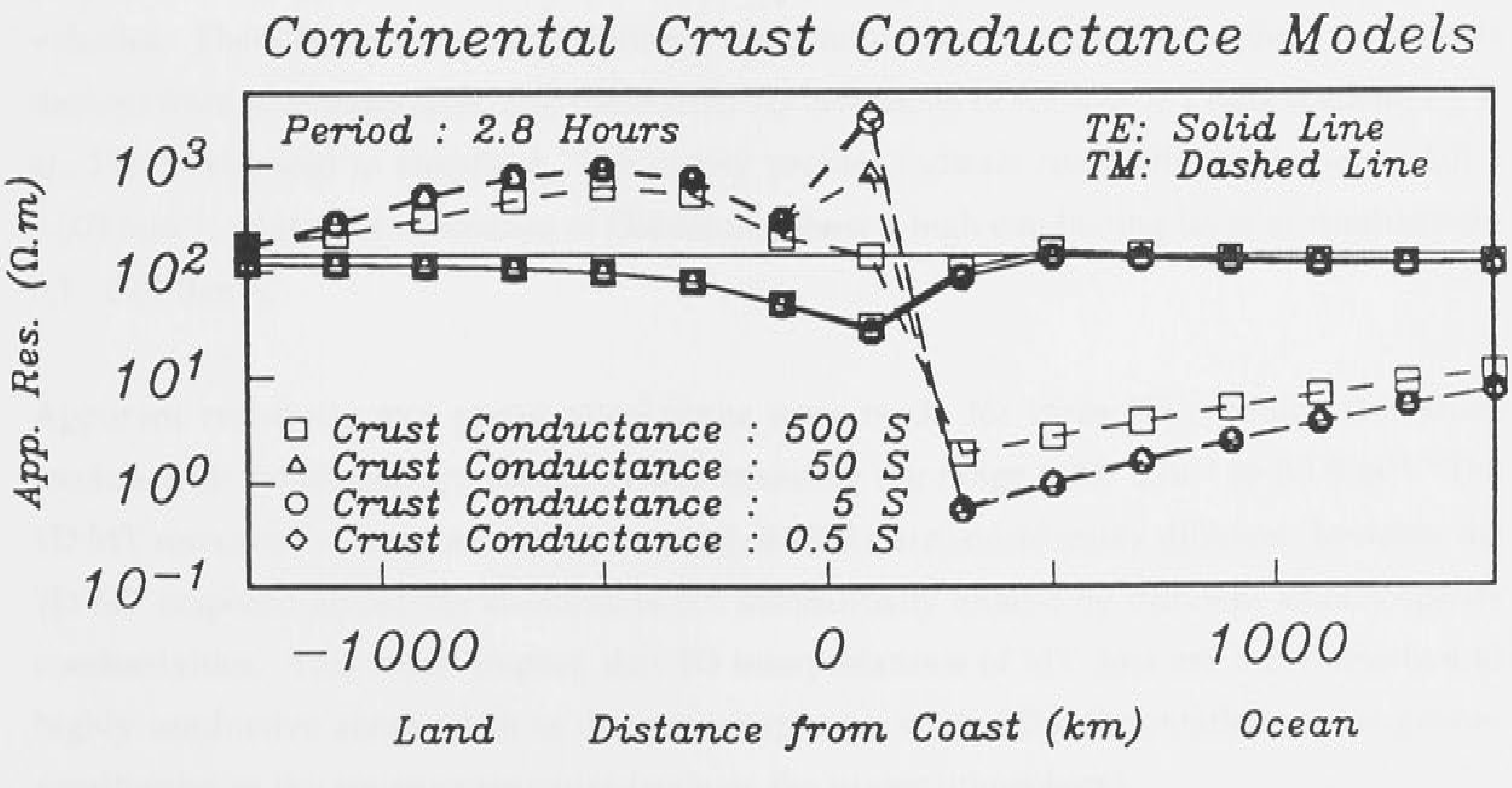

Figure 5.18 As for Figure 5.7, but for four cases of continental crust conductance.

This result implies that MT parameters are independent of the conductivity of continental crust, if it has a mean conductivity of less than 1.4×10^{-3} $S.m^{-1}$. Similarly, GDS induction arrows, from the top of the sheet, show no change for crustal conductivities less than this value. Conductivities smaller than 10^{-3} $S.m^{-1}$ are not untypical of the continental crust (Bailey *et al.*, 1989), so differences in the continental conductance do not have a profound effect on ocean floor EM observations. However, they are not unimportant: Fischer & Weaver (1986), in a modelling study of the coast effect, note that GDS methods are well suited to discriminate lateral lithological structure, provided that there is no major continental shelf present. Using a 2D numerical modelling algorithm, Kellett *et al.* (1991) have shown a significant conductivity contrast between continental and oceanic lithosphere for the coastline of southeast Australia. Unless stated otherwise, all further thin-sheet models documented in this thesis include a continental crust of conductance 50 S.

5.2.4 Conductivity of the Asthenosphere

The conductivities, depths and thickness of the asthenosphere and lower mantle are poorly determined from seafloor MT observations (Oldenburg *et al.*, 1984), and upper mantle models derived from laboratory measurements of conductivity of olivine are dependent upon assumptions implicit in their construction. Uncertainty estimates for the asthenosphere and lower mantle are listed in Table 5.3.

The conductivity of a region corresponding to the low-velocity zone is of major importance in geophysics. A highly conducting zone may imply a region of partial melt, or the presence of volatiles. There is a contradiction between the conductivity of the asthenosphere for models derived from laboratory data, and those from 1D inversions of seafloor MT data (Oldenburg *et al.*, 1984), reviewed in chapter 4. Laboratory profiles indicate conductivities between 0.01 - 0.003 $S.m^{-1}$, whilst the inversions of Oldenburg show a high conducting layer of conductivity 0.1 - 0.01 $S.m^{-1}$.

Apparent resistivity and phase calculations were made for three 2D coastline thin-sheet models with asthenosphere conductivities spanning the range 0.003 $S.m^{-1}$ to 0.1 $S.m^{-1}$. The 1D MT responses of these models at a period of 2000 s are considerably different: however the 2D MT response across the coastline is not substantially altered by different asthenosphere conductivities. This result implies that 1D interpretations of MT data are most sensitive to highly conductive zones (such as the asthenosphere), while 2D interpretations show greater sensitivities to the resistive structure (such as the upper lithosphere).

5.2.5 The Presence of a Continental Shelf and Continental Rise

The 2D coastline models described previously have been unrealistic, in that no continental shelf or slope is included. The width of the continental shelf varies considerably with tectonic environment. At passive margins, the continental shelf may extend out several hundred kilometres from the coastline, as far as the 200 m depth contour. Continental slopes are generally narrow, less than 50 km across, below which the continental rise forms the gentle slope of the ocean floor towards the abyssal plain. The continental rise may be absent, or up to several hundred kilometres wide. By contrast, the continental shelf is narrow or absent at active regions, which may be characterised by a deep trench on the ocean side.

A continental shelf of width 200 km and mean depth 250 m, and a continental rise (also of width 200 km and mean depth 2500 m) are included in a 2D thin-sheet coastline model. Real GDS induction arrows from the top of the sheet show a peak in response over the continental shelf, in contrast to the peak on land when no shelf is present. In addition, the peak in the real induction arrow is broader when a continental rise and shelf are present. Figure 5.20 shows a comparison between sub-sheet MT parameters from three models of passive margins. Magnetotelluric apparent resistivities are not profoundly influenced by the presence of the continental shelf and continental rise. The phase is more sensitive to the shallowing of the ocean, particularly close to the coastline. At a distance approximately 1000 km from the coastline, the MT response between the three models is similar.

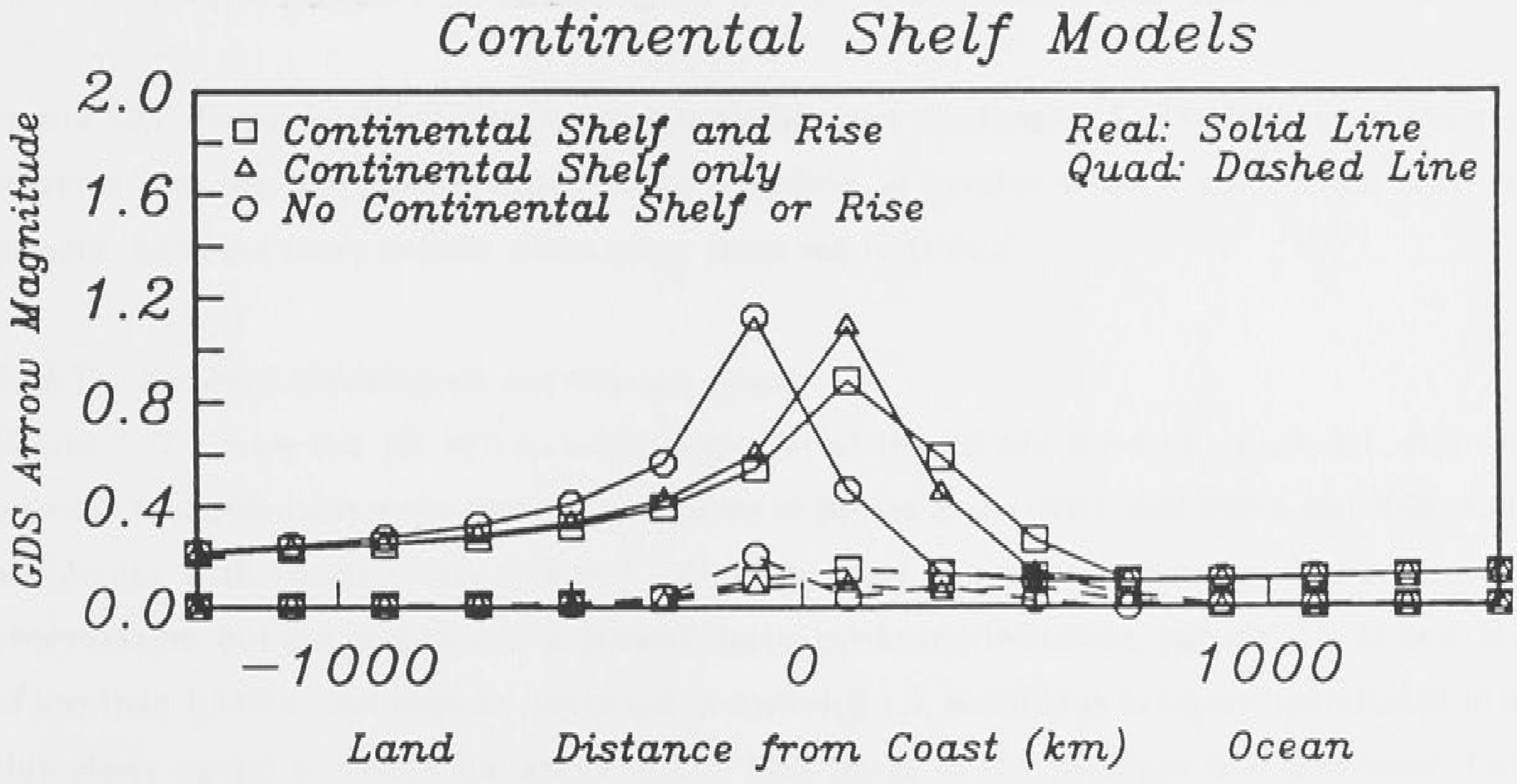

Figure 5.19 As for Figure 5.12, but testing the effects of a continental shelf and rise.

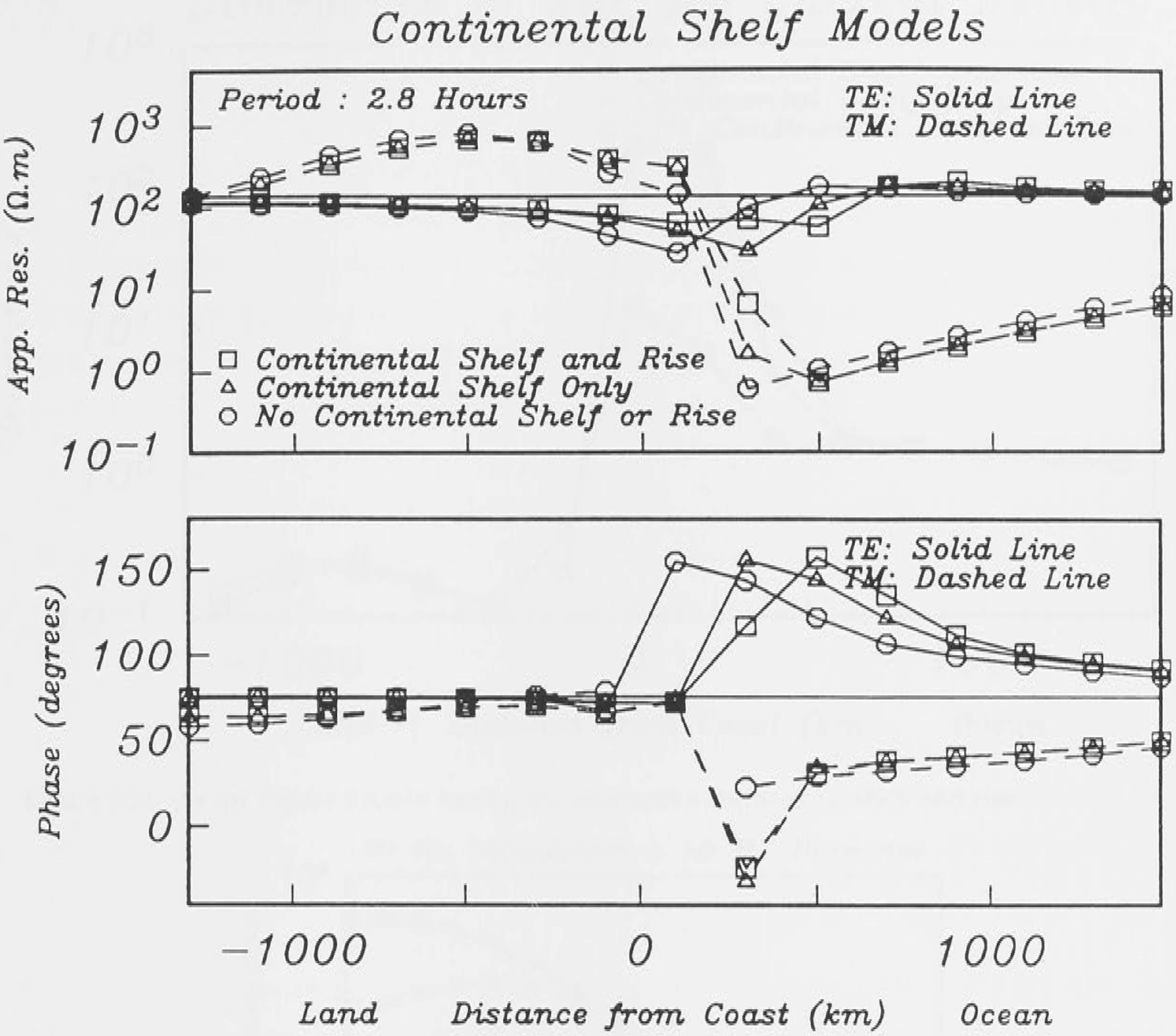

Figure 5.20 As for Figure 5.7, but testing the effects of a continental shelf and rise.

Figure 5.21 shows the 2D divergence of the surface current-density, J. The leakage of electric currents into the lithosphere, close to the coastline, is greater when a continental shelf is present; however there is little effect away from the coastline.

5.2.6 The Presence of Sediments and Oceanic Crust

Figure 5.22 shows the 1D MT forward response of the 70 Ma lithosphere model with an oceanic crust defined from in-situ measurements of Becker *et al.* (1982), and 500 m and 1000 m of sediments with conductivity 1 $S.m^{-1}$. Oceanic crust is not of major significance to MT observations, but the presence of sediments has a profound influence, particularly at periods of less than 10000 s. For reasons discussed in section 5.1.3, sediments can only be included in a thin-sheet model is within the sheet itself. This leads to the problem that thin-sheet EM fields are calculated at the top and bottom of the sheet, equivalent to observations on the sea-surface and beneath the sediments, whereas for the purpose of comparison with seafloor observations it is desirable to calculate the response at the top of the sediments.

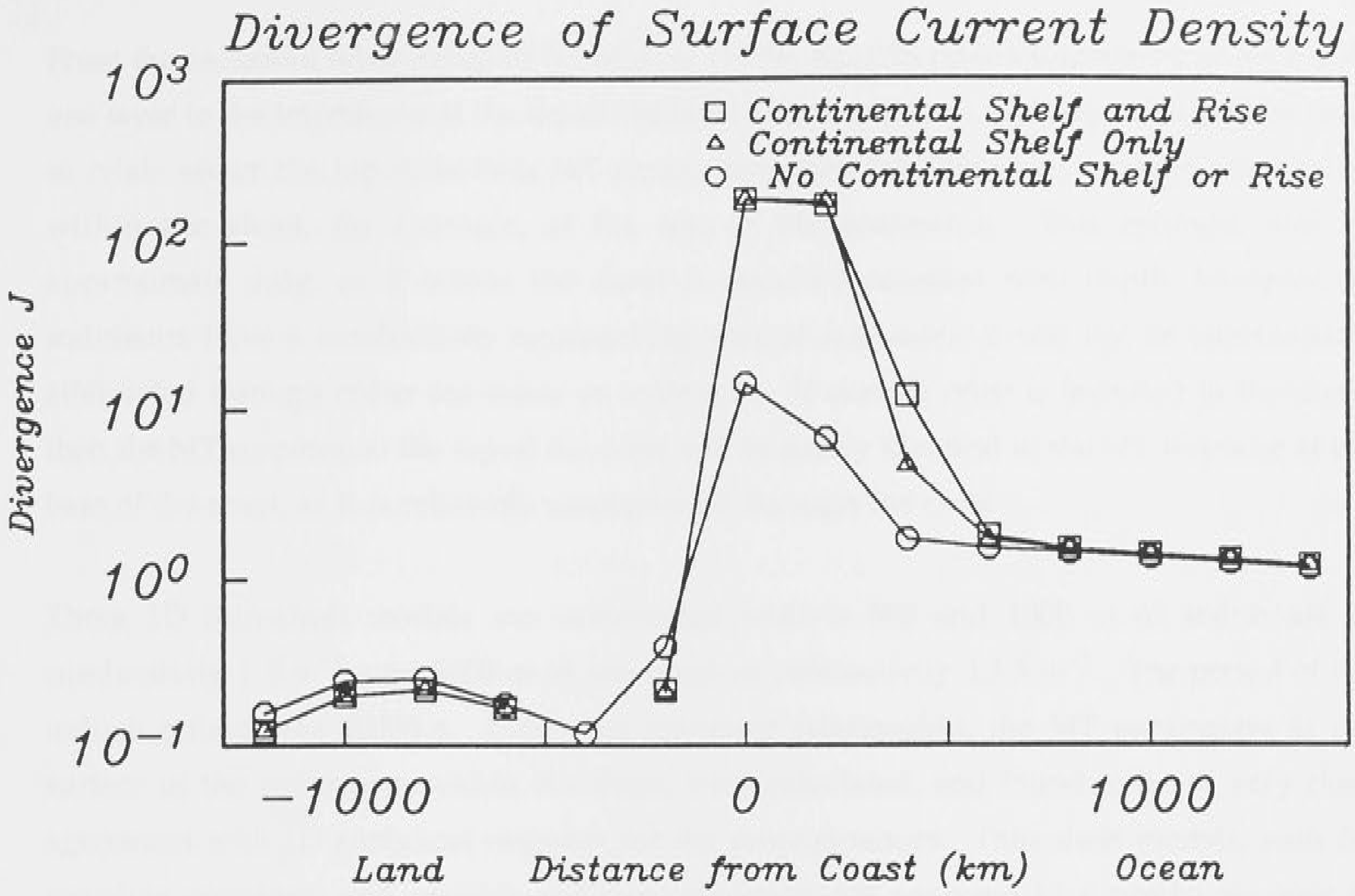

Figure 5.21 As for Figure 5.6, but testing the effects of a continental shelf and rise.

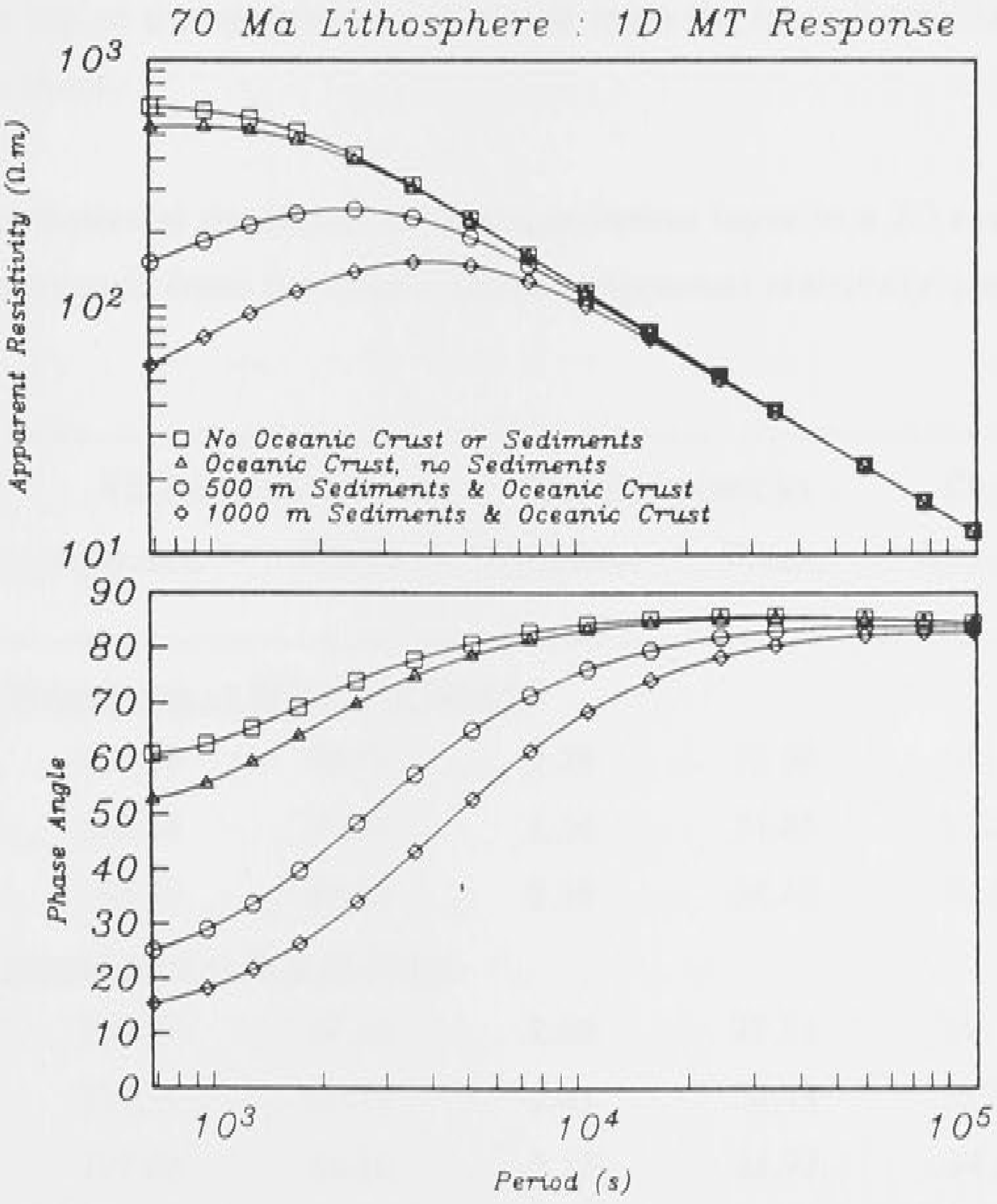

Figure 5.22 The 1D MT response of the 70 Ma lithosphere conductivity structure defined in Table 5.3, for four cases of oceanic crust and sediments, over a range of periods typical of seafloor MT observations.

From the recursive relationship of Schmucker (1970), eq. 2.55 relates impedance at the top of one layer to the impedance at the top of the layer above or below. This equation may be used to relate either the top of bottom MT parameters from the thin-sheet to some other point within the sheet, for example, at the top of the sediments. This estimate will be approximate only, as **E** within the sheet is assumed constant with depth; however, as sediments have a conductivity approaching that of sea-water, **E** will not be substantially attenuated through either sea-water or sediments. If oceanic crust is included in the sheet, then the MT response at the top of the crust will be nearly identical to the MT response at the base of the sheet, as **B** is relatively unattenuated through the crust.

Three 1D thin-sheet models are constructed with 0, 500 and 1000 m of sediments of conductivity 1 $S.m^{-1}$, and 5000 m of sea-water of conductivity 3.3 $S.m^{-1}$. The period of the inducing field was 10000 s. Using the recursive relationship, the MT parameters at the surface of the sediments, within the sheet, were calculated, and found to be in very close agreement with the 1D analytical response for the same structure. Thin-sheet models, with 2D coastline structure, and variable sediment thickness are analysed in a similar manner to determine the MT response at the top of the sediment layer. Table 5.8 lists the MT parameters at the top of the sediments, calculated from the impedances at both the top and the bottom of the sheet.

Table 5.8 MT parameters at the top of an ocean sediment layer in a 2D coastline model, at a location 900 km seawards from the coast. Units of apparent resistivity are Ω.m and units of phase are °.

Sediment	TE Polarisation		TM Polarisation		One-Dimensional	
(m)	App.Res.	Phase	App.Res.	Phase	App.Res.	Phase
Calculated From Impedance at Bottom of Sheet						
0	157.99	99.76	2.78	35.38	141.34	75.77
500	162.54	90.29	2.56	34.85	132.75	69.79
1000	158.29	80.83	2.38	34.42	94.80	52.42
Calculated From Impedance at Top of Sheet						
0	233.27	97.46	2.69	27.51	141.34	75.77
500	233.30	80.12	2.41	26.15	132.75	69.79
1000	197.83	64.20	2.17	24.92	94.80	52.42

The MT parameters, calculated from the impedances at the top and bottom of the sheet, are different. Comparison with the calculated 1D response for the seafloor site shows that the situation is generally dominated by 2D effects; though the TE phase angles show sensitivity to increasing sediment thickness.

5.3. Sensitivity of EM Observations to Ocean Basin Geometry

5.3.1 Introduction

It has been suggested by Wannamaker *et al.* (1989b) that a subducting slab may act as a leakage path for induced electric currents in the ocean to the deeper, and more conductive, parts of Earth. Spreading ridges, with anomalously high temperatures and zones of partial melt, may also act as a low resistance path (Filloux, 1982b) for induced electric current in the ocean. The resistivity of the uppermost parts of the lithosphere is of profound importance to the distribution of induced telluric currents. Controlled source EM data (Cox *et al.*, 1986; Evans *et al.*, 1991) have indicated that the lithosphere is electrically resistive; however, Vanyan *et al.* (1990) have argued that anisotropy in the lithosphere, manifest as fluid-filled cracks, may improve the vertical conductivity, and so leakage of electric current through the lithosphere will be correspondingly higher. Leakage paths at passive continental margins may also be present through the continental lithosphere (Kellett *et al.*, 1991).

These factors complicate a simple 3D induction interpretation in terms of conductive ocean - resistive lithosphere contact. Nevertheless, a large fraction of Earth's coastlines are passive margins, with no obvious leakage paths, and the major part of Earth's oceanic lithosphere is older than 10 Ma, so a simple approximation of having no leakage paths to deeper parts of the upper mantle is a suitable analogue for some of Earth's ocean basins, although such models probably represent an upper-bound on the 3D EM induction effects.

Even where obvious leakage paths are present, such as the subducting Juan de Fuca Plate (Wannamaker *et al.*, 1989b), the conductance of the leakage path is small compared to the conductance of the ocean. Wannamaker *et al.* (1989b) modelled the conductance of the subducting slab as approximately 1000 S under the coast to less than 100 S at a distance 60 km inland. Fainberg (1980) shows that a large fraction of the ocean basins, particularly away from the continental shelf, have conductances of greater than 10000 S.

In this section, the EM induction effects in 2D and 3D basins are examined. A thin-sheet model is used to represent simple ocean basin geometries which are analogous to Earth's real oceans. The influence of the position of the coastline on synthetic seafloor MT parameters are considered, to assess how such synthetic data may be distorted from the 1D response of the underlying structure, and from a 2D single coastline interpretation.

5.3.2 Model Description

Simple ocean-basin configurations, shown in Figure 5.23, are incorporated into a thin-sheet which comprises a uniform depth ocean, with oceanic and continental crust. Underlying the thin-sheet is the 70 Ma layered half-space, chosen as being appropriate for a typical ocean basin, such as the Pacific.

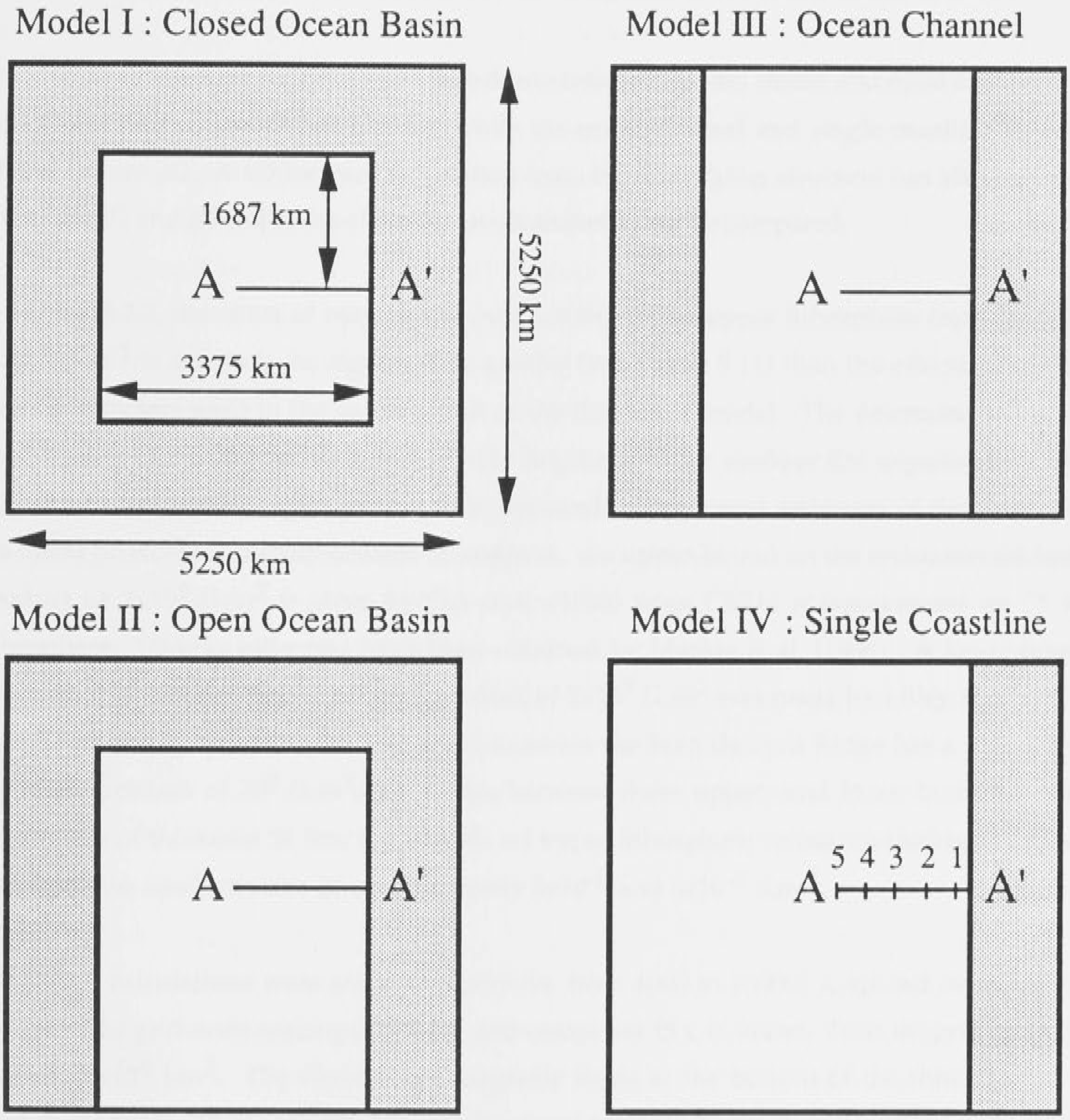

Figure 5.23 Four simple ocean basin geometries modelled by the thin-sheet method. The continental margins are shown in grey . The thin-sheet is 5 km thick, and comprises continental crust or sea-water, with conductivities 0.01 and 3.3 Sm^{-1} respectively. MT parameters are calculated along transect A-A', at grid-nodes 1 to 5 (shown in Model IV).

The thin-sheet models shown in Figure 5.23 are not intended to be accurate representations of real ocean basins, owing to the limitation of a 1D substructure and the coarseness of the 15 x 15 numerical grid. Also, induction in large oceans is more complicated than considered here, and spherical geometry may become important (see Beamish *et al.*, 1983 for induction in Earth's oceans by the daily variational source-field). However, the shapes of the basins do have simple analogues: for example the north Pacific Ocean and Indian Ocean for the open ocean basin (Model II), Atlantic and Tasman Sea for the open ocean channel (Model III), and the Pacific coast of South America for the single coastline (Model IV); thus some of the EM response characteristics of these models may be recognised in the ocean basins of Earth.

The thin-sheet configurations can be classed into two groups: the closed and open ocean basins (Models I and II) have 3D geometries, while the ocean channel and single coastline (Models III and IV) are 2D. A 1D forward calculation from the underlying structure can also be made. Thus, 1D, 2D and 3D induction effects in an ocean basin may be compared.

In section 5.2.2, the effect of varying the conductivity of the upper lithosphere from 3×10^{-6} to 3×10^{-3} S.m^{-1} is shown to be significantly greater (see Figure 5.11) than the effects of varying other parameters used in the construction of the thin-sheet model. The determination of the conductivity of mature lithosphere has wide implications for seafloor EM experiments. Two thin-sheet models investigate published upper- and lower-bound estimates of the resistance-thickness product for the sub-oceanic lithosphere. An upper-bound on the resistance-thickness product of 2×10^{9} Ω.m^{2} is given by Cox *et al.* (1986) from CSEM measurements on 25 Ma lithosphere. Similar estimates have been obtained by Mackie *et al.* (1988). A lower-bound estimate on the resistance - thickness product of 2×10^{7} Ω.m^{2} was made by Lilley *et al.* (1989). The 2D resistivity model of the Lincoln line, across the Juan de Fuca Ridge has a resistivity - thickness product of 10^{8} Ω.m^{2}, which lies between these upper- and lower-bounds. For a lithosphere of thickness 58 km, the bounds on upper lithosphere resistance-thickness product translate into conductivities of approximately 3×10^{-5} and 3×10^{-3} S.m^{-1}.

Thin-sheet calculations were made at 6 periods, from 1000 to 100000 s, spaced evenly in log domain. The grid-node spacing is 375 km, and comprises 15 x 15 nodes. Thus the grid covers an area of 28×10^{6} km^{2}. The electric and magnetic fields at the bottom of the thin-sheet were used to calculate MT parameters, along a 'seafloor' transect A - A' at grid-nodes 1 to 5, shown in Figure 5.23. The parameters are presented, in figures now to be described, for 'TE' and 'TM' modes (parallel and perpendicular to a north-south coastline).

5.3.3 Upper-Bound Estimate of Resistance-Thickness Product : $2x10^9$ $\Omega.m^2$

Figures 5.24 (a and b) show computed TE parameters for the thin-sheet models, using an upper-bound on the resistance-thickness product for the lithosphere. There are significant differences between the 1D, 2D and 3D models at all periods. The apparent resistivities of Models I and II are attenuated by factors ranging from 10 to 100, relative to the true 1D apparent resistivity, and the phases show corresponding differences. The attenuation is greatest, and almost independent of period, for Model I. By contrast, the attenuation reduces with period for Model II. There is no significant difference between sites at different grid-nodes, except at the grid-node 1 (closest to the coastline) where the low period apparent resistivities are significantly higher than at the other sites. Models III and IV have a 2D geometry, and show close agreement at all periods (except at 1000 s); they recover the 1D apparent resistivity response of the underlying structure at long periods. There is, however, a peak in the apparent resistivity at a period of about 6000 s and the magnitude of the peak is dependent upon distance from the coastline. Boteler (1988) has suggested that such a peak occurs due to the seafloor magnetic field strength passing through a minimum as a function of distance from the coastline, the location of which is dependent upon the skin depths in the continent and in the ocean.

The TE phase in Figure 5.24 b is more complicated, but again there are major differences between the 1D, 2D and 3D models. The 1D phase is not recovered by either 2D or 3D models. In general, the 2D model phases increase rapidly from 10° to 20° less than the 1D phase at the shortest periods, to 20° more than the 1D phase at period 10000 s. From this period to 100000 s, the phase is constant, at around 80°. The 3D models have phase angles similar to the 1D model at 1000 s, but are less than the 1D model phase at all other periods. Model II has a minimum in phase at a period of about 8000 s, then approaches the 1D phase at longer periods; whilst the difference between the phase angles from Model I and the 1D forward response increases with increasing period.

Figures 5.25 (a and b) show computed TM parameters. The TM apparent resistivities are considerably smaller than the 1D forward response (due to electric charge accumulation at the coastline) by a factor of 100 to 1000, for both 2D and 3D ocean basins. In particular, there is close agreement for Models I, II and III where the ocean is bounded on two sides. Single-coastline Model IV shows greater apparent resistivities, which approach the 1D forward response at the longest periods. Thus, TM estimates are relatively insensitive to 3D induction effects; however, they are sensitive to the inclusion of additional 2D structure, such as a second coastline.

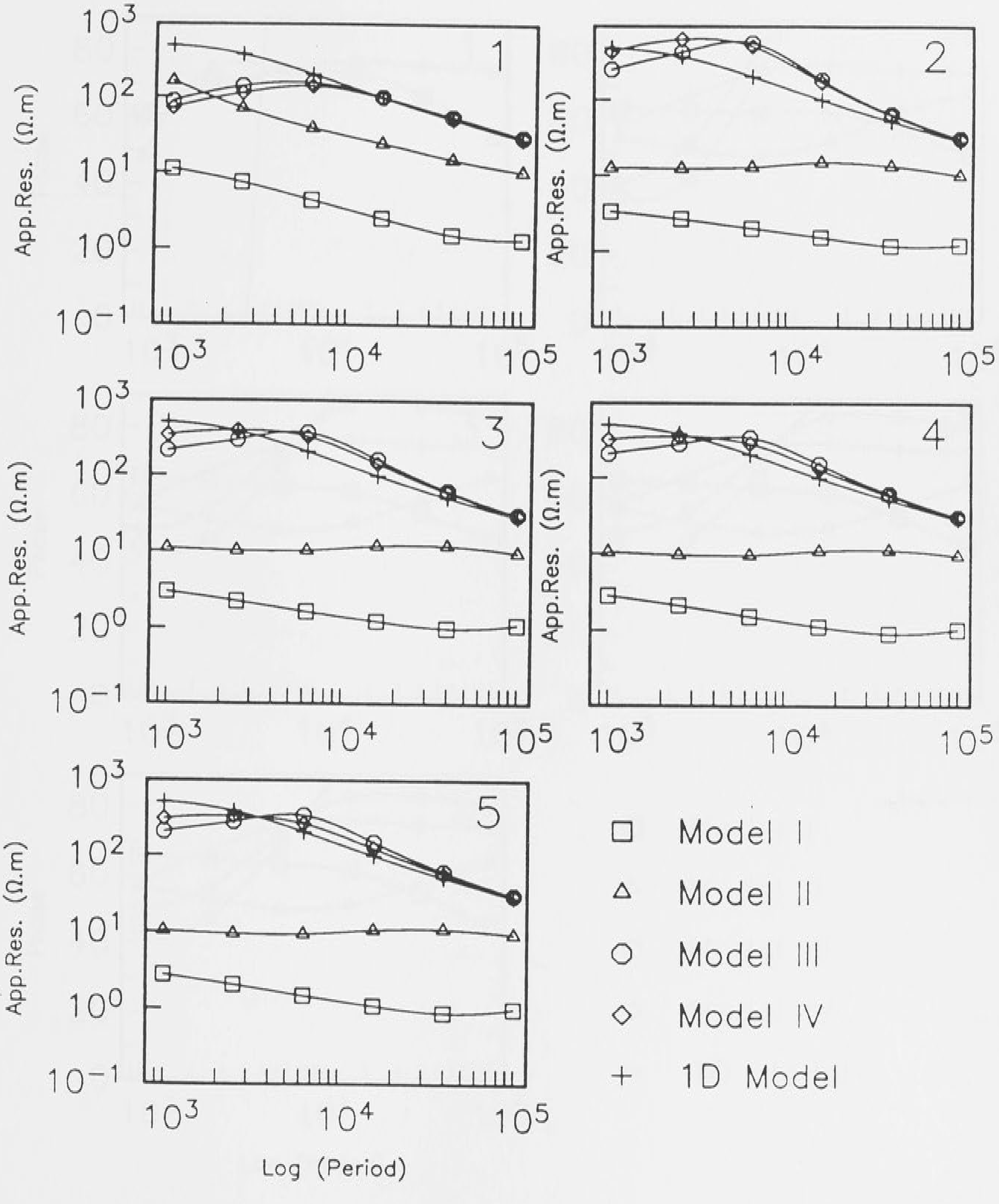

Figure 5.24 (a) TE apparent resistivity curves. The number in the top right of each diagram states the grid-node position along transect A-A'. Results for the four ocean models are shown, and also the 1D response of the underlying structure. These results are for a lithosphere of resistance-thickness product $2\text{x}10^{9}$ $\Omega.\text{m}^{2}$.

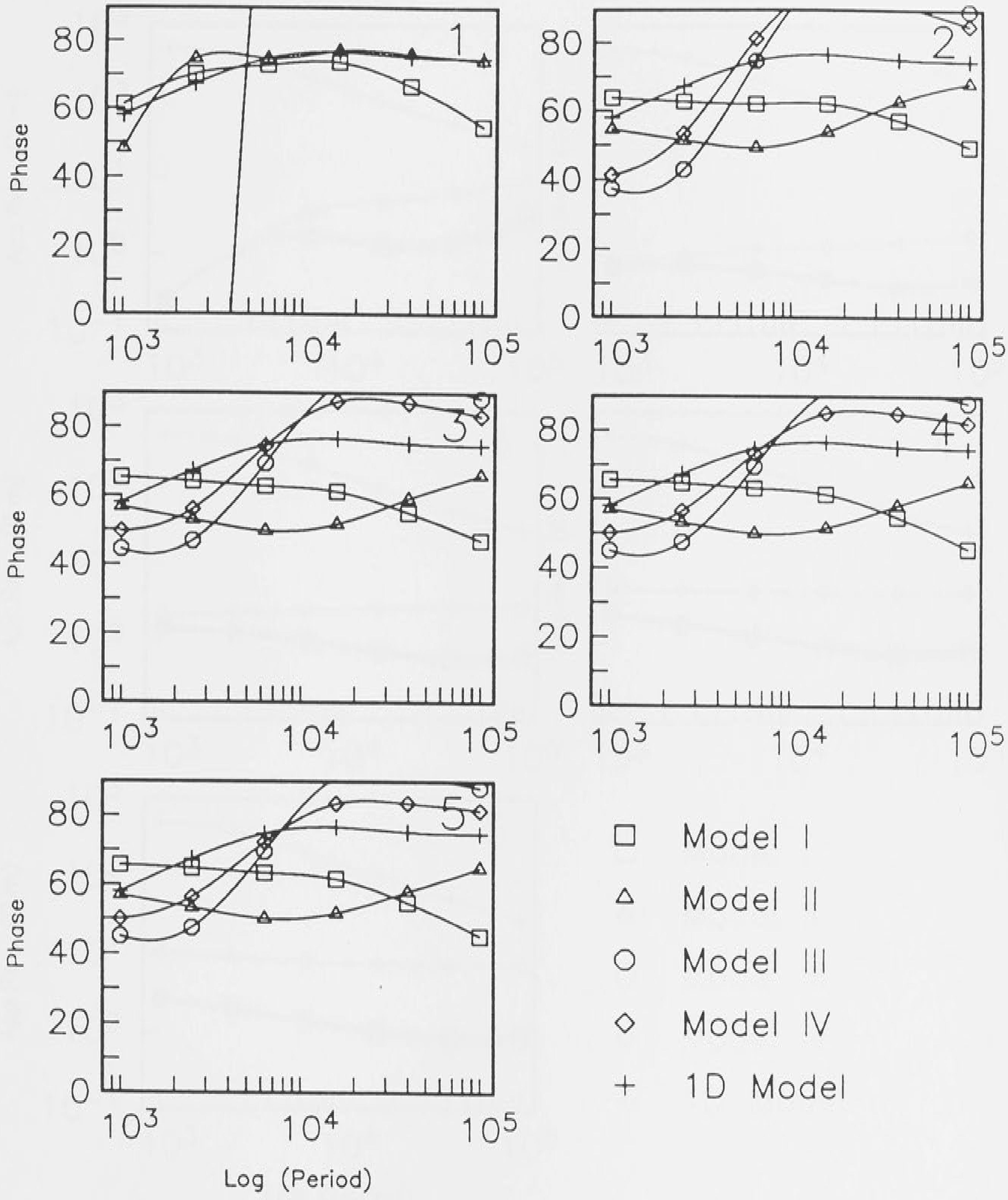

Figure 5.24 (b) As for Figure 5.24 a, but phase values.

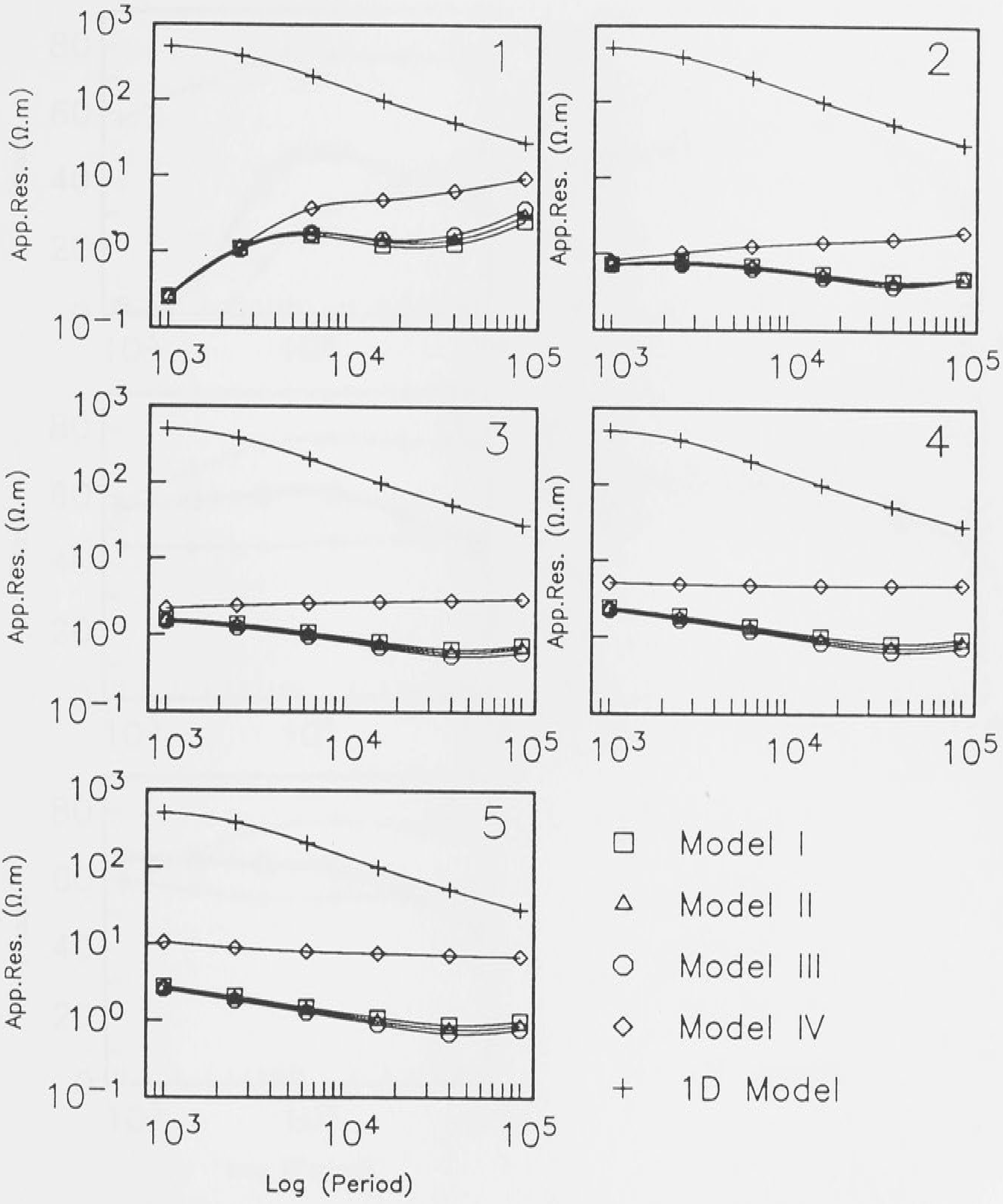

Figure 5.25 (a) As for Figure 5.24 a, but TM mode.

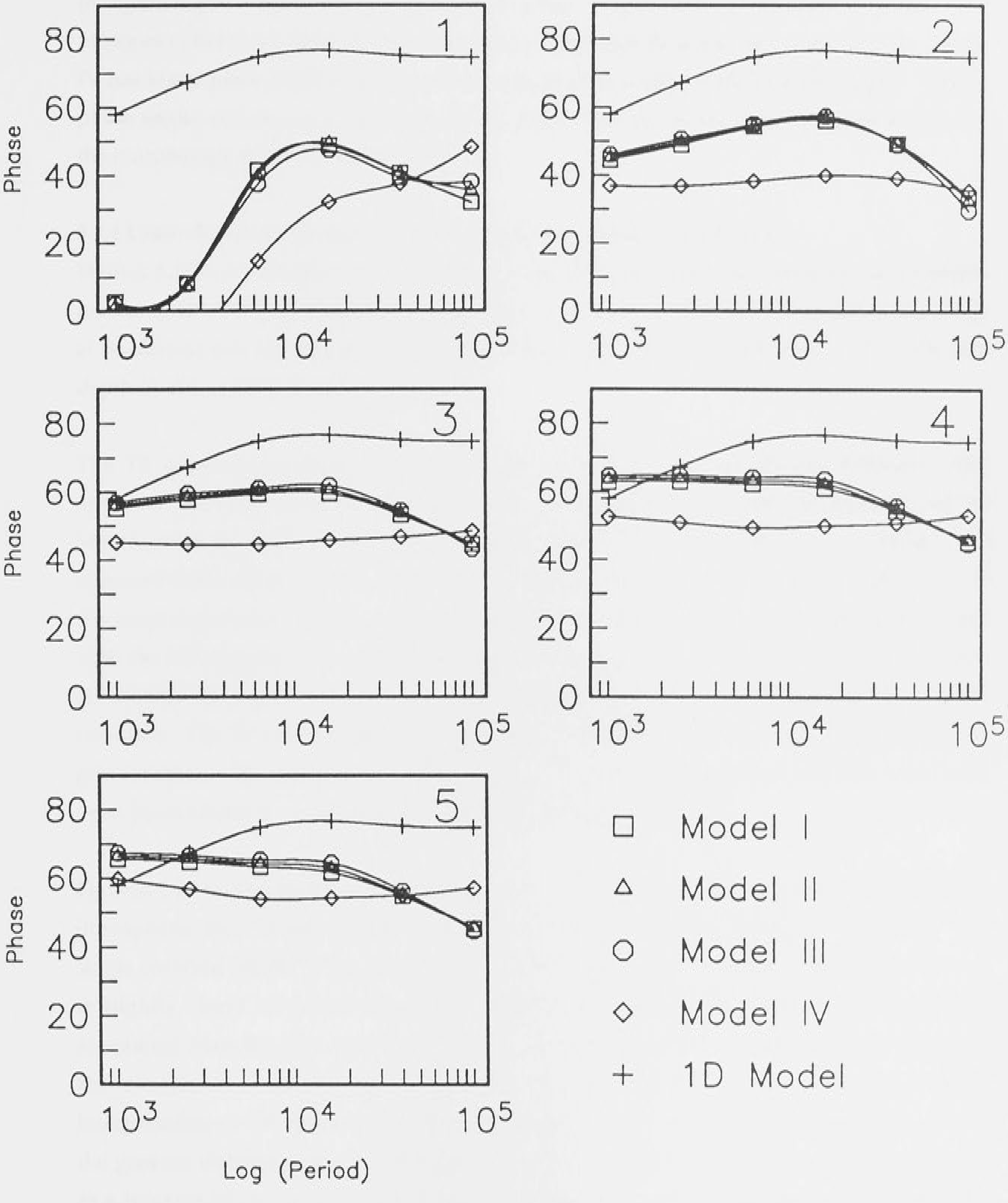

Figure 5.25 (b) As for Figure 5.24 b, but TM mode.

There is similar agreement between Models I, II and III in the TM phase calculations, shown in Figure 5.25 b. At the shortest period, the phase is close to the 1D forward response. The response is flat to a period of 20000 s, and the phase angle decreases at longer periods. Model IV has lower phase angles than the other three models, except at the longest period. The TM phase angles are generally less than the 1D phase, and the shows little correspondence with the morphology of the 1D forward response.

5.3.4 Lower-Bound Estimate of Resistance-Thickness Product : $2x10^7\ \Omega.m^2$

Figures 5.26 (a and b) show the TE responses for the same models, but using the lower-bound resistance-thickness product for the lithosphere. Thin-sheet calculations could not be made at the lowest two periods, as the spacing between grid-nodes is greater than 33 % of the skin depth in the underlying layer.

The TE apparent resistivity from the three models is not substantially different. The apparent resistivity from the 2D models show close agreement with the 1D response, but the MT response from the 3D models is slightly lower than the 1D response: for Model I, the apparent resistivity is less by a factor of ~5, whilst for Model II, it is less by a factor of ~2. At the longest periods, the phase shows close agreement between all ocean basin models, and with the 1D response. There is more disagreement at the shorter periods: the phase from the 2D models are slightly lower than the 1D response at all grid locations except close to the coastline. The 3D models phase are greater than the 1D response at all periods and at all grid locations. The closed ocean basin phase from Model I is greater than that from the ocean open basin Model II, and is greater than 90° at the shortest periods.

Figures 5.27 (a and b) show the TM responses. As for the models with the most resistive lithosphere, the TM parameters show close agreement between Models I, II and III. The single coastline Model IV response has the same morphology as the other models; however it is slightly closer to the 1D response. Apparent resistivities for Models I, II and III are attenuated from the 1D response by a factor of approximately 5, except at the site closest to the coastline, at which the attenuation is much greater at the shortest periods. Interpretation of TM phase is less obvious.' There is general agreement between all models; the greatest difference is with Model IV. The morphology of the thin-sheet phase response, as a function of period, is completely different from the true 1D response, and is dependent upon the distance from the coastline: it shows that the phase of the seafloor **B** , parallel to the coastline, changes rapidly away from the coast. The trend from the coastline to the centre of the basin is for the phase angle to increase to angles greater than 90°. At the longest period, the phase shows good agreement with the 1D response.

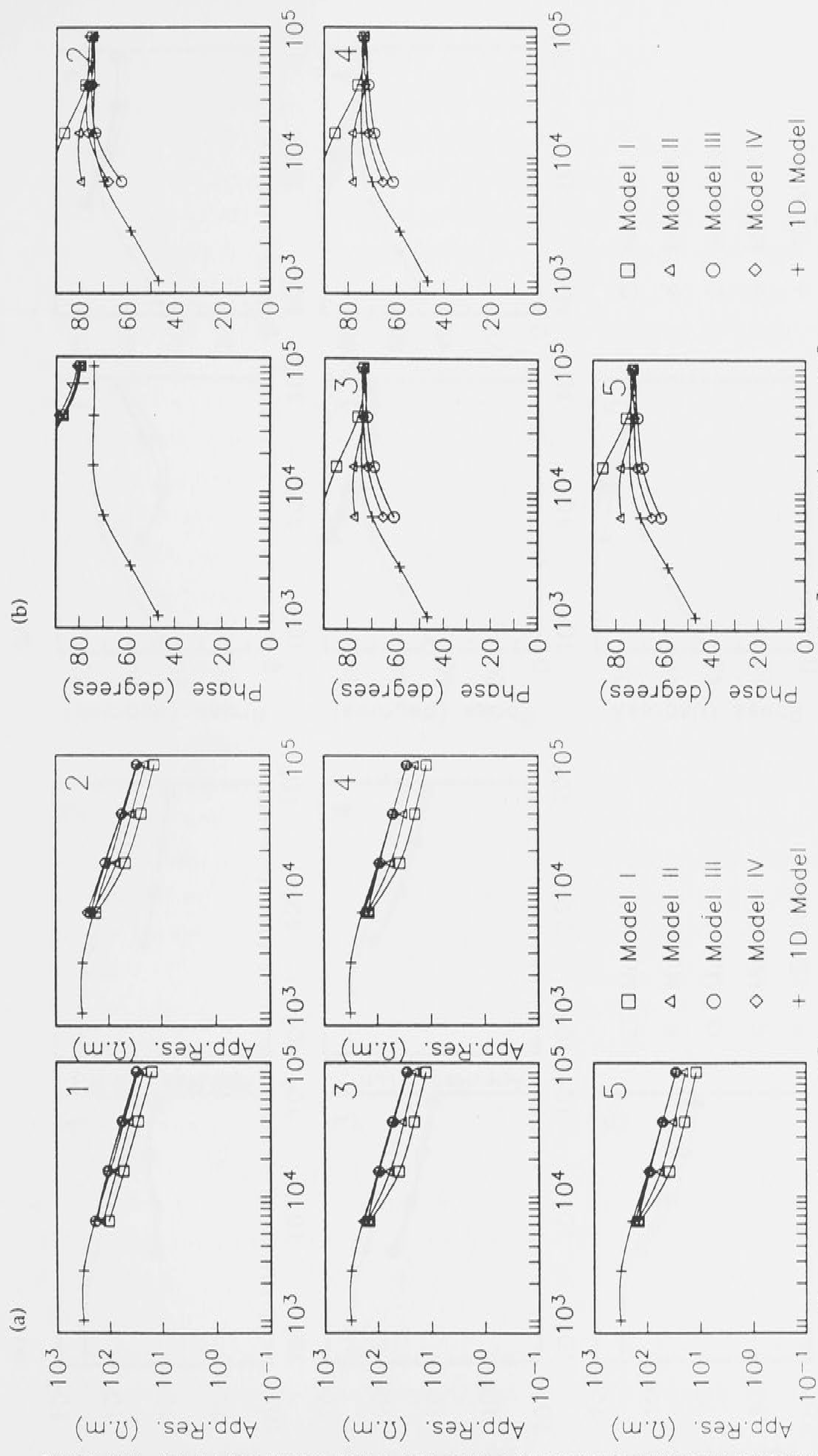

Figure 5.26 (a) As for Figure 5.24 a, but with a lithosphere resistance-thickness product of 2×10^7 $\Omega.m^2$. (b) As for Figure 5.26 a, but phase values.

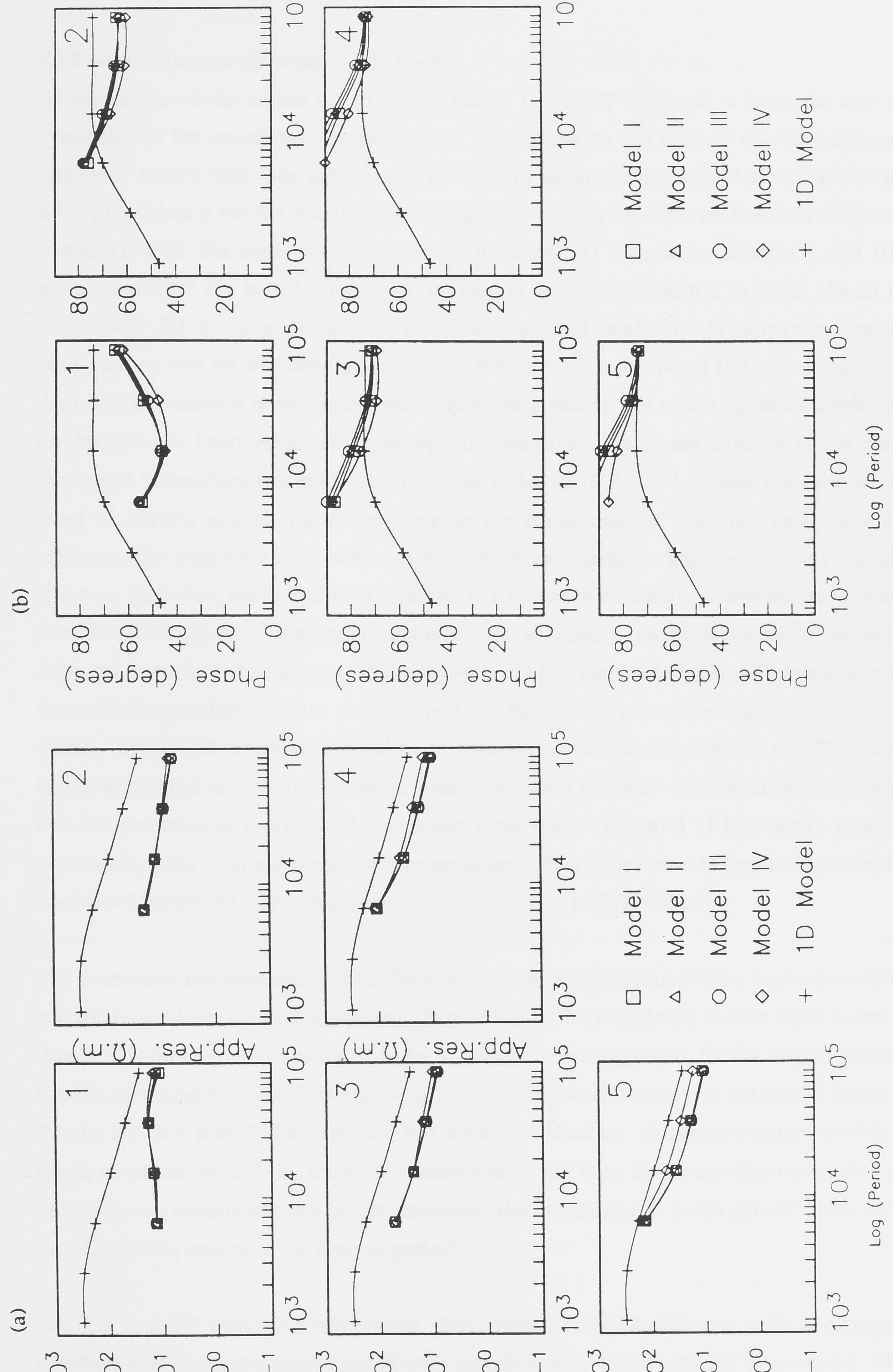

Figure 5.27 (a) As for Figure 5.26 a, but TM mode. (b) As for Figure 5.26 b, but TM mode.

5.3.5 Interpretations Of Ocean Basin Models

At the centre of the closed ocean basin (Model I) the MT response is isotropic due to the symmetry of the coastlines. However, MT parameters do not recover the 1D response; the apparent resistivities are attenuated by factors of approximately 100 for the resistive lithosphere and 5 for the conductive lithosphere. At any location on the floor of the ocean basin, TE and TM apparent resistivities (for both 3D thin-sheet Models I and II), are attenuated from the true 1D response, by factors which vary from 2 to 1000. As all ocean basins are 3D to some extent, it suggests that real seafloor MT apparent resistivity observations will be similarly reduced from the true 1D response of the upper mantle. The degree of attenuation is dependent more upon the conductivity of the upper lithosphere than on the distance from the coastline, except for grid-nodes which are adjacent to the coast. If the upper lithosphere has conductivity of the order of 10^{-3} $S.m^{-1}$ or less, then the widths of most of Earth's oceans are comparable to the compensation distance, especially as the compensation distances from each coastline which surrounds the basin will have a cumulative effect on the whole ocean basin. Therefore, MT apparent resistivity observations may be less than the 1D response of the underlying structure, at most, if not all, locations on the seafloor. Thus, an important conclusion is that single-site 1D MT interpretations will generally produce conductivity profiles that are too conductive. Better interpretations may result from a 2D model, using TM apparent resistivities and phase which are robust to 3D structures (Wannamaker *et al.*, 1984). However, the differences between Models III and IV suggests that the presence of a second 2D coastline, even many thousand of kilometres away, may profoundly alter a single coastline interpretation. This conclusion is applicable even in the case of a lithosphere with resistance-thickness product of 2×10^7 $\Omega.m^2$.

The anisotropy between the TE and TM apparent resistivity is found to be dependent upon the conductivity of the upper lithosphere. Table 5.9 lists the anisotropy for the open ocean basin (Model II) and the ocean channel (Model III) as a function of period, for the upper- and lower-bounds of lithosphere conductivity, at grid-node 4. The anisotropy in the closed ocean basin (Model I) is less than 2 at all periods, and for both resistance - thickness product models. The single coastline (Model IV) shows a smaller anisotropy than the ocean channel model, as the TM apparent resistivities are larger; however, the anisotropy is much greater than either of the 3D models, except at the longest period.

The 2D and 3D induction effects are thus shown to be significant, with the important corollary that induction effects introduce a complex distortion of the MT parameters. The 1D MT responses of the underlying structures, shown in Figures 5.24 and 5.26, vary smoothly with period, and neither apparent resistivity nor phase indicate major complexity in the electrical sub-structure. By contrast, the synthetic MT sounding curves at the seafloor sites contains many spurious peaks and troughs, which, if interpreted as 1D structure, would result in misleading conductivity profiles.

Table 5.9 Anisotropy (TE apparent resistivity / TM apparent resistivity) for the open ocean basin (Model II) and the ocean channel model (Model III) as a function of period, for a grid-node approximately 1300 km away from the coastline

Period (s)	Resistive Upper Lithosphere		Conductive Upper Lithosphere	
	Model II	Model III	Model II	Model III
1000	4.52	92.09	-	-
2512	5.46	169.50	-	-
6309	7.48	285.19	1.14	1.35
15850	11.69	179.68	1.66	2.62
39811	15.21	95.59	1.79	2.96
100000	11.17	41.01	1.78	2.79

The thin-sheet models described above represent simple cases. In real ocean basins there may be other effects, such as leakage paths (of a subducting slab or spreading ridge) to the deep conductive parts of Earth.

5.3.6 Three-Dimensional Interpretations of Seafloor Magnetotelluric Data

The north Pacific Ocean, shown in Figure 2.6, has a geometry which is most closely analogous to the ocean basin closed on three sides (Model II). Figure 5.27 shows comparisons between seafloor MT data from experiments in the north Pacific Ocean, the 1D forward-response above the modelled lithosphere beneath the thin-sheet (with resistance-thickness product of 2×10^9 $\Omega.m^2$) and the Model II MT data from the bottom of the sheet at grid-nodes which are in a similar location to the observing site.

Model II is not intended to be an accurate representation of the north Pacific Ocean, and furthermore, the attenuation exhibited in the thin-sheet model is probably more extreme than exists for real ocean basins, as no leakage paths to the deeper parts of the mantle are included. However, thin-sheet MT data from Model II have a remarkably similar morphology to seafloor MT data, especially conspicuous in phase values.

The difference between the 1D response of the lithosphere beneath the sheet, and the thin-sheet MT data from Model II, suggests why D^+ inversions of observed seafloor MT data give rise to negative serial correlation in the residuals. Three-dimensional induction effects in Model II are manifest in the thin-sheet MT parameters most strongly at short periods: the difference in attenuation of apparent resistivity with increasing period is reflected in the negative correlation of D^+ apparent resistivity residuals. Negative correlation between the D^+ residuals were found for each of the 20 seafloor MT data analysed, which suggests that perhaps all such observed data are attenuated at short periods, in a similar manner to the calculated MT response from Model II.

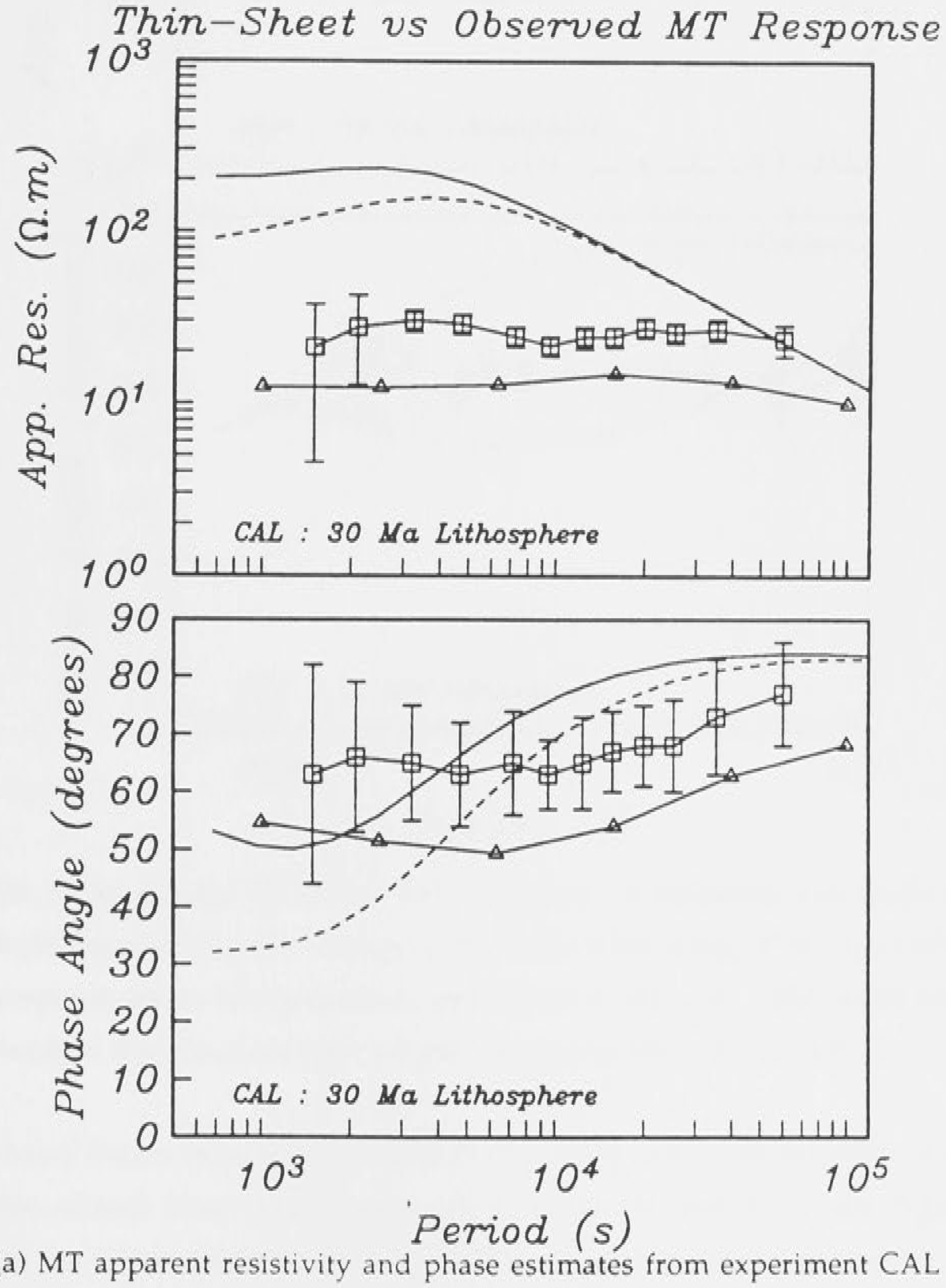

Figure 5.27 (a) MT apparent resistivity and phase estimates from experiment CAL (Filloux, 1980a, 1980b; Oldenburg, 1981) (error bars and small squares); the predicted 1D response above 30 Ma seafloor, with (dashed line) and without (solid line) 500 m sediment; and the thin-sheet MT response (triangles) in ocean basin Model II at a grid-node corresponding to the location of the CAL experiment. The upper lithosphere beneath the thin-sheet has resistance-thickness product of 2×10^9 $\Omega.m^2$.

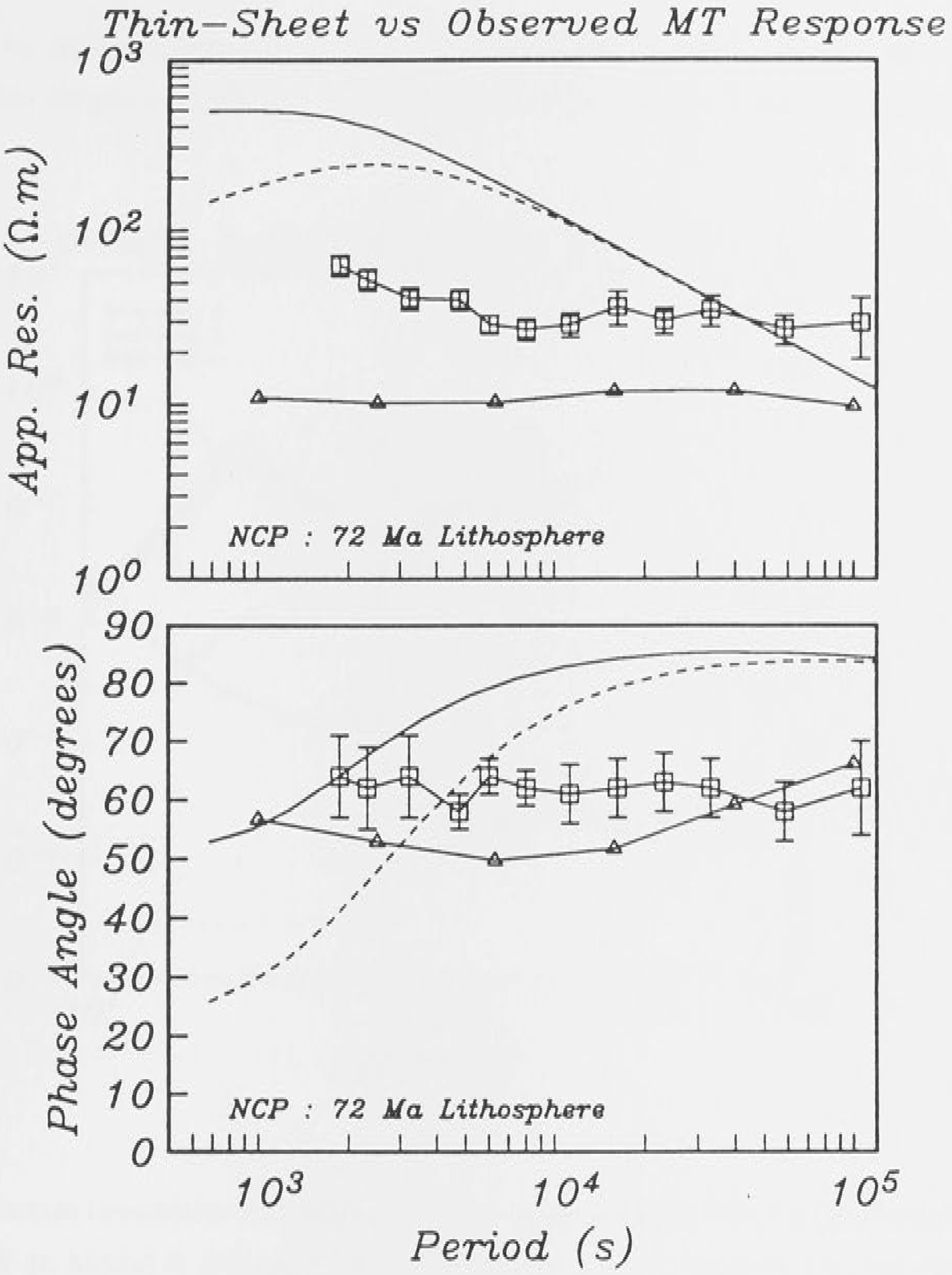

Figure 5.27 (b) As for Figure 5.27 (a) but with MT apparent resistivity and phase estimates from experiment NCP (Filloux, 1977, 1980b; Oldenburg, 1981), the predicted 1D response above 72 Ma seafloor, and Model II MT data. The upper lithosphere beneath the thin-sheet has resistance-thickness product of 2×10^9 $\Omega.m^2$.

Figure 5.28 shows Occam inversions of Model II MT data (with 5 % randomly-distributed Gaussian noise added) from the five grid-nodes along transect A-A' (see Figure 5.23), compared with the 1D structure underlying the thin sheet. The Occam inversions are more conductive than the underlying structure, and furthermore, spurious high conductivity peaks are generated. The deep rise in conductivity is modelled at the correct depth for the underlying structure, but is too conductive. If seafloor MT data are distorted from the true 1D response of Earth in a similar manner as the thin-sheet MT responses in Model II, it implies that the oceanic lithosphere and upper mantle are more resistive than has previously been interpreted. The question of whether Earth's true electrical conductivity structure is close to that defined by olivine conductivity with a small fraction of melt and/or volatiles is not resolved by this simple analysis, but is considered in detail for the Tasman Sea in chapter 7.

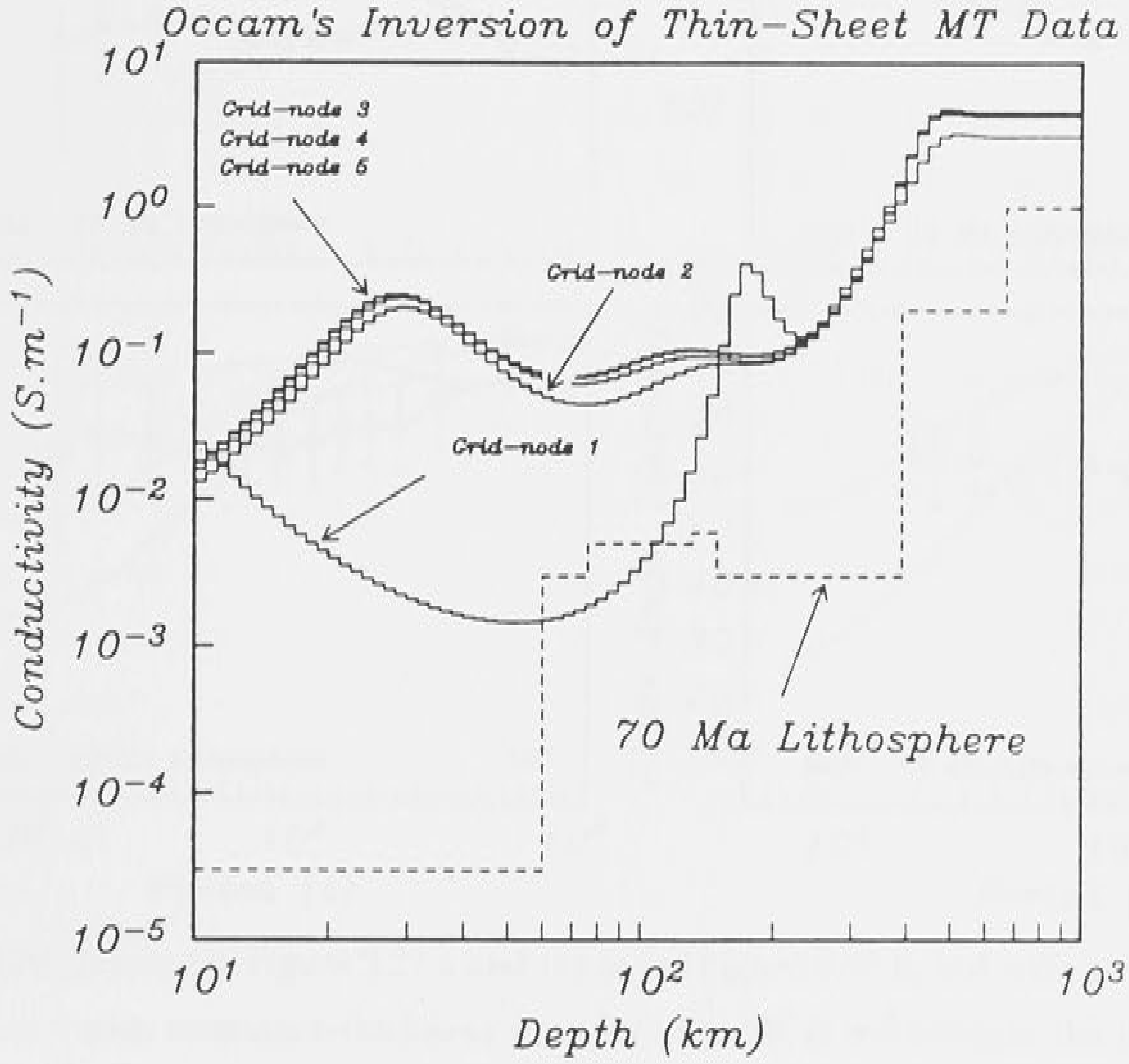

Figure 5.28 Occam inversions of synthetic MT data at grid-nodes 1 to 5 across transect A-A' in Model II (Figure 5.23). The layered profile beneath the thin-sheet is shown by the dashed line.

The similarity between observed seafloor MT data and thin-sheet MT response has only been demonstrated for one conductivity structure and one particular ocean basin shape. From the evidence of 1D inversions of seafloor MT data in chapter 2, the lithosphere and oceanic mantle beneath the north Pacific Ocean has a complex conductivity structure, which is oversimplified by the thin-sheet models. However, it is worth noting that the association between observed MT data and thin-sheet MT response is considerably weakened by including a less resistive upper lithosphere. Figure 5.29 shows the same comparisons between observed data and model responses as in Figure 5.27, but now including an upper lithosphere of resistance-thickness product ~10^7 $\Omega.m^2$. Although the evidence is by no means circumstantial, it suggests that a resistive upper lithosphere is a necessary feature of all oceanic conductivity models.

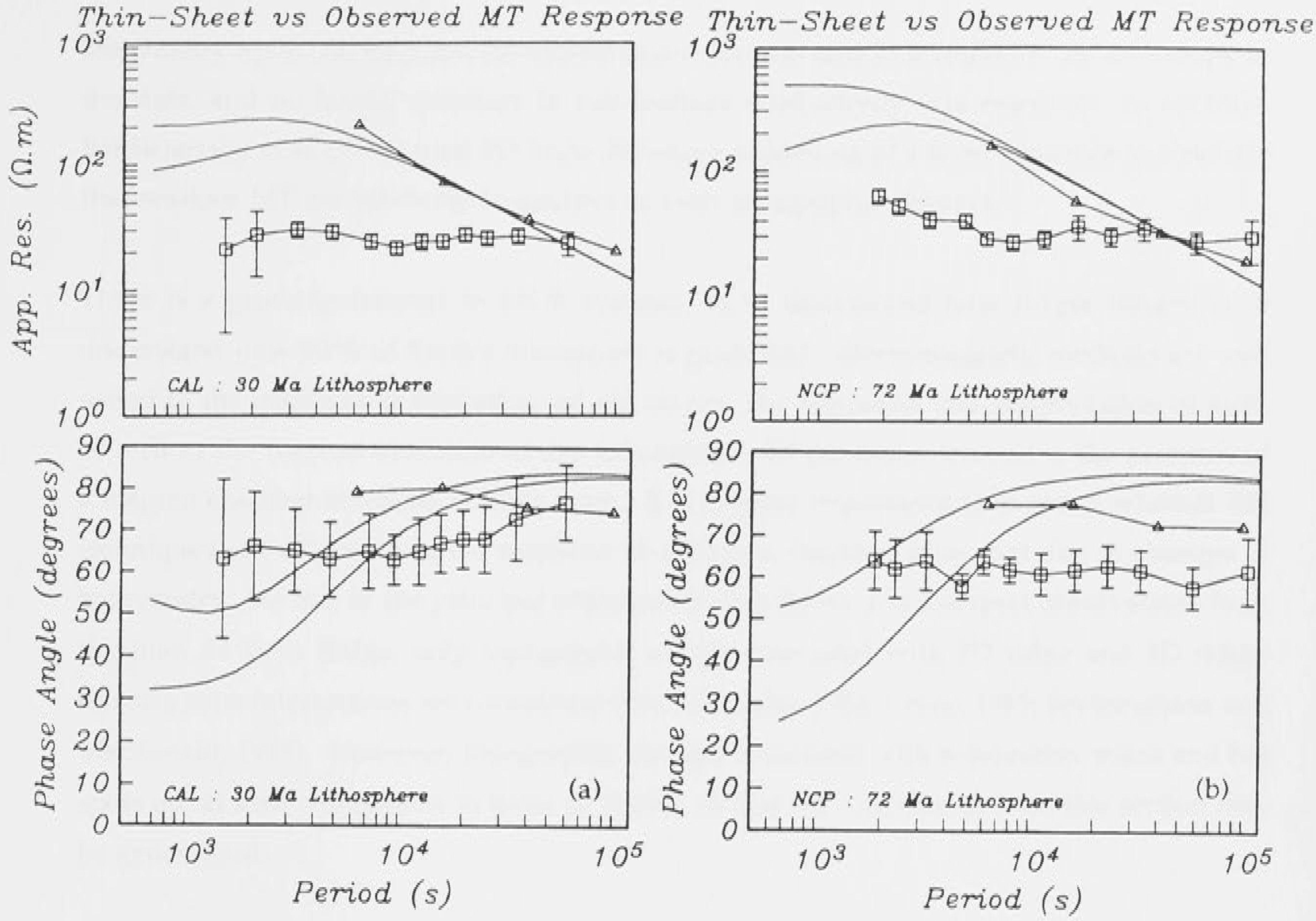

Figure 5.29 (a) As for Figure 5.27 a and (b) as for Figure 5.27 b, but with an upper lithosphere with resistance-thickness product of $2x10^7$ $\Omega.m^2$ beneath the thin-sheet.

5.4 Sensitivity of EM Observations to Seafloor Topography

5.4.1 Introduction

In previous interpretations of seafloor EM experiments, the significance of changes in bathymetry on EM observations has not been widely recognised. Ferguson *et al.* (1990) found that EM observations in the Tasman Sea were anisotropic; the direction of anisotropy was dependent primarily upon the influence of the coastline and also, to a secondary extent, on changes in bathymetry associated with the Lord Howe Rise (Figure 2.1). The Lord Howe Rise has an influence over a distance comparable to that due to electric charge accumulation at the coastline. Small scale changes in bathymetry may similarly influence seafloor EM observations over distances of tens, rather than thousands, of kilometres. This effect is of particular importance to geoelectric targets over major tectonic structures such as spreading ridges, fracture zones, hot spots or subduction zones, where ocean depths may vary considerably over relatively short distances.

Niblett *et al.* (1987) operated an MT station on sea-ice in the Arctic Ocean for one month, and found that observations were very sensitive to seafloor topography. A 2D model of bathymetry up to 300 km from the measurement site was able to account for the anisotropy in the data, and no lateral structure in sub-seafloor conductivity was required. In contrast, Berdichevsky *et al.* (1984) used 2D finite difference modelling of a horst structure to conclude that seafloor MT are relatively insensitive to such topographic changes.

There is a growing interest in MOR systems, as to understand how ridges behave is to understand how 60 % of Earth's lithosphere is generated. Electromagnetic methods are well suited to the mapping of hydrothermal circulation, the migration and accumulation of melt, as well as the thermal evolution of dry lithosphere. Of particular interest is the presence of a magma chamber in young oceanic crust. It is of great importance to examine whether EM techniques can discriminate the response of a magma chamber from that due to changes in bathymetry. As one of the principal objectives of this thesis is to interpret observations from the Juan de Fuca Ridge, only topographic effects associated with 2D ridge and 3D ridge-fracture zone intersections are considered (Fox and Gallo, 1984; Crane, 1985; Severinghaus and Macdonald, 1988). However, topographic changes associated with subduction zones and hot spots are at least comparable to those of MORs, so that the conclusions from this section may be generalised.

5.4.2 Model Description

Simple models of 2D and 3D ridge structures, shown in Figure 5.30, are used to illustrate the sensitivity of MT and GDS parameters to ridge and fracture zone topography (Fox , with or without the presence of a linear magma chamber at the ridge axis. The ridge is of medium-spreading rate (half-rate 25 km.Ma^{-1}) and 2D ridge topography is derived from an approximate square root of age dependence given in Parsons & Sclater (1977), as shown in Figure 5.31. The 3D topography, shown in Figure 5.32, is also generated using such a method; however, to approximate the effects of the lateral stress in the lithosphere either side of the transform fault, the bathymetry is progressively low-pass filtered as a function of age. Thus, at the ridge-transform intersection, there is a rapid change in seafloor depth, but away from the ridge, the bathymetry varies smoothly. A linear magma chamber of 100 % melt along the entire length of the ridge axis is included in the model, as it represents an upper-bound on melt distribution in the crust.

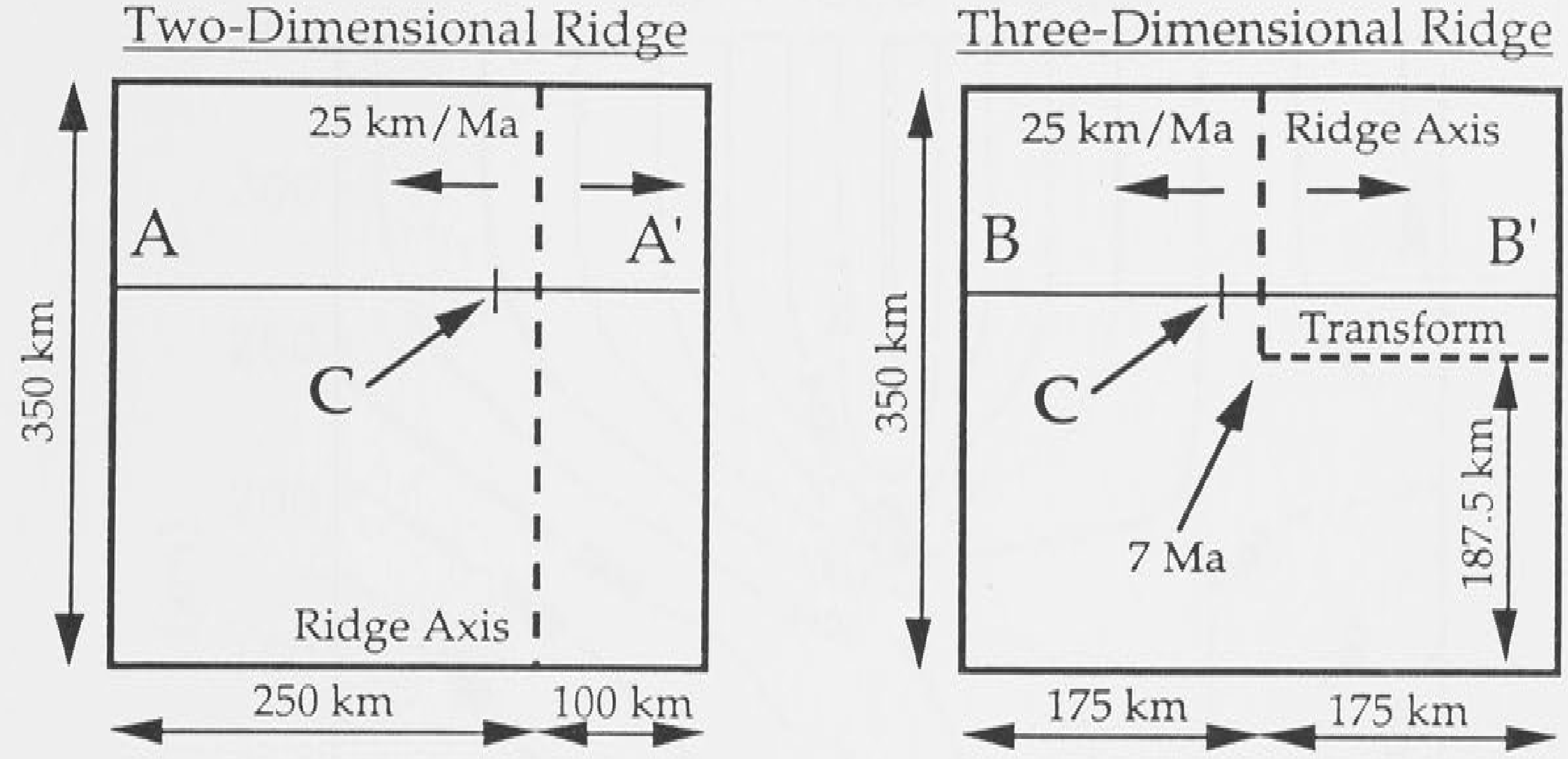

Figure 5.30 The geometry of the 2D and 3D ridge thin-sheet models. The dashed lines show the positions of the ridge axis and the transform fault. Synthetic seafloor MT parameters are calculated at location C. The structure underlying the thin-sheet grid is listed in Table 5.10.

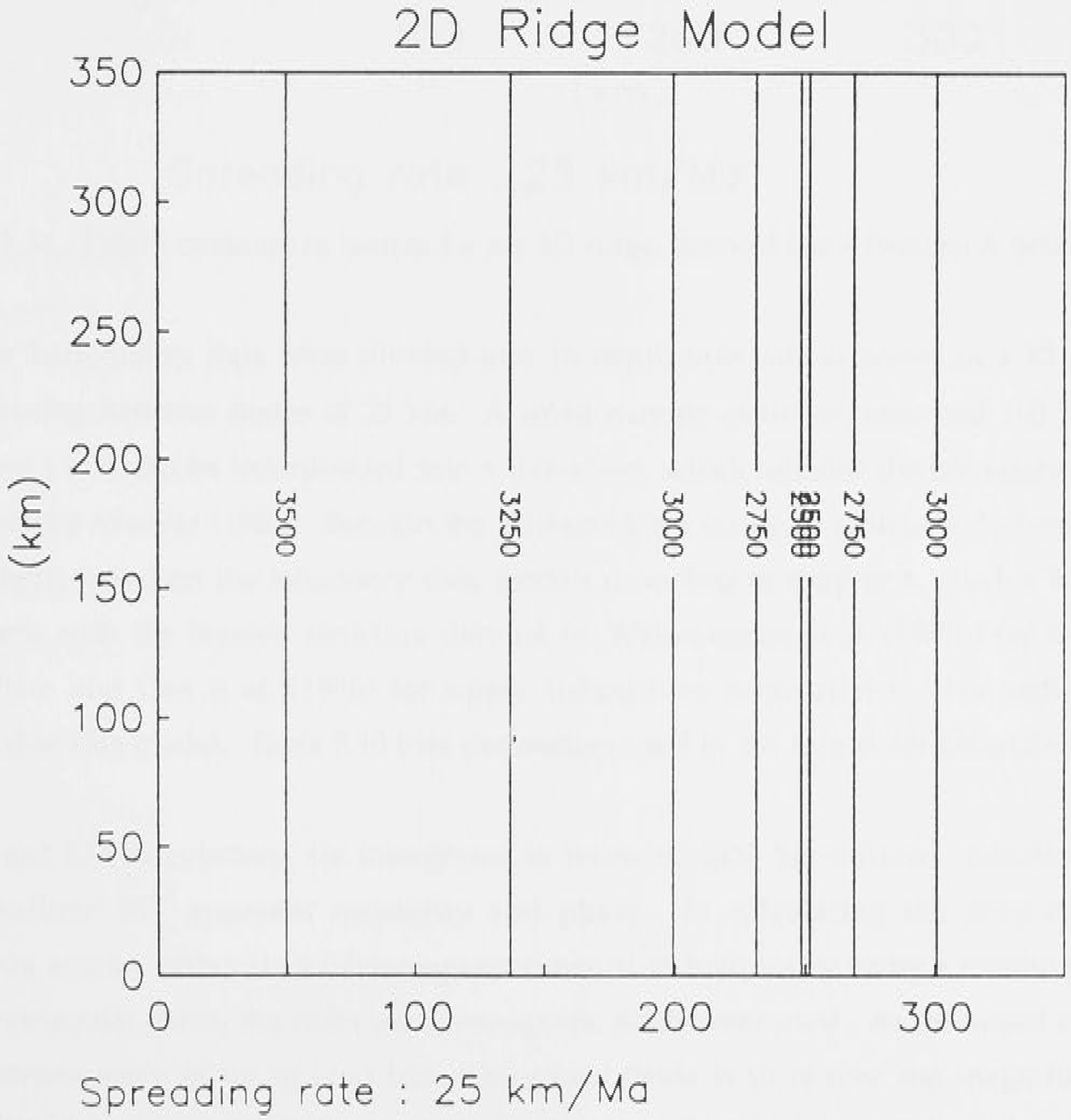

Figure 5.31 Depth contours in metres for the 2D ridge, derived from Parsons & Sclater (1977).

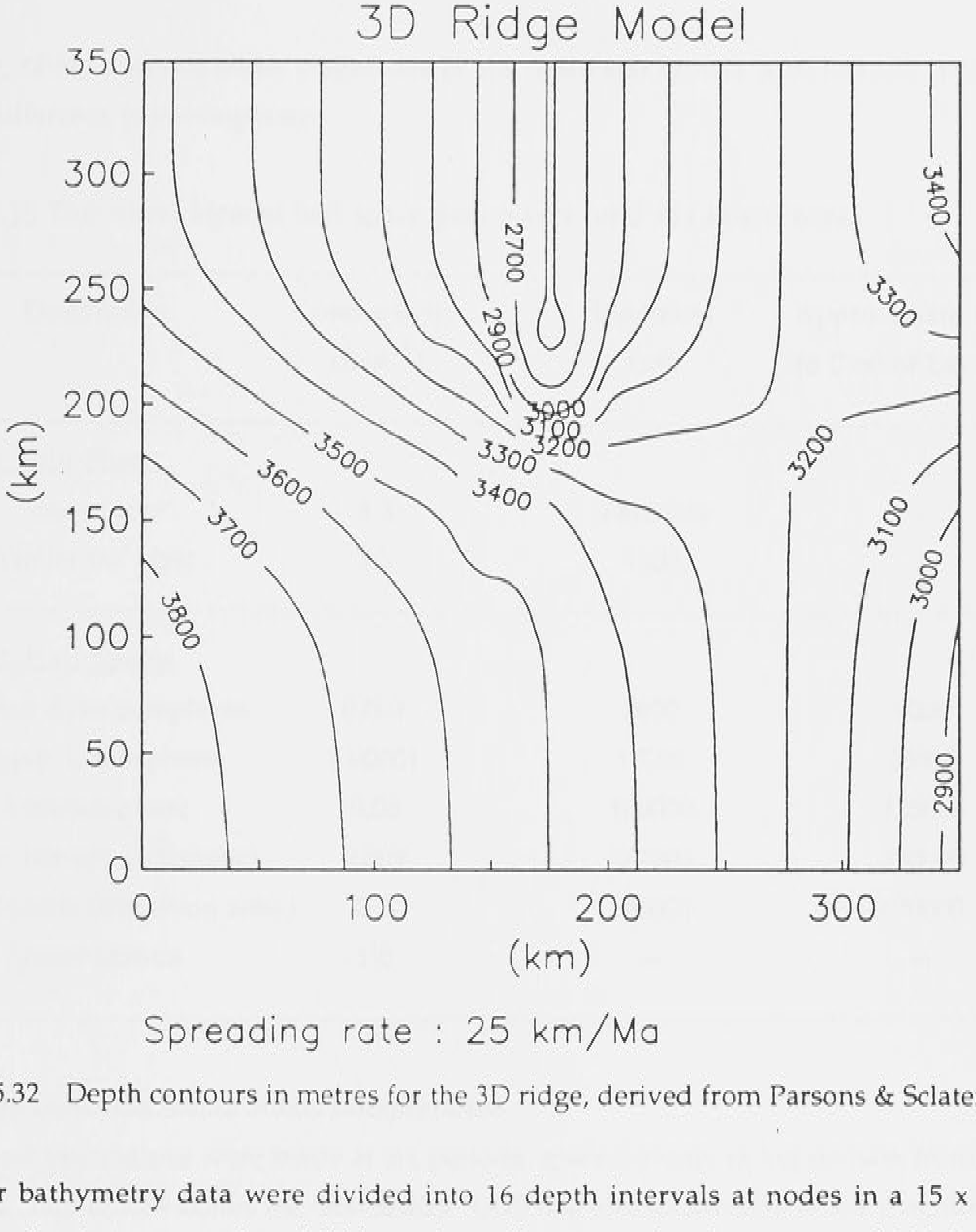

Figure 5.32 Depth contours in metres for the 3D ridge, derived from Parsons & Sclater (1977).

Seafloor bathymetry data were divided into 16 depth intervals at nodes in a 15 x 15 grid, with spacing between nodes of 25 km. A small magma chamber, assumed 100 % melt, of thickness 1 km, can be incorporated into a thin-sheet, which satisfies the boundary condition discussed by Weaver (1982). Beneath the thin-sheet is a six-layer structure derived for 2 Ma lithosphere, based on the laboratory data models described in chapter 4. Such a structure is consistent with the layered structure derived by Wannamaker *et al.* (1989b) for the Juan de Fuca Plate and Cox *et al.* (1986) for upper lithosphere conductivity. No sediments are included in this model. Table 5.10 lists parameters used in the thin-sheet calculation.

Thin-sheet EM calculations are interpreted in terms of GDS 'sea-surface' induction arrows, and 'seafloor' MT apparent resistivity and phase. In calculating the sea-surface GDS induction arrows, rather than following experimental techniques by using a remote set of land based horizontal fields, the sheet surface magnetic fields were used. As discussed earlier, the main consequence of using land based magnetic fields is to reduce the magnitude of the induction arrows by a scalar factor, over that obtained by using the ocean-surface field. The relative, rather than absolute, magnitude of the induction arrows is of interest here, so this scalar difference is not important.

Table 5.10 Thin-sheet layered half-space parameters for 2 Ma lithosphere.

Description	Conductivity ($S.m^{-1}$)	Thickness (m)	Approximate Depth to Base of Layer (m)
Surface Thin-Sheet:			
Sea-water	3.3	Variable	-
Tholeiitic Melt	3.3	1000	-
Layered Half-Space:			
Sheeted dyke complexes	0.001	3000	8000
Upper Lithosphere	0.00001	17000	25000
Asthenosphere	0.05	100000	125000
Upper Mantle (adiabatic)	0.003	265000	390000
Upper Mantle (transition zone)	0.2	280000	670000
Lower Mantle	1.0	∞	∞

5.4.3 GDS Induction Arrow Model Interpretation

Thin-sheet calculations were made at six periods, spaced evenly in log domain from, 1000 to 100000 s. Figure 5.33 shows the 'sea-surface' GDS real and quadrature arrow magnitudes at a period of 15849 s, along transect A-A' of the 2D ridge (Figure 5.30): arrows pointing eastwards are shown by a positive value, arrows pointing westward are negative. The thin-sheet algorithm of McKirdy *et al.* (1985) models inducing fields with a positive time dependence, so reversed real arrows 'point' towards a good conductor, while quadrature arrows point away from the conductor.

Changes in bathymetry due to cooling of lithosphere away from the ridge axis, and the presence of a linear magma chamber have opposite effects on the sea-surface GDS response. Close to the ridge axis, a linear magma chamber may be detected, but far from the ridge, sea-surface GDS arrows point towards the deep ocean. The GDS effects of changes in bathymetry in the ridge environs may cancel out the response of a linear magma chamber at the ridge axis if the melt fraction is small.

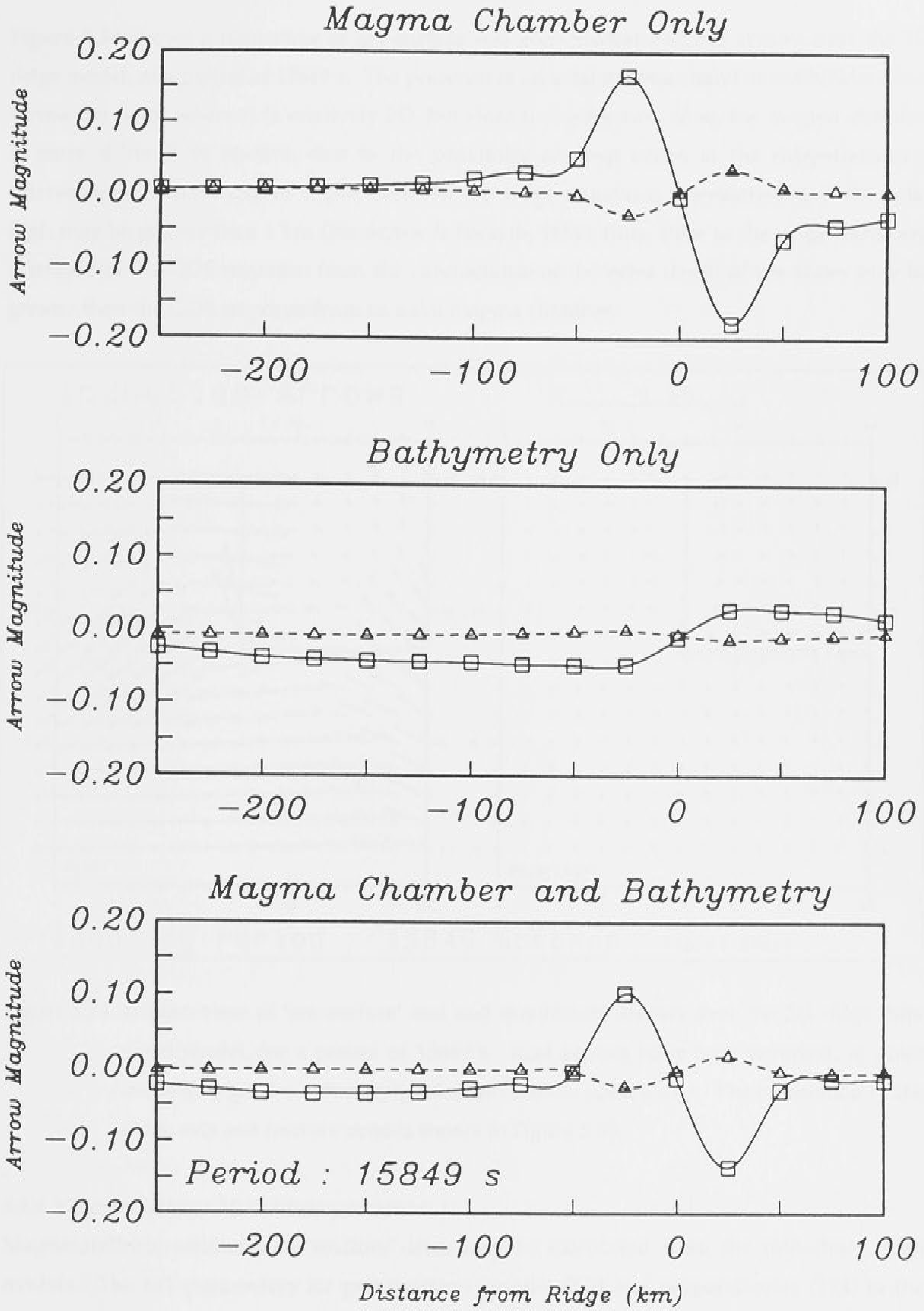

Figure 5.33 Magnitudes of 'sea-surface' real (solid line) and quadrature (dashed line) arrows for the 2D ridge models, along transect A-A' (of Figure 5.30), for a period of 15849 s. Positive values indicate an arrow direction eastwards, while westward pointing arrows have negative values.

Figure 5.34 shows a plan view of sea-surface real and quadrature GDS arrows over the 3D ridge model, at a period of 15849 s. The presence of an axial magma chamber can be identified across the ridge where it is relatively 2D, but close to the fracture zone, the magma chamber is more difficult to resolve, due to the proximity of deep ocean at the ridge-transform intersection. Differences in depth between the ridge-transform intersection and the axial high may be greater than 1 km (Blackman & Forsyth, 1989); thus, close to the ridge-transform intersection the GDS response from the conductance of the extra depth of sea-water may be greater than the GDS response from an axial magma chamber.

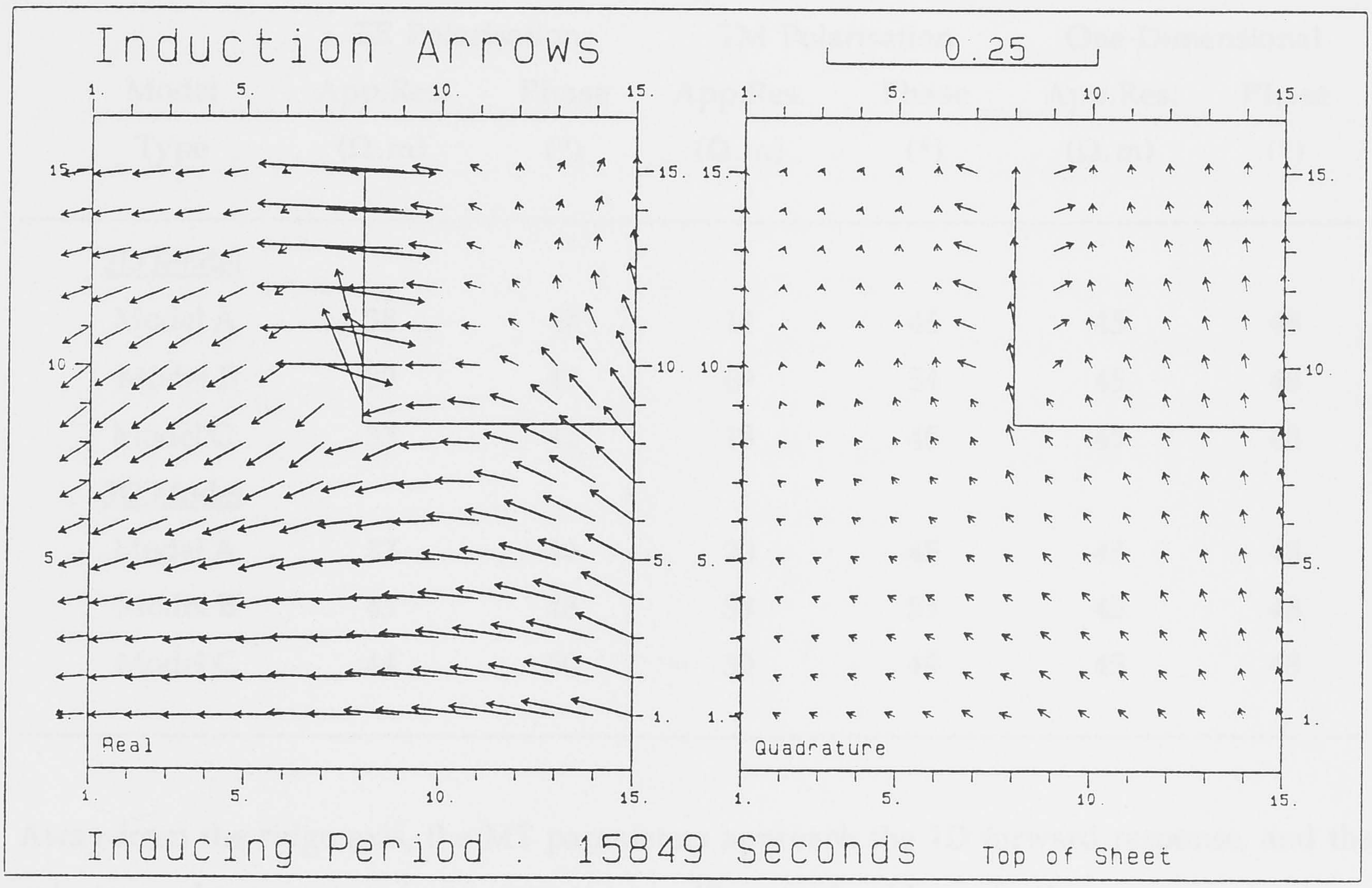

Figure 5.34 A plan view of 'sea-surface' real and quadrature arrows over the 3D ridge thin-sheet model, for a period of 15849 s. Real arrows have been reversed, to point towards a good conductor; quadrature arrows point away. The orientation of the ridge axis and fracture zone is shown in Figure 5.30.

5.4.4 *Magnetotelluric Model Interpretation*

Magnetotelluric estimates at 'seafloor' sites may be calculated from the thin-sheet ridge models. The MT parameters for polarisations parallel (TE) and perpendicular (TM) to the ridge axis from site C shown in Figure 5.30 are listed in Table 5.11, at period 16000 s.

If no magma chamber is present, the effect of the topography is to introduce anisotropy in the apparent resistivity by a factor of up to 1.75, with the larger TM apparent resistivity orientated towards the ridge axis and greater than the 1D response of the underlying structure. The TE apparent resistivity parallel to the ridge is less than the 1D response. If a linear magma chamber is present, there is an anisotropy in apparent resistivity of 1.86; however, the larger apparent resistivity is the TE polarisation. The apparent resistivities in both polarisations are less than the 1D forward response.

Table 5.11 MT Parameters from seafloor site C, shown in Figure 5.30. Model A refers to the model with a linear magma chamber, but no bathymetry; Model B includes bathymetry, but no magma chamber; and Model C has both magma chamber and bathymetry

	TE Polarisation		TM Polarisation		One-Dimensional	
Model Type	App.Res. (Ω.m)	Phase (°)	App.Res. (Ω.m)	Phase (°)	App.Res. (Ω.m)	Phase (°)
2D Model						
Model A	38	43	14	46	45	48
Model B	39	47	69	54	45	48
Model C	33	42	18	48	45	48
3D Model						
Model A	37	41	20	45	45	48
Model B	43	48	58	51	45	48
Model C	44	50	30	49	45	48

Away from the ridge axis, the MT parameters approach the 1D forward response, and the anisotropy decreases to a factor close to one. Close to the ridge axis, the presence of a linear magma chamber has a distinct effect on the MT parameters. Thus, it appears that MT observations close to the ridge axis can discriminate between the model with just bathymetry, and the model with bathymetry and a linear magma chamber.

5.4.5 Interpretation of Seafloor Topography Models

The influence of seafloor topography on EM observations is significant. In contrast to the conclusion of Berdichevsky *et al.* (1984), it has been found that changes in topography may distort the MT response away from the 1D forward MT parameters. The GDS parameters are particularly sensitive to changes in bathymetry.

It has been shown that the changes in bathymetry associated with a 2D ridge are not large enough to completely obscure the EM signature of a linear magma chamber; however, in cases where the bathymetry varies more rapidly, such as at a ridge-transform intersection, the extra depth of sea-water profoundly influences the distribution of induced telluric current in the ocean. Such rapid changes in topography are also present at subduction zones and hot spots. The model studies presented above imply that although it may be possible to target such tectonic features in seafloor EM studies, forward-modelling studies are required to determine whether the signature of the ridge may be unambiguously identified.

The example detailed above is for a medium-spreading ridge. At slower spreading ridges, the seafloor topography is more rugged. Emerman & Turcotte (1984) have shown that at slow-spreading ridges there is a deep axial valley, of depth 1.5 to 3.0 km; at intermediate-spreading centres the axial valley is only 50 to 200 m deep; at fast-spreading ridges, the axial valley disappears, and is replaced by an axial high. The extra depth of sea-water in such an axial valley will act in a manner similar to a body of magma of comparable thickness. Also, the model of a linear magma chamber in the above example is probably unrealistic, and recent evidence suggests that magma chambers are focused at discrete segments, and may be transient features. Such factors cast doubt on whether a small magma chamber could be identified beneath the ridge, using EM techniques in regions where the seafloor topography varies rapidly. However, the evidence from the 2D model indicates that EM methods are well suited to the detection of magma beneath a fast-spreading ridge.

Chapter 6 : EMRIDGE : Electromagnetic Exploration of the Juan de Fuca Ridge

6.1 Introduction

In chapter 2, the experimental objectives of EMRIDGE were described, and preliminary analyses of the time series were made. The absence of a strong EM signature at the ridge axis was of particular note: this observation is consistent with similar EM soundings over the northern end of the Juan de Fuca Ridge, and at the East Pacific Rise. While all information is present in the time series, it is generally instructive to present such data as MT and GDS parameters. In this section such parameters are interpreted in terms of oceanic 3D induction effects which are due to changes in topography, examined in chapter 5. The thin-sheet method is again used to quantify EM induction in the ocean.

6.2 GDS Soundings Across the Juan de Fuca Ridge

6.2.1 Introduction

A convenient way of presenting three-component observations of the natural fluctuations of Earth's magnetic field is by the use of GDS induction arrows (Parkinson, 1962). The interpretation of seafloor GDS arrows is complicated by the effects of the overlying ocean on the horizontal fields. Equivalent 'sea-surface' GDS arrows may be calculated with a reference set of horizontal fields from an appropriate land site, using the assumption that the vertical field (Z) on the seafloor is the same as would be measured at the sea-surface, i.e. the Z component is continuous with depth through the ocean. This assumption is valid at the range of periods used in seafloor MT and GDS soundings. The advantage of such sea-surface arrows is that they map the relative changes in the Z field between different seafloor sites, and they can be interpreted in the traditional way.

6.2.2 GDS Observations

Horizontal magnetic fields at Oregon, U.S.A. were used to characterise the fluctuations of the magnetic field over the surface of the ocean. Sea-surface GDS arrows were then calculated for each seafloor magnetometer site for which there were reliable observations. A robust processing scheme was employed (Egbert & Booker, 1986) for periods between 300 to 30000 s; examples of the results at three periods are shown in Figure 6.1. Egbert & Booker (1986) use a time dependence of the form $e^{+i\omega t}$, which is consistent with the formulations developed in chapter 1. Following the guide-lines of Lilley & Arora (1982), the reversed real arrow points towards the current channelling, while the quadrature arrows point away.

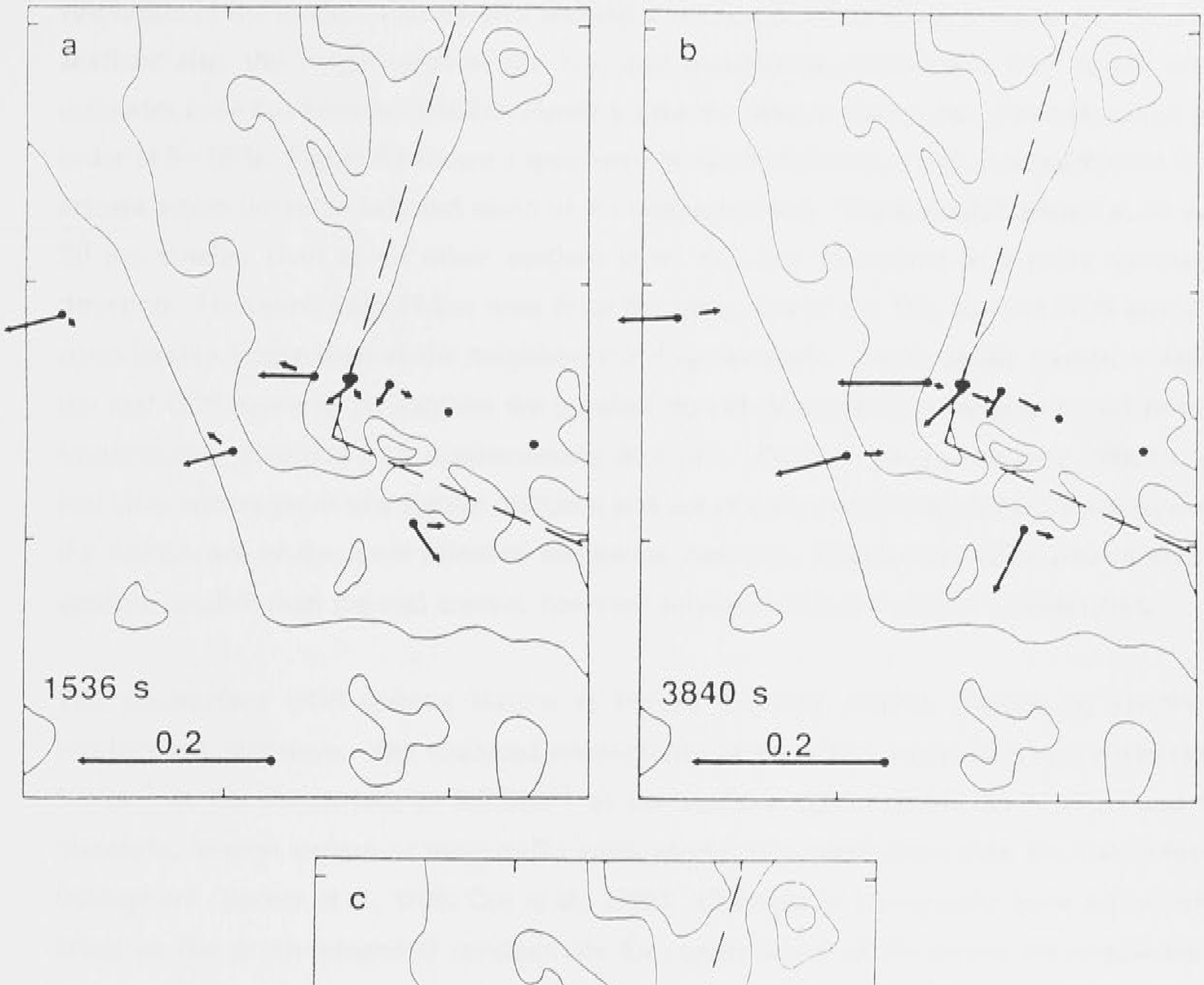

Figure 6.1 Real (solid arrow) and quadrature (dashed arrow) 'sea surface' GDS arrows, superimposed on bathymetric maps of the Juan de Fuca Ridge - Blanco Fracture Zone intersection (shown by heavy stippled lines).

Reliable GDS arrow estimates cannot be made at periods less than 1500 s, due to the limited resolution of the seafloor instruments and the small amplitude of the Z component. For each seafloor site, the magnitudes of the real and quadrature arrows are very small: error estimates have not been included in Figure 6.1 for the sake of clarity, but generally are of the order of 5 - 10 %. Figure 6.1 shows a symmetry in the distribution of real and quadrature GDS arrows across the ridge axis and south of the transform fault. The real GDS arrows at R2 and E0 are smaller than at all other seafloor sites, and are orientated in a more southerly direction. However, only 14 km west from the ridge axis at site W0, the real GDS arrow is considerably larger than at the neighbouring ridge-axis site. South of the transform fault, the real GDS arrow at S1 exhibits the greatest period dependence, swinging round from a southeasterly direction to a southwesterly direction. For periods greater than 20000 s, all real GDS arrows point in a similar direction and are of comparable magnitude, resulting from the dominance of the coast effect of northwest America. Quadrature GDS arrows are, in general, smaller than the real arrows, however similar trends can clearly be identified.

The sea-surface GDS arrows shown in Figure 6.1 map lateral changes in electrical conductivity structure. The electrical conductivity of sea water varies from approximately 5 $S.m^{-1}$ at the sea-surface to 3.2 $S.m^{-1}$ at the seafloor (Quist & Marshall, 1968) and is, therefore, several orders of magnitude more electrically conductive than the sub-oceanic lithosphere (Becker *et al.*, 1982; Cox *et al.*, 1986). Changes in topography have a profound effect on the depth-integrated conductivity (or conductance) of the ocean: the conductance increases as the ocean becomes deeper. Thus, the directions of GDS 'sea-surface' arrows respond to changes in depth of the ocean. At short periods, local bathymetry changes appear to dominate the pattern of electric current distribution, whilst at longer periods large-scale features assert a stronger influence. The juxtaposition of new oceanic crust of age younger than 1 Ma on the northern side of the transform fault with crust of age 9 Ma (Blackman & Forsyth, 1989) to the south gives rise to a sharp change in bathymetry on a north-south transect.

Other factors may also influence the distribution of GDS arrows. It is envisaged that lateral changes in Earth close to the ridge axis may also have an EM expression, observable by seafloor instruments. In particular, there is evidence of a circulation of hydrothermal fluids in the fresh oceanic crust of the Juan de Fuca Ridge (Crane *et al.*, 1985; Embley & Chadwick, 1989), implying that anomalously high temperatures and possibly a magma chamber are present; these effects would have high electrical conductivity relative to the cooler host medium. In chapter 5, it was shown that the GDS effects of changes in bathymetry in the ridge environs may cancel out the response of a linear magma chamber at the ridge axis.

In the following section, the hypothesis is tested that the directions of observed GDS arrows are caused by changes in bathymetry (only). If changes in bathymetry can reproduce the observed trends to some acceptable level of accuracy, the conclusion is that the EM signature of processes active in the formation of new oceanic crust is quite small. However differences between the observations and model response, which are systematic with distance from the ridge axis, may be the result of lateral conductivity variations beneath the seafloor.

6.2.3 A Thin-Sheet Model of the Juan de Fuca Ridge

A numerical thin-sheet model was constructed of the ocean in the EMRIDGE area. The model covered the Juan de Fuca Ridge and Blanco Fracture Zone areas, and was constructed with the parameters listed in Table 6.1. The section of modelled seafloor was centred on the main ridge structure and fracture zone, and included surrounding areas of reasonably flat seafloor, so that anomalous structure was kept well away from the edges of the model. Calculations were made at eleven periods with equal logarithmic spacing, from 1000 to 100000 s: Figure 6.2 presents a comparison between thin-sheet and observed sea-surface GDS real induction arrows.

Table 6.1 Thin-sheet layered half-space parameters for the Juan de Fuca Ridge. Model parameters are identical to those used for the 2D and 3D ridge-transform geometries, listed in Table 6.11.

Description	Conductivity ($S.m^{-1}$)	Thickness (m)	Depth to Base of Layer (m)
Surface Thin-Sheet:			
Sea-water	3.3	Variable	-
Tholeiitic Melt	3.3	1000	-
Layered Half-Space:			
Sheeted dyke complexes	0.001	3000	8000
Upper Lithosphere	0.00001	17000	25000
Asthenosphere	0.05	100000	125000
Upper Mantle (adiabatic)	0.003	265000	390000
Upper Mantle (transition zone)	0.2	280000	670000
Lower Mantle	1.0	∞	∞

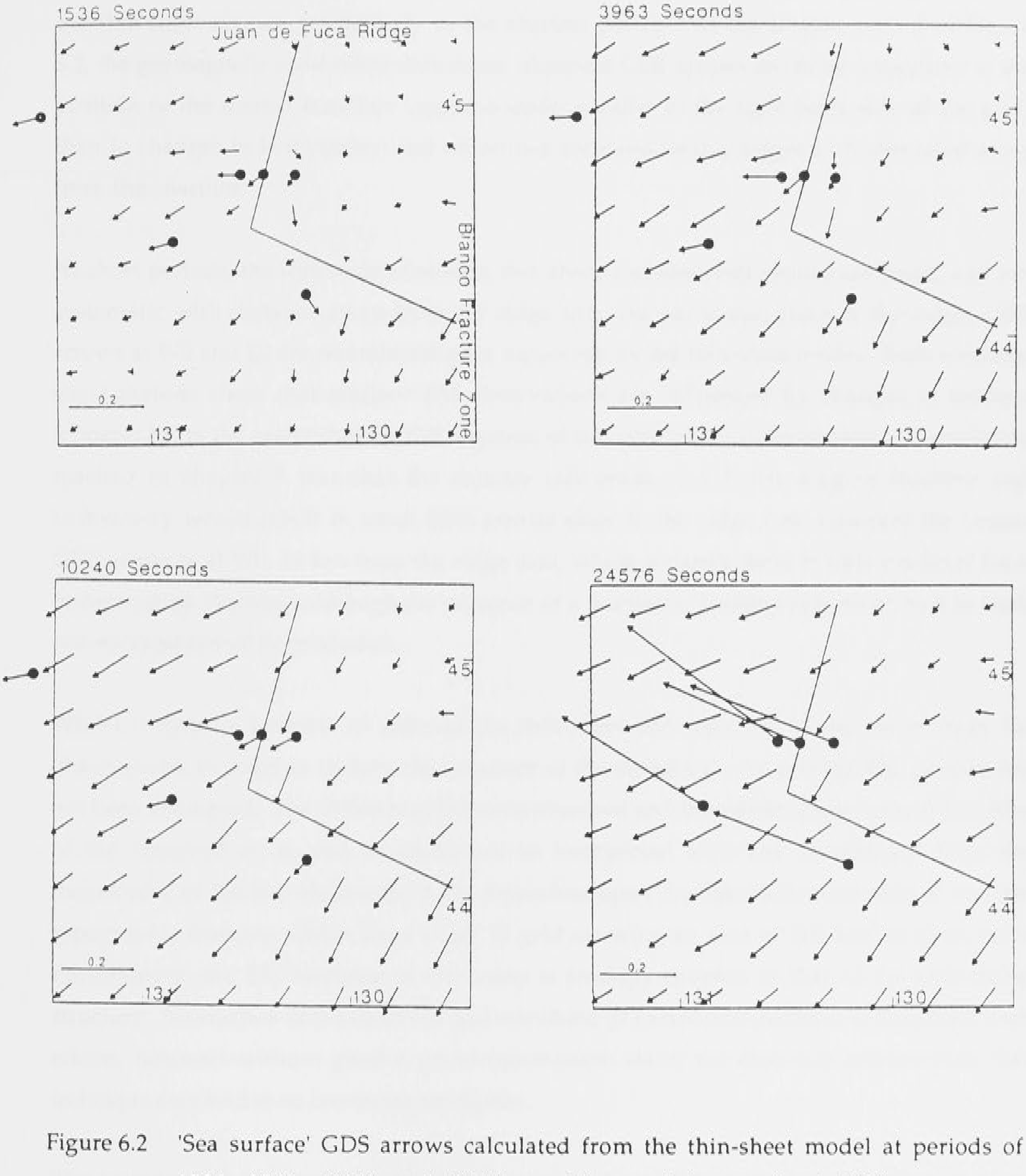

Figure 6.2 'Sea surface' GDS arrows calculated from the thin-sheet model at periods of 1536, 3963, 10240 and 24576 s. Observed 'sea-surface' GDS arrows are superimposed, located by the black circles. Real arrows only are shown, as the quadrature arrows are much smaller.

Observed sea-surface GDS are calculated with land-based horizontal magnetic fields recorded in Oregon, while thin-sheet GDS arrows are calculated at the top of the sheet. Furthermore, the thin-sheet model does not cover sufficient area to include the coastline of northwest America. It is therefore difficult to compare absolute magnitudes of GDS arrows without more detailed analysis of the geomagnetic coast effect from northwest America. However, directions and relative magnitudes of the observed arrows show close agreement to the thin-sheet arrows, particularly at the shortest period. At the longest period in Figure 6.2, the geomagnetic coast effect dominates: observed GDS arrows are more responsive to the position of the distant coastline (approximately parallel to the right-hand side of the grid) than to changes in bathymetry; and all arrows are considerably larger and orientated away from the coastline.

At short periods, the differences between thin-sheet and observed arrows are small, and not systematic with distance away from the ridge axis. In particular, close to the ridge, GDS arrows at W0 and E0 are reproduced quite accurately by the thin-sheet model. Such results at short periods show that seafloor EM observations are influenced by changes in seafloor topography, to the extent that the EM response of sub-structure may be masked. A conclusion reached in chapter 5 was that the counter influences of a linear magma chamber and bathymetry would result in small GDS arrows close to the ridge axis: however the largest GDS arrow is at W0, 14 km from the ridge axis, which suggests there is little evidence for a linear magma chamber, although the presence of a number of isolated regions of melt in fresh oceanic crust cannot be precluded.

Whilst it may be possible to subtract the thin-sheet EM response of the ocean from the observations, in order to remove the influence of the topography, in practice this process has not been attempted. The differences between observed and thin-sheet arrows are of the order of the observed error, and so could not be interpreted with any reliability. Also, the magnitudes of the thin-sheet arrows are dependent upon the thin-sheet resolution of seafloor topographic features, which for a 15 by 15 grid covering an area of 180 km^2 is quite poor. Furthermore, the EM response of the ocean is strongly coupled to that of the underlying structure. Subtraction of the observed and calculated EM responses attempts to de-couple such effects, however without good a priori information about the electrical substructure, this technique may lead to an erroneous conclusion.

The magnitude and orientation of thin-sheet sea-surface GDS arrows are dependent both on the seafloor topography and, to a lesser extent, on the conductivity of the underlying lithosphere. By varying the conductivity of the uppermost layer given in Table 6.1 from 10^{-3} to 10^{-5} $S.m^{-1}$, it was found that an upper lithosphere with conductivity of at most 10^{-5} $S.m^{-1}$ was required to match the observations. This conductivity compares well with the value obtained by the CSEM experiment conducted by Cox *et al.* (1986). The effect of changing the conductivity of the asthenosphere or deep electrical structure is of lesser consequence to the synthetic GDS response, but was not rigourously tested.

6.3 Magnetotelluric Sounding on 1.2 Ma Oceanic Crust

6.3.1 Introduction

Horizontal electric field observations were made at site E2, approximately 35 km east of the ridge axis, on lithosphere of age approximately 1.2 Ma. The least count of the electrometer at site E2 was 0.01 mV.m $^{-1}$ at a sample interval of two-minutes. Approximately sixty days of electric field data were recorded, though over the first forty days the east component (Ed) was corrupted by large fluctuations of uncertain origin. Reliable observations for the two horizontal components were available for the last twenty days of the record length; fortunately this period includes some of the most active geomagnetic events which occurred during the experiment. A magnetometer was also deployed at site E2, however data quality were poor and of short duration, not coinciding with the good sections of electric field data. Therefore, to calculate MT estimates, magnetic field data were taken from ridge axis site R2, which recorded with a least count of 0.1 nT at a two-minute interval. The uniformity of the fluctuating magnetic field at the seafloor in the area supports the use of data from R2.

6.3.2 Magnetotelluric Observations

A remote-reference robust processing method was used to calculate MT estimates (Goubou *et al.*, 1978; Gamble *et al.*, 1979a,b; Egbert & Booker, 1986; Jones *et al.*, 1989) over a period range 300 s to 30000 s. A remote-reference set of horizontal magnetic fields was taken from the records of the Victoria Magnetic Observatory (VMO), approximately 689 km away from the ridge axis. The choice of VMO was not ideal, as it is close to auroral latitudes (and consequently non-uniform source-fields), but unfortunately, no simultaneous magnetic field records were available from the site in Oregon during the time window of good electric-field data. Magnetic field data from other seafloor sites were not satisfactory as a remote-reference due to a variety of reasons.

Tidal periods (Chave & Filloux, 1984) were notched out of the data in the frequency domain, and coherences were examined to judge reliability. At short periods, the limited resolution of the magnetometer (even at a least count of 0.1 nT) reduced coherences to unacceptably low values (< 0.6). At longer periods, the record lengths were not long enough to produce well-constrained MT estimates. The response functions are of high quality (< 5 % errors) between 800 and 10000 s, but coherences are greater than 0.9 for a few estimates only. The MT parameters of apparent resistivity and phase polarised parallel and perpendicular to the coastline of northwest America are listed in Table 6.2. The impedance tensors were subsequently rotated to maximise the off-diagonal elements (Swift, 1967), aligning the tensor with the principal 2D strike at the observation site: the corresponding azimuth of 2D strike and the tensor skew angle (Vozoff, 1972) are also listed in Table 6.2.

Non-uniform induction effects are clearly demonstrated by the data, as indicated by the changes in the principal-axis azimuth, the degree of anisotropy between the MT estimates in the two polarisations, and the skew angle. The azimuth of principal-axis orientation is largely determined by the polarisation of the electric field, and it is clear that seafloor topography is influencing the pattern of EM induction at short periods. At periods longer than 10000 s, the principal-axis orientation rotates to become parallel to the coastline, which dominates the seafloor EM response.

Table 6.2 (a) MT estimates from electric field data at E2 and magnetic field data at R2, for orientations parallel and perpendicular to the coastline of northwest America.

	Parallel to Coastline				Perpendicular to Coastline			
Period (s)	App.Res. (Ω.m)	1 S.e. (Ω.m)	Phase (°)	1 S.e. (°)	App.Res. (Ω.m)	1S.e. (Ω.m)	Phase (°)	1S.e. (°)
399.0	22.51	4.08	42.69	5.19	-	-	-	-
503.6	25.82	4.88	38.16	5.41	31.40	4.85	46.07	4.42
626.9	31.97	4.11	42.47	3.69	45.16	5.34	51.36	3.39
787.7	21.36	1.87	46.88	2.50	51.38	4.97	50.95	2.77
991.0	22.93	1.73	49.39	2.16	57.47	4.79	49.66	2.39
1228.8	29.90	1.71	48.45	1.64	60.59	4.17	57.34	1.97
1536.0	26.99	1.66	51.64	1.76	49.02	2.91	57.87	1.70
1920.0	25.13	1.37	49.28	1.56	43.67	2.37	58.12	1.56
2560.0	25.89	1.09	50.13	1.20	34,94	1.51	59.74	1.23
3150.8	27.13	1.45	48.07	1.53	25.01	1.39	59.26	1.60
3963.9	33.25	1.64	50.14	1.41	26.53	1.75	65.80	1.89
5120.0	27.05	1.59	51.93	1.68	29.22	1.72	59.94	1.68
6144.0	25.24	1.67	49.73	1.90	24.96	1.74	56.38	2.00
7680.0	32.78	1.98	45.78	1.73	25.88	1.90	56.05	2.11
10240.0	39.92	2.96	47.59	2.13	22.21	2.56	59.98	3.31
12288.0	33.42	4.87	52.76	4.17	29.44	5.40	63.48	5.26
15360.0	51.48	8.76	41.64	4.87	-	-	-	-
20480.0	35.81	6.89	64.99	5.51	-	-	-	-
24576.0	45.93	10.50	73.34	6.55	-	-	-	-
30720.0	54.55	9.80	73.66	5.15	-	-	-	-

(b) Azimuth of the principal axis and skew angle.

Period (s)	Azimuth† (°)	Skew (°)	Period (s)	Azimuth† (°)	Skew (°)
399.0	59.32	7.66	3963.9	43.41	18.58
503.6	45.26	8.26	5120.0	41.46	17.21
626.9	49.49	7.08	6144.0	46.47	16.76
787.7	54.35	9.28	7680.0	44.15	17.68
991.0	54.64	11.66	10240.0	41.38	17.86
1228.8	51.64	13.44	12288.0	43.64	15.28
1536.0	51.36	15.42	15360.0	23.30	12.49
1920.0	52.13	16.61	20480.0	29.23	19.46
2560.0	47.88	16.98	24576.0	31.49	14.04
3150.8	44.91	18.88	30720.0	-1.79	23.88

Note

† - azimuth relative to geographic north.

No MT estimates are shown where coherence drops below 0.5.

Azimuth and skew angles are approximate at periods for which the coherence is low.

The skew angles are small (< 10°) for periods less than 800 s, then rise to an almost constant value of ~16° at periods greater than 1500 s, which implies that the EM response is approximately 2D at short periods, but becomes 3D at longer periods. Thus, changes in seafloor topography complicate any simple interpretation in terms of an electrical structure underlying the ridge and the geomagnetic coast effect.

6.3.3 Thin-Sheet Modelling of the Magnetotelluric Response

MT estimates at 'seafloor' sites may be calculated from the thin-sheet model of the Juan de Fuca Ridge - Blanco Fracture Zone discussed in the previous section. Figure 6.3 shows pseudo-sections of apparent resistivity and phase calculated for polarisations parallel and perpendicular to the coastline of northwest America, for a profile across the Juan de Fuca Ridge which approximates the EMRIDGE transect. Also shown is the 1D response of the six layer model which underlies the thin-sheet. For a grid-node corresponding to site E2, neither polarisation of apparent resistivity recovers the 1D response of the structure underlying the thin-sheet. The anisotropy between the major and minor axis apparent resistivity is greatest at periods less than 10000 s, but at longer periods, this anisotropy decreases to a reasonably isotropic response. The phase is more robust to the presence of bathymetry and shows much smoother changes.

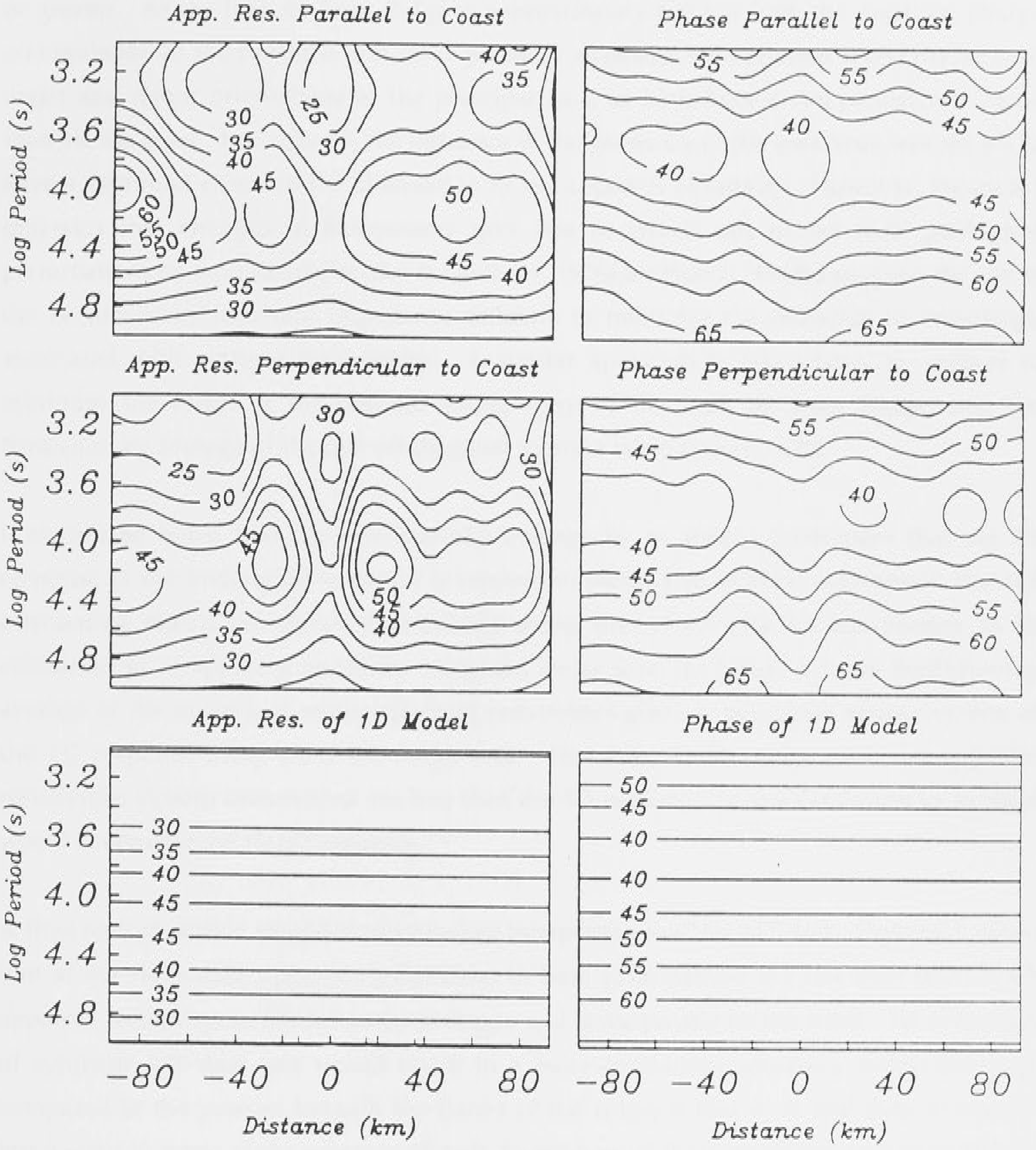
App. Res. Parallel to Coast

Phase Parallel to Coast

App. Res. Perpendicular to Coast

Phase Perpendicular to Coast

App. Res. of 1D Model

Phase of 1D Model

Figure 6.3 Pseudo-sections of thin-sheet 'seafloor' apparent resistivity and phase from the the Juan de Fuca Ridge model, polarised parallel and perpendicular to the coastline of northwest America. The 1D MT response of the underlying layered structure (Table 6.1) is shown for comparison. The profile approximates the location of the EMRIDGE transect, and distances are measured from the ridge axis site R2.

It is clear from the azimuth of the principal axis in Table 6.2 that the major direction of 2D strike is not aligned with the coastline of northwest America, but approximately parallel to the strike of the bathymetry at short periods. The 2D model of Wannamaker *et al.* (1989b) suggests that the compensation distance L_0 from the coastline will be of the order of 1000 km or greater. As the Juan de Fuca Ridge is approximately 600 km from the coastline, charge accumulation at the coastline will most probably attenuate the apparent resistivity in both major and minor orientations of the principal axis, as both have a component orientated towards the coast. In chapter 5, the influence of the geometry of the coastlines was shown to have a profound effect on the attenuation of the apparent resistivity. However, Figure 6.3 indicates that changes in bathymetry give rise to effects not unlike local geological perturbations on land (Berdichevsky & Dmitriev, 1976a,b); Filloux (1982b) suggests the use of the Berdichevsky invariant impedance estimate to minimise the influence of anisotropy associated with seafloor topography. A similar approach is taken here, to attempt to minimise the effect of the seafloor topography of the Juan de Fuca Ridge, and the Berdichevsky average of the two off-diagonal terms is taken (see eq. 1.75).

It should be noted that the Berdichevsky average by no means guarantees that the 1D response of the underlying structure is recovered: there is an implicit assumption that the attenuating effects on apparent resistivity along the minor axis are comparable to an enhancement of apparent resistivity along the major axis. In Figure 6.3, the Berdichevsky average of the major and minor apparent resistivities gives a reasonable approximation of the 1D response away from the ridge axis. However, at the ridge axis, the apparent resistivities in both orientations are less than the 1D response, so the Berdichevsky average would not recover the 1D MT response.

A final note of caution should be made when interpreting seafloor MT data. Figure 6.3 shows that at the ridge axis, apparent resistivities in both polarisations are less than the 1D MT apparent resistivity, so Berdichevsky averages will consequently be too small. 1D inversions of synthetic MT data sets would result in a more conductive structure below the ridge compared to the profiles beneath the flanks of the ridge; if this were real data, it may be interpreted in terms of the presence of melt, hydrothermal fluid circulation and anomalously high temperatures beneath the ridge axis. However, perturbations in the thin-sheet MT values are the result only of non-uniform induction in the ocean, as beneath the thin-sheet is a 1D layered half-space. Thus, seafloor topography must be considered in the interpretation of seafloor MT data sets.

6.3.4 One-Dimensional Inversion

The results of a D^+ inversion (Parker, 1980; Parker & Whaler, 1981) of EMRIDGE MT data set (using Berdichevsky averages) are listed in Table 6.3. The RMS misfit is less than the expected value of unity (see chapter 2), which implies that EMRIDGE MT estimates may be compatible with a 1D model Earth structure.

Table 6.3 Model parameters from a D$^+$ inversion of the EMRIDGE Berdichevsky invariant MT estimates

Depth (km)	Conductance (S)
22	1648
115	8336
322	Perfect conductor
$\chi 2$ misfit :	38.6
RMS misfit :	0.98

As discussed in chapter 2, the 1D criterion of RMS misfit is valid only if the model residuals have a Gaussian distribution with zero-mean. Figure 6.4 shows the D$^+$ residuals (defined as the model response minus the observed data): one standard deviation errors on the EMRIDGE MT data are also shown. The distribution of the apparent resistivity residuals, ranked by period, has a significant negative correlation; phase residuals are less obviously correlated. Such trends were noted in chapter 2 for all seafloor MT data, and in chapter 3 an explanation for the correlation in terms of ocean basin 3D induction effects was demonstrated. However, other factors which may also account for correlated residuals are important. The lowest-period MT estimates are likely to be biased downward, due to lack of resolution of the magnetic field by the seafloor magnetometer: the signal-to-noise ratio is quite small, and introduces white noise into the spectral estimates in the frequency domain, which results in reduced coherence with the electric field. At long periods the Berdichevsky averages may be a poor approximation of the true MT response of the underlying solid-Earth, due to the geomagnetic coast effect.

The results of a D$^+$ joint-inversion of the EMRIDGE data set with ROSE 1B MT data (Filloux, 1982) from the East Pacific Rise (see Table 2.3) are listed in Table 6.4. Figure 6.5 shows the D$^+$ residuals from the joint inversion: the similarity of residuals indicate that EMRIDGE and ROSE MT data are compatible with the same conductivity structure. However, D$^+$ joint-inversions with seafloor data on older oceanic crust do not show such agreement of residuals, which suggests that there is a distinct mid-oceanic ridge MT signature. This result is consistent with evidence presented in chapter 2 for systematic changes in seafloor conductivity with age of oceanic lithosphere.

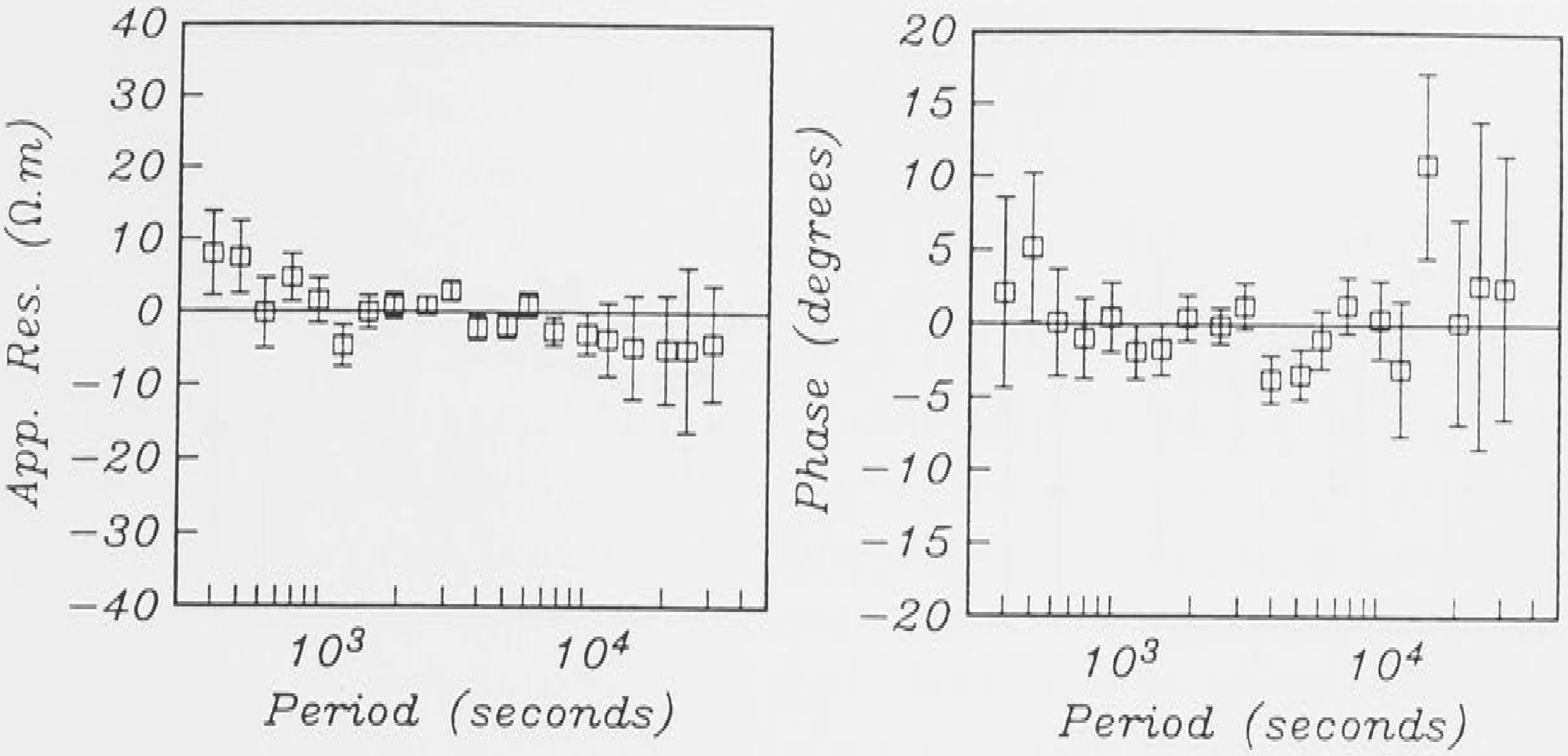

Figure 6.4 The D^+ inversion residuals, defined as D^+ response minus the EMRIDGE MT data. One standard deviation error bars on the observations are shown.

Table 6.4 Model parameters from a D^+ joint-inversion of the EMRIDGE MT Berdichevsky invariant estimates and a similar set of Berdichevsky invariant MT estimates taken from the ROSE 1B site on the East Pacific Rise (Filloux, 1982b).

Depth (km)	Conductance (S)
21	1593
111	8863
320	17475
360	Insulating half-space
$\chi 2$ misfit :	102.89
RMS misfit :	1.30

Although Parker's D^+ model provides important mathematical information, the delta function conductance spikes are geologically unreasonable representations of Earth. Figure 6.6 shows an Occam inversion (Constable *et al.*, 1987) of EMRIDGE MT Berdichevsky invariant estimates; the Occam RMS misfit is a factor of 1.25 times greater than the D^+ RMS misfit shown in Table 6.3 (see chapter 2). The conductivity profile peaks at approximately the same depths as the D^+ conductance spikes, that is at about 20 to 30 km and 100 to 150 km, with a sharp rise in conductivity at a depth of approximately 300 km.

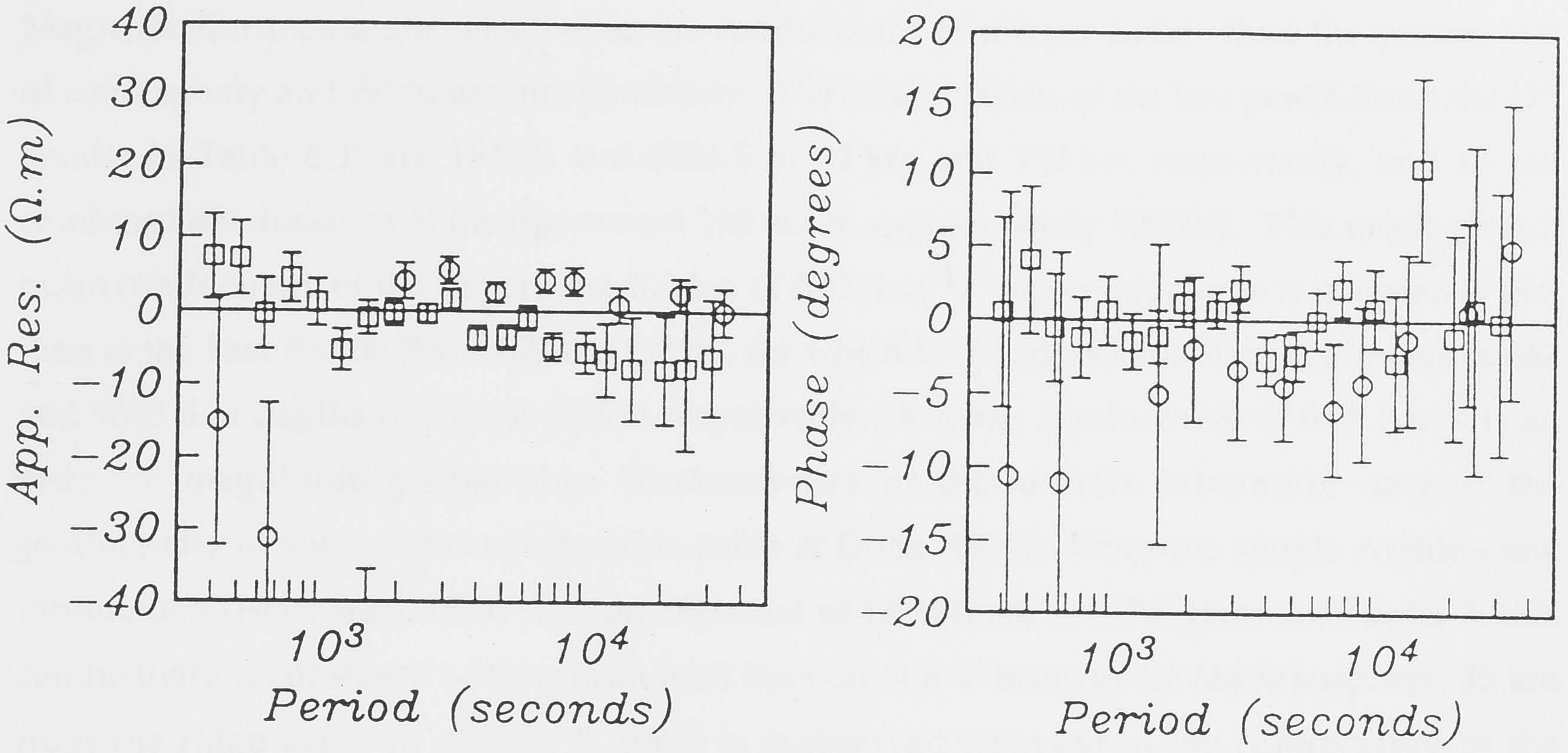

Figure 6.5 As for Figure 6.4, but for the EMRIDGE (squares) and ROSE (circles) MT data combined.

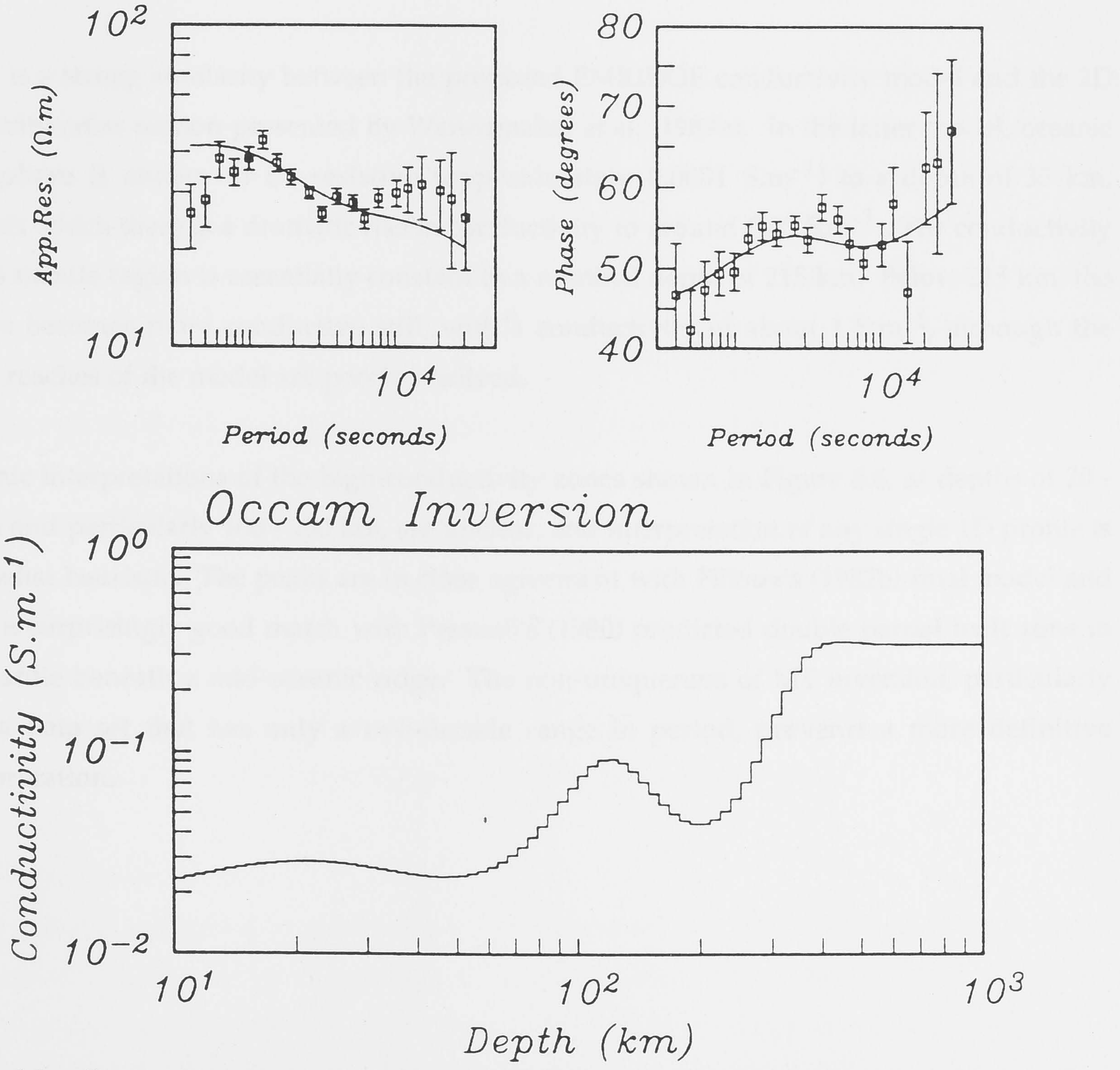

Figure 6.6 Occam inversion of the EMRIDGE MT Berdichevsky invariant estimates. The MT data with one standard deviation error and the 1D response of the Occam model are also shown.

Magnetotelluric data are sensitive to the conductance of a layer rather than the parameters of conductivity and thickness independently. The conductances of the two peaks (from the D^+ results in Table 6.3) are 1648 S and 8336 S at 22 km and 115 km respectively, and so the combined conductance of the uppermost 200 km is approximately 10000 S. This result gives a mean conductivity of the uppermost 200 km of 0.05 $S.m^{-1}$. This conductance is marginally less than at the East Pacific Rise (Filloux, 1982b), for which D^+ produces conductance spikes of 867 and 9695 S at depths of 13 and 92 km respectively. A mean conductivity of 0.05 $S.m^{-1}$ is an order of magnitude greater than conductivities predicted from laboratory data of the conductivity of sub-solidus olivine (Constable & Duba, 1990). From the simple Archie's law formulation (Hermance, 1979) with an exponent of 1.5 (Madden, 1976) given in chapter 3, this conductivity is consistent with a mean melt fraction of 6 % beneath 1.2 Ma lithosphere, 35 km from the ridge axis. In chapter 2, there is an observed decrease in the conductance of the asthenosphere with seafloor age (Figure 2.17): the high conductance at asthenospheric depths beneath the EMRIDGE MT site may be due to a large fraction of decompressional melt.

There is a strong similarity between the proposed EMRIDGE conductivity model and the 2D resistivity cross section presented by Wannamaker *et al.* (1989b). In the latter model, oceanic lithosphere is shown to be resistive (approximately 0.0001 $S.m^{-1}$) to a depth of 35 km, beneath which there is a dramatic rise in conductivity to around 0.05 $S.m^{-1}$. The conductivity of this mantle region is essentially constant to a nominal depth of 215 km. Below 215 km, the mantle becomes more conductive still, with a conductivity of about 1 $S.m^{-1}$, although the lower reaches of the model are poorly resolved.

Tectonic interpretations of the high-conductivity zones shown in Figure 6.6, at depths of 20 - 30 km and particularly 100 - 150 km, are unclear, and interpretation of any single 1D profile is somewhat heuristic. The peaks are in close agreement with Filloux's (1982b) final model and show a surprisingly good match with Presnall's (1980) predicted double partial melt zone in the mantle beneath a mid-oceanic ridge. The non-uniqueness of MT inversion, particularly with a data set that has only a two-decade range in period, prevents a more definitive interpretation.

Chapter 7 : A Tasman Project Thin-Sheet Model and the Conductivity Structure Beneath the Tasman Sea

7.1 Introduction

Seafloor MT and GDS results from the Tasman Project and CSE have been analysed in terms of the 1D conductivity structure beneath the observation sites (Ferguson *et al.*, 1985; Ferguson, 1988; Ferguson *et al.*, 1990), and the 2D conductivity structure across the coastline of southeast Australia (Ferguson, 1988; Lilley *et al.*, 1989; Kellett, 1989; White et al., 1989; Kellett *et al.*, 1991). However, 3D EM induction in the ocean, due to changes in bathymetry and the coastlines of Australia and New Zealand, is observed in the anisotropy and skew of Tasman Project MT data. The principal aim of this chapter is to examine 3D induction effects in the Tasman Sea by use of the thin-sheet approximation.

This chapter describes a systematic approach of thin-sheet modelling to reproduce the main characteristics of the Tasman Project seafloor observations. In doing so, there is an implicit assumption that the effects of EM induction in the ocean are considerably greater than those due to heterogeneities in the crust and upper mantle, as the thin-sheet algorithm is restricted to a uniform half-space, or layered half-space, beneath the sheet. This is probably a valid assumption for old oceanic lithosphere, but it is doubtful whether this is the case for young oceanic lithosphere (at which decompressional melting would result in major lateral changes of conductivity), and at subduction zones, which have been shown by Wannamaker *et al.* (1989b) to be highly-conducting leakage paths, due to the presence of fluids.

7.2 Tasman Project Data

7.2.1 Introduction

It is useful at this point to show the Tasman Project seafloor MT data; although these have been presented previously by Ferguson (1988) and Ferguson *et al.* (1990), a summary of the main results will act as reference to 3D induction effects described below.

7.2.2 Magnetotelluric Data

In this section, and throughout this chapter, references are made to the TE and TM modes of geomagnetic induction: these correspond to the orientations of the principal axis, after rotation of the impedance tensor to maximise the off-diagonal tensor elements, in the manner defined by Swift (1967) and adapted for thin-sheet analysis by Weaver (1982). The principal 2D strike for the Tasman Sea are the coastlines of southeast Australia and New

Zealand, although changes in bathymetry over the Lord Howe Rise are also important to 3D induction.

In Figure 7.1, TE and TM apparent resistivities for six seafloor MT sites across the Tasman Sea are shown, (errors are not included for greater clarity), while Figure 7.2 shows the phases of the impedances. The large peaks in TE apparent resistivities at sites TP1, TP6 and TP7 are possibly the result of the amplitude of seafloor magnetic field fluctuations passing through a minimum with distance from the coastline (Boteler, 1988). At periods greater than 8000 s, all six TE curves show a consistent decrease in apparent resistivity with period, which suggests that the conductivity structure at depths of several hundred kilometres beneath each site is similar. By contrast, TM apparent resistivities are much smaller; they increase in magnitude away from the coastlines, and are largest for site TP3. The anisotropy in apparent resistivity between TE and TM apparent resistivity is of an order of magnitude or greater. A final observation is that TM phases at all sites show close agreement, while TE phases are considerably more scattered.

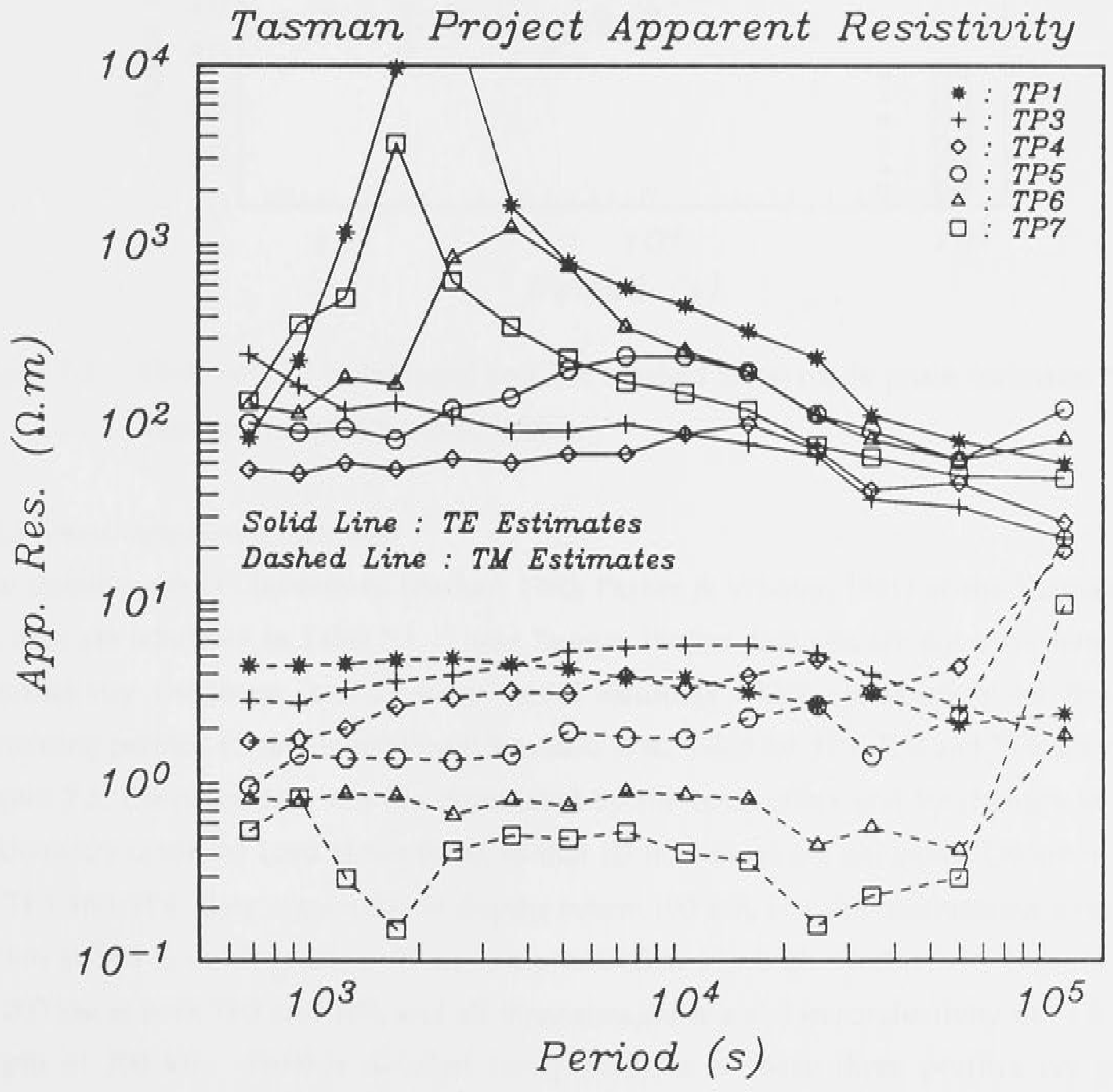

Figure 7.1 Observed TE (solid lines) and TM (dashed lines) mode apparent resistivity estimates from the Tasman Project (Ferguson, 1988).

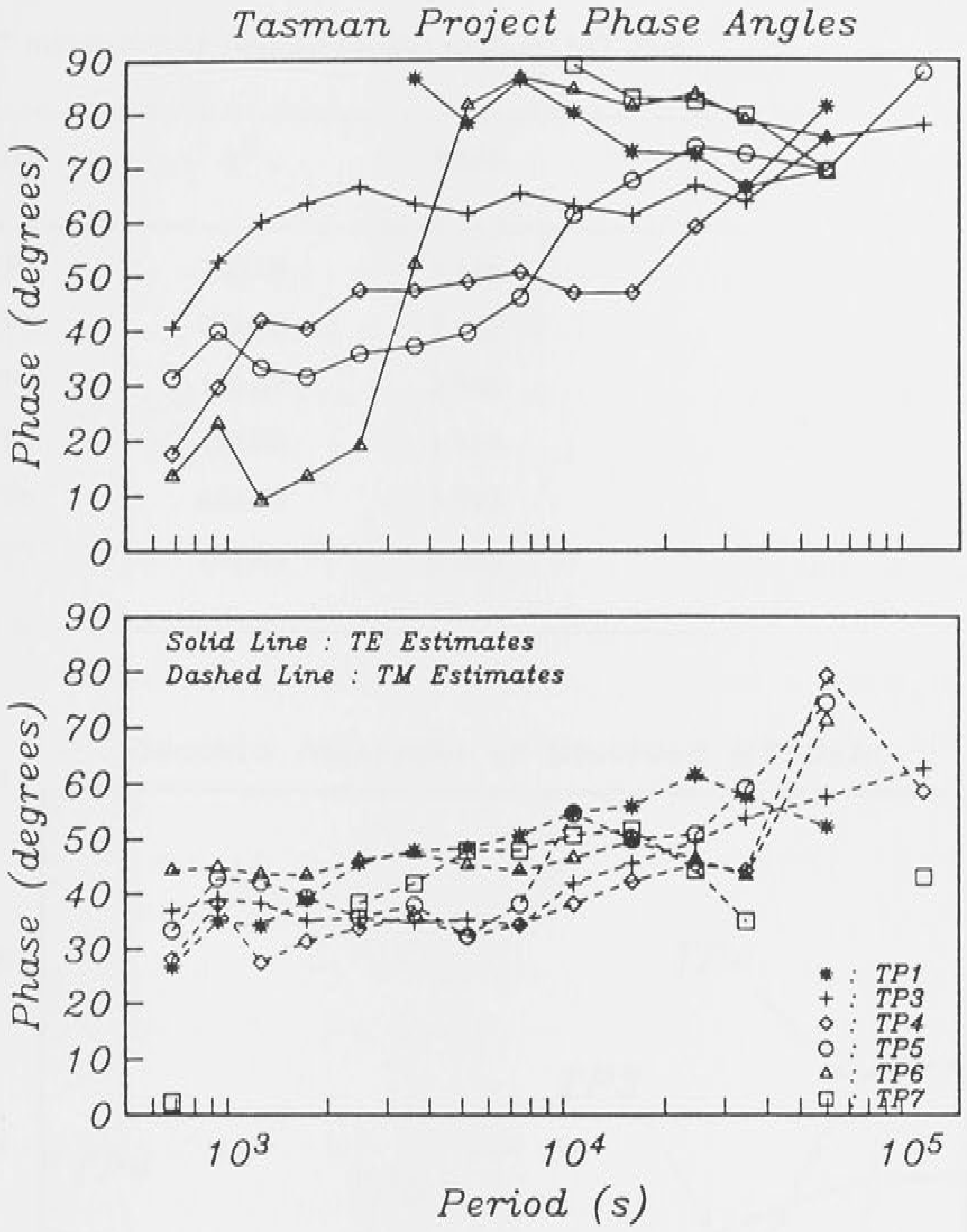

Figure 7.2 Observed TE (solid lines) and TM (dashed lines) mode phase estimates from the Tasman Project (Ferguson, 1988).

7.2.3 One-Dimensional Inversion

The statistics for D^+ inversions (Parker, 1980; Parker & Whaler, 1981) of the Tasman Project TE data are tabulated in Table 7.1. These Tasman Project data sets are not consistent with 1D conductivity structures, and all have model residuals which are strongly correlated with increasing period. Occam inversions (Constable *et al.*, 1987) for TP3, TP4 and TP5 are shown in Figure 7.3: the other data sets are dominated by the coast effect and by changes in seafloor bathymetry (over the Lord Howe Rise), so that 1D inversions are not valid. Occam inversions of TP3 and TP4 data are similar at depths below 100 km, but the conductance over the top 50 km at TP4 is much greater. There is an indication of a high-conductivity layer at a depth of 200 km at both TP3 and TP4, and all three sites show a rise in conductivity to ~1 $S.m^{-1}$ at a depth of 300 km. Further detailed interpretations of these three profiles are given by Ferguson (1988) and Ferguson *et al.* (1990).

Table 7.1 D$^+$ inversions of Tasman Project seafloor MT data.

Site	χ^2	RMS
TP1	200.79	3.168
TP3	279.20	3.157
TP4	134.59	2.368
TP5	48.000	1.549
TP6	626.58	5.597
TP7	191.65	3.096

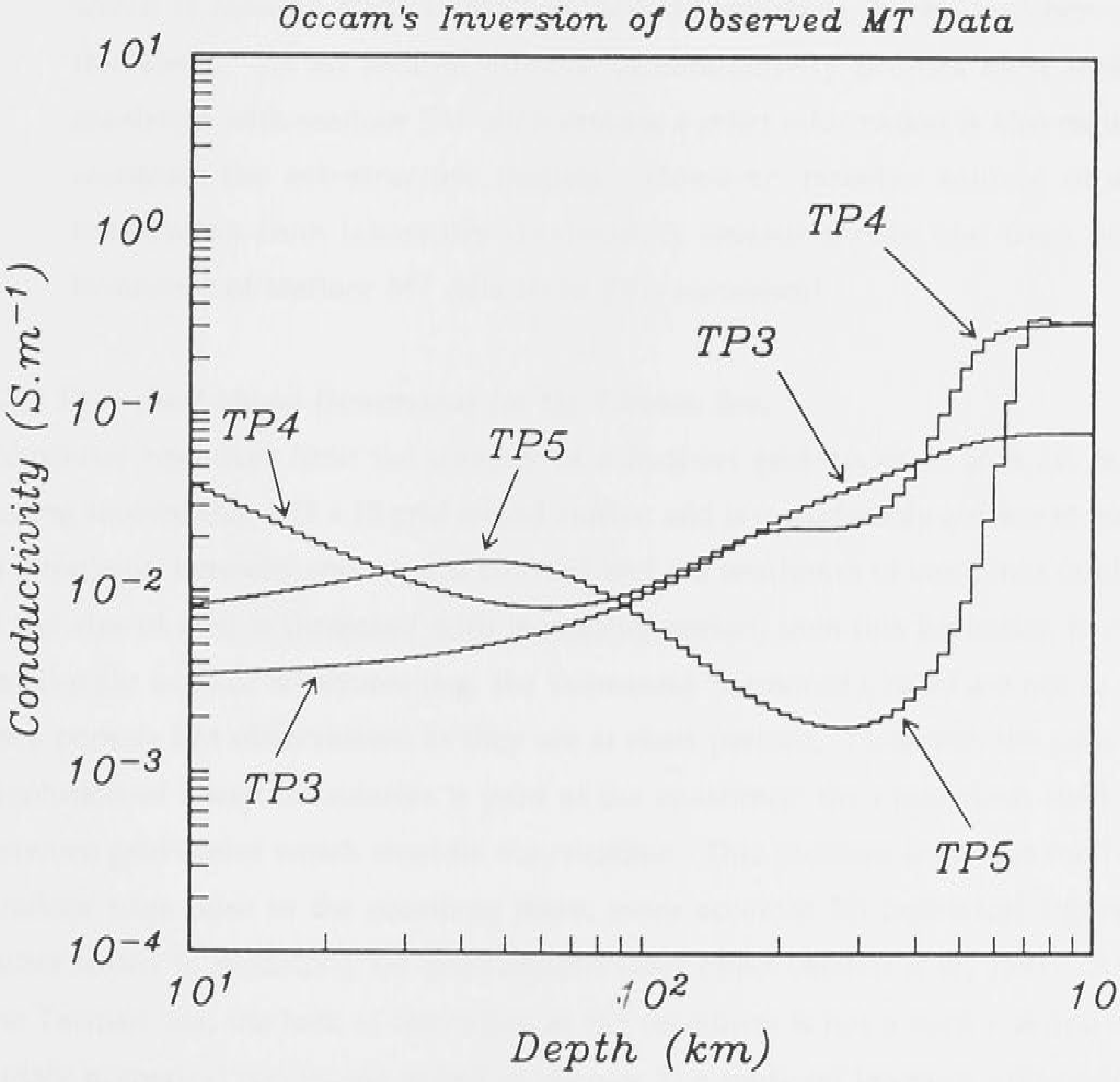

Figure 7.3 Occam inversions of TE MT estimates from sites TP3, TP4 and TP5.

7.3 Construction of Tasman Sea Thin-Sheet Models

7.3.1 Introduction

In constructing the thin-sheet model of the Tasman Sea, two factors need to be addressed:

(1) The size of the thin-sheet grid study area must be appropriate for the 3D EM induction problem. From Cox (1980) and the model studies in chapter 5, the boundary-distance for 3D induction effects away from the coastlines is characterised by the compensation distance L_0. At distances much greater than L_0 away from the coastline, geomagnetic induction is approximately 1D. A suitably large grid must therefore include all of the coastlines and changes in seafloor bathymetry which influence seafloor EM observations.

(2) As discussed in chapter 5, the conductivity structure beneath the seafloor is a significant controlling factor for 3D induction in the ocean. Thus, to accurately calculate 3D induction effects in the ocean, a layered conductivity profile, which is close to Earth's true conductivity structure, is required beneath the thin-sheet. As an infinite number of conductivity profiles exist which are consistent with seafloor EM observations, *a priori* information is also required to constrain the sub-structure models. However, possible sources of *a priori* information from laboratory conductivity measurements, and from previous inversions of seafloor MT data show little agreement.

7.3.2 Thin-sheet Model Dimensions for the Tasman Sea.

Computer resources limit the number of thin-sheet grid-nodes to 30 x 30, however initial testing showed that a 15 x 15 grid would suffice, and is considerably quicker to compute. There is a trade-off between area of grid covered and the resolution of coastlines (and bathymetry). If the size of grid is increased with increasing period, then this limitation is not so serious; small-scale tectonic structures (e.g. the Tasmantid Seamount Chain) are not as important for long periods EM observations as they are at short periods. However, the penalty for lack of resolution of sharp boundaries is paid at the coastlines: the anomalous field is 'smoothed' between grid-nodes which straddle the coastline. This problem is serious for Tasman Project seafloor sites close to the coastline; there, more accurate 2D numerical algorithms may be better suited to modelling the geomagnetic coast effect (Kellett *et al.*, 1991). At the centre of the Tasman Sea, the lack of resolution at the coastlines is not a such a serious problem. To satisfy numerical conditions (listed in chapter 3) a trade-off between grid-node spacing and the skin-depth in the layer beneath the thin-sheet is another important consideration.

The thin-sheet modelling of the Tasman Sea involved using three grids, with grid-node spacings of 200, 300 and 400 km (a fourth was later used to include Antarctica). Grey-scale contour plots of these models are shown in Figures 7.4, 7.5 and 7.6. Seafloor topography was hand-digitised from GEBCO bathymetry charts Nos 5.9 and 5.10 of the Tasman Sea, South

Pacific and Antarctic Ocean (Department of Fisheries and Oceans, Ottawa, Canada). The charts have Mercator projection, which is not an entirely suitable projection for these studies, as distortion becomes significant towards the geographic South Pole. However, the charts provide accurately contoured seafloor bathymetry, and as the Tasman Sea lies in a reasonably small range of latitudes, the distortion was considered to be less important than the ability to accurately model changes in ocean depth. Table 7.2 lists the range of periods used for each grid.

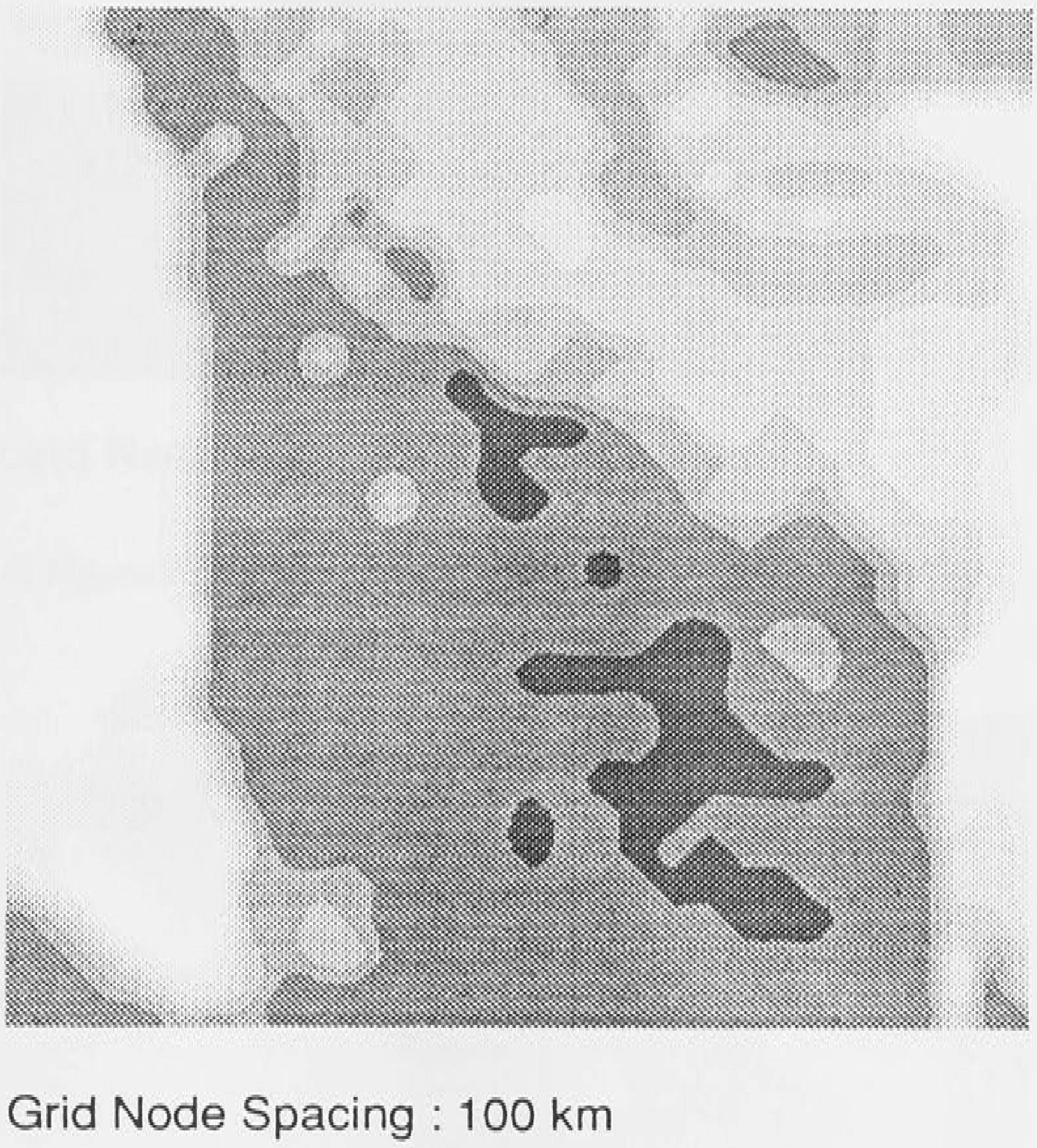

Figure 7.4 Grey-scale contoured Tasman Sea thin-sheet grid, with a grid-node spacing of 100 km, and 30 x 30 grid-nodes. The contours are based on the 8 conductance categories listed in Table 7.3, where the darkest represents category 8, and white corresponds to category 1. Final Tasman Sea models in this thesis use a 15 x 15 subset of this grid.

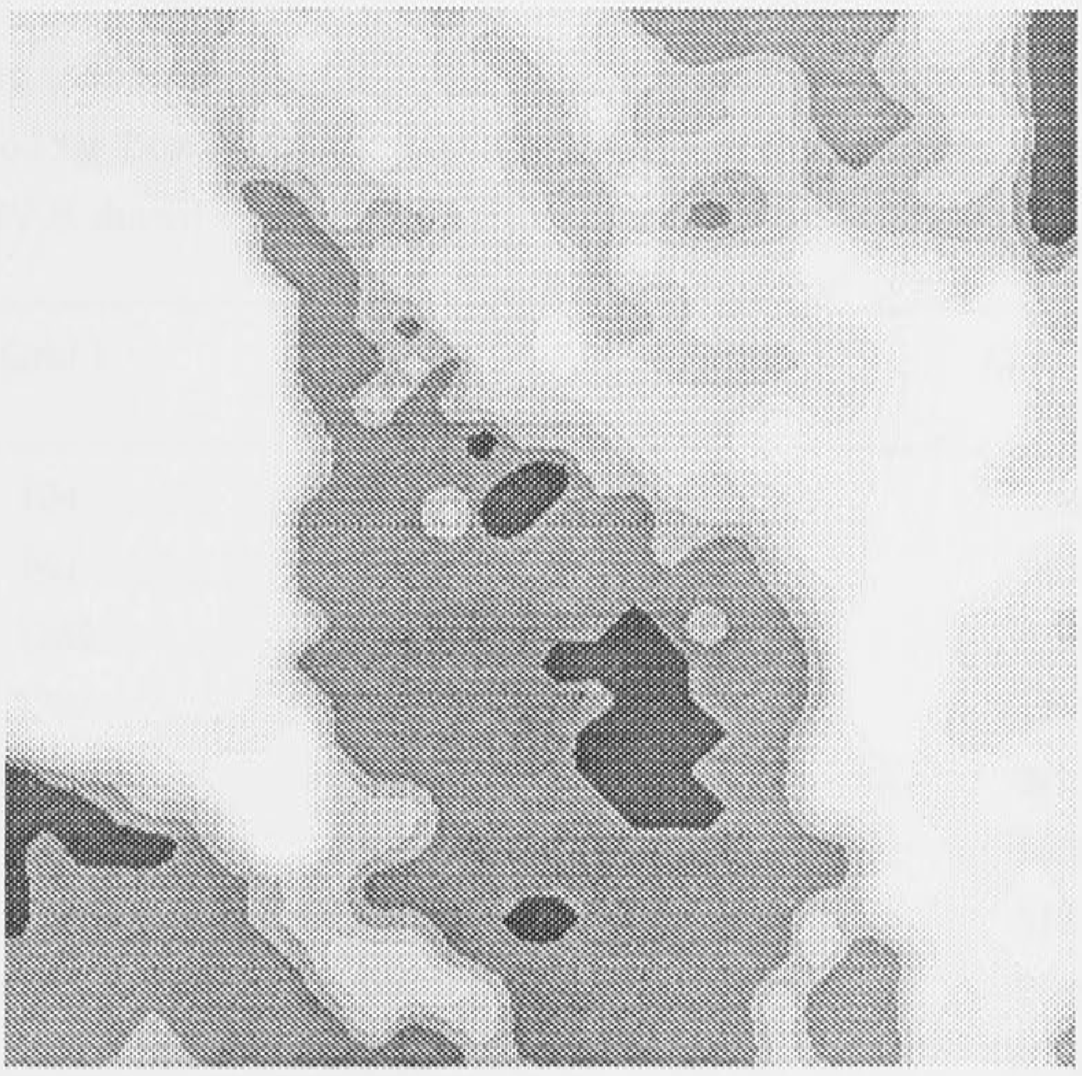

Figure 7.5 As for Figure 7.4, but with a grid-node spacing of 150 km.

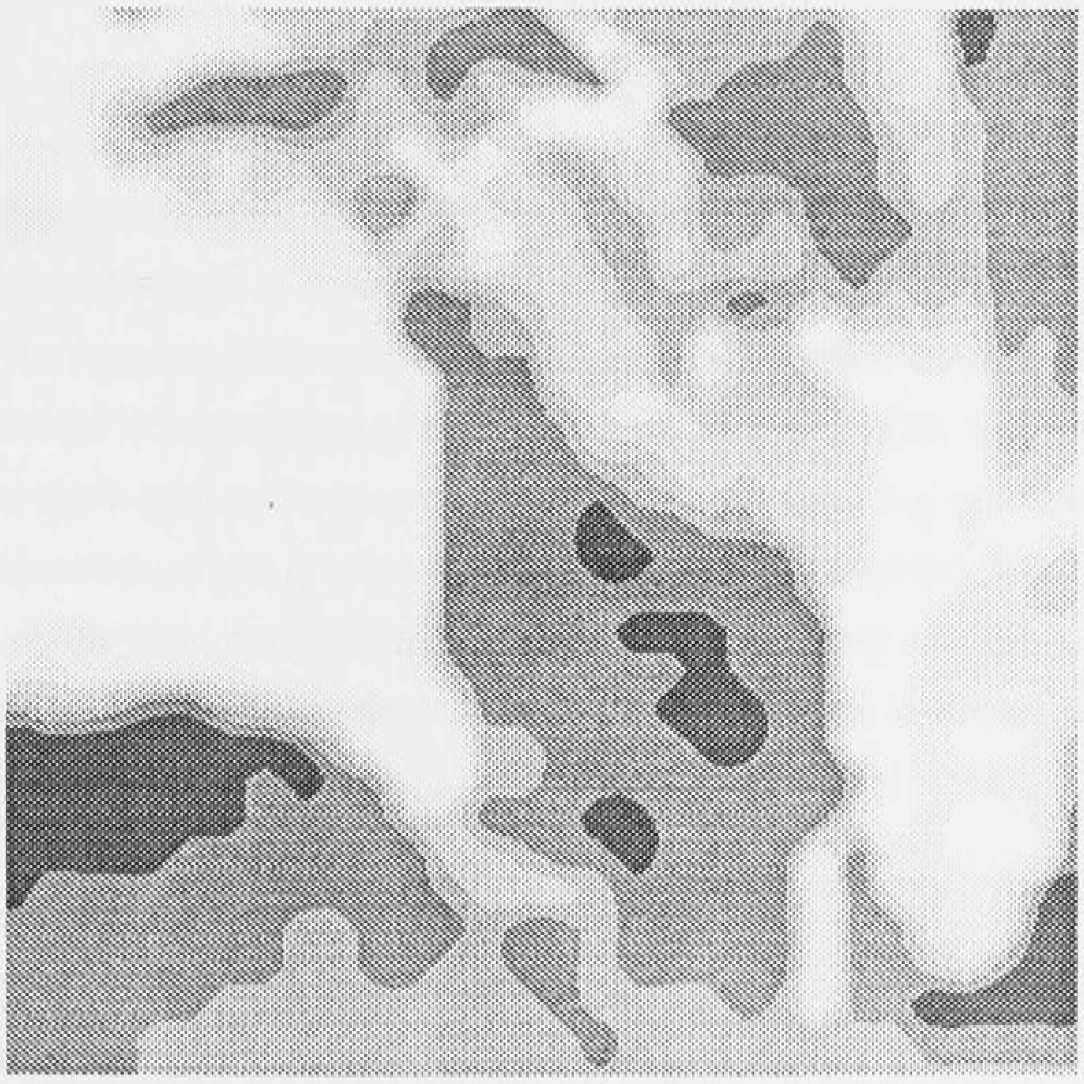

Figure 7.6 As for Figure 7.4, but with a grid-node spacing of 200 km.

Table 7.2 Periods, in seconds, used in thin-sheet calculations, based on Ferguson's (1988) band-averaging method for Tasman Project data. Grids I, II and III are shown in Figures 7.4, 7.5 and 7.6, while Grid IV is shown in Figure 7.15.

Grid I	Grid II	Grid III	Grid IV
684			684
961			961
1285			1285
1732	1732		1732
2495	2495		2495
3600	3600		3600
5191	5191		5191
7485	7485		7485
	10796	10796	10796
	15995	15995	15995
	24656	24656	24656
	34614	34614	34614
		59940	59940
		117029	117029

Although spot-depth estimates could be made at each grid-node, it is more prudent to carefully select a depth which is representative of an area the size of one grid cell, centred on the grid-node. Thus seafloor topography is subjectively low-pass filtered, depending on the grid-node separation. Consequently, the resolution of changes in seafloor bathymetry is highly dependent upon grid-node spacing. In the present modelling exercise, the bathymetry estimates at grid-nodes were grouped into seven basic categories (with one additional category for the continental crust), listed in Table 7.3. Relatively few categories are used to characterise the main changes in seafloor depth, as it is important to not introduce a degree of complexity not warranted by the resolution of the grid.

7.4 Thin-Sheet Modelling of The Tasman Sea

7.4.1 Introduction

The main objective of the systematic forward-modelling exercise now described is to elucidate the range of possible conductivity structures beneath the Tasman Sea, which are consistent with the Tasman Project observations.

Table 7.3 Thin-sheet grid categories for seafloor depths and continental crust.

Category	Description	Ocean Depth Range (m)	Mean Ocean Depth (m)	Conductance (S)
1	Continental crust	-	-	0.5 to 500
2	Continental shelf	0 - 500	250	825
3	Continental slope	500 - 1000	750	2475
4	Submerged continental crust e.g. Lord Howe Rise	1000 - 2000	1500	4950
5	Submerged continental crust	2000 - 3000	2500	8250
6	Shallow ocean	3000 - 4000	3500	11550
7	Abyssal plain	4000 - 5000	4500	14850
8	Abyssal plain and subduction zones	5000+	5000	16500

Thin-sheet forward-modelling requires good *a priori* information. Some *a priori* information, such as seafloor bathymetry and conductivity of salt-water, is known accurately. However, the properties of solid-Earth are not so well determined. For the forward-modelling exercise, it is necessary to define a 1D Earth conductivity profile. Two approaches to this task are possible: one can use the results of previous observational experiments; and one can develop models of conductivity which are based on laboratory measurements, and knowledge of mantle petrology and temperature etc. (as in chapter 4).

In the thin-sheet modelling of the Tasman Sea, the first approach has been taken by adopting the profile for Tasman Project site TP3 (Ferguson *et al.*,1990); and the second approach by using the profile derived for 70 Ma seafloor, as in Figure 4.7 and Table 5.3. However, there is little agreement between the two conductivity profiles. The TP3 profile has upper lithosphere conductivities two- to three-orders of magnitude greater than the laboratory data profile, and over the depth range 100 - 400 km differences are of an order of magnitude. The two models show similarity below 400 km only, but resolution of deep structure by seafloor MT, and knowledge of electrical conduction and temperature in the lower mantle are both poor. The problem addressed here is to examine the extent to which the two profiles may be reconciled by 3D induction in the Tasman Sea. To carry out this task, the conductivity profile beneath the thin-sheet is varied between bounds suggested by the TP3 profile and the laboratory data profile, in order to reproduce the observations shown by Ferguson (1988), Kellett (1989), Ferguson *et al.* (1990) and Kellett *et al.* (1991).

Each thin-sheet model calculation generates an enormous quantity of synthetic data; covering the whole of the Tasman Sea, surrounding oceans and continental crust. In this section, comparisons are made with observations from sites TP3, TP4 and TP5 only, shown in Figure 2.1. All models share common grid-nodes at the coastline site of Durras and at site TP3 (Table 2.1). The proximity of sites TP6 and TP7 to the coastline precludes their use in this thin-sheet model comparison, as the model is not successful in replicating the sharp changes in conductivity at the coast. Data from site TP1 are also not used, as the site is close to the edge of the small grid (Grid I), and the rapid changes in seafloor bathymetry at the Lord Howe Rise are not well represented by a grid-node spacing of 200 km (or greater). Site TP3 is on normal oceanic lithosphere, far from the major tectonic features in the Tasman Sea, and attention will focus particularly on reproducing, in the model response, the observed MT parameters for this site.

7.4.2 Oceanic Upper Lithosphere Conductivity

Figure 7.7 shows conductivity profiles for the Tasman Sea, in which the conductivity of the upper lithosphere is varied from 10^{-3} to 10^{-5} S.m^{-1}, and the structure is otherwise that of 70 Ma lithosphere and upper mantle (as in Table 5.3).

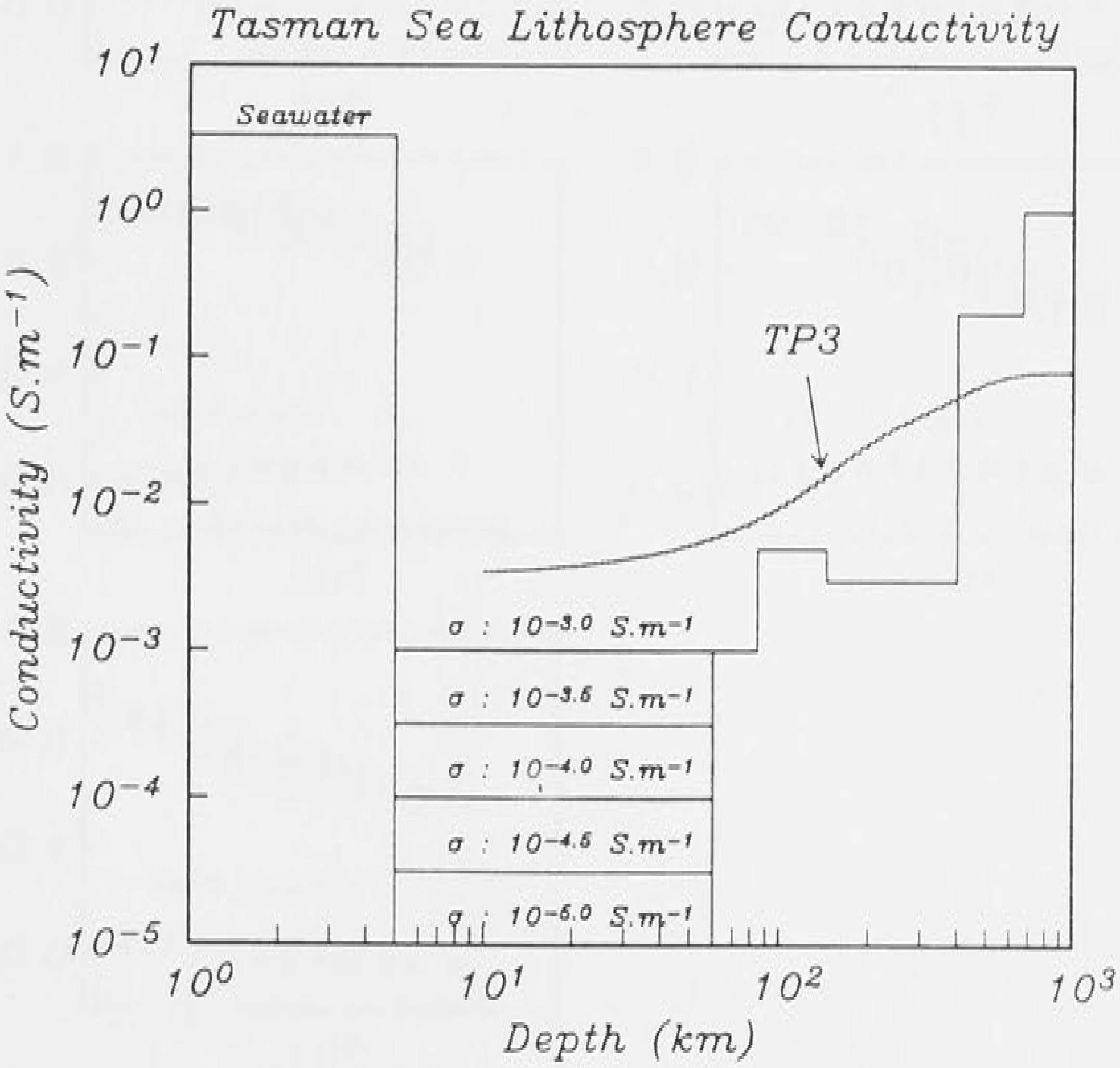

Figure 7.7 Conductivity structures used in Tasman Sea models, based on the 70 Ma lithosphere and upper mantle model in Table 5.3, with 5 upper lithosphere conductivities. Also shown is the Occam inversion of MT data from site TP3.

Thin-sheet models (Figures 7.4, 7.5 and 7.6) were run for Grids I, II and III at periods listed in Table 7.2. In total, a maximum of 25 separate calculations were made at 14 distinct periods, with overlapping period values to check for consistency between grids. The numerical results for the Tasman seafloor were adjusted by correction-factors described in section 5.1.5. These correction-factors were obtained from a set of 1D thin-sheet models (comprising a uniform depth ocean) overlying the sub-structure used in the Tasman Sea model, for the same set of 25 calculations as for each Tasman Sea model. These corrections-factors have a 1D static-shift type of effect; it is not possible to calculate equivalent numerical adjustments for 2D and 3D structures. Figure 7.8 shows the correction-factors, which are greatest (i.e. their real parts differ most from unity) for the most resistive models. The scatter of the correction-factors may show the degree of numerical consistency between grids of different size.

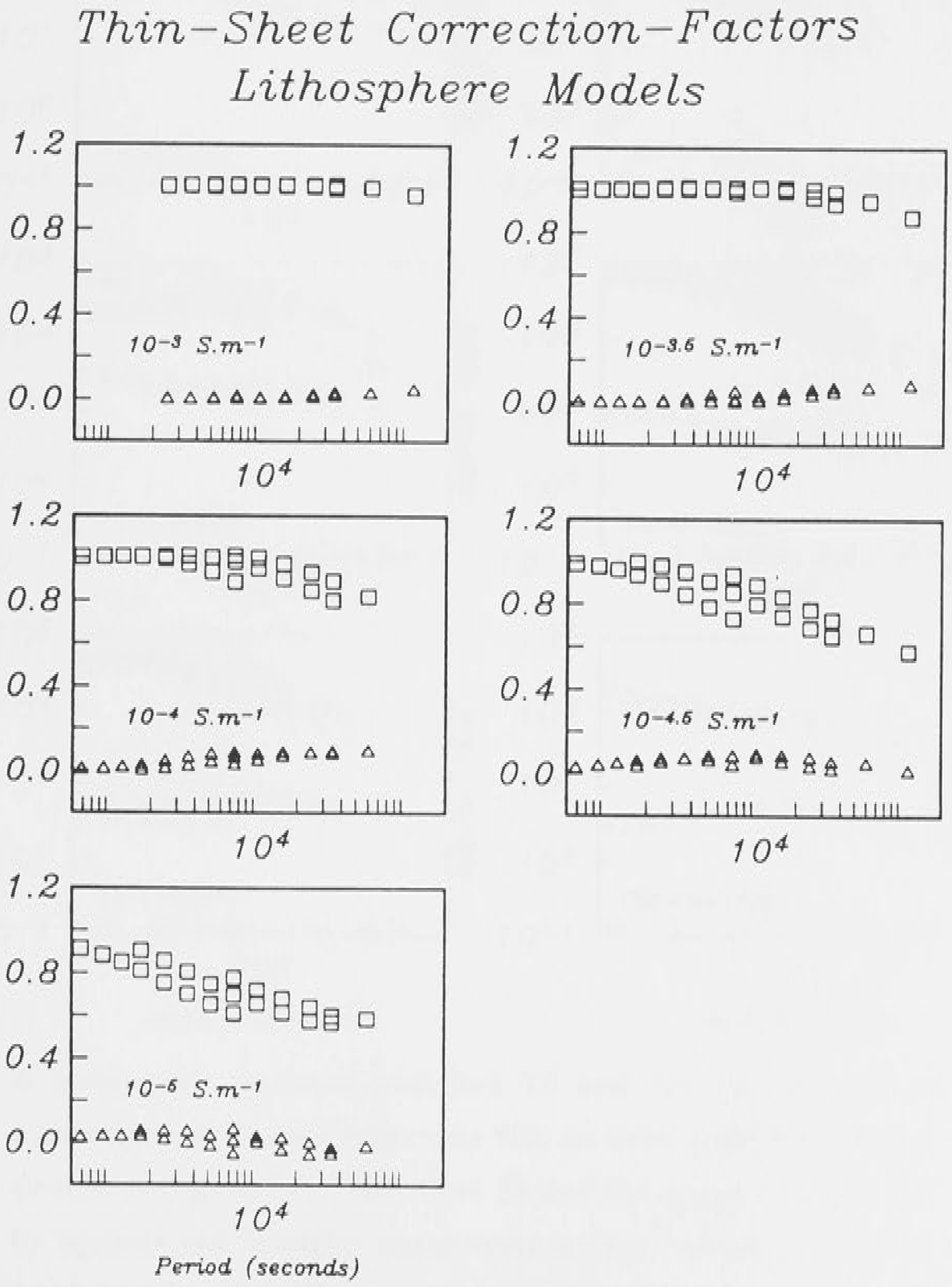

Figure 7.8 Correction-factors for the 1D thin-sheet model of uniform ocean depth, beneath which are the conductivity structures shown in Figure 7.7.

At each period, the modelled MT impedance tensors were calculated at the bottom of the sheet (corresponding to 'seafloor' MT impedances), and rotated to maximise the off-diagonal elements by the method of Swift (1967). Figure 7.9 shows the seafloor TE and TM apparent resistivities for TP3, and the 1D MT responses of the 5 underlying conductivity structures, shown in Figure 7.7. Also shown are observed TE and TM apparent resistivities from Ferguson *et al.* (1990) for TP3.

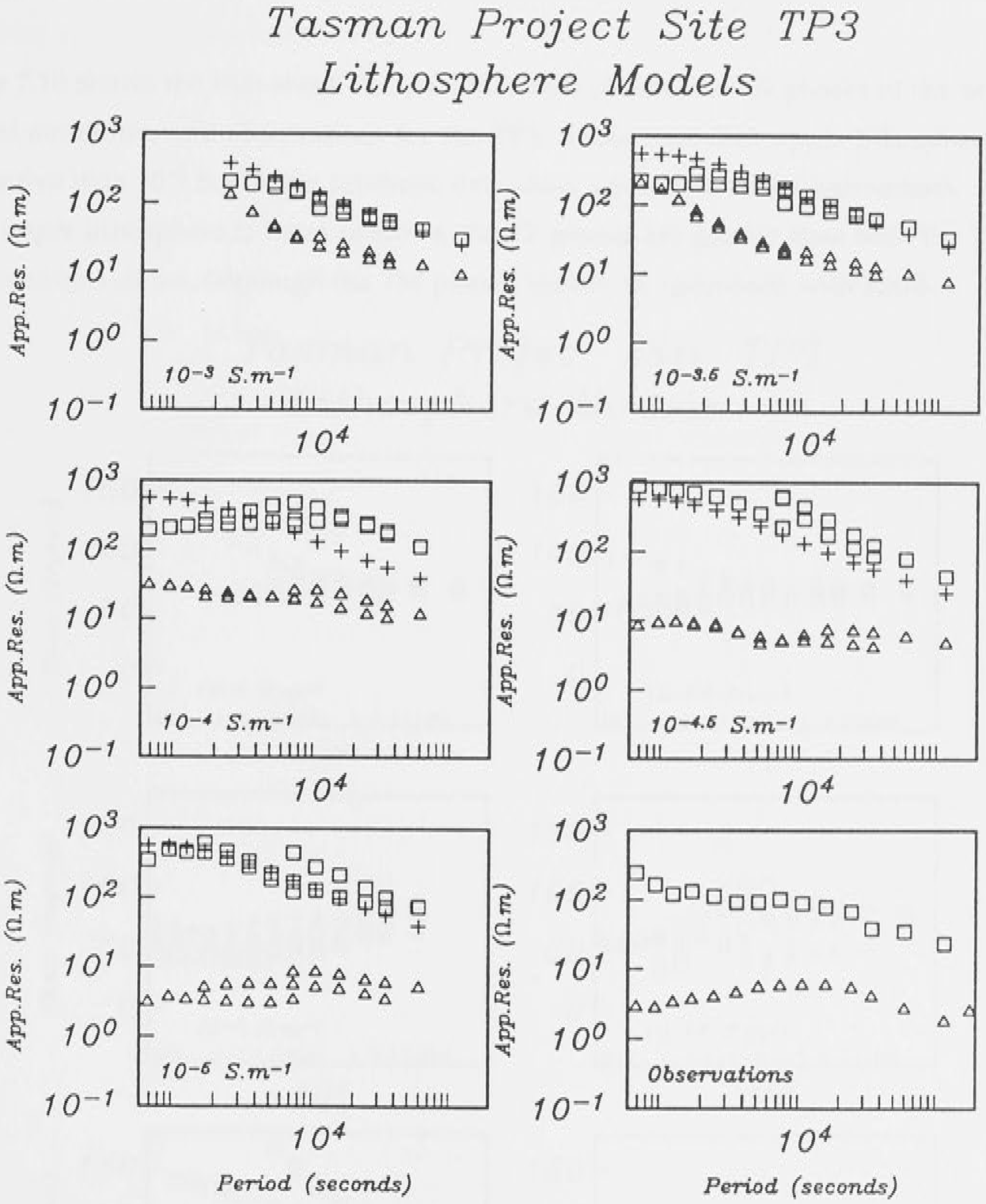

Figure 7.9 A comparison between modelled TE and TM apparent resistivities, and observations at Tasman Project site TP3, for the 5 upper lithosphere conductivity structures (Figure 7.7). Thin-sheet TE and TM apparent resistivities are shown by squares and triangles respectively for the 5 models of upper lithosphere conductivities. The 1D responses of the 5 conductivity structures are shown by the plus (+) signs. For comparison, observed TE (squares) and TM (triangles) apparent resistivity at site TP3 are shown.

A number of immediate observations can be made from Figure 7.9. The anisotropy between the TE and TM modes appears to be diagnostic of the upper lithosphere conductivity; this conductivity must be 10^{-4} S.m^{-1}, or less, to produce the anisotropy as observed. Similar trends for TP4 and TP5 support this conclusion. As the lithosphere becomes more resistive, the anisotropy increases, with the main change occurring for the TM mode; the shape of the TM responses change markedly over the range of models. At periods longer than 5000 s, the TE mode recovers the 1D response quite well .

Figure 7.10 shows the thin-sheet TE and TM model phases, the 1D phases of the underlying layered structures, and observations for site TP3. If the modelled upper lithosphere is more conductive than 10^{-4} S.m^{-1}, the synthetic data show agreement with observations. However, if the upper lithosphere is more resistive, the TE phases are greater than both the 1D phases and the observations, (although the TM phases remain in agreement with both).

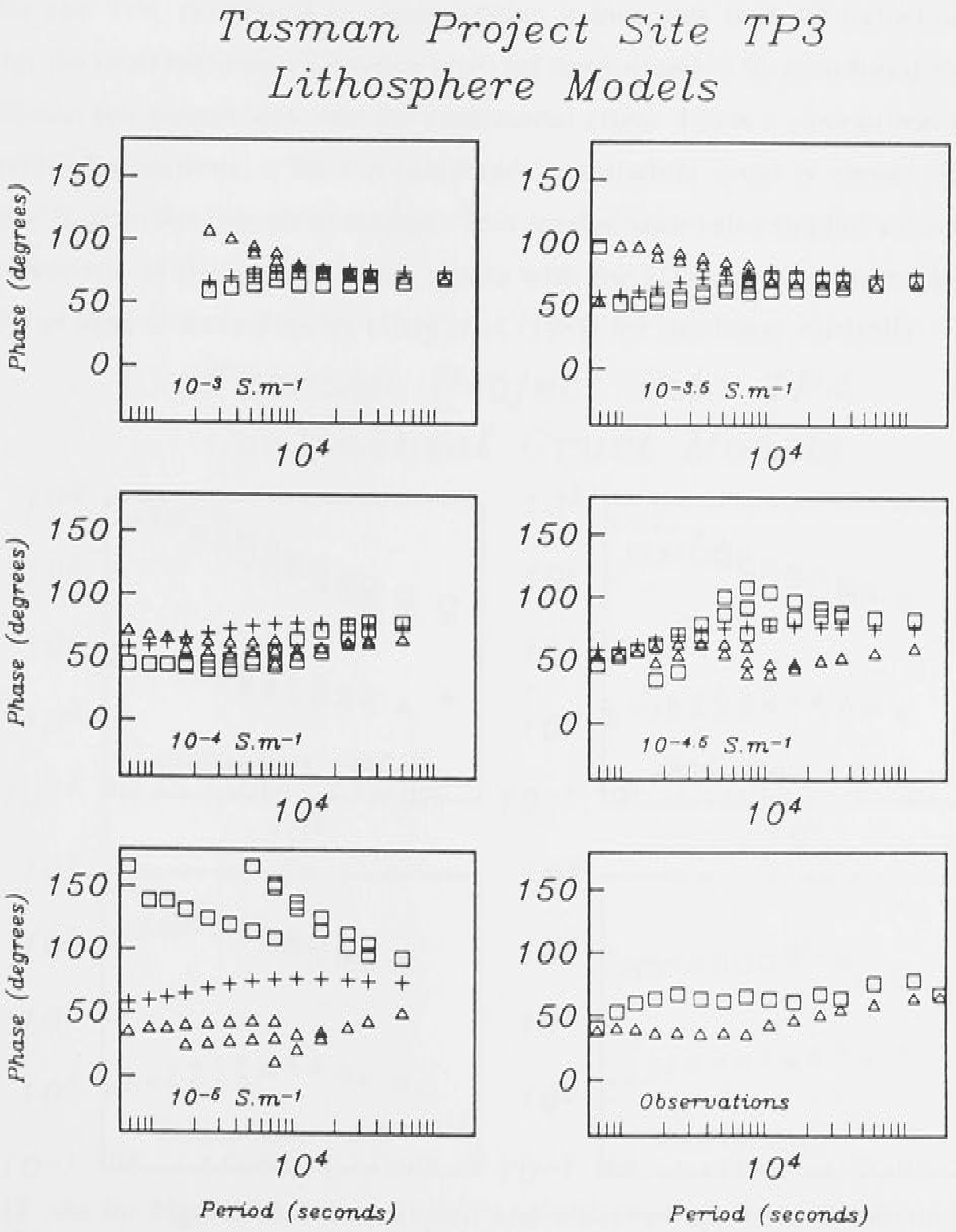
Tasman Project Site TP3
Lithosphere Models

Figure 7.10 As for Figure 7.9, but modelled and observed phases at site TP3.

Numerical error increases with the upper lithosphere resistivity, characterised by the disparity between TE values from different grids; however the trend of TE phases is evident.

The anisotropy in observed MT estimates suggests that a resistive upper lithosphere is a necessary feature of Tasman Sea conductivity models. However, a satisfactory match of model response and observations has not yet been achieved. Furthermore, conclusions so far are based on varying just one parameter (the upper lithosphere conductivity), and so may be restricted by the model structure defined in Figure 7.7 over the depth range 60 to 400 km.

7.4.3 Conductance of the Continental Crust

Three thin-sheet models with different continental crust conductances of 5, 50 and 500 S included in the thin-sheet were computed, underlain by the structure in Figure 7.7 (with upper lithosphere conductivity 10^{-5} S.m^{-1}). Figure 7.11 shows thin-sheet apparent resistivity results for site TP4, compared to observations: it indicates that 3D induction effects are greatest for the most resistive continental crust (of conductance 5 S), as induced electric current in the Tasman Sea cannot leak into the continental crust. From a comparison of the model results with observations, a 50 S conductance continental crust is chosen for use in all subsequent Tasman Sea thin-sheet models. This conductance value implies a mean continental crust conductivity of 0.01 S.m^{-1}, which agrees with the 2D modelling estimates of Kellett *et al.* (1991) and land observations by Lilley *et al.* (1981) for southeast Australia

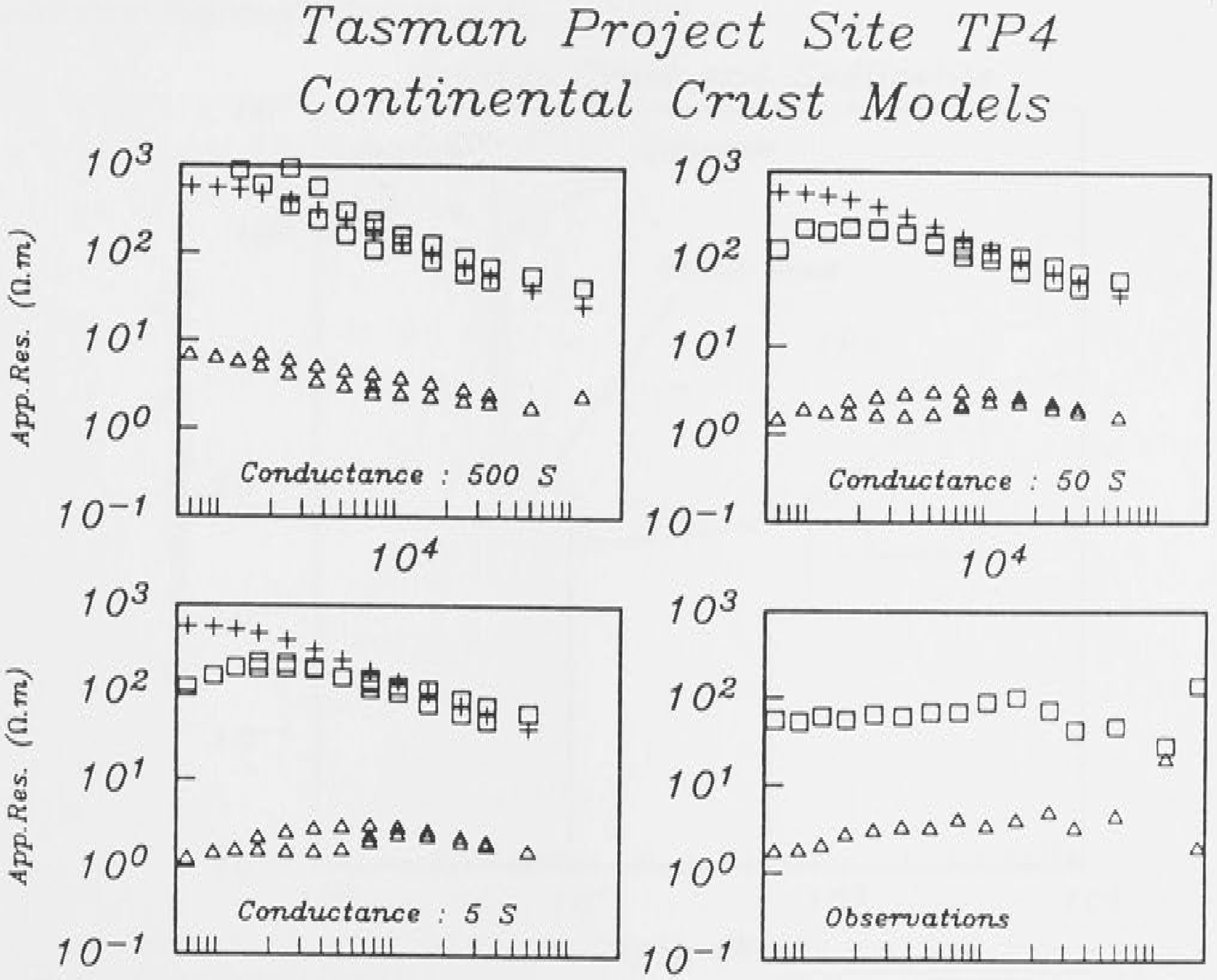

Figure 7.11 As for Figure 7.9, but modelled and observed apparent resistivities at TP4, for different continental crust conductances.

7.4.4 The Oceanic Crust and Sediments

Common to all Tasman Sea thin-sheet models described so far is that no oceanic crust or sediments have been included in the layered half-space, or within the sheet. Previous *in-situ* measurements (Becker *et al.*, 1982) and CSEM interpretations (Evans *et al.*, 1991) show conductivities higher than in the upper mantle, probably due to permeating fluids in pillow lavas, and in sheeted dyke complexes. Porosity (and hence conductivity) falls with increasing depth, due to crack sealing with increased pressure. It is relatively simple to include an oceanic crust in the layered half-space beneath the Tasman Sea models, although the thin-sheet approximation is no longer satisfied at the shortest periods.

The oceanic crust beneath the Tasman Sea has been estimated to be of thickness 10 km by Shor *et al.* (1971). An oceanic crust can be included in the thin-sheet model (Figure 7.12), with a 5 km upper crust of conductivity 10^{-2} S.m^{-1}, and a lower crust conductivity 10^{-5} S.m^{-1}. Figure 7.13 shows the thin-sheet TE and TM apparent resistivities at site TP5, with the observations. The comparison of thin-sheet and observed data suggests that the MT data are considerably more sensitive to the presence of the resistive upper lithosphere than to the more conductive oceanic crust, except at short periods (Drury, 1981; Ranganayaki & Madden, 1981). However, an oceanic crust is included in all subsequent thin-sheet models as it is a real feature of the Tasman Sea tectonic structure, and also for computational reasons. The more conductive crust results in smaller numerical inaccuracy from the 1D thin-sheet model, and thus correction-factors are close to unity.

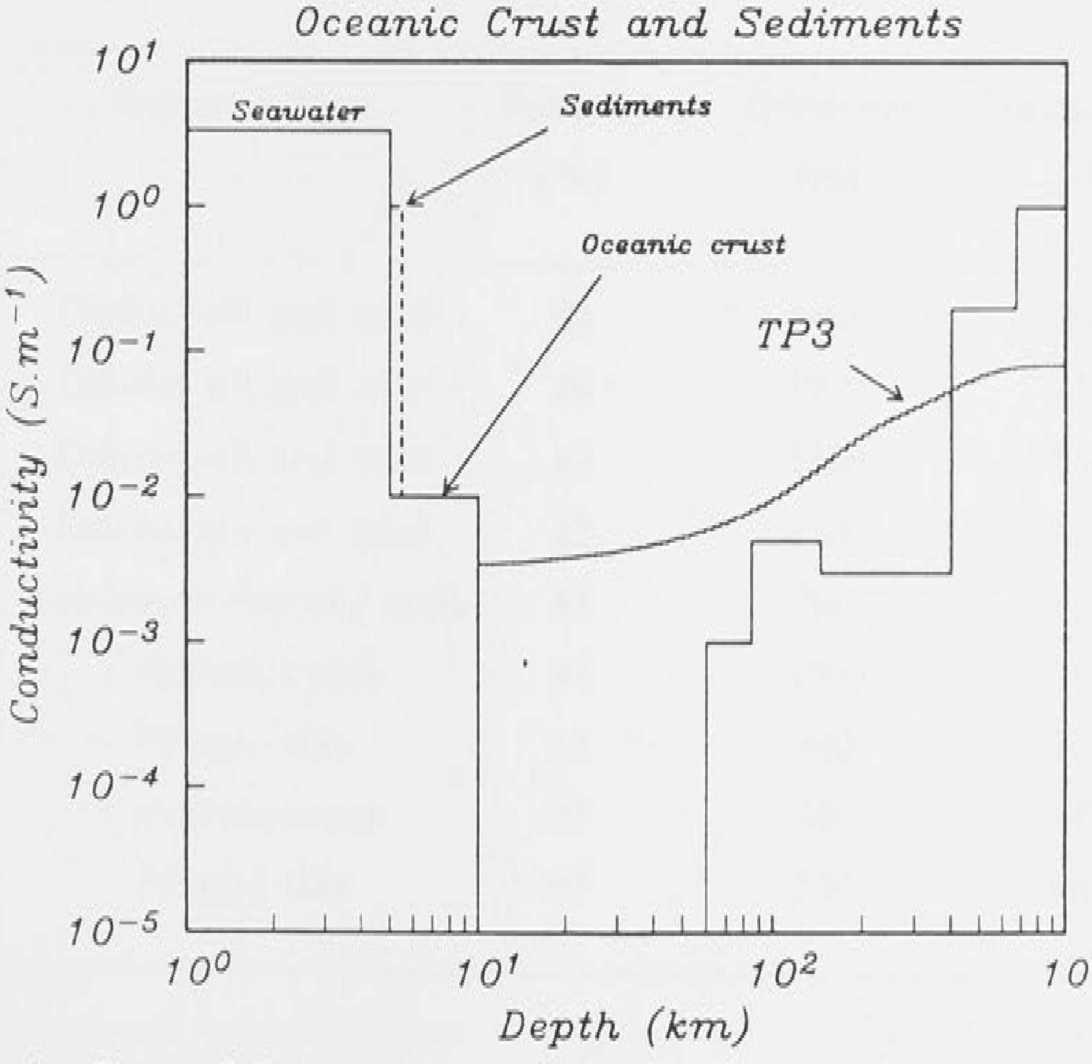

Figure 7.12 As for Figure 7.7, but with upper lithosphere conductivity fixed at 10^{-5} S.m^{-1}, and including an oceanic crust and sediments.

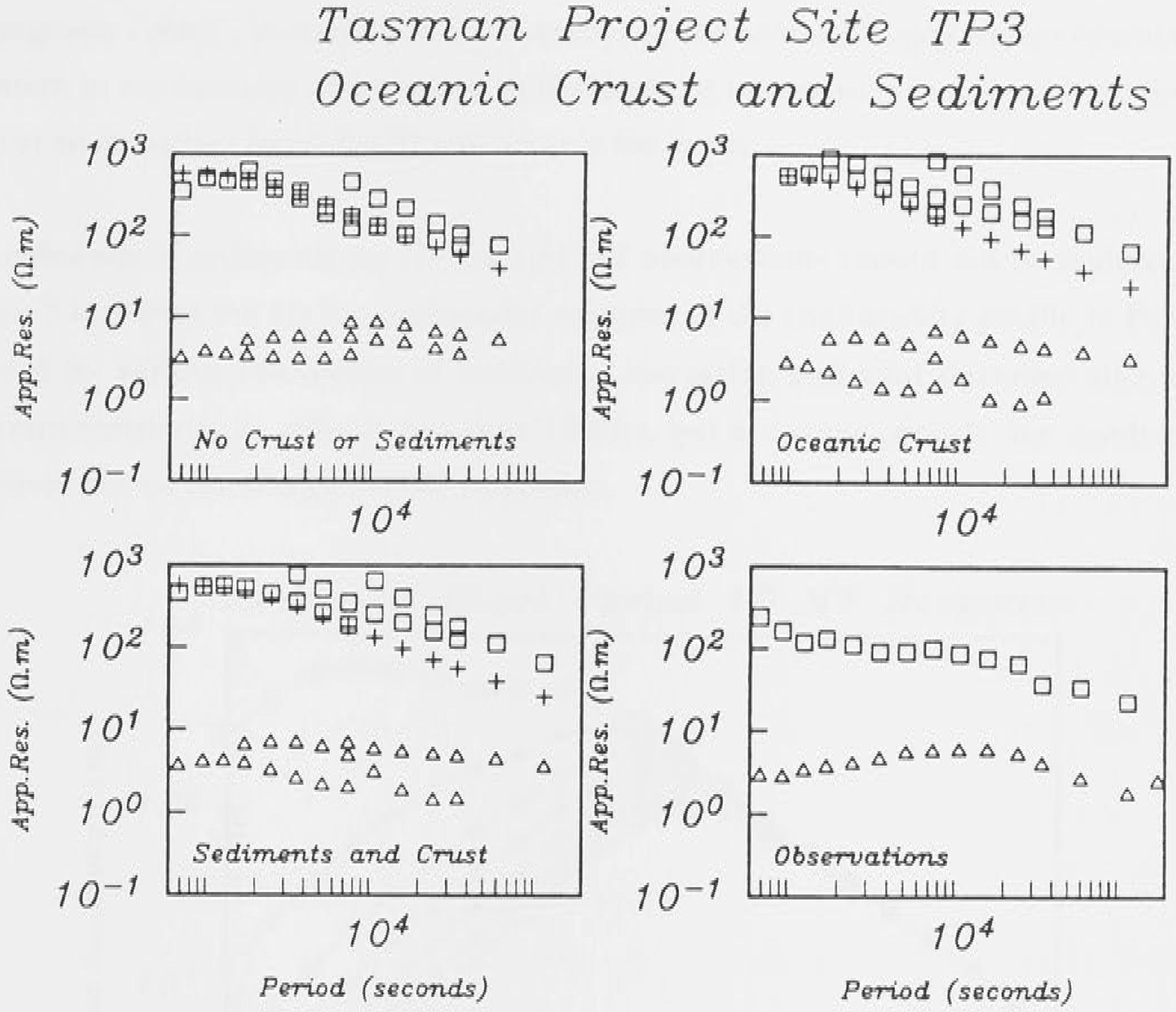

Figure 7.13 As for Figure 7.9, but with the conductivity structures shown in Figure 7.12.

Table 7.4 Sediment type, porosity, thickness and conductance at Tasman Project sites

Site	Sediment Type	Porosity (%)	Thickness (m)	Conductance (S)
TP8	Detrital silt and mud	44	990	733
TP9	Detrital silt and mud	40	1250	813
TP7	Detrital silt and mud	40	1250	813
TP6	Detrital silt and mud	42	1100	1000
TP5	Calcareous clay and mud	48	760	638
TP4	Calcareous ooze	44	1000	740
TP3	Pelagic clay	64	400	504
TP2	Calcareous ooze	57	440	480
TP1	Pelagic clay	67	340	462

Table 7.4 lists sediment type, thicknesses, porosity and estimated conductance at each Tasman Project site. Data were provided by P. J. Mulhearn, of DSTO, Sydney, and tabulated

in Ferguson (1988). Variations in conductance of the sediment layer are comparable to the variation in conductance of sea-water as the depth of the ocean is varied, and are thus likely to be of an important factor for 3D induction in the ocean.

The influence of sediments on 1D seafloor MT observations should not be underestimated. Figure 7.14 shows the 1D forward-model response of the conductivity profile in Figure 7.12, covered by various thicknesses of sediment. Increasing sediment thickness attenuates the apparent resistivity at periods less than 10000 s, but at longer periods, the conductivity of the lower mantle dominates the MT response.

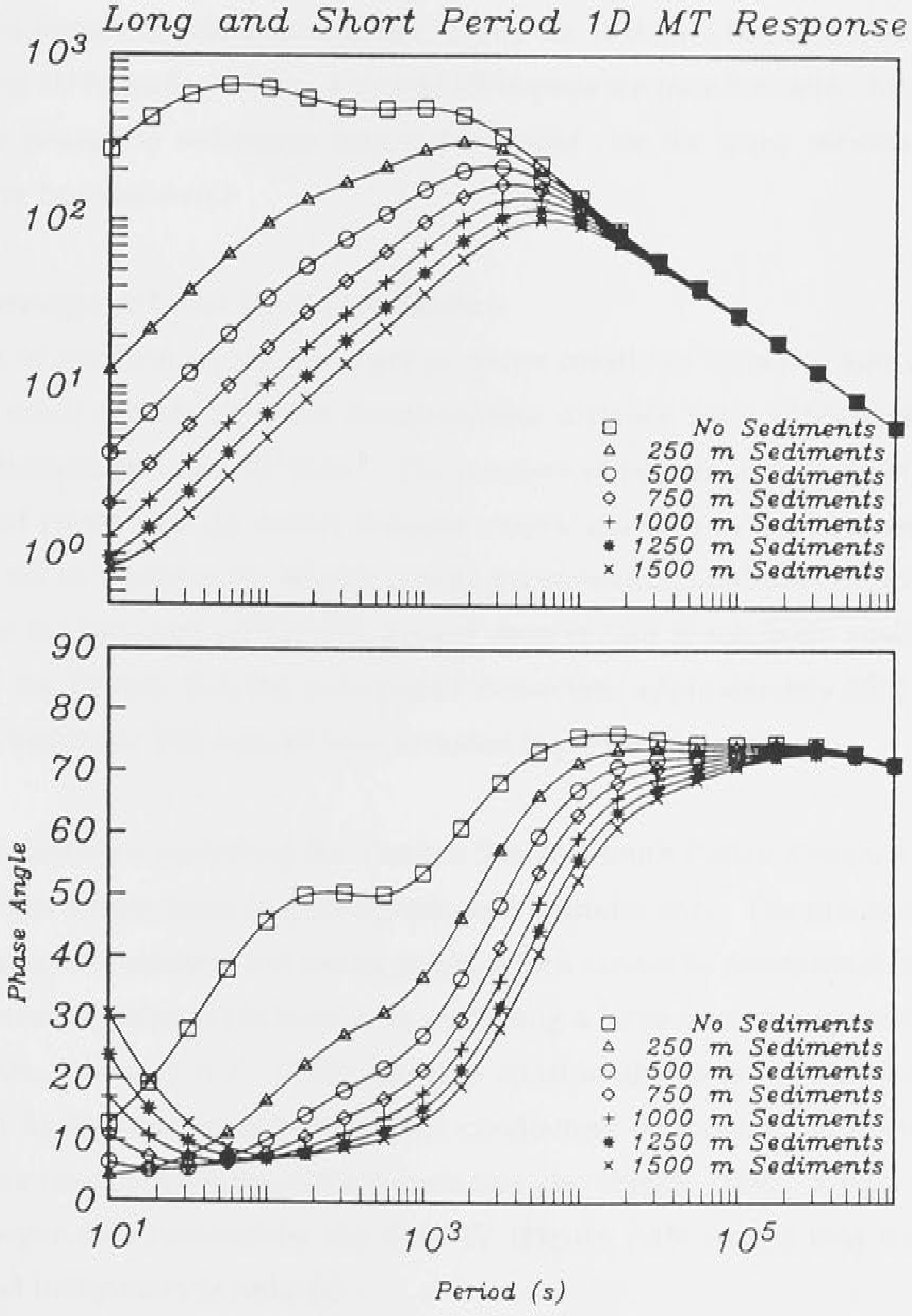

Figure 7.14 The 1D responses of the conductivity structure shown in Figure 7.7, with an upper lithosphere conductivity of 10^{-5} S.m^{-1}, and varying thicknesses of sediment of conductivity 1 S.m^{-1}. The sediment thicknesses cover the estimated range across the Tasman Sea, shown in Table 7.4.

For reasons discussed in chapter 5, it is not possible to include a sediment layer within the layered half-space beneath the thin-sheet. A Tasman Sea model with a sediment layer was constructed by adding the conductance of 500 m of sediment (with conductivity 1 $S.m^{-1}$) to the conductance of sea-water in the thin-sheet (see Table 7.3). It is then possible to make a first-order correction for sediments by a 1D impedance transformation from the bottom of the thin-sheet to the top of the sediments, as described in section 5.2.6, Table 5.8. Figure 7.13 shows a comparison between the TE and TM apparent resistivity above the modelled sediments, and that at TP5. This comparison suggests that the 3D induction effects dominate the 1D perturbations by the extra thickness of sediment, so that sediments have little effect on seafloor EM observations (although thick sediment wedges, which channel electric currents, are important factors at subduction zones). However, it should be noted that in the presence of such strong 3D induction effects, a simple 1D impedance transformation from the bottom of the sheet to above the sediments may not be valid (for the same reasons that a 1D MT inversion may be inaccurate).

7.4.5 The Geomagnetic Coast Effect of Antarctica

To the north of the Tasman Sea, there are no major coastlines for many tens of thousands of kilometres, much further than the compensation distance for a lithosphere of estimated resistance-thickness product $10^9\ \Omega.m^2$. The presence of islands, and shallowing of the ocean over the Lord Howe Rise do deflect induced electric currents in the Tasman Sea; however, they do not act as a barrier for electric charge accumulation, and thus thin-sheet modelling suggests that the influence on Tasman Project observations is relatively small. However, to the south of the Tasman Sea, the coastline of Antarctica, approximately 2500 km away from the Tasman Project site TP3, has not been included in previous models.

There are problems in modelling the Tasman Sea and south Pacific Ocean, as the thin-sheet model no longer covers areas of geomagnetic mid-latitudes only. The presence of the auroral zones will cause non-uniform EM source fields, which cannot be represented by the present thin-sheet model. Another significant problem is in modelling a large area of a spherical Earth with a flat thin-sheet. Beamish *et al.* (1983) develop considerably more sophisticated models of induction in Earth's oceans; however their conducting ocean-sheet is electrically isolated from the more conductive parts of the mantle (see also Winch, 1989). A final problem is that the much larger area covered by the Grid IV (Figure 7.15) means that the resolution of coastlines and bathymetry is reduced.

Despite these problems, a first-order calculation of the influence of Antarctic can be made. Underlying the thin-sheet model is the structure in Figure 7.7, with upper lithosphere conductivity of 10^{-5} $S.m^{-1}$. A comparison between the thin-sheet results and observations at

TP3 suggests there is no evidence of distortion, by the coastline of Antarctica, of TE data from the 1D response of the substructure, except at periods less than 2000 s. The attenuation at short periods may be due more to the coastlines of southeast Australia and New Zealand, than due to Antarctica. Similar trends are evident in comparisons with observed data at TP4 and TP5. The proximity of Antarctica to the Tasman Project sites might be assumed to have a more profound effect on the observed MT data in the Tasman Sea; possibly the attenuating effect of Antarctica is counteracted by channelling of electric current between coastlines of southeast Australia and New Zealand. The thin-sheet model is not sufficiently accurate (due to the limited number of grid-nodes) to pursue this case study further.

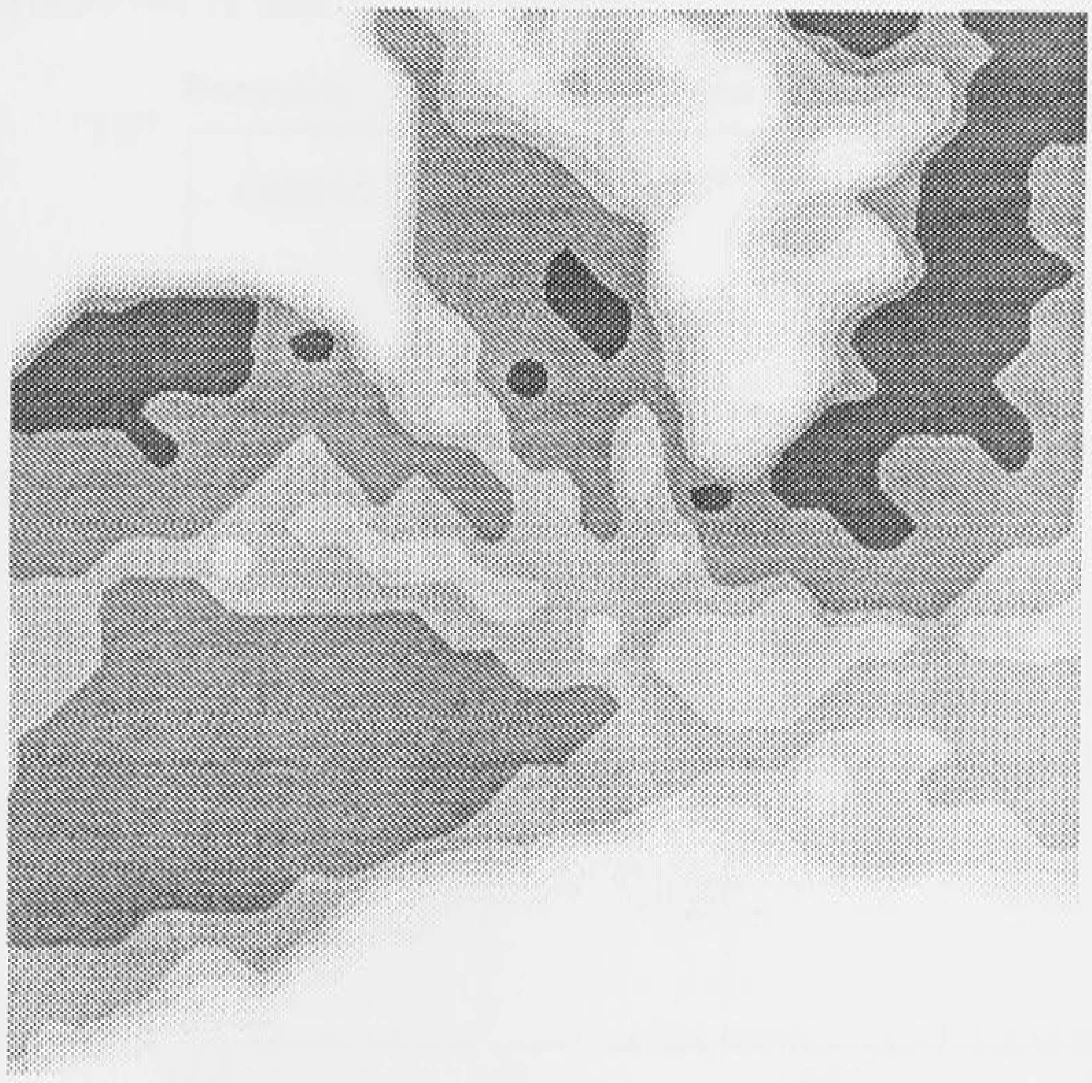

Figure 7.15 As for Figure 7.4, but for a grey-scale contoured Tasman Sea and Antarctica thin-sheet grid, with grid-node spacing of 300 km

7.4.6 Asthenosphere Conductivity

Ferguson *et al.* (1990) identify a high-conductivity layer from MT soundings at TP3 and TP4, at a depth of approximately 200 km. Using Archie's Law, this high-conductivity layer corresponds to a melt fraction of approximately 10 %; much greater than the estimate of 2 % or less, predicted from the intersection of the Parsons & Sclater (1977) geotherms with the 'wet' mantle solidus (Ringwood, 1975), shown in chapter 4. The conductivity of a partial melt zone is extremely dependent on the connection of the melt. Different melt geometries for the predicted 2 % melt fraction are modelled to examined the consequence for 3D induction in the Tasman Sea.

Figure 7.16 shows three conductivity profiles which have (a) no region of partial melt, (b) a region of less than 2% melt, with a conductivity described by Archie's Law (with an exponent of 2), and (c) with the same fraction of melt, but connected by tubes along grain boundaries. From these three cases, the conductivity of the asthenosphere spans almost an order of magnitude, from 2×10^{-3} to 10^{-2} $S.m^{-1}$. While these may represent reasonable bounds for the predicted 70 Ma lithosphere conductivity model, they are still less than that given by the inversion of TP3 observed TE data.

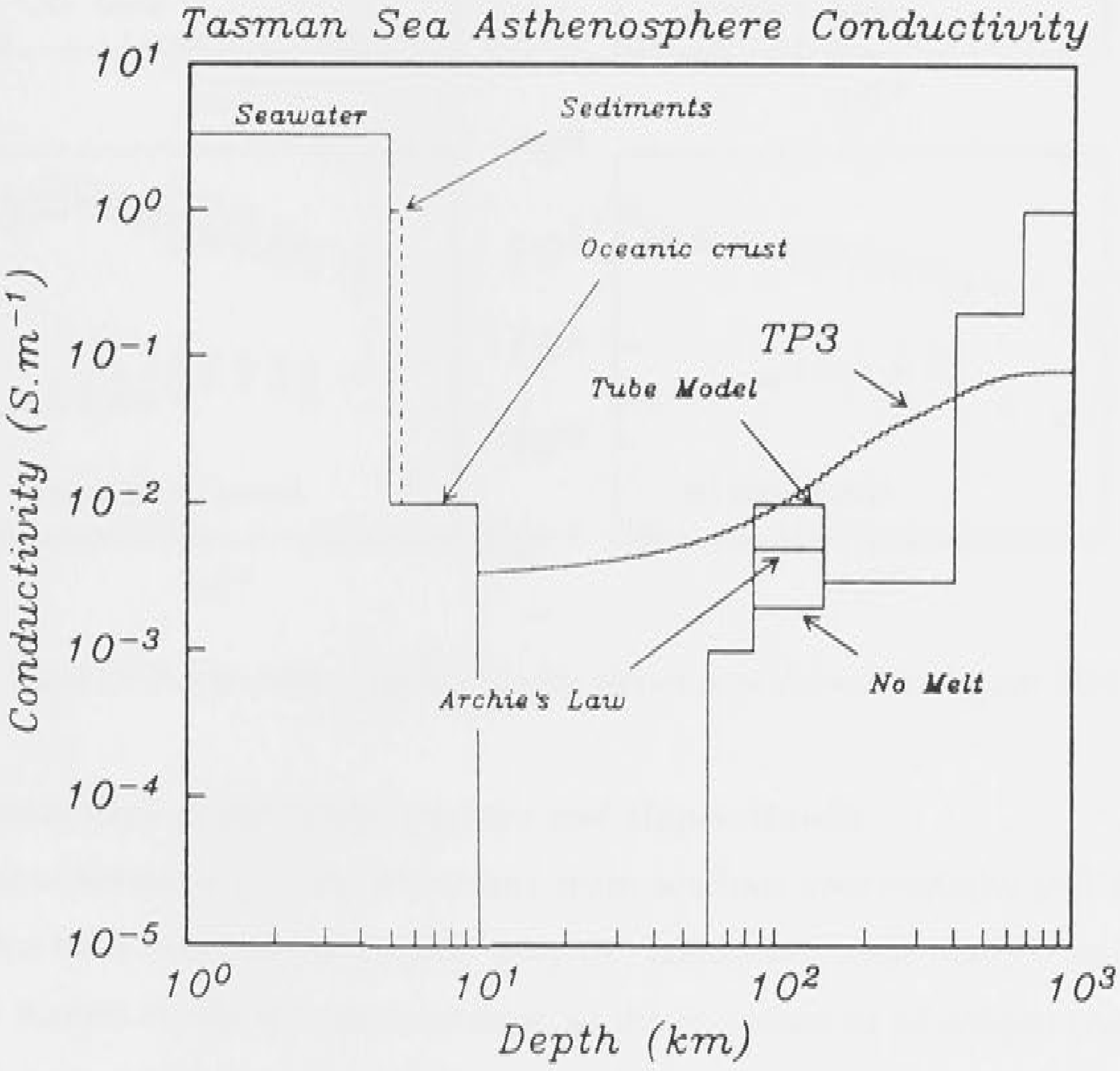

Figure 7.16 As for Figure 7.12, (but with no sediments) and (a) no region of partial melt, (b) a region of less than 2% melt, with a conductivity described by Archie's Law (with an exponent of 2), and (c) with the same fraction of melt, but connected by tubes along grain boundaries.

In Figure 7.17, a comparison is made between the thin-sheet TE and TM apparent resistivities with the observations from TP3. Different melt geometries have an influence on 3D induction effects at short periods, but have little or no effect at long periods. There remains a systematic difference between the long period 1D response from the structure beneath the thin-sheet and the observations; increasing the conductivity of the asthenosphere by invoking a greater percentage of melt (or improved melt connection) reduces the difference.

However, without introducing a substantial fraction of melt (which is not supported by other geophysical observations), it is not possible to reconcile the difference in MT responses solely to melt confined to low-velocity zone depths only.

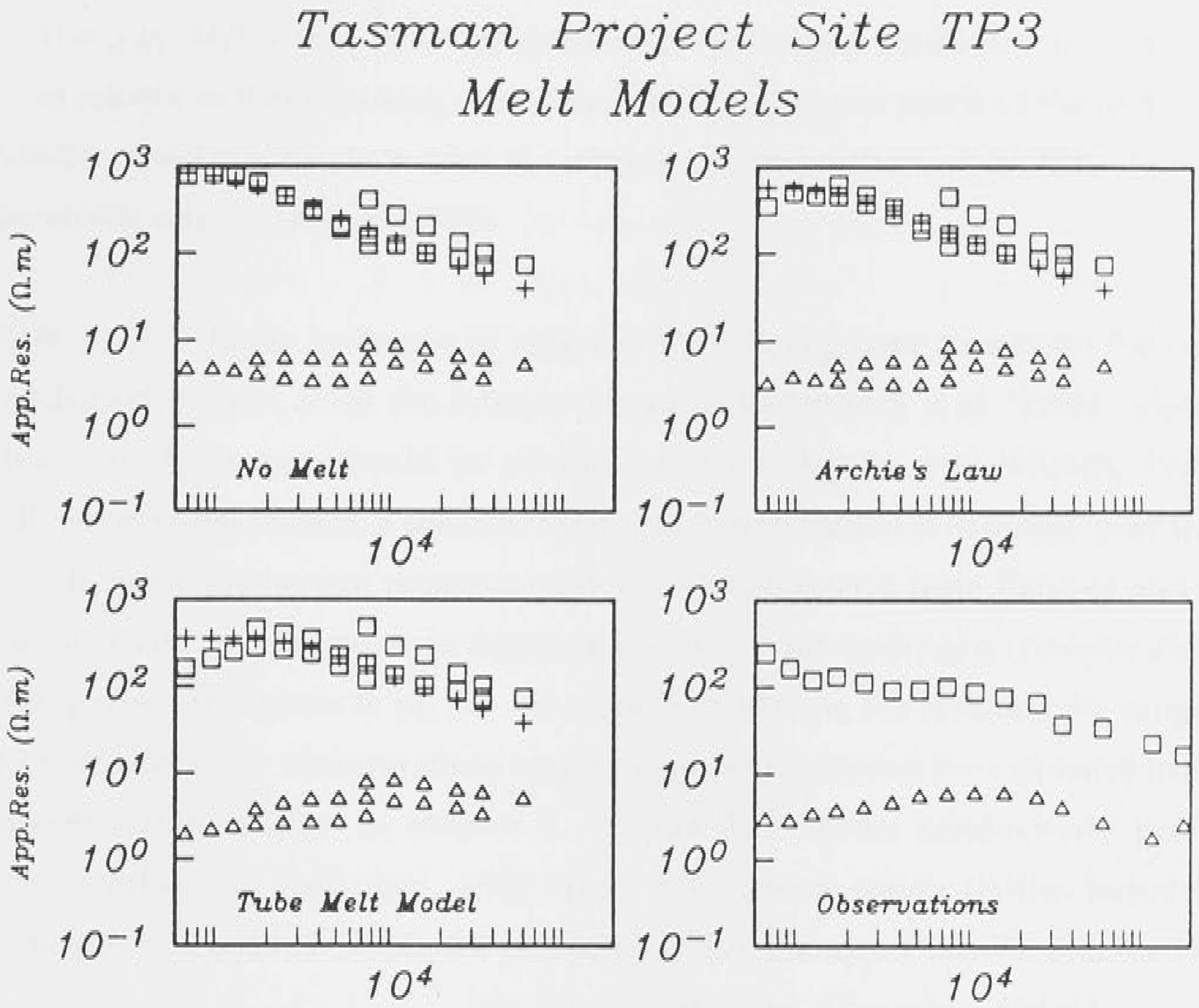

Figure 7.17 As for Figure 7.9, but with conductivity structures shown in Figure 7.16.

7.4.7 Chemical Composition of the Asthenosphere and Upper Mantle

Previous comparisons between 1D interpretations from seafloor observations and theoretical conductivity profiles have considered reasons why the laboratory data may be too resistive. One recent idea by Karato (1990) is examined here, of the inclusion of hydrogen charged ions in olivine. Karato states that the contribution of charged, mobile species to the electrical conductivity of a solid is given by the Nernst-Einstein relation

$$\sigma = f\,Dcq^2/kT \tag{7.1}$$

where σ is the conductivity, f is a numerical correlation factor, approximately unity, D is the diffusivity, c the concentration, q is the charge of the charged species, k is Boltzmann's constant and T is the temperature. The Nernst-Einstein equation has been demonstrated to be valid for olivine at high temperatures (T > 1200 °C), at which conduction is due to diffusion of Fe^{2+} or Mg^{2+} (Karato, 1990; Schock *et al.*, 1989). Hydrogen diffusivity measurements by Mackwell *et al.* (1985) and Mackwell & Kohlstedt (1990) suggest that hydrogen contributes as charged ions (presumably protons) to enhance conductivity. Only modest amounts of hydrogen are sufficient to raise the conductivity of olivine at upper mantle temperatures by an order of magnitude or more. Karato (1990) suggests that for a conductivity of 0.1 to 0.01 $S.m^{-1}$ at a temperature of 1300 °C, the hydrogen concentration is in the range 200 to 2000 p.p.m. H/Si: this small proportion of hydrogen could enhance the upper mantle conductivity without causing extensive partial melting in much of the asthenosphere. This would then be consistent with the chemical composition of MORB, derived from 'dry' peridotite sources (Karato, 1990).

Karato (1990) limits hydrogen to only the low-velocity zone to explain the coincident high-conductivity layer, from the interpretations of Oldenburg *et al.* (1984). However, it is not clear why hydrogen should be confined to such depths only (Hirsch, 1990), and in the following model studies, a constant hydrogen concentration is assumed over the entire upper mantle, with geothermal structure as defined in chapter 4 from Parsons and Sclater (1977). Conductivity as a function of depth is calculated for hydrogen concentrations of 200 and 2000 p.p.m. H/Si given in eq. 7.1. At a depth of 100 km, the conductivity ranges from 0.01 to 0.1 $S.m^{-1}$ for these concentrations respectively, which bound the estimates from seafloor MT interpretations shown in chapter 2. Figure 7.18 shows conductivity profiles for these concentrations of hydrogen, with upper lithosphere conductivities based on the CSEM estimates by Cox et al. (1986), the profile for the 70 Ma upper mantle, and for TP3.

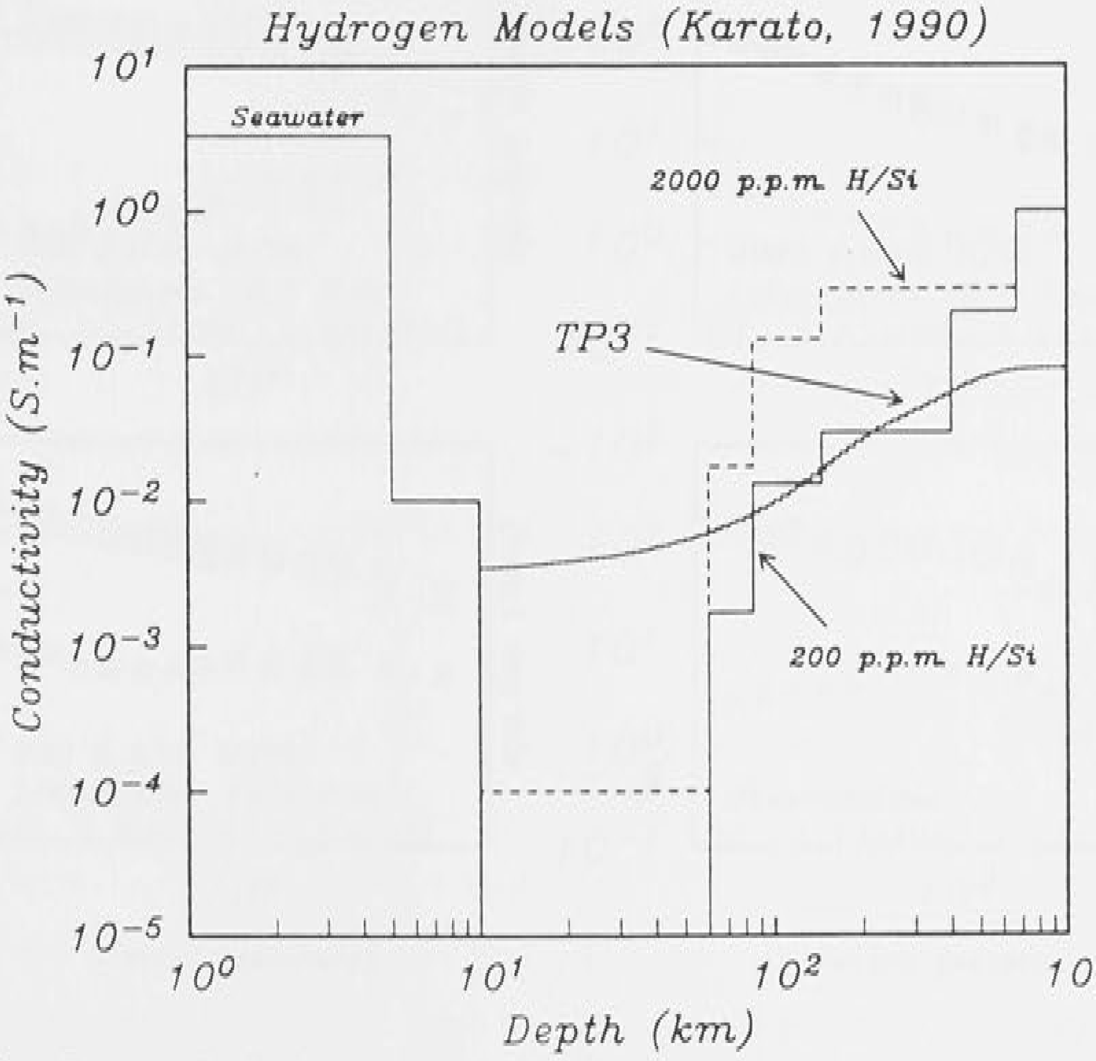

Figure 7.18 As for Figure 7.12, but with no sediments, and with conductivity based on hydrogen concentrations 200 and 2000 p.p.m. H/Si, and lithosphere conductivity 10^{-4} to 10^{-5} $S.m^{-1}$.

Figure 7.19 shows thin-sheet data at site TP3, from the three Tasman Sea models with conductivity profiles as shown in Figure 7.18, compared with observations. The observed TM apparent resistivity at TP3 (also TP4 and TP5) are well modelled by the structure based on 200 p.p.m. H/Si, with a lithosphere of conductivity 10^{-5} S.m^{-1}. Figure 7.20 shows the phases for the three models, which clearly illustrates the sensitivity of phases to the conductivity of the upper lithosphere beneath the Tasman Sea. The thin-sheet model with a hydrogen concentration 200 p.p.m. H/Si, and an upper lithosphere conductivity 10^{-4} S.m^{-1} reproduces the observed apparent resistivity and phase most accurately, except at the shortest periods. At periods less than 2000 s, the thin-sheet TM apparent resistivity and phase are greater than observed values. There are two possible reasons for this: firstly, the presence of sediments (Figure 7.13), which are not included in the thin-sheet model, and variations of continental crust conductance and leakage paths (Figure 7.11) were shown to attenuate apparent resistivity and cause a drop in phase, particularly at short periods. The other explanation is that the upper lithosphere is more resistive than 10^{-4} S.m^{-1} and other factors must explain the high phases from thin-sheet calculations.

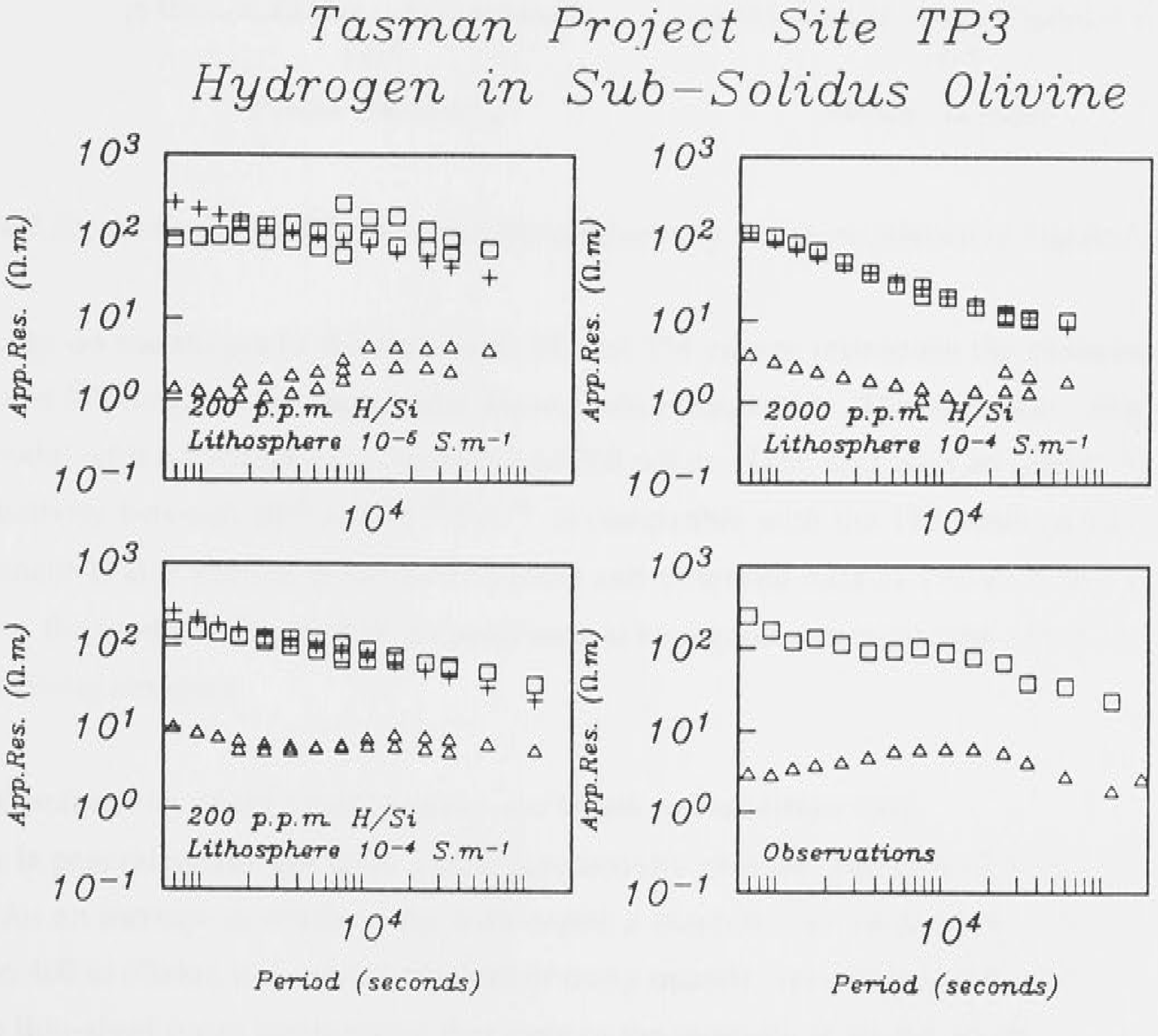

Figure 7.19 As for Figure 7.9, but with the conductivity structures shown in Figure 7.18.

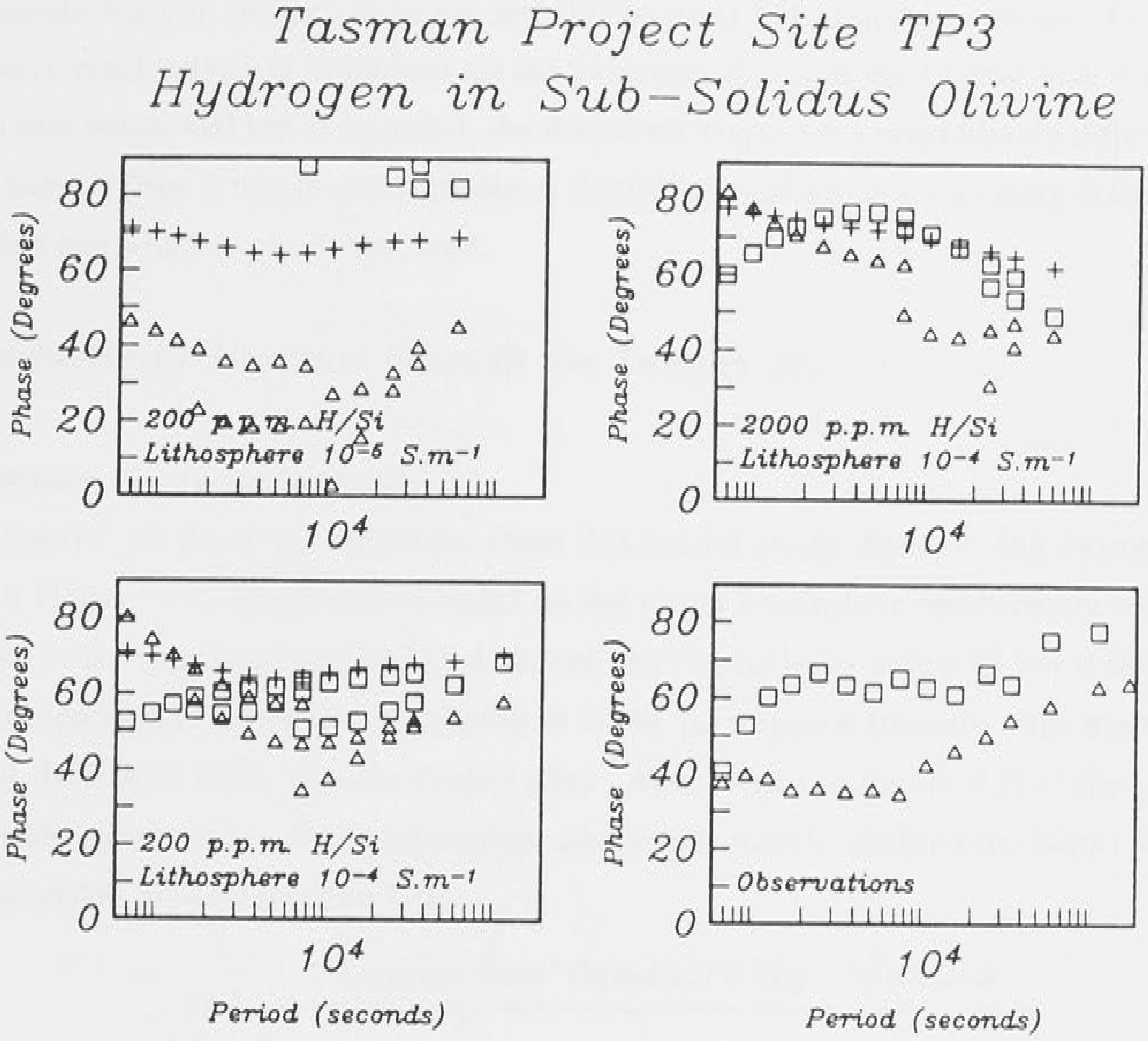

Figure 7.20 As for Figure 7.10, but with the conductivity structures shown in Figure 7.18.

Not only do the shapes of the thin-sheet TE and TM curves reproduce the characteristics of observed MT data, but the magnitudes are now also comparable. This agreement suggests that the model with a hydrogen concentration of 200 p.p.m. H/Si, and with an upper lithosphere conductivity between 10^{-4} and 10^{-5} $S.m^{-1}$, is compatible with the TP3 observations. Similar agreement is also present between thin-sheet and observed data at TP4 and TP5. For these reasons the model in Figure 7.18 is considered to be a good representation of the Tasman Sea conductivity structure.

7.4.8 Conductivity of the Lower mantle, and Depth to Transition Zone

There is general agreement from global conductivity profiles, and inversions of seafloor MT data, for an increase in conductivity with depth; a sharp rise in conductivity to ~1 $S.m^{-1}$ over depths 400 to 670 km is a common feature of many models. Inversion of the synthetic MT data in the thin-sheet ocean basin shows that even in the presence of strong 3D induction effects, a rise in conductivity can still be resolved by the data (Figure 5.28), although Parker (1982) has shown that a 1D inversion of seafloor MT data has little resolution at such depths. Varying the deep conductivity structure from 0.2 to 5 $S.m^{-1}$ below 400 km has no noticeable influence on

3D induction effects in the Tasman Sea, so it is not possible to resolve the conductivity of the lower mantle from an inspection of the full 3D observed MT impedance tensor. However, a deep rise in conductivity is important for 3D induction effects in the Tasman Sea: if no rise in conductivity below 400 km is included, the thin-sheet response is considerably different from observations.. Thus a rise in conductivity at depths of ~400 km is a necessary feature of the model, but one which is poorly resolved.

7.5 Conductivity Structure Beneath the Tasman Sea

7.5.1 Optimum Conductivity Profile

The 'optimum' conductivity structure, from this model study, beneath the Tasman Sea is shown in Figure 7.21. The profile is based on the upper lithosphere conductivity required to reproduce anisotropy in observed MT data; and the conductivity below 85 km is determined from a comparison of thin-sheet 3D distortion of the 1D response from the sub-structure with observed data from three Tasman Project sites. Also shown in Figure 7.21 is the predicted conductivity structure for 70 Ma lithosphere and upper mantle, derived in chapter 4, and an Occam inversion of MT data from TP3.

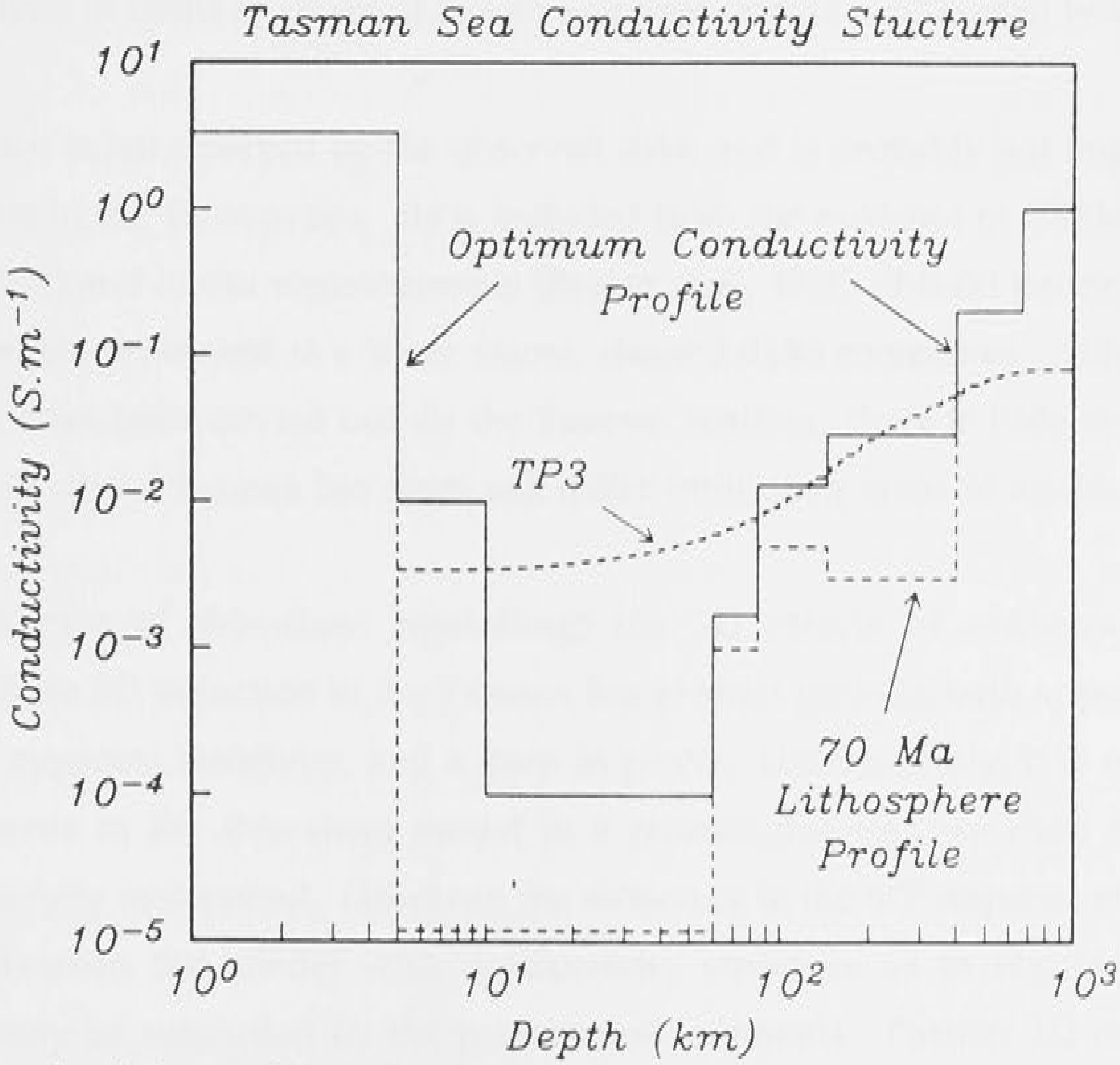

Figure 7.21 Conductivity profile of the proposed 'optimum' 1D structure (solid line) beneath the Tasman Sea, based on a hydrogen concentration of 200 p.p.m. H/Si and upper lithosphere conductivity of 10^{-4} S.m^{-1}. Also shown is the Occam inversion for observed data at site TP3 and the predicted profile for 70 Ma lithosphere and upper mantle (dashed lines).

The conductivity of the upper lithosphere, from this model study, is consistent with interpreted values from seafloor CSEM studies (Cox *et al.*, 1986; Evans *et al.*, 1991). An upper lithosphere which is less conductive than the optimum value of 10^{-4} S.m^{-1}, is better at reproducing anisotropy in observed apparent resistivities, but modelled TE phases are consistently higher than observed data. The conductivity of 10^{-4} S.m^{-1} over depths 10 to 60 km gives a resistivity-thickness product of 5x10 ^{8} Ω.m^{2}, (equivalent to a compensation distance of 600 km). However, the actual resistivity-thickness product, and consequently the compensation distance, may be greater than these values, as the mantle only become significantly conductive at depths much greater than the 60 km thick upper lithosphere. This upper lithosphere conductivity is also in agreement with the 2D profile of Wannamaker *et al.* (1989b), although it is modelled for the Tasman Sea over a greater depth, which may be appropriate for older and cooler oceanic lithosphere.

The asthenosphere is more conductive than predicted from laboratory measurements on olivine. The optimum profile in Figure 7.21 is based on enhanced conductivity due to hydrogen diffusion through sub-solidus olivine (Karato, 1990), although this does not imply that this is necessarily the mechanism to promote higher conductivities. An interpretation of the conductivity in terms of chemical factors and temperature is discussed below.

The oceanic crust is not resolved by the observed data, and is probably not important for 3D induction effects in the Tasman Sea. Its is included from the evidence of CSEM observations (Evans *et al.*, 1991) and *in situ* measurements (Becker *et al.*, 1982) of fluid permeating through cracks in the pillow lavas, and to a lesser extent, sheeted dyke complexes. Although no such measurements have been carried out on the Tasman seafloor, there is little reason to doubt that the conductivity of Tasman Sea crust will differ from other areas of seafloor.

From the evidence of thin-sheet modelling, the 1D effects of sediments cannot be distinguished from 3D induction in the Tasman Sea at short periods; both appear to cause an attenuation of apparent resistivity, and a drop in phase. Unfortunately, it is not possible to include sediments in the thin-sheet model in a meaningful way, so their impact on 3D induction is not fully understood. However, the difference in the MT response at short periods between the Tasman Sea model with conductivity structure as in Figure 7.21 and the observations, may be reconciled by the presence of sediments. Further 2D modelling may quantify the effects of sediments more accurately.

The conductivity structure below 400 km is not resolved, but a rise in conductivity below 300 km is a required feature of the Occam inversions of Tasman Project data, and is also necessary to reproduce 3D induction effects in the Tasman Sea. The magnitude of conductivity at this depth is also not resolved, although the 1D inversions suggest that 1 $S.m^{-1}$ at ~400 km is consistent with observations and global conductivity profile determinations (e.g. Banks, 1969, 1972).

7.5.2 Lateral Variations in Conductivity Structure

Calculated 3D induction in the Tasman Sea may be removed from observed data, so that (ideally) the observed data are then solely a measure of the MT response of structure beneath the Tasman Sea. This method (Heinson & Lilley, 1991) is based on the assumption that ocean 3D induction effects are considerably more significant to seafloor MT soundings than lateral changes within Earth. The evidence from chapter 4 suggests that is probably valid for the old oceanic lithosphere of the Tasman Sea. However, removal of 3D distortion effects are only possible if the thin-sheet models are able to accurately reproduce the 3D induction in the Tasman Sea.

Tasman Sea thin-sheet models are restricted to 1D sub-structures. From the arguments developed in chapter 4, if the general conductivity characteristics of old oceanic lithosphere and upper mantle are included in the thin-sheet model, then 3D induction effects in the Tasman Sea may, to first-order, be accurately modelled. A simple matrix method is used to characterise the 3D induction due to the ocean. The impedance tensor calculated at the bottom (or top) of the thin-sheet (Z^{TS}) is 'distorted' from the 1D impedance response of the underlying structure (Z^{1D}) by the transformation

$$Z^{TS} = D\,Z^{1D} \tag{7.2}$$

where D is a 'distortion' matrix. The inverse of the distortion matrix D^{-1} can then be applied to the Tasman Project MT impedance tensors, to remove the (modelled) 3D induction in the Tasman Sea. If the real 3D induction in the Tasman Sea has been accurately modelled by the thin-sheet model, then the 'de-distorted' Tasman Project observations will have a near 1D form (provided that the structure beneath the Tasman Sea is approximately 1D). The subsequent removal of the 3D induction in the ocean from each Tasman Project site may then allow a preliminary examination of any lateral conductivity changes between the sites.

Figure 7.22 illustrates the original (Ferguson *et al.*, 1990) and 'de-distorted' (as described) MT data for sites TP3 and TP4. There are several values of 'de-distorted' data at each period, corresponding to the different distortion matrices D obtained from numerical grids of different spacings. The 'de-distorted' data in Figure 7.22 show that 3D induction in the Tasman Sea is generally well modelled by the Tasman Sea thin-sheet models in Figures 7.4 to 7.6, underlain by the conductivity structure in Figure 7.21.

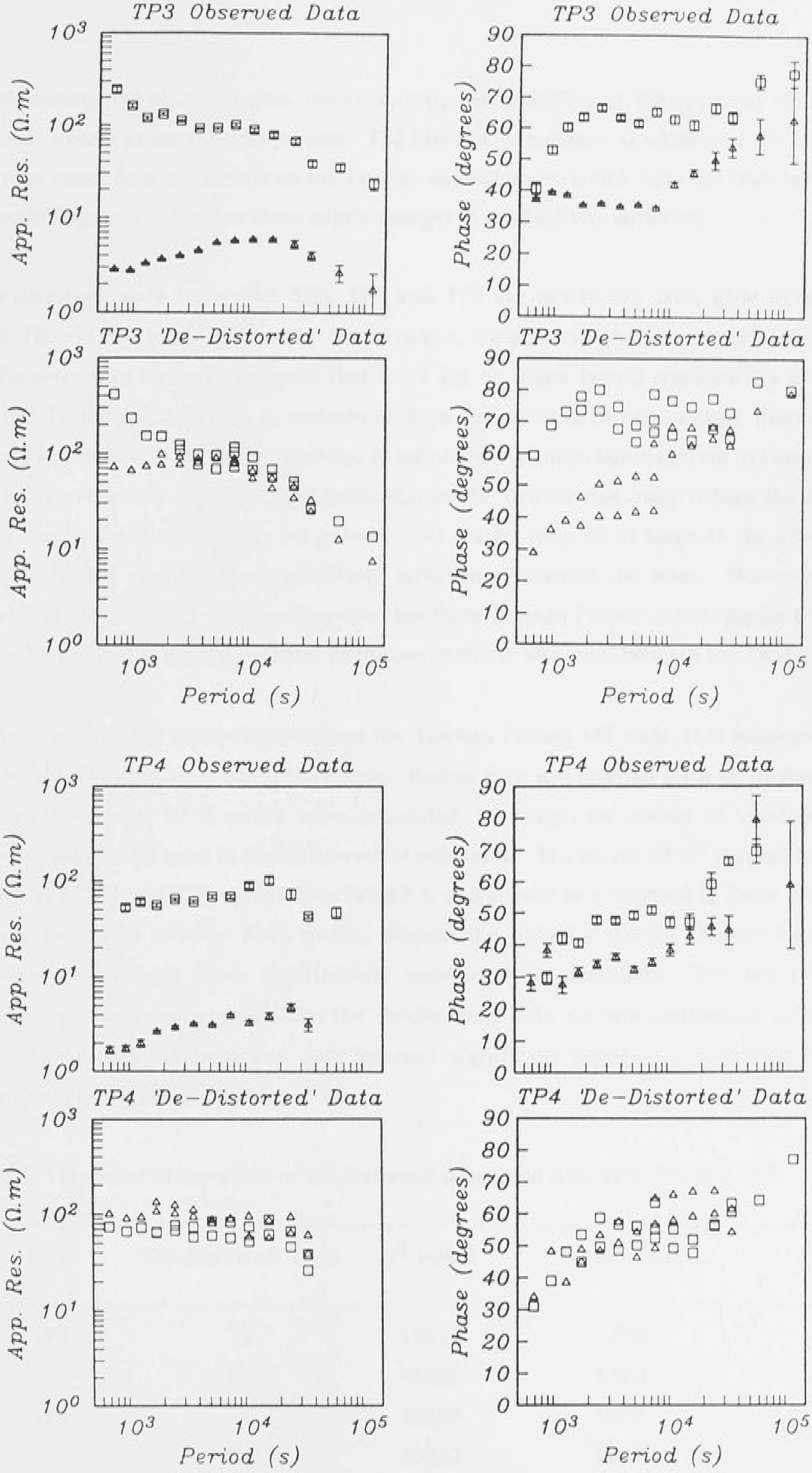
TP3 Observed Data

TP3 Observed Data

TP3 'De-Distorted' Data

TP3 'De-Distorted' Data

TP4 Observed Data

TP4 Observed Data

TP4 'De-Distorted' Data

TP4 'De-Distorted' Data

Figure 7.22 Observed and 'de-distorted' TE (squares) and TM (triangles) apparent resistivity and phase estimates from sites TP3 and TP4 .

By 'de-distorting' the observed data, the anisotropy between TE and TM apparent resistivity is removed, except at the shortest periods. The differences between 'de-distorted' TE and TM phases may result from sediments on the Tasman abyssal plain, which have not been included in the modelling, or due to other more subtle changes in conductivity structure.

The 'de-distorted' data from sites TP3, TP4 and TP5 are nearly 1D, with little difference between TE and TM mode estimates. Furthermore, the data are also similar between sites: these characteristics strongly suggests that there are no major lateral conductivity changes across the Tasman Sea, which is consistent with the models of old oceanic lithosphere developed in chapter 4. Further modelling, to refine the optimum sub-structure in Figure 7.21 and so more accurately reproduce 3D induction in the Tasman Sea, may reduce the scatter between 'de-distorted' estimates. At present, this scatter may be as large as the effects of small-scale lateral changes in conductivity structures between the sites. However, the uniformity of 'de-distorted' response between the three Tasman Project sites suggests that the profile in Figure 7.21 is a good estimate of the conductivity structure beneath the Tasman Sea.

To further confirm the similarity between the Tasman Project MT data, it is interesting to invert the 'de-distorted' data for 1D structure. Rather than use original error estimates from Ferguson (1988), new 10 % errors were calculated, (although the scatter of 'de-distorted' estimates could also be used to define new error estimates). The results of D^+ inversion of the data from TP3, TP4 and TP5 are listed in Table 7.5, and should be compared to Table 7.1. The data have generally smaller RMS misfit, despite the obvious scatter of estimates, and furthermore, no longer show significantly correlated D^+ residuals. This last point is extremely important, and suggests that the 'de-distorted' data are now compatible with a 1D structure (note that the observed data showed significant negative correlations in D^+ apparent resistivity residuals).

Table 7.5 D^+ statistics of inversion of 'de-distorted' data from sites TP3, TP4 and TP5.

Site	'De-distorted' data	χ^2 misfit	RMS misfit
TP3	TE	110.29	1.548
	TM	88.683	1.388
TP4	TE	107.59	1.635
	TM	100.62	1.627
TP5	TE	134.25	1.931
	TM	117.05	1.803

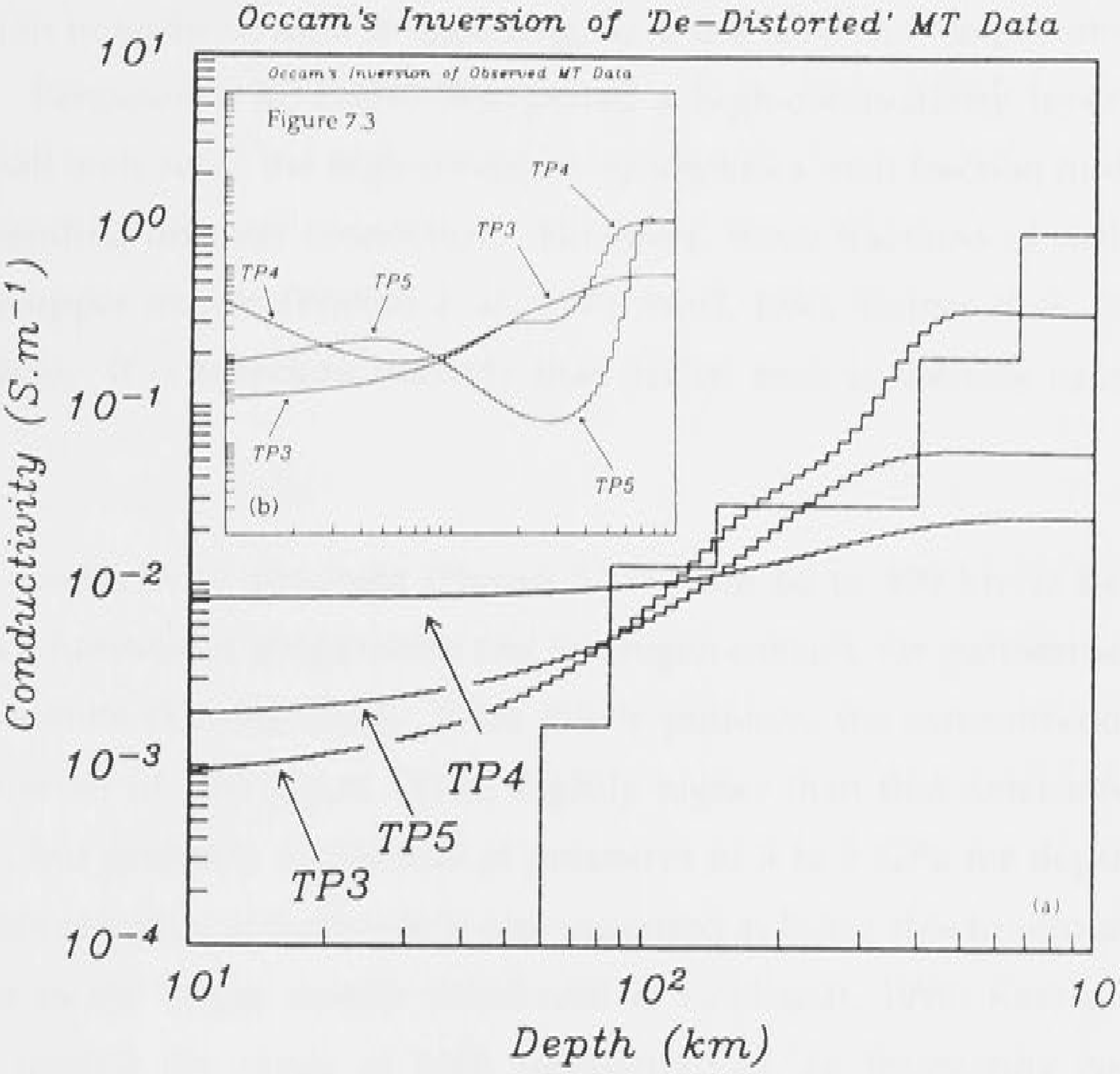

Figure 7.23 Occam inversions of 'de-distorted' MT estimates from sites TP3, TP4 and TP5. Also shown is the optimum conductivity profile from Figure 7.21.

Figure 7.23 shows Occam inversions of 'de-distorted' MT data for sites TP3, TP4 and TP5, with the proposed optimum 1D structure beneath the Tasman Sea, (compared to the Occam inversions of the observed TE MT data, as shown in Figures 7.3). All three sites show a rise in conductivity rise at depth of 100 km, and similar morphology over the entire depth range. The differences in conductivity gradients between the curves is probably more dependent on the scatter of 'de-distorted' data than on any true lateral changes between the sites. The uniformity of conductivity structure contrasts with the different structures obtained from Occam inversions of the observed TE data, shown in Figure 7.3.

7.5.3 Chemical Composition of the Upper Mantle beneath the Tasman Sea

The upper mantle beneath the Tasman Sea is an order of magnitude more conductive than laboratory measurements on olivine at temperatures at 800 to 1300 °C. It is not possible to determine over what depth range this increase occurs, and it should be stressed that the optimum profile in Figure 7.21 has only been shown to be consistent with the data, and is by no means a unique representation of the Tasman Sea geoelectric profile.

An interpretation in terms of melt is appealing, as it is a consistent explanation for the low-velocity zone. Ferguson *et al.* (1990) interpreted a high-conductivity layer at a depth of 200 km as a small melt zone: the high-conductivity implies a melt fraction in the ranges from 5 to 10 %, depending on melt connection. However, these fractions of melt are probably unstable in the upper mantle (Walker *et al.*, 1978; Waff, 1980; Stolper *et al.*, 1981; Toramuru & Naoyuki, 1986). It is therefore unlikely that partial melt is the sole cause of the high-conductivities.

The optimum conductivity structure (Figure 7.21) from 60 to 400 km is based on olivine conductivity as a function of temperature and hydrogen content, for geothermal models of the oceanic upper mantle (Karato, 1990). With this hypothesis, the concentration of hydrogen must be of the order of 200 p.p.m. H/Si; slightly higher than that determined at 300 MPa experimentally, but probably reasonable at pressures of 3 to 5 GPa for depths greater than 100 km. This concentration of hydrogen is also proposed as being able to account for low shear wave velocities in the upper mantle (Mackwell & Kohlstedt, 1990; Karato, 1990). If this mechanism is indeed the cause of high conductivities, an interesting corollary is that pronounced anisotropy in conductivity will occur. Seismic velocity analysis suggest that the upper mantle is anisotropic, with a deformation-induced lattice preferred orientation of olivine concentrating in the direction of flow parallel to the [100] axis (Ribe, 1989), and Mackwell & Kohlstedt (1990) show hydrogen to be mobile only along the same axis. Thus, contrary to evidence for conduction in sub-solidus olivine due to diffusion of Mg^{2+} or Fe^{2+}, (which gives only small anisotropy in conductivity), if hydrogen ions are the dominant conduction mechanism, then conductivity will be very strongly anisotropic, perhaps by an order of magnitude.

There are, of course, a number of other proposed mechanism for the high-conductivity layer, and it is probably not possible to discriminate between these hypotheses from MT sounding data alone. Other explanations include volatiles (Tozer, 1981; Tarits, 1986), grain boundary effects (Shankland & Waff, 1977) including carbon on grain boundaries (Duba & Shankland 1982), or the presence of a conducting phase (e.g. garnet, clinopyroxene) for which few laboratory conductivity measurements have been made.

The conductivity of sub-solidus olivine at temperatures below 500 °C is low ($\ll 10^{-6}$ $S.m^{-1}$) so that other factors must be used to explain the conductivity of the upper lithosphere, at depths of 10 to 60 km. The most plausible arguments are for a small percentage of volatiles (H_2O or CO_2). Using Archie's Law, and the tube model of interconnected fluid, the upper lithosphere conductivity of 10^{-4} $S.m^{-1}$ beneath the Tasman Sea has porosity of 0.1 - 0.5 % H_2O. The petrological composition of the upper lithosphere in the pyrolite mantle is depleted harzburgite, residual from the melting of 'dry' (~0.1 % H_2O) sources of peridotite to form MORB (Takahashi & Kushiro, 1983). Although a small percentage of volatiles will permeate through new oceanic crust at spreading ridges, it is unlikely that they will contribute to the hydration of the upper mantle (Ringwood, 1975).

7.5.4 Temperature variations beneath the Tasman Sea

High temperatures alone are probably unable to account for the conductivity of the upper lithosphere. If conduction is principally by olivine, then temperatures of the order of 1150 °C are required at depths less than 60 km (Shankland & Duba, 1990); such geotherms would just intersect the 'dry' spinel lherzolite solidus and garnet peridotite solidus (Takahashi, 1986; Scarfe & Takahashi, 1986), causing a small amount of partial melting; however, there is no evidence from seismic surface wave analysis (Orcutt, 1987) or seafloor bathymetry (Parsons & Sclater, 1977) for such melt fractions.

The conductivity at depths below 85 km is of the order of 0.01 $S.m^{-1}$, which corresponds to the measured conductivity of olivine at 1500 °C. This temperature is ~100 °C higher than the proposed temperature of the $\alpha \rightarrow \alpha + \beta$ transition (Katsura & Ito, 1989; Akaogi *et al.*, 1989), although low shear wave velocities to depths of 400 km have been determined beneath the Tasman Sea (Woodhouse & Dziewonski, 1984), which may imply anomalously high temperatures. A temperature of 1500 °C at a depth of 85 km would intersect the 'wet' mantle solidus (Kushiro *et al.*, 1968; Ringwood, 1975), causing extensive partial melting. However, if the lithosphere below 60 km is 'dry', as argued by Sato *et al.* (1988), then this temperature is below the 'dry' mantle solidus of spinel lherzolite and garnet peridotite . Thus, high temperature alone may be sufficient to account for the conductivity at these depths, for a 'dry' upper mantle.

Chapter 8 : Conclusions

8.1 Thin-Sheet Modelling

As 3D induction in the ocean has been shown to be important to seafloor EM studies, it is therefore necessary to model such effects as closely as possible. The thin-sheet algorithm is ideally suited for this purpose.

Thin-sheet modelling of coastlines, simple ocean basins, and seafloor topography (over a ridge axis and transform fault) suggest that 3D induction in the oceans may profoundly influence MT and GDS observations, to the extent that 1D structure beneath the oceans can not reliably be extracted from observed data. However, the magnitude and period dependence of the distortion in the observed EM fields is, in fact, diagnostic of the underlying conductivity structure.

Analysis of EMRIDGE and Tasman Project MT data suggest that a 1D inversion of TE estimates is not necessarily a good representation of Earth's conductivity structure, and a 3D interpretation in terms of the coastlines and seafloor topography is required; (the same conclusion may apply to inversions of 'invariants', such as the Berdichevsky average). By contrast, thin-sheet modelling indicates that TM estimates, polarised perpendicular to a coastline, are very sensitive to the 2D strike of the coast, but not to 3D structure further away. This reason gives confidence in the 2D profile across the Juan de Fuca plate by Wannamaker *et al.* (1989).

Thin-sheet modelling shows that 3D induction in ocean basins closed on two, three or four sides distort synthetic MT responses in a manner that is similar to observed seafloor MT data. This result may explain why almost every seafloor MT sounding appears distorted from an ideal D^+ response in a similar manner. Extensive thin-sheet modelling of Tasman Sea data suggests that the effects of 3D induction are strongest at short periods, but long period TE estimates are undistorted from the 1D response of the underlying structure.

8.2 The Conductivity Structure Beneath the Juan de Fuca Ridge

The EM observations across the Juan de Fuca Ridge and to the south of the Blanco Fracture Zone have discerned no significant electrical conductivity anomaly associated with the ridge axis. The lack of evidence for a linear magma chamber is significant in the light of recent Sea Beam mapping, high resolution sidescan and ocean bottom photography which reveal there to be almost continuous hydrothermal venting along the neo-volcanic zone, suggesting that at least a portion of this ridge segment may be currently undergoing a phase of seafloor spreading.

Changes in seafloor topography are found to be a strong influence on EM observations. Two- and three-dimensional modelling, using the thin-sheet method, show that the observed EM signature at a ridge axis and transform fault is due primarily to changes in ocean bathymetry. However, EM induction in the ocean is also strongly dependent on the resistivity of the lithosphere: thin-sheet modelling requires an upper lithosphere of conductivity ~10^{-5} S.m^{-1} (resistivity 10^5 Ω.m) to reproduce observed anisotropy.

Magnetotelluric estimates from a site 35 km east of the ridge axis, on lithosphere of age 1.2 Ma, are anisotropic at short periods due to small-scale topographic changes, and (at longer periods) due to the coastline of northwest America. One-dimensional interpretations are inconclusive, but comparisons with the EMSLAB transect on older oceanic lithosphere, and a similar MT experiment on the East Pacific Rise, indicate that the top 200 km of Earth beneath MORs has average conductivity 0.05 S.m^{-1}, compatible with an upper-bound on the decompressional melt fraction of 6 %. There is a rise in conductivity to ~1 S.m^{-1} at a depth of 300 km.

8.3 The Conductivity Structure Beneath the Tasman Sea

Modelling of the Tasman Sea using the 3D thin-sheet approximation shows that observed anisotropy in MT soundings is primarily the result of induction in the salt-water of the Tasman Sea and its adjoining oceans, overlying a low conductivity (< 10^{-4} S.m^{-1}) upper lithosphere. This conductivity corresponds to a small percentage (0.1 to 0.5 %) of volatiles.

Conductivities at depths greater than 85 km beneath the Tasman Sea imply high temperatures (of ~1500 °C), if conduction is due to sub-solidus olivine only. Free Earth oscillation data and seismic velocity analyses do suggest that the upper mantle beneath the Tasman Sea has anomalously high temperatures; but not as high as 1500 °C at 85 km, given that the temperature of the $\alpha \rightarrow \alpha+\beta$ transition of 1400 °C occurs at depth 400 km. Partial melting is unlikely as the sole mechanism for high conductivity, as improbably large fractions of melt (> 5%) are required. Other factors, such as enhanced conductivity of grain boundaries, and the presence of volatiles or hydrogen in a sub-solidus mantle have been postulated; it not possible to discriminate between these hypotheses. At the transition zone, the conductivity rises to ~1 S.m^{-1}, although the depth and magnitude are poorly resolved.

There appears to be no strong changes in lateral structure across the Tasman Sea, as observations are reproduced with a uniform 1D structure beneath the thin-sheet model. The uniformity of conductivity structure beneath observation sites on 65, 70 and 75 Ma lithosphere is consistent with the predicted models of conductivity structure, which are similar for lithosphere older than 40 Ma.

8.4 The Conductivity of the Oceanic Lithosphere and Upper Mantle

It has been shown in this thesis that for the Tasman Sea MT soundings, the anisotropy in impedance is primarily due to a lithosphere of conductivity similar to that determined by Cox *et al.* (1986) from CSEM soundings. Similarly, a resistive lithosphere is necessary to reproduce GDS observations near the Juan de Fuca Ridge. The similarity between synthetic MT data modelled for general ocean basins, and previously published seafloor MT estimates, suggests that a resistive lithosphere may be a general feature of the oceanic upper mantle. Even so, the conductivity of 10^{-4} to 10^{-5} S.m^{-1} is higher than for thermally-activated conduction in olivine at temperatures below 1000 °C, and may result from a small percentage (0.1 to 0.5 %) of volatiles, consistent with petrological analysis of MORB.

One-dimensional analysis of published seafloor MT soundings shows that the conductance of the lithosphere decreases with increasing seafloor age: such trends are consistent with models of cooling lithosphere away from the ridge axis. A high-conductivity layer evident in the 1D inversion of seafloor data on 1 Ma seafloor at a depth of 75 km, becomes progressively deeper and smaller with increasing seafloor age. Such a layer is no longer resolved by seafloor data above lithosphere older than 60 Ma. Such high conductivities are usually interpreted in terms of a small fraction of decompressional melt in the asthenosphere. The high-conductivity layer is coincident with the low-velocity zone: the presence of melt is consistent with observed low shear wave velocities and evidence from MORB samples for the depths of separation of melt in the asthenosphere.

A rise in conductivity at depths greater than 300 km is common to almost all seafloor MT soundings, and global conductivity profiles. The thin-sheet models suggest that this rise in conductivity is well resolved even by synthetic MT data which are profoundly distorted by 3D induction effects. The conductivity of the lower mantle from these profiles is at least 0.1 S.m^{-1}.

8.5 Future Work

The following areas are suggestions for further research which may improve further the understanding of oceanic lithosphere and upper mantle conductivity, and hence complementary characteristics of temperature, melt fraction, porosity, chemical composition, etc.

8.5.1 Thin-Sheet Modelling

Several suggestion are now made to improve the ability of the thin-sheet algorithm, particularly to take advantage of recent developments in computing power.

There are two factors which limit the use of the thin-sheet algorithm. These are the c.p.u. time required for each model, and the immense disk storage requirements for matrix coefficients. Both are related to high I/O required for the code, as it was developed at the University of Victoria several years ago at a time where internal memory specifications were small. If the high I/O and disk storage can be reduced, the thin-sheet algorithm will be considerably quicker and able to operate on smaller machines.

There are two proposed means of achieving this objective. Firstly, if thin-sheet grids are restricted to square grids, rather than arbitrary rectangular grids, the kernels have the property that they are symmetric about axes of symmetry of the square grid. A square grid has four axes of symmetry in the plane of the grid, as opposed to two for a rectangle, so that disk storage could be cut to one eighth of the storage required at present for which all kernel elements are stored. The second method involves utilizing RAM more effectively. At present, coefficients are stored for the half space and layered space calculations separately on disk, and then combined. The calculation of both elements can be performed sequentially for each grid-node, and stored on disk only once. Also, by reducing disk storage down by symmetry, I/O is reduced in iterating for the thin-sheet solution. The final iterative stage may possibly be replaced by a single matrix N x N matrix inversion, and increased RAM will permit such a change. The computation may not be quicker than the iterative method, but kernel elements need be read in only once, so I/O is much reduced.

It may be possible to adapt the underlying structure beneath the thin-sheet from a 1D to 2D structure. A convolution integral linking thin-sheet current densities to the horizontal magnetic fields above and below the thin-sheet is required. Weaver *et al.* (1985, 1986) publish a quasi analytical 2D model solution, the expression for which may be possible to use as a boundary condition for the thin-sheet calculation. Alternatively, 2D finite elements, or finite difference techniques, may be used to calculate the EM response beneath the thin-sheet numerically.

8.5.2 Re-Analysis of Seafloor Magnetotelluric Data

Some preliminary work on the interpretation of a global set of seafloor MT responses has been shown to be beneficial in understanding more of the general features of lithosphere and upper mantle conductivity. There is great scope for more analysis of this kind.

In chapter 2, some statistical analysis of D^+ inversion misfits suggested that all seafloor data were distorted in a similar manner, which was demonstrated to be consistent with 3D induction effects in a partially-closed ocean basin. Evidently, analysis of the distribution of inversion residuals may be as informative as the 1D and 2D structures which these inversions define.

8.5.3 Further Seafloor Magnetotellurics

The major suggestion for future work arising from this thesis is, however, more seafloor MT exploration of Earth's ocean floors. It is considered that thin-sheet modelling has been shown to adequately control the strong effects of 3D induction in the oceans.

References

Agarwal, A. & Weaver, J. T., 1990. A three-dimensional numerical study of induction in South India by an electrojet source, *Phys. Earth planet. Inter.*, **60**, 1-17.

Akaogi, M., Ito, E., & Navrotsky, A., 1989. Olivine - modified spinel - spinel transitions in Mg_2SiO_4 - Fe_2SiO_4: calorimetric measurements, thermochemical calculations, and geophysical application, *J. geophys. Res.*, **94**, 15671-15685.

Akimoto, S. & Fujisawa, H., 1965. Demonstration of the electrical conductivity jump produced by the olivine - spinel transition, *J. geophys. Res.*, **70**, 443.

Anderson, D. L. & Bass, J. D., 1986. Transition region of the earth's upper mantle, *Nature*, **320**, 321-328.

Anderson, D. L., 1982. Chemical composition and evolution of the mantle, in *High-Pressure Research-Applications in Geophysics*, pp. 301-317, ed. Manghnani, M. & Akimoto, S., Academic Press, New York.

Bahr, K., 1988. Interpretation of the magnetotelluric impedance tensor: regional induction and local telluric distortion, *J. Geophys.*, **62**, 119-127.

Bailey, R. C., 1970. Inversion of the geomagnetic induction problem, *Proc. Roy. Soc. London*, **315**, 185-194.

Bailey, R. C., Craven, J. A., Macnae, J. C. & Polzer, B. D., 1989. Imaging of deep fluids in Archaean crust, *Nature*, **340**, 136-138.

Baines, P. G. & Bell, R. C., 1987. The relationship between ocean current transports and electric potential differences across the Tasman Sea, measured using an ocean cable, *Deep-Sea Res.*, **34**, 531-546.

Banks, R. J., 1969. Geomagnetic variations and the electrical conductivity of the upper mantle, *Geophys. J. R. astr. Soc.*, **17**, 457-487.

Banks, R. J., 1972. The overall conductivity distribution of the Earth, *J. Geomagn. Geoelectr.*, **24**, 337-351.

Banks, R. J., 1973. Data processing and interpretation in geomagnetic deep sounding, *Phys. Earth planet. Inter.*, **7**, 339-348.

Beamish, D., Hewson-Browne, R. C., Kendall, P. C., Malin, S. R. C. & Quinney, D. A., 1983. Induction in arbitrarily shaped oceans - VI. Oceans of variable depth, *Geophys. J. R. astr. Soc.*, **75**, 387-396.

Beblo, M. & Bjornsson, A., 1980. A model of electrical resistivity beneath NE-Iceland, correlation with temperature, *J. geophys. Res.*, **47**, 184-190.

Beblo, M., Bjornsson, A., Arnason, K., Stein, B. & Wolfgram, P., 1983. Electrical conductivity beneath Iceland - constraints imposed by magnetotelluric results on temperature, partial melting, crustal and mantle structure, *J. Geophys.*, **53**, 16-23.

Becker, K., Von Herzen, R. P., Francis, T. J. G., Anderson, R. N., Honnorez, J., Adamson, A. C., Alt, J. C., Emmermann, R., Kempton, P. D., Kinoshita, H., Laverne, C., Mottl, M. J. & Newmark, R. L., 1982. In situ electrical resistivity and bulk porosity of the oceanic crust Costa Rica Rift, *Nature*, **300**, 594-598.

Bendat, J. S. & Piersol, A. G., 1971. *Random Data: Analysis and Measurement Procedures.* 407 pp, Wiley-Interscience, New York.

Bennett, D. J. & Lilley, F.E.M., 1974. Electrical conductivity structure in the South-east Australian Region, *Geophys. J. R. astr. Soc.*, **37**, 191-206.

Bennett, D. J., 1972. Geomagnetic depth sounding studies in south-eastern Australia, *Ph.D. thesis*, Australian National University, Canberra, Australia.

Berdichevsky, M. N. & Dmitriev, V. I., 1976a. Basic principles of interpretation of magnetotelluric sounding curves, in *Geoelectric and Geothermal Studies*, pp. 165-221, ed. Adam, A., KAPG Geophys. Monogr., Budapest.

Berdichevsky, M. N. & Dmitriev, V. I., 1976b. Distortion of magnetic and electric fields by near-surface lateral inhomogeneities, *Acta Geod., Geophys. Mont. Hung.*, **11**, 447-483.

Berdichevsky, M. N. & Zhdanov, M. S., 1984. *Advanced Theory of Deep Geomagnetic Sounding*, pp. 408, Elsevier, Amsterdam.

Berdichevsky, M. N., Zhdanova, O. N. & Yakovlev, A. G., 1984. Anomalous electromagnetic fields and electromagnetic sounding on the bottom of the ocean, *Geomag. Aeronomy*, **24**, 542-547.

Bina, C. R. & Wood, B. J., 1987. Olivine spinel transitions: experimental and thermodynamic constraints and implications for the nature of the 400 km seismic discontinuity, *J. geophys. Res.*, **92**, 4853-4866.

Bindoff, N. L., 1988. Electromagnetic induction by oceanic sources in the Tasman Sea, *Ph.D. thesis*, Australian National University, Canberra, Australia.

Bindoff, N. L., Filloux, J. H., Mulhearn, P. J., Lilley, F. E. M. & Ferguson, I. J., 1986. Vertical electrical field fluctuations at the floor of the Tasman Abyssal Plain, *Deep-Sea Res.*, **33**, 587-600.

Bindoff, N. L., Lilley, F. E. M. & Filloux, J. H., 1988. A separation of ionospheric and oceanic tidal components in magnetic fluctuation data, *J. Geomagn. Geoelectr.*, **40**, 1445-1467.

Blackman, D. K. & Forsyth, D. W., 1989. Axial topographic relief associated with ridge-transform intersections, *Earth planet. Sci. Lett.*, **95**, 115-129.

Booker, J. R. & Egbert, G. D., 1990. Very long period magnetotellurics at Tuscon Observatory: implications for mantle conductivity, *EOS*, 71, 1294.

Boteler, D. H., 1988. Electromagnetic induction and telluric currents in northern New Zealand, *Ph.D. thesis*, Victoria University of Wellington, Wellington, New Zealand.

Bott, M. H. P., 1971. *The Interior of the Earth*, 1st ed., Edward Arnold, London.

Brace, W. F., Oramnge, A. S. & Madden, T. R., 1965. The effect of pressure on the electrical resistivity of water-saturated crystalline rocks, *J. geophys. Res.*, **70**, 5669-5678.

Brewitt-Taylor, C. R. & Weaver, J. T., 1976. On the finite-difference solution of two-dimensional induction problems, *Geophys. J. R. astr. Soc.*, **47**, 375-396.

Brown, J. M. & Shankland, T. J., 1981. Thermodynamic parameters in the earth as determined from seismic profiles, *Geophys. J. R. Astron. Soc.*, **66**, 579-596.

Bullard, E. C. & Parker, R. L., 1970. Electromagnetic induction in the oceans, in *The Sea*, Vol **4**, Ch. 18, 695-730, ed Maxwell, A., Wiley-Interscience, New York.

Cagniard, L., 1953. Basic theory of the magneto-telluric method of geophysical prospecting, *Geophys.*, **18**, 605-635.

Campbell, W. H., 1987. Introduction to electrical properties of the Earth's mantle, *Pure Appl. Geophys.*, **125**, 193-204.

Canas, J. A. & Mitchell, B. J., 1978. Lateral variations of surface wave anelastic attenuation across the Pacific, *Bull. seismol. Soc. Am.*, **68**, 1637-1650.

Carslaw, H. S. & Jaeger, J. C., 1959. *Conduction of heat in solids*, 2nd Ed., Oxford University Press, New York.

Chamalaun, F. H. & Barton, C., 1990. Comprehensive mapping of Australia's geomagnetic variations, *EOS*, **71**, 1867 & 1873.

Chave, A. D. & Filloux, J. H., 1984. Electromagnetic induction fields in the deep ocean off California: oceanic and ionospheric sources, *Geophys. J. R. astr. Soc.*, **77**, 143-171.

Chave, A. D. & Filloux, J. H., 1985. Observation and interpretation of of the seafloor vertical electric field in the eastern North Pacific, *Geophys. Res. Lett.*, **12**, 793-796.

Chave, A. D., Constable, S. C. & Edwards, R. N., 1991. Electrical exploration methods for the seafloor, in *Electromagnetic Methods in Applied Geophysics*, ed. Nabighian, M. N., (in press) SEG, Washington.

Chave, A. D., Filloux, J. H., Luther, D. S., Law, L. K. & White, A., 1989. Observations of motional electromagnetic fields during EMSLAB, *J. geophys. Res.*, **94**, 14153-14166.

Chave, A. D., Filloux, J. H., Schultz, A., Groom, R. W. & Tarits, P., 1990. One-dimensional magnetotelluric soundings from BEMPEX, *10th Workshop on Electromagnetic Induction in the Earth*, Ensenada, Mexico.

Chave, A. D., Von Herzen, R. P., Poehls, K. A. & Cox, C. S., 1981. Electromagnetic induction fields in the deep ocean north-east of Hawaii: implication for mantle conductivity and source fields, *Geophys. J. R. astr. Soc.*, **66**, 379-406.

Constable, S. C. & Duba, A.,1990. Electrical conductivity of olivine, a dunite and the mantle, *J. geophys. Res.*, **95**, 6967-6978.

Constable, S. C. & Shankland, T. J., 1991. The electrical conductivity of isotropic olivine rock, *J. geophys. Res.* (submitted).

Constable, S. C., 1990. Marine electromagnetic induction studies, *Surveys in Geophysics,* **11**, 303-327.

Constable, S. C., 1991. Electrical studies of the Australian lithosphere, in *The Australian Lithosphere,* ed. Drummond, B. J., Geol. Soc. Aust. Spec. Pub. (in press).

Constable, S. C., Parker, R. L. & Constable, C. G., 1987. Occam's Inversion; a practical algorithm for generating smooth models from electromagnetic sounding data, *Geophysics,* **52**, 289-300.

Cox, C. S., 1980. Electromagnetic induction in the oceans and inferences on the constitution of the Earth, *Geophys. Surv.* **4**, 137-156.

Cox, C. S., 1981. On the electrical conductivity of the oceanic lithosphere, *Phys. Earth planet. Inter.,* **25**, 196-201.

Cox, C. S., Constable, S. C., Chave, A. D. & Webb, S. C., 1986. Controlled-source electromagnetic sounding of the oceanic lithosphere, *Nature,* **320**, 52-54.

Cox, C. S., Filloux, J. H. & Larsen, J. C., 1971. Electromagnetic studies of ocean currents and electrical conductivity below the seafloor, in *The Sea,* Vol **4**, Ch. 18, 637-693, ed Maxwell, A., Wiley-Interscience, New York.

Cox, C. S., Filloux, J. H., Gough, D. I., Larsen, J. C., Poehls, K. A., Von Herzen, R. P. & Winter, R., 1980. Atlantic lithosphere sounding, *J. Geomagn. Geoelectr.,* **32**, *Suppl I,* SI 13-SI 32.

Cox, C. S., Kroll, N., Pistek, P. & Watson, K., 1978. Electromagnetic fluctuations induced by wind waves on the deep-sea floor, *J. geophys. Res.,* **83**, 431-442.

Crane, K., 1985. The spacing of rift axis highs: dependence upon diapiric processes in the underlying asthenosphere, *Earth planet. Sci. Lett.,* **72**, 405-414.

Crane, K., Aikman, F., Ryan, W. B. F., Embley, R. W., Hammond, S. R., Malahoff, A. & Lupton, J. E., 1985. The distribution of geothermal fields on the Juan de Fuca Ridge, *J. geophys. Res.,* **90**, 727-744.

Cull, J. P., 1982. An appraisal of Australian heat-flow data, *BMR J. Aust. Geol. Geophys.,* **7**, 11-21.

Dawson, T. W. & Weaver, J. T., 1979. Three-dimensional induction in a non-uniform thin sheet at the surface of a uniformly conducting Earth, *Geophys. J. R. astr. Soc.,* **59**, 445-462.

deGroot-Hedlin, C & Constable, C. S., 1990. Occam's inversion to generate smooth two-dimensional models from magnetotelluric data, *Geophysics,* **55**, 1613-1624.

Delaney, J. R., Muenow, D. W. & Graham, D. G., 1978. Abundance and distribution of water, carbon and sulfur in the glassy rims of submarine pillow basalts, *Geochim. Cosmochim. Acta.,* **42**, 581-594.

DeLaurier, J. M., Auld, D. R. & Law, L. K., 1983. The geomagnetic response across the continental margin off Vancouver Island, comparison of results from numerical modelling and field data, *J. Geomagn. Geoelectr.*, **35**, 517-528.

Denham, D., 1985. The Tasman Sea earthquake of 25 November 1983 and stress in the Australian plate, *Tectonophysics.*, **111**, 329-338.

Detrick, R. S., Buhl, P., Vera, E., Mutter, J., Orcutt, J., Madsen, J. & Brocher, T., 1980. Multichannel seismic imaging of a crustal magma chamber along the East Pacific Rise, *Nature*, **326**, 35-41.

Dixon, J. E., Clague, D. A. & Eissen, J-P., 1986. Gabbroic Xenoliths and host ferrobasalt from the southern Juan de Fuca Ridge, *J. geophys. Res.*, **91**, 3795-3820.

Drury, M. J., 1981. Comment on 'Generalised thin-sheet analysis in magnetotellurics: an extension of Price's analysis' by R. P. Ranganayaki and T. R. Madden, *Geophys. J. R. astr. Soc.*, **65**, 237-238.

Duba, A. & Lilley, F. E. M., 1972. Effect of an ocean ridge model on geomagnetic variations, *J. geophys. Res.*, **77**, 7100-7105.

Duba, A. & Shankland, T. J., 1982. Free carbon and electrical conductivity in the Earth's mantle, *Geophys. Res. Lett.*, **9**, 1271-1274.

Duba, A., 1976. Are laboratory electrical conductivity data relevant to the Earth? *Acta Geod. Geophys. Mont. Hung.*, **11**, 485-495.

Duba, A., Boland J. N. & Ringwood, A. E., 1973. The electrical conductivity of pyroxene, *J. Geol.*, **81**, 727-735.

Duba, A., Heard, H. C. & Schock, R. N., 1974. Electrical conductivities of olivine at high pressure and under controlled oxygen fugacity, *J. geophys. Res.*, **79**, 1667-1673.

Duffy, T. S. & Anderson, D. L., 1989. Seismic velocities in mantle minerals and the mineralogy of the upper mantle, *J. geophys. Res.*, **94**, 1895-1912.

Dvorak, Z., 1973. Electrical conductivity of several samples of olivinites, peridotites, and dunites, as a function of pressure and temperature, *Geophysics*, **38**, 14-24.

Dziewonski, A. M. & Anderson, D. L., 1981. Preliminary reference Earth model, *Phys. Earth planet. Inter.*, **25**, 297-356.

Dziewonski, A. M., 1984. Mapping the lower mantle: determination of lateral heterogeneity in P velocity up to degree and order 6, *J. geophys. Res.*, **89**, 5929-5952.

Dziewonski, A. M., Hales, A. L. & Lapwood, E. R., 1975. Parametrically simple Earth models consistent with geophysical data, *Phys. Earth planet. Inter.*, **10**, 12-48.

Edwards, R. N., Law, L. K., Wolfgram, P. A., Nobes, D. C., Bone, M. N., Trigg, D. F. & DeLaurier, J. M., 1985. First results of the MOSES experiment, Bute Inlet, British Columbia, by magnetometric offshore electrical sounding. *Geophysics*, **50**, 153-161.

Egbert, G. D. & Booker, J. R., 1986. Robust estimation of geomagnetic transfer functions, *Geophys. J. R. astron. Soc.*, **87**, 173-194.

Eggers, D. W., 1982. An eigenstate formulation of the magnetotelluric impedance tensor, *Geophysics*, **47**, 1204-1214.

Embley, R. W. & Chadwick, W. W., 1990. Is the southern Juan de Fuca Ridge undergoing an episode of seafloor spreading?, *EOS*, **71**, 259.

Emerman, S. E. & Turcotte, D. L., 1984. The mid-ocean ridge axial valley as a steady state neck, *Earth planet. Sci. Lett.*, **26**, 222-232.

EMRIDGE Instrument Deployment Cruise, 1988. Deployment of the ocean bottom instruments for the seafloor measurements of electromagnetic signals, *R/V Hakuhomaru Cruise Report*, University of Tokyo, Tokyo, Japan.

EMSLAB Group, 1988. The EMSLAB Electromagnetic Sounding Experiment, *EOS*, **69**, 89, 98-99.

Evans, R. L., Constable, S. C., Sinha, M. C. & Cox., C. S., 1991. Upper crustal resistivity structure of the East Pacific Rise near 13 ° N, *Nature*, (submitted).

Everett. J. E. & Hyndman, R. D., 1967. Geomagnetic variations and the electrical conductivity structure of south-western Australia, *Phys. Earth planet. Inter.*, **1**, 24-34.

Fainberg, E. B., 1980. Electromagnetic induction in the world ocean, *Geophys. Surv.*, **4**, 157-171.

Ferguson, I. J., 1988. The Tasman Project of Seafloor Magnetotelluric Exploration, *Ph.D. thesis*, Australian National University, Canberra, Australia.

Ferguson, I. J., Filloux, J. H., Lilley, F. E. M., Bindoff, N. L. & Mulhearn, P. J., 1985. A seafloor magnetotelluric sounding in the Tasman Sea, *Geophys. Res. Lett.*, **12**, 545-548.

Ferguson, I. J., Lilley, F. E. M. & Filloux, J. H., 1990. Geomagnetic induction in the Tasman Sea and electrical conductivity structure beneath the Tasman Seafloor, *Geophys. J. Int.*, **102**, 299-312.

Filloux, J. H., 1967. Oceanic electric currents, geomagnetic variations and the deep electrical conductivity structure of the ocean-continent transition of central California, *Ph.D. Thesis*, University of California, San Diego, U.S.A.

Filloux, J. H., 1977. Ocean-floor magnetotelluric sounding over North Central Pacific, *Nature*, **269**, 297-301.

Filloux, J. H., 1980a. Magnetotelluric soundings over the Northeast Pacific may reveal spatial dependence of depth and conductance of the asthenosphere, *Earth planet. Sci. Lett.*, **46**, 244-252.

Filloux, J. H., 1980b. North Pacific magnetotelluric experiments, *J. Geomagn. Geoelectr.*, **32**, *Suppl I*, SI 33-SI 43.

Filloux, J. H., 1980c. Observation of very low frequency electromagnetic signals in the ocean, *J. Geomagn. Geoelectr.*, **32**, *Suppl I*, SI 1-SI 12.

Filloux, J. H., 1981. Magnetotelluric exploration of the North Pacific: progress report and preliminary soundings near a spreading ridge, *Phys. Earth planet. Inter.*, **25**, 187-195.

Filloux, J. H., 1982a. Electrical conductivity structure of the seafloor beneath the North Pacific. *Trans. Earthquake Res. Inst.*, Conductivity Anomaly Conference, 41-48.

Filloux, J. H., 1982b. Magnetotelluric experiment over the ROSE Area, *J. geophys. Res.*, **87**, 8364-8378.

Filloux, J. H., 1982c. Seafloor magnetotelluric soundings in the Mariana Island arc area, in *A.G.U Geophysical Monograph Series*, Vol. **27**, *The Tectonic Evolution of Southeast Asian Seas and Islands*, Part 2., 225-265.

Filloux, J. H., 1987. Instrumentation and experimental methods for oceanic studies, in *Geomagnetism*, Vol. **1**, pp. 143-248, ed. Jacobs, J. A., Academic Press, London.

Filloux, J. H., Law, L. K., Yukutake, T., Segawa, J., Hamano, Y., Utada, H., White, A., Chave, A. D., Tarits, P. & Green, A. W., 1989. OFFSHORE EMSLAB: objectives, experimental phase and early results, *Phys. Earth planet. Inter.*,**53**, 422-431.

Filloux, J. H., Lilley, F. E. M., Ferguson, I. J., Bindoff, N. L. & Mulhearn, P. J., 1985. The Tasman Project of Seafloor Magnetotelluric Exploration, *Exploration Geophysics*, **16**, 221-224 .

Fischer, G. & Le Quang, B. V., 1981. Topography and minimization of the standard deviation in one-dimensional magnetotelluric modelling, *Geophys. J. R. astr. Soc.*, **67**, 279-292.

Fischer, G. & Le Quang, B. V., 1982. Parameter trade-off in one-dimensional magnetotelluric modelling, *J. Geophys.*, **51**, 206-215.

Fischer, G. & Schnegg, P. -A., 1980. The dispersion relations of the magnetotelluric response and their incidence on the inversion problem, *Geophys. J. R. astr. Soc.*, **62**, 661-673.

Fischer, G. & Weaver, J. T., 1986. Theoretical investigations of the ocean-coast effect at a passive continental margin, *Phys. Earth & planet. Int.*, **42**, 246-254.

Fischer, G., Schnegg, P. -A., Peguiron, M. & Le Quang, B. V., 1981. An analytic one-dimensional magnetotelluric inversion scheme, *Geophys. J. R. astr. Soc.*, **67**, 257-278.

Fonarev, G. A., 1982. Electromagnetic research in the ocean, *Geophys. Surv.*, **4**, 501-508.

Forsyth, D. W., 1977. The evolution of the upper mantle beneath mid-ocean ridges, *Tectonophysics*, **38**, 89-118.

Fox, P. J. & Gallo, D. G., 1984. A tectonic model for ridge-transform-ridge plate boundaries: implications for the structure of oceanic lithosphere, *Tectonophysics*, **104**, 205-242.

Francis, T. J. G., 1985. Resistivity measurements of an ocean floor sulphide mineral deposit from the submersible Cyana, *Marine Geophys. Res.*, **7**, 419-438.

Frey, H., 1985. Magsat and POGO magnetic anomalies over the Lord Howe Rise: evidence against a simple continental crustal structure, *J. geophys. Res.*, **90**, 2631-2639.

Frost, B. R., Fyfe, W. S., Tazaki, K. & Chan, T., 1989. Grain-boundary graphite in rocks and implications for high electrical conductivity in the lower crust, *Nature*, **340**, 134-136.

Gamble, T. D., Goubau, W. M. & Clarke, J., 1979a. Error analysis for remote reference magnetotellurics, *Geophysics*, **44**, 959-968.

Gamble, T. D., Goubau, W. M. & Clarke, J., 1979b. Magnetotellurics with a remote reference, *Geophysics*, **44**, 53-68.

Godfrey, J. S., Cresswell, G. R., Golding, T. J. & Pearce, A. F., 1980. The separation of the East Australian Current, *J. Phys. Oceanog.*, **10**, 430-440.

Goubau, W. M., Gamble, T. D. & Clarke, J., 1978. Magnetotelluric data analysis: removal of bias, *Geophysics*, **43**, 1157-1166.

Grant, F. S. & West, G. F., 1965. *Interpretation Theory in Applied Geophysics*, pp. 583, McGraw-Hill Book Comp., New York.

Green, D. H. & Liebermann, R. C., 1976. Phase equilibria and elastic properties of a pyrolite model for the oceanic upper mantle, *Tectonophysics*, **32**, 61-92.

Green, H. W. & Gueguen, Y., 1974. Origin of kimberlite pipes by diapiric upwelling in the upper mantle, *Nature*, **249**, 617-620.

Green, V. R. & Weaver, J. T., 1978. Two-dimensional induction in a thin-sheet of variable integrated conductivity at the surface of a uniformly conducting earth, *Geophys. J. R. astr. Soc*, **55**, 721-736.

Grim, P. J., 1969. Heat flow measurements in the Tasman Sea, *J. geophys. Res.*, **74**, 3933-3934.

Groom, R. W. & Bailey, R. C., 1989. Decomposition of the magnetotelluric impedance tensor in the presence of local three-dimensional galvanic distortion, *J. geophys. Res.*, **94**, 1913-1925.

Habese, K., Fujii, N. & Uyeda, S., 1970. Thermal processes under island arcs, *Tectonophysics*, **10**, 335-355.

Hashin, Z. & Stricknam, S., 1963. A variational approach to the theory of the elastic behaviour of multi-phase materials, *J. Mech. Phys. Solids*, **11**, 127-140.

Hayes, D. E. & Ringis, J., 1973. Seafloor spreading in the Tasman Sea, *Nature*, **243**, 454-458.

Heinson, G. S. & Lilley, F. E. M., 1989. Thin-sheet EM modelling of the Tasman Sea, *Exploration Geophysics*, **20**,177-180.

Heinson, G. S. & Lilley, F. E. M., 1991. The electrical conductivity structure of the oceanic lithosphere beneath the Tasman Sea, *Exploration Geophysics*, **22**, 175-178.

Heinson, G. S., White, A., Law, L. K., Segawa, J., Hamano, Y., Utada, H., Yukutake, H. & Toh, H., 1991. EMRIDGE: the electromagnetic exploration of the Juan de Fuca Ridge, *Marine Geophys. Res.*, (submitted).

Hermance, J. F., 1979. The electrical conductivity of materials containing partial melts: a simple model from Archie's Law, *Geophys. Res. Lett.*, **6**, 613-616.

Hirsch, L. M., 1990. Enhancing mantle conductivity, *Nature*, **347**, 232.

Hobbs, B. A. & Brignall, A. M. M., 1976. A method for solving general problems of electromagnetic induction in the oceans, *Geophys. J. R. astr. Soc.*, **45**, 527-542.

Hobbs, B. A. & Dawes, G. J. K., 1979. Calculations of the effect of the oceans on geomagnetic variations with an application to the Sq field during the IGY, *J. Geophys.*, **46**, 271-289.

Hyndman R. D. & Salisbury, M. H., 1984. The physical nature of young upper oceanic crust on the mid-Atlantic Ridge, DSDP Hole 395A, in Hyndman, R. D. et al., *Init. Repts. DSDP*, **78B**, pp. 839-848, U.S. Govt. Printing Office, Washington.

Hyndman, R. D. & Shearer, P. M., 1989. Water in the lower continental crust: modelling magnetotelluric and seismic reflection results, *Geophys. J. Int.*, **98**, 343-365.

Ingham, M. R. & Hutton, V. R. S., 1982. Crustal and upper mantle electrical conductivity contrasts in southern Scotland, *Geophys. J. R. astr. Soc.*, **69**, 579-594.

Ingham, M. R., 1988. The use of invariant impedances in magnetotelluric interpretation, *Geophys. J*, **92**, 165-169.

J. geophys. Res. Special Section, 1989. Special Section on EMSLAB - Juan de Fuca Ridge experiment, *J. geophys. Res.*, **94**, 14093-14283.

Johansen, H. S. & Sørensen, K., 1979. Fast Hankel transforms, *Geophys. Prosp.*, **27**, 876-901.

Johnson, H. P. & Holmes, M. L., 1990. Evolution in plate tectonics: the Juan de Fuca Ridge, in *The Eastern Pacific Ocean and Hawaii*, pp.??, eds Winterer, E. L., Hussong, D. M. & Decker, R. W., Geology of North America Series, Vol N, GSA., U.S.A.

Jones, A. G., 1982. Observations of the electrical asthenosphere beneath Scandinavia, *Tectonophysics*, **90**, 37-55.

Jones, A. G., 1983. The problem of current channelling: a critical review, *Geophys. Surv.*, **6**, 79-122.

Jones, A. G., 1988. Static shift of magnetotelluric data and its removal in a sedimentary basin environment, *Geophysics*, **53**, 967-978.

Jones, A. G., Chave, A. D., Egbert, G., Auld, D. & Bahr, K., 1989. A comparison of techniques for magnetotelluric response function estimation, *J. geophys. Res.*, **94**, 14201-14213.

Jouanne, V., Bitterly, J., Menvielle, M. & Tarits, P., 1990. One year permanent magnetotelluric recordings at Port aux Francais observatory (Kerguelen Islands), *10th Workshop on Electromagnetic Induction in the Earth*, Ensenada, Mexico.

Karato, S., 1990. The role of hydrogen in the electrical conductivity of the upper mantle, *Nature*, **347**, 272-273.

Kariya, K. A. & Shankland, T. J., 1983. Electrical conductivity of dry lower crustal rocks, *Geophysics*, **48**, 52-61.

Katsura, T. & Ito, E., 1989. The system Mg_2SiO_4 - Fe_2SiO_4 at high pressures and temperatures: precise determination of stabilities of olivine, modified spinel and spinel, *J. geophys. Res.*, **94**, 15663-15670.

Kellett, R. L., 1989. Electrical conductivity structure of the southeast Australian Margin, *Ph.D. thesis*, Australian National University, Canberra, Australia.

Kellett, R. L., White, A., & Lilley, F. E. M., 1991. A two-dimensional interpretation of the geomagnetic coast effect of southeast Australia, observed on land and seafloor, *Tectonophysics*, (in press).

Kellett, R. L., White, A., Ferguson, I. J. & Lilley, F.E.M., 1988. Geomagnetic fluctuation anomalies across the southeast Australian coast, *Exploration Geophysics*, **19**, 294-297.

Kent, G. M., Harding, A. J. & Orcutt, J. A., 1990. Evidence for a smaller magma chamber beneath the East Pacific Rise at 9^{o} 30'N, *Nature*, **344**, 650-653.

Klein, D. P. & Larsen, J. C., 1978. Magnetic induction fields (2-30 cpd) on Hawaii Island and their implications regarding electrical conductivity in the oceanic mantle, *Geophys. J. R. astr. Soc.*, **53**, 61-77.

Kushiro, I., Syono, Y. & Akimoto, S., 1968. Melting of a peridotite nodule at high pressures and high water pressures, *J. geophys. Res.*, **73**, 6023-6029.

Larsen, J. C., 1975. Low frequency (0.1 - 6.0 cpd) electromagnetic study of the deep mantle electrical conductivity beneath the Hawaiian Islands, *Geophys. J. R. astr. Soc.*, **43**, 17-46.

Law, L. K. & Greenhouse, J. P., 1981. Geomagnetic variation sounding of the asthenosphere beneath the Juan de Fuca Ridge, *J. geophys. Res.*, **86**, 967-978.

Law, L. K., 1978. An ocean bottom magnetometer: design an first deployment near the Explorer ridge, *EOS*, **59**, 235.

Law, L. K., 1983. Marine electromagnetic research, *Geophys. Surv.*, **6**, 123-135.

Leeds, A. R., Knopoff, L. & Kausel, E. G., 1974. Variations of upper mantle structure under the Pacific Ocean, *Science*, **186**, 141-143.

Li, X. & Jeanloz, R., 1987. Measurement of the electrical conductivity of (MgFe)Si_3 perovskite and a perovskite dominated assemblage at lower mantle conditions, *Geophys. Res. Lett.*, **14**, 1075-1078.

Lilley, F. E. M. & Arora, B. R., 1982. The sign convention for quadrature Parkinson arrows in geomagnetic induction studies, *Rev. Geophys. Space Phys.*, 20, 513-518.

Lilley, F. E. M., 1975. Running waves and standing waves in geomagnetic depth sounding, *J. Geomagn Geoelectr.*, **27**, 491-504.

Lilley, F. E. M., Burden, F. R., Boyd, G. W. & Sloane, M. N., 1975. Performance tests of a set of Gough-Reitzel magnetic variometers, *J. Geomagn. Geoelectr.*, **27**, 75-83.

Lilley, F. E. M., Filloux, J. H. & Ferguson, I. J., 1991. Evidence for a magnetic signature from the East Australian current, *Australian Physical Oceanography Conference*, Canberra, Australia.

Lilley, F. E. M., Filloux, J. H., Bindoff, N. L., Ferguson, I. J. & Mulhearn, P. J., 1986. Barotropic flow of a warm-core ring from seafloor electric measurements, *J. geophys. Res.*, **91**, 12979-12984.

Lilley, F. E. M., Filloux, J. H., Ferguson, I. J., Bindoff, N. L. & Mulhearn, P. J., 1989. The Tasman Project of Seafloor Magnetotelluric Exploration: experiment and observations, *Phys. Earth planet. Inter.*, **53**, 405-421.

Lilley, F. E. M., Woods, D. V. & Sloane, M. N., 1981. Electrical conductivity from Australian magnetometer arrays using spatial gradient data, *Phys. Earth planet. Inter.*, **25**, 202-209.

Lin, J., Purdy, G. M., Schouten, H., Sempéré, J. -C. & Zervas, C., 1990. Evidence from gravity data for focused magmatic accretion along the Mid-Atlantic Ridge, *Nature*, **344**, 627-632.

Lister, G. S., Etheridge, M. A. & Symonds, P. A., 1986. Detachment faulting and the evolution of passive continental margins, *Geology*, **14**, 246-250.

Liu, L-G., 1989. Water, low-velocity zone and the descending lithosphere, *Tectonophysics*, **164**, 41-48.

Luther, D. S., Chave, A. D. & Filloux, J. H., 1987. BEMPEX: A study of barotropic ocean currents and lithospheric electrical conductivity, *EOS*, **68**, 618-619, 628-629.

Macdonald, K. C., Fox, P. J., Perram, L. J., Eisen, M. F., Haymon, R. M., Miller, S. P., Carbotte, S. M., Cormier, M.-H. & Shor, A. N., 1988. A new view of the mid-ocean ridge from the behaviour of ridge-axis discontinuities, *Nature*, **335**, 217-225.

Mackie, R. L., Bennet, B. R. & Madden, T. R., 1988. Long-period magnetotelluric measurements near the central Californian coast: a land-locked view of the conductivity structure under the Pacific Ocean, *Geophys. J.*, **95**, 181-194.

Mackwell, S. J. & Kohlstedt, D. L., 1990. *J. geophys. Res.*, **95**, 5079-5088.

Mackwell, S. J., Kohlstedt, D. L. & Paterson, M. S., 1985. The role of water in the deformation of olivine single crystals, *J. geophys. Res.*, **90**, 11319-11333.

Madden, T. R., 1976. Random networks and mixing laws, *Geophysics*, **41**, 574-588.

Mareschal, M., Vasseur, G., Srivastava, B. J. & Singh, R. N., 1987. Induction models of southern India and the effect of off-shore geology, *Phys. Earth planet. Inter.*, **45**, 137-148.

Marty, J. C. & Cazenave, A., 1989. Regional variations in subsidence rate of oceanic plates: a global analysis, *Earth planet. Sci. Lett.*, **94**, 301-315.

McDougall, I. & Duncan, R. A., 1988. Age progressive volcanism in the Tasmantid Seamounts, *Earth planet. Sci. Lett.*, **89**, 207-220.

McDougall, I. & van der Lingen, G. J., 1974. Age of rhyolites of the Lord How Rise and the evolution of the southwestern Pacific Ocean, *Earth planet. Sci. Lett.*, **21**, 117-126.

McKenzie, D. P., 1967. Some remarks on heat flow and gravity anomalies, *J. geophys. Res.*, **72**, 6261-6273.

McKenzie, D. P., 1989. Some remarks on the movement of small melt fractions in the mantle, *Earth planet. Sci. Lett.*, **95**, 53-72.

McKirdy, D. McA. & Weaver, J. T., 1983. A numerical study of the channelling of induced currents between two oceans, *J. Geomagn. Geoelectr.*, **35**, 623-641.

McKirdy, D. McA., Weaver, J. T. & Dawson, T. W., 1985. Induction in a thin sheet of variable conductance at the surface of a stratified earth; II, three-dimensional theory, *Geophys. J. R. astron. Soc.*, **80**, 177-194.

Mercier, J. C. & Carter, N. L., 1975. Pyroxene geotherms, *J. geophys. Res.*, **80**, 3349-3362.

Molnar, P. & Oliver, J., 1969. Lateral variations of attenuation in the upper mantle and discontinuities in the lithosphere, *J. geophys. Res.*, **74**, 2648-2682.

Morin, R. H. & Von Herzen, R. P., 1986. Geothermal measurements at Deep Sea Drilling Project site 587, in Kennett, J. P. et al., *Init. Repts. DSDP*, **90**, pp. 1317-1324, U.S. Govt. Printing Office, Washington.

Muenow, D. W., Graham, D. G., Kin, N. W. K. & Delaney, J. R., 1979. The abundance of volatiles in Hawaiian tholeiite submarine basalts, *Earth planet. Sci. Lett.*, **42**, 71-76.

Mulhearn, P. J., Filloux, J. H., Lilley, F. E. M., Bindoff, N. L. & Ferguson, I. J., 1988. Abyssal currents during the formation and passage of a warm-core ring in the East Australian Current, *Deep-Sea Res.*, **33**. 1563-1576.

Mutter, J. C., Barth, G. A., Buhl, P., Detrick, R. S., Orcutt, J. & Harding, A., 1988. Magma distribution across ridge-axis discontinuities on the East Pacific Rise from multichannel seismic images, *Nature*, **336**, 156-158.

Navrotsky, A. & Akaogi, M., 1984. The α, β, γ phase relations in Fe_2SiO_4 - Mg_2SiO_4 and Co_2SiO_4 - Mg_2SiO_4: calculations from thermodynamical data and geophysical applications, *J. geophys. Res.*, **89**, 10135-10140.

Niblett, E. R., Kurtz, R. D. & Michaud, C., 1987. Magnetotelluric measurements over the Alpha Ridge, *Phys. Earth planet. Inter.*, **45**, 101-118.

Nicoll, M. A. & Weaver, J. T., 1977. H-polarisation over an ocean edge coupled to the mantle by a conducting crust, *Geophys. J. R. astr. Soc.*, **49**, 427-441.

Nobes, D. C., Law, L. K. & Edwards, R. N., 1986a. The determination of resistivity and porosity of the sediment and fractured basalt layers near the Juan de Fuca Ridge, *Geophys. J. R. astr. Soc.*, **86**, 101-118.

Nobes, D. C., Villinger, H., Davis, E. R. & Law, L. K., 1986b. Estimation of sediment bulk physical physical properties at depth from sea floor geophysical measurements, *J. geophys. Res.*, **91**, 14033-14043.

O'Reilly, S. Y. & Griffin, W. L., 1985. A xenolith-derived geotherm for southeastern Australia and its geophysical implications, *Tectonophysics*, **111**, 41-63.

Oldenburg, D. W., 1981. Conductivity structure of oceanic upper mantle beneath the Pacific Plate, *Geophys. J. R. astron. Soc.*, **65**, 359-394.

Oldenburg, D. W., Whittall, K. P. & Parker, R. L., 1984. Inversion of ocean bottom magnetotelluric data revisited, *J. geophys. Res.*, **89**, 1829-1833.

Omura, K., Kurita, K. & Kumazawa, M., 1989. Experimental study of pressure dependence of electrical conductivity of olivine at high temperatures, *Phys. Earth planet. Inter.*, **57**, 291-303.

Oni, E. & Agunloye, O., 1974. A predominant parameter n_p of the inducing source field for induction studies in low-latitudes, *Pure Appl. Geophys.*, **112**, 967-975.

Orcutt, J. A., 1987. Structure of the Earth; oceanic crust and uppermost mantle, *Rev. Geophys.*, **25**, 1177-1196.

Palshin, N. A., Shneyer, V. S., Abramov, Yu. M., Poray.Koshitz, A. M., Abramova, L. M., Vanyan, L. L., Zhdanov, M. S., De Santis, A. & Phillippopoulos, G. N., 1990. Geomagnetic sounding in Mediterranean Sea, *10th Workshop on Electromagnetic Induction in the Earth*, Ensenada, Mexico.

Park, S. K. & Livelybrooks, D. W., 1989. Quantitative interpretation of rotationally invariant parameters in magnetotellurics, *Geophysics*, **54**, 1483-1490.

Park, S. K., 1985. Distortion of magnetotelluric sounding curves by three-dimensional structures, *Geophysics*, **50**, 785-797.

Park, S. K., Orange, A. S. & Madden, T. R., 1983. Effects of three-dimensional structures in magnetotelluric sounding curves, *Geophysics*, **48**, 1402-1405.

Parker, R. L. & Oldenburg, D. W., 1973. Thermal model of ocean ridges, *Nature Phys. Sci.*, **242**, 137-139.

Parker, R. L. & Whaler, K. A., 1981. Numerical methods for establishing solutions to the inverse problem of electromagnetic induction, *J. geophys. Res.*, **86**, 9574-9584.

Parker, R. L., 1980. The inverse problem' of electromagnetic induction - existence and construction of solutions based on incomplete data, *J. Geophys Res.*, **85**, 4421-4428.

Parker, R. L., 1982. The existence of a region inaccessible to magnetotelluric sounding, *Geophys. J. R. astr. Soc.*, **68**, 165-170.

Parker, R. L., 1983. The magnetotelluric inverse problem, *Geophys. Surv.*, **6**, 5-25.

Parker, R. L., Shure, L. & Hildebrand, J. A., 1987. The application of inverse theory to seamount magnetism, *Rev. Geophys.*, **25**, 17-40.

Parkinson, W. D., 1962. The influence of continents and oceans on geomagnetic variations, *Geophys. J. R. astron. Soc.*, **6**, 441-449.

Parkinson, W. D., 1983. *Introduction to Geomagnetism.* pp. 433, Scottish Academic Press, Edinburgh.

Parsons, B. & Sclater, J. G., 1977. An analysis of the variation of ocean floor bathymetry and heat flow with age, *J. geophys. Res.*, **82**, 803-827.

Patra, H. P. & Mallick, K., 1980. *Geosounding Principles, 2 Time-Varying Geoelectric Soundings.* pp. 449, Elsevier, Amsterdam.

Perfit, M. R., Jonasson, I. R. and Embley, R. W., 1989. Geochemical and observational evidence for recent eruption and rifting as a cause of 'megaplume' events along the southern Juan de Fuca Ridge, 1989, *EOS*, **70**, 1400.

Piwinskii, A. J. & Duba, A., 1974. High temperature electrical conductivity of albite, *Geophys. Res. Lett.*, **1**, 209-211.

Poehls, K. A. & Von Herzen, R. P., 1976. Electrical resistivity structure beneath the North-west Atlantic Ocean, *Geophys. J. R. astron. Soc.*, **47**, 331-346.

Presnall, D. C., 1980. A double partial melt zone in the mantle beneath mid-ocean ridges, *Phys. Earth planet. Inter.*, **23**, 103-111.

Presnall, D. C., Dixon, J. R., O'Donnell, T. H. & Dixon, S. A., 1979. Generation of mid-ocean ridge tholeiites, *J. Petrology*, **20**, 3-35.

Price, A. T., 1950. Electromagnetic induction in a semi-infinite conductor with a plane boundary, *Quart. J. Mech. App. Math.*, **3**, 385-410.

Price, A. T., 1962. The theory of magnetotelluric methods when the source field is considered, *J. geophys. Res.*, **67**, 1907-1918.

Quist, A. S. & Marshall, W. L., 1968. Electrical conductance of aqueous sodium chloride solutions from 0 to 800 °C and at pressures to 4000 Bars, *J. phys. Chem.*, **71**, 684-703.

Rai, C. S. & Manghnani, M. H., 1978. Electrical conductivity of ultramafic rocks to 1812 Kelvin, *Phys. Earth planet. Inter.*, **17**, 6-13.

Ranganayaki, R. P. & Madden, T. R., 1980. Generalized thin sheet analysis in magnetotellurics: an extension of Price's analysis, *Geophys. J. R. astr. Soc.*, **60**, 445-457.

Ranganayaki, R. P. & Madden, T. R., 1981. Reply to 'Comment on 'Generalised thin-sheet analysis in magnetotellurics: an extension of Price's analysis' by R. P. Ranganayaki and T. R. Madden' by Malcolm Drury, *Geophys. J. R. astr. Soc.*, **65**, 239-240.

Ranganayaki, R. P., 1984. An iterative analysis of magnetotelluric data, *Geophysics*, **49**, 1730-1748.

Ribe, N., 1989. Seismic anisotropy and mantle flow, *J. geophys. Res.*, **94**, 4213-4223.

Price, A. T., 1949. The induction of electric currents in non-uniform thin sheets and shells, Quart. J. Mech. App. Math., 2, 283-310.

Ringwood, A. E., 1975. *Composition and Petrology of the the Earth's Mantle.*, McGraw-Hill, New York.

Ringwood, A. E., 1982. Phase transformations and differentiation in subducted lithosphere: implications for mantle dynamics, basalt petrogenesis and crustal evolution, *J. Geol.*, **90**, 611-643.

Salisbury, M. H., Stephen, R., Christensen, N.I., Francheteau, J., Hamano, Y., Hobart, M. & Johnson, D., 1980. The physical state of the upper levels of cretaceous oceanic crust from the results of logging, laboratory studies, and the oblique seismic experiment at deep sea drilling project sites 417 and 418. **51-53**, 2, pp. 237-244, U.S. Govt. Printing Office, Washington.

Sato, H., Selwyn-Sacks, I. & Murase, T., 1989. The use of laboratory velocity data for estimating temperatures and partial melt fraction in the low-velocity zone: comparison with heat flow and electrical conductivity studies, *J. geophys. Res.*, **94**, 5689-5704.

Sato, H., Selwyn-Sacks, I., Takahashi, E. & Scarfe, C. M., 1988. Geotherms in the Pacific Ocean from laboratory and seismic attenuation studies, *Nature*, **336**, 154-156.

Scarfe, C. & Takahashi, E., 1986. Melting of garnet peridotite to 13 GPa and early history of the upper mantle, *Nature*, **322**, 354-356.

Schmeling, H., 1986. Numerical models on the influence of partial melt on elastic, anelastic and electrical properties of rocks. Part II: electrical conductivity, *Phys. Earth planet. Inter.*, **43**, 123-136.

Schmucker, U. & Jankowsky, J., 1972. Geomagnetic induction studies and the electrical state of the upper mantle, *Tectonophysics*, **13**, 233-256.

Schmucker, U., 1970. Anomalies of geomagnetic variations in the southwestern United States, *Bull. Scripps Inst. Oceanog.*, **13**, pp. 165.

Schock, R. N., Duba, A. & Shankland, T. J., 1989. Electrical conduction in olivine, *J. geophys. Res.*, **94**, 5829-5839. .

Schubert, G. & Sandwell, D., 1989. Crustal volumes of the continents and of oceanic and continental submarine plateaus, *Earth planet. Sci. Lett.*, **92**, 234-246.

Schultz, A., 1990. On the vertical gradient and associated heterogeneity in mantle electrical conductivity, *Phys. Earth planet. Inter.*, **64**, 68-86.

Schwarz, G., 1990. Electrical conductivity of the Earth's crust and upper mantle, *Surveys in Geophysics*, **11**, 133-163.

Segawa, J., 1986. Review of the development of ocean bottom magnetometers, *8th Workshop on Electromagnetic Induction in the Earth and Moon*, Neuchatel, Switzerland.

Segawa, J., Hamano, Y., Yukutake, T. & Utada, H., 1983. A new model of ocean bottom magnetometer, *J. Geomagn. Geoelectr.*, **35**, 407-421.

Sempéré, J. -C., Purdy, G. M. & Schouten, H., 1990. Segmentation of the Mid-Atlantic Ridge between 24°N and 30°40'N, *Nature*, **344**, 427-431.

Severinghaus, J. P. & Macdonald, K. C., 1988. High inside corners at ridge-transform intersections, *Mar. Geophys. Res.*, **9**, 353-367.

Shankland, T. J. & Anders, M. E., 1983. Electrical conductivity, temperatures and fluids in the lower crust, *J. geophys. Res.*, **88**, 9475-9484.

Shankland, T. J. & Duba, A., 1990. Standard electrical conductivity of isotropic, homogeneous olivine in the temperature range 1100-1500 °C, *Geophys. J. Int.*, **103**, 25-32.

Shankland, T. J. & Waff, H. S., 1977. Partial melting and electrical conductivity anomalies in the upper mantle, *J. geophys. Res.*, **82**, 5409-5417.

Shankland, T. J., 1981. Electrical conduction in mantle materials, in *Evolution of the Earth, Geodynamics Ser.*, vol. **5**, pp. 256-263, eds O'Connell, R. J. & Fyfe, W. S., AGU, Washington D.C. & Geological Society of America, Boulder, Colorado.

Shor, G. G. Jr, Kirk, H. K. & Menard, H. W. 1971. Crustal structure of the Melanesian Area, *J. geophys. Res.* **76**, 2562-2586.

Smith, J. T. & Booker, J. R., 1988. Magnetotelluric inversion for minimum structure, *Geophysics*, **53**, 1565-1576.

Smith, J. T. & Booker, J. R., 1991. The rapid relaxation inverse for two and three-dimensional magnetotelluric data, *J. geophys. Res.*, (in press).

Smith, R. S. & West, G. F., 1987. Electromagnetic induction in an inhomogeneous conductive thin-sheet, *Geophysics*, **52**, 1677-1688.

Srivastava, S. P., 1966. Theory of the magneto-telluric method for a spherical conductor, *Geophys. J. R. astr. Soc.*, **11**, 373-387.

Stacey, F. D., 1977a. A thermal model of the Earth, *Phys. Earth planet. Inter.*, **15**, 341-348.

Stacey, F. D., 1977b. *Physics of the Earth*, John Wiley, New York.

Stolper, E. M., Walker, D., Hager, B. H. & Hays, J. F., 1981. Melt segregation from partially molten source regions: the importance of melt density and source region size, *J. geophys. Res.*, **86**, 6261-6271.

Sundaralingam, K. & Denham, D. 1987. Structure of the upper mantle beneath the Coral and Tasman Seas, as obtained from group and phase velocities of Rayleigh waves, *N. Z. J. Geol. Geophys.*, **30**, 329-341.

Swift, C. M., 1967. A magnetotelluric investigation of an electrical conductivity anomaly in the southwestern United States, *Ph.D. thesis*, M.I.T., U.S.A.

Takahashi, E. & Kushiro, I., 1983. Melting of a dry peridotite at high pressures and basalt magma genesis, *Am, Mineral.*, **68**, 859-879.

Takahashi, E., 1986. Melting of a dry peridotite KLB-1 up to 14 GPa: implications on the origin of peridotitic upper mantle, *J. geophys. Res.*, **91**, 9367-9382.

Tammemagi, H. Y. & Lilley, F. E. M., 1971. Magnetotelluric studies across the Tasman Geosyncline, Australia, *Geophys. J. R. astr. Soc.*, **22**, 505-516.

Tarits, P., 1986. Conductivity and fluids in the oceanic upper mantle, *Phys. Earth planet. Inter.*, **42**, 215-226.

Tarits, P., Filloux, J. H., Chave, A. D., Menvielle, M. & Sichler, B., 1990. Seafloor electromagnetic sounding of the Tahiti hot spot, *10th Workshop on Electromagnetic Induction in the Earth*, Ensenada, Mexico.

Tarits, P., Filloux, J. H., Larsen, J. C. & Klein, D. P., 1986. Seafloor electromagnetic sounding near Hawaiian Islands, *8th Workshop on Electromagnetic Induction in the Earth and Moon*, Neuchatel, Switzerland.

Tikhonov, A. N., 1950. On investigation of the electrical characteristics of deep strata of Earth's crust, *Dokl. Akad. Naik. SSSR*, **73**, 295-297.

Toomey, D. R., Purdy, G. M., Solomon, S. C. & Wilcock, W. S. D., 1990. The three-dimensional seismic velocity structure of the East Pacific Rise near latitude 9° 30' N, *Nature*, **347**, 639-645.

Toramaru, A. & Naoyuki, F., 1986. Connectivity of melt phase in a partially molten peridotite, *J. geophys. Res.*, **91**, 9239-9252.

Tozer, D. C., 1979. The interpretation of upper-mantle electrical conductivities, *Tectonophyics*, **56**, 147-163.

Tozer, D. C., 1981. The mechanical and electrical properties of Earth's asthenosphere, *Phys. Earth planet. Inter.*, **25**, 280-296.

Trofimov, I. L. & Fonarev, G. A., 1976. Deep magnetotelluric surveys in the Arctic Ocean, in *Geoelectric and Geothermal Studies*, pp. 712-715, ed. Adam, A., KAPG Geophys. Monogr., Budapest.

Trofimov, I. L., 1979. Magnetotelluric sounding in the Canadian Basin, *Geomag. and Aeronomy*, **19**, 602-604.

Turcotte, D. L. & Schubert, G., 1982. *Geodynamics*, pp. 450,John Wiley, New York.

Turcotte, D. L., 1982. Magma migration, *Ann. Rev. Earth planet. Sci.*, **10**, 397-408.

Tyburczy, J. A. & Roberts, J. J., 1990. Low frequency electrical response of polycrystalline olivine compacts: grain boundary transport, *Geophys. Res. Lett.*, 17, 1985-1988.

Tyburczy, J. A. & Waff, H. S., 1983. Electrical conductivity of molten basalt and andesite to 25 kilobars pressure: geophysical significance and implications for charge transport and melt structure, *J. geophys. Res.*, **88**, 2413-2430.

USGS Juan de Fuca Study Group, 1986. Submarine fissure eruptions and hydrothermal vents on the southern Juan de Fuca Ridge: preliminary observations from the submersible ALVIN, *Geology*, **14**, 823-827.

Vanyan, L. L., Palshin, N., Koldaev, D., Cox, C. S. & Constable, S. C., 1990. Anisotropy of the ocean lithosphere, *10th Workshop on Electromagnetic Induction in the Earth,* Ensenada, Mexico.

Vasseur, G. & Weidelt, P., 1977. Bimodal electromagnetic induction in non-uniform thin sheets with an application to the northern Pyrenean induction anomaly, *Geophys. J. R. astr. Soc.*, **51**, 669-690.

Von Herzen, R. P., Francis, T. J. G. & Becker, K., 1983. *In situ* large-scale electrical resistivity of ocean crust, hole 504B, in Cann, J. R. et al., *Init. Repts. DSDP*, **69**, pp. 237-244, U.S. Govt. Printing Office, Washington.

Vozoff, K., 1972. The magnetotelluric method in the exploration of sedimentary basins, *Geophys.*, **37**, 98-141.

Waff, H. S. & Weill, D. F., 1975. Electrical conductivity of magmatic liquids; effects of temperature, oxygen fugacity and composition, *Earth planet. Sci. Lett.*, **28**, 254-260.

Waff, H. S., 1974. Theoretical considerations of electrical conductivity in partially molten mantle and implications for geothermometry, *J. geophys. Res.*, **79**, 4003-4010.

Waff, H. S., 1980. Effects of the gravitational field on liquid distribution in partial melts within the upper mantle, *J. geophys. Res.*, **85**, 1815-1825.

Wait, J. R., 1954. On the relation between telluric currents and the Earth's magnetic field, *Geophysics*, **19**, 281-289.

Walker, D., Stoplar, E. M. & Hays, J. F., 1978. A numerical treatment of melt / solid segregation: size of the eucrite parent body and stability of the terrestrial low-velocity zone, *J. geophys. Res.*, **83**, 6005-6013.

Wannamaker, P. E., Booker, J. R., Filloux, J. H., Jones, A. G., Jiracek, G. R., Chave, A. D., Tarits, P., Waff, H. S., Egbert, G. D., Young, C. T., Stodt, J. A., Martinez, M., Law, L. K., Yukutake, T., Segawa, J., White, A.and Green Jr., A. W., 1989a. Magnetotelluric observations across the Juan de Fuca Subduction system in the EMSLAB project, *J. geophys. Res. - Special Section On EMSLAB*, **94**, 14111-14125.

Wannamaker, P. E., Booker, J. R., Jones, A. G., Chave, A. D., Filloux, J. H., Waff, H. S. & Law, L. K., 1989b. Resistivity cross section through the Juan de Fuca Ridge subduction system and its tectonic implications, *J. geophys. Res. - Special Section On EMSLAB*, **94**, 14127-14144, 14277-14283.

Wannamaker, P. E., Hohmann, G. W. & Ward, S. H., 1984. Magnetotelluric responses of three-dimensional bodies in layered earths, *Geophys.*, **49**, 1517-1533.

Wannamaker, P. E., Stodt, J. A. & Rijo, L.,1986, A stable finite element solution for two-dimensional magnetotelluric modeling, *Geophys. J. R. astr. Soc.*, **88**, 277-296.

Weaver, J. T., 1973. Induction in a layered plane earth by uniform and non-uniform source fields, *Phys. Earth planet. Inter.*, **7**, 266-281.

Weaver, J. T., 1982. Regional induction in Scotland; an example of three-dimensional numerical modelling using the thin sheet approximation, *Phys. Earth planet. Inter.*, **28**, 161-180.

Weaver, J. T., Le Quang, B. V. & Fischer, G., 1985. A comparison of analytical and numerical results for a two-dimensional control model in electromagnetic induction - I. B-polarisation calculations, *Geophys. J. R. astr. Soc.*, **82**, 263-277.

Weaver, J. T., Le Quang, B. V. & Fischer, G., 1986. A comparison of analytical and numerical results for a two-dimensional control model in electromagnetic induction - II. E-polarisation calculations, *Geophys. J. R. astr. Soc.*, **87**, 917-948.

Webb, S. C., Constable, S. C., Cox, C. S. & Deaton, T. K., 1985. A seafloor electric field instrument, *J. Geomagn. Geoelectr.*, **37**, 1115-1129.

Weidelt, P., 1972. The inverse problem of geomagnetic induction, *Z. Geophys.*, **38**, 257-289.

Weidelt, P., 1975. Electromagnetic induction in three-dimensional structures, *J. Geophys.*, **41**, 85-109.

Weidelt, P., 1977. Numerical study of a conductive channelling effect, *Acta Geod. Geophys. Mont. Hung.*, **11**, 195-205.

Weissel J. K. & Hayes, D. E., 1977. Evolution of the Tasman Sea re-appraised, *Earth planet. Sci. Lett.*, **36**, 77-84.

White, A. & Polatajko, O. W., 1978. The coast effect in geomagnetic variations in South Australia, *J. Geomagn. Geoelectr.*, **30**, 109-120.

White, A., 1979. A seafloor magnetometer for the continental shelf, *Mar. Geophys. Res.*, **4**, 105-114.

White, A., Kellett, R. L. & Lilley, F. E. M., 1989. The Continental Slope Experiment along the Tasman Project profile, southeast Australia, *Phys. Earth planet. Inter.*, **60**, 147-154.

White, D. J. & Clowes, R. M., 1990. Shallow crustal structure beneath the Juan de Fuca Ridge from 2-D seismic refraction tomography, *Geophys. J. Int.*, **100**, 349-367.

Whitehead, J. A., Dick, H. J. B., and Schouten, H., 1984. A mechanism for magmatic accretion under spreading centres, *Nature*, **312**, 146-148.

Winch, D. E, 1981. Spherical harmonic analysis of geomagnetic tides, *Phil. Trans. R. Soc. London*, Ser. A, **303**, 1-101.

Winch, D. E., 1989. Induction in a model ocean, *Phys. Earth planet. Inter.*, **53**, 328-336.

Woodhouse, J. H. & Dziewonsky, A. M., 1984. Mapping the upper mantle: three dimensional modelling of Earth structure by inversion of seismic waveforms, *J. geophys. Res.*, **89**, 5953-5986.

Woods, D. V. & Lilley, F. E. M., 1980. Anomalous geomagnetic variations and the concentration of telluric currents in south-west Queensland, Australia, *Geophys. J. R. astr. Soc.*, **62**, 6750689.

Wyllie, P. J., 1977. Mantle fluid compositions buffered by carbonates in peridotite-CO_2-H_2O, *J. Geol.*, **85**, 187-207.

Young, P.D. & Cox, C.S., 1981. Electromagnetic active source sounding near the East Pacific Rise, *Geophys. Res. Lett.*, **8**, 1043-1046.

Yukutake, T., Filloux, J. H., Segawa, J., Hamano, Y. & Utada, H. 1983. Preliminary report on a magnetotelluric array study in the Northwest Pacific, *J. Geomagn. Geoelectr.*, **35**, 575-587.